

**AN EXPERIMENTAL SPATIO-TEMPORAL ANALYSIS OF  
SEPARATED FLOWS OVER BLUFF BODIES USING  
QUANTITATIVE FLOW VISUALIZATION**

*By*  
***Pavlos P. Vlachos***

*Dissertation submitted to the faculty of the  
Virginia Polytechnic Institute and State University  
in partial fulfillment of the requirements for the degree of*

**DOCTOR OF PHILOSOPHY**

*in*  
***Engineering Science and Mechanics***

**Dr. D.P. Telionis , Chair**

**Dr. M. R. Hajj**

**Dr. H.W. Tieleman**

**Dr. R. Kriz**

**Dr. W. J. Devenport**

***August 2000,***  
***Blacksburg, Virginia***

***Keywords: Particle Image Velocimetry, flow visualization, bluff body wakes,  
free-surface flows, cylinder wake, three-dimensional separation  
separated shear layer, separation bubble***

**© Copyright, 2000, Pavlos P. Vlachos**

# **AN EXPERIMENTAL SPATIO-TEMPORAL ANALYSIS OF SEPARATED FLOWS OVER BLUFF BODIES USING QUANTITATIVE FLOW VISUALIZATION**

*by*

*Pavlos P. Vlachos*

*Committee Chairman Demetri P Telionis*

***(Abstract)***

In order to study three-dimensional unsteady turbulent flow fields such as the wakes of bluff bodies, a Digital Particle Image Velocimetry (DPIV) system was developed. This system allows non-intrusive two-dimensional and time varying velocity measurements. Software and hardware modifications necessary to enhance the capabilities of the system were performed, resulting in increased frequency resolution. However, due to hardware limitations and limitations inherited from the implementation of the method, space resolution is reduced. Subsequently, digital image processing tools to improve the space resolutions were developed. The advantages and limitations of the method for the study of turbulent flows are presented in detail.

The developed system is employed in the documentation of time-varying turbulent flow fields. Initially we study the spanwise variation of the near wake of a low-aspect ratio, surface-mounted, circular cylinder piercing a free surface. The asymmetry of the end conditions combined with the natural unsteadiness of the vortex shedding generates a very complex flow field which is difficult to study with conventional methods. By employing the aforementioned system we are able to reveal a departure of the two-dimensional character of the flow in the form

of oblique vortex shedding. The effect of free surface on the vortex formation length and on the vortex reconnection process is documented. Near the free surface the alternate mode of vortex shedding is suppressed, leading to simultaneous shedding of vortices in the wake. Indications of vortex dislocations and change of the vortex axis in order to reconnect to the free surface are observed. Finally, a novel approach of reconstructing the three-dimensional, time -varying volume of the flow field by obtaining simultaneous measurements of Laser Doppler Velocimetry and Particle Image Velocimetry planes is presented.

The same field is investigated with focus on the streamwise structures. Three-dimensional streamwise vortical structures are known to exist due to instabilities of plane shear layers. Similar streamwise vortices, also known as braid vortices have been observed in the past in the wake of circular cylinders with symmetric boundary conditions. The present spatio-temporal analysis demonstrated coexistence of two types of streamwise vortices in the wake, bilge and braid type of vortices. These may be due to the three dimensionality introduced by the free surface. In addition, the sufficient time resolution allowed the detection of the primary Von-Karman vortex through a plane of interrogation normal to the free stream, thus revealing the spanwise variation of the vortex shedding and its evolution at different downstream stations.

The combination of the effect of the asymmetric boundary conditions with a free surface is investigated by adding one more source of three-dimensionality in terms of inclination of the cylinder axis. Hydrogen-bubble and particle-flow visualizations are preformed in combination with Laser-Doppler Velocimetry measurements. From both qualitative and quantitative results the effects of inclination and Froude number are documented. It is proved that the vortex shedding is suppressed for high values of the Froude number, however the inclination counteracts the vortex suppression and favors the vortex shedding mechanism. In addition, in the region of the no-slip boundary condition the flow is dominated by the effect of the horseshoe vortex.

The case of a three-dimensional separated flow over a surface-mounted prism is investigated using a modified version of the system. The character of the separated from the

leading edge corner shear layer and the formed separation bubble are documented in space and time along the mid-plane of symmetry of the body. Three different flows corresponding to different Reynolds numbers are studied. The unsteadiness of the flow is presented indicating a pseudo-periodic character. Large-scale, low-frequency oscillations of the shear layer that have been observed in the past using point measurement methods are now confirmed by means of a whole field velocity measurement, technique allowing a holistic view of the flow. In addition, the unsteadiness of the point of reattachment is associated with the flapping of the shear layer and the shedding of vorticity in the wake. Finally, it is demonstrated that the apparent vortex shedding mechanism of such flows is dependent on the interaction of the primary vortex of the separation bubble with a secondary vortex formed by the separation of the reverse flow boundary layer. By performing measurements with such time and space resolution the inadequacy of time averaged or point measurement methods for the treatment of such complex and unsteady flow fields becomes evident.

In final case we employ Particle-Image Velocimetry to show the effect of unsteady excitation on two-dimensional separated flow over a sharp edged airfoil. It is proved that such an approach can be used to effectively control and organize the character of the flow, potentially leading to lift increase and drag reduction of bluff bodies.

*Dedicated*  
*to my parents Theoni and Polychroni Vlachou*  
*and to my soul mate Maria Boura.*

*I did what I had to do.*  
*They did more than they have ever expected or imagined that they could do.*  
*This is their achievement, more than it is mine*  
*...and to the memory of my grandfather Ioanni Kollia*

## After thoughts...instead of a preface

It is my feeling that no intellectual effort is complete without an attempt of “*self-criticism*”. Especially the case of the degree of Doctor of Philosophy would not justify the word *philosophy* without including criticism and skepticism on an overall evaluation of the work carried out. Furthermore I ought to my ancient Greek ancestors to try to be a little philosophical in order to honor their inheritance to our contemporary way of thinking.

What determines the success or the failure of any type of effort is the answer to one small and simple question: If I had the chance to do it again or start all over from the beginning, would I do it? Without the slightest hesitation I would reply: Yes. However if we take this to the next level and ask a few more questions, like... are you satisfied with the final result? Is the level representative to the amount of work and effort invested? Were you efficient enough? Or more importantly ...would you do it the same way? The answer is No, for all of the above. More could have been done, better. An old traditional Greek saying goes: “If only I knew then what I know now”. But, “*ifs*” can hound us for the rest of our lives and still never know *if something could have been different*. So, one has to compromise. Furthermore, a doctorate is a learning experience. You are not supposed to know “a-priori” the things that you know at the end. From this perspective it has been the best possible experience and I feel grateful, privileged and blessed to work and learn from people who unconditionally allowed me to steal from them, as much of their knowledge as I could carry with me.

I apologize for grasping the opportunity to use this text as a podium to express my personal thoughts and feelings into a medium that time will not alter. The completion of post-

graduate studies in the area of fluid mechanics is for me a childhood “dream come true” since the early age of fifteen. Even in my wildest dreams I never anticipated that it would take me so far: five thousand miles away from home family and friends, literally and metaphorically. So, this by itself must be worth something. However, this point leaves me on a crossroad wondering which way to go. Should I stay on the same path or should I choose a different one? Is there a new one? Where do they lead? What if they are all the same? It is easy to get trapped into a vicious circle of endless questions with no answers. What is the right choice? Is there a right choice? Is there a choice at all or are we deluding ourselves believing that we have the power of choice. Can you avoid the inevitable? This is an oxymoron, one out of many that life is full of. I do not feel ready to answer any of these questions. I believe I will never be. More importantly, I am certain that I don't have to.

Fluid mechanics exposes you into nature's philosophy. To flow with the flow. To love turbulence. The random chaotic self-organizing structures. Nature loves oxymorons and their underlying irony that our limited intellectuality on many occasions fails to comprehend. Nature loves turbulence because under any condition she allows each element to find its own state of equilibrium with respect to its neighborhood. Break the apparent symmetry to reveal a new order of self-similar structures as if the small replicates the big and the younger learns from the older. Rise, grow, dominate and finally decay. All these occur sequentially in a dynamically changing and evolving system. From chaos rises order and with teleonomic consistency, randomness leads to organization.

I like to believe that the study of fluid mechanics is a study of nature, society and life. Very arrogantly, I hope, that perhaps one day my limited understanding of my surroundings will allow me to put a small part of all these into one frame. But until then, I have to flow with the flow, and not ask questions expecting always to find the answers. Ask the questions in order to keep the discussion going, so that the next person will ask a better question, in an ongoing process, until we reach the point when we are going to ask the *right* question. That is the duty and obligation of every scientist and the most important objective of any intellectual effort.

As far as making decisions for the future ...

*“...you plan as if you will never die and act as if you are going to die tomorrow...”*

*Alexis Zorbas (N. Kazantakis)*

As far as choosing the *right* path... you hope that you won't have to choose. If that road already exists, it is because someone else has crossed before. You do not choose someone else's options, you make your own. You find a small piece of land where there is no path. There, you take the risk to try and make your own:

*"Believe me! The secret of reaping the greatest fruitfulness and the greatest enjoyment from life is to live dangerously!"*

*Zaratoustra (F. W. Nietzsche)*

Finally, upon completion of the dissertation, one starts a career that is supposed to advance our discipline towards the betterment of our society. Since we have been fortunate enough to be introduced to the marvels of nature and the challenge of scientific knowledge it is our moral obligation and privilege to try to advance further knowledge and technology and to guide others to follow and serve society. Thus we will be true to our universities' call:

*“UT PROSIM”*

Unfortunately, standing in front of the colossal amount of information and knowledge that we have created during centuries of continuous efforts, you cannot help wondering if such an ambition is possible. Even more, isn't it arrogant to hope such a thing? With these thoughts, I came to the conclusion that by exposing myself to the continuously learning process of scientific research it has been the most intellectually humiliating experience. For once more the Greek philosopher Socrates was right saying:

**«Εν οίδα, ό,τι ουδέν οίδα»**

*“I only know one thing, that I know nothing at all” or differently “...the more I learn, the more I realize that I know nothing”*

*(Socrates)*

However, there are two undeniable and undisputable truths and one unanswered question that stands larger than any other. The first truth is: “*God exists*”. The second truth is: “*I am not She.*” *But I am grateful to Her for everything. And the final question that maybe even SHE can't answer is:*

**“Why turbulence?”**

*(Heisenberg)*

## ***Acknowledgements***

Alexander the Great used to say for his teacher Aristotelis, that: “...*my father gave me life, but my teacher gave me good life*”. Professor Demetri P. Telionis has been to me an advisor, a teacher and a friend. My mentor. He provided me with the opportunity and support to pursue and accomplish a life’s dream. He taught me about fluid mechanics, science and life with his advice but more importantly with his example. He shared his excitement and enthusiasm, always encouraging and motivating me to do more. Thanks to him, a whole new world is now open in front of me. There are no words to express how grateful I am.

Dr. M. R. Hajj supported me from the first day I started this effort. He unconditionally provided me with a wealth of fluid mechanics understanding through endless discussions and friendly advices. Working under his supervision as a graduate teaching assistant and collaborating in pursue of scientific results was an educational and enjoyable experience.

Dr. H. Tieleman introduced me to turbulence and unveiled the beauty and complexity of turbulent flows. He provided thorough and detailed revisions of this text trying to help me perfect it. His contribution is gratefully acknowledged.

Dr. R. Kriz showed me the power of visual tools in the analysis of complex physical phenomena. He offered me information and advice throughout the course of this effort. Our discussions have always been exciting. I am thankful to Dr. W. Devenport for serving on my committee and providing his experimental expertise and knowledge. Dr. Saad Ragab served on my committee for a limited time but had to resign spend a sabbatical year off campus. His absence deprived me of his valuable insight and understanding of fluid mechanics. However, his advice was always unconditionally available.

Thanks to my colleges in the Fluid Mechanics Laboratory who guided my first steps in the lab and shared with me, on an everyday basis, the problems and frustrations of experimental work, Martin Donnelly, Matt Zeiger and Norman Schaeffler. You can accomplish more through teamwork. They are a great team.

Special thanks to D. Stamos and S. Miranda for showing to me that all experiences can be educational. Taught me to expect the unexpected, hope for the best but prepare for the worst. My interaction with them was a life's lesson.

Big thanks, to all my students so far. In many occasions they made this effort worthwhile. Having the opportunity to teach was more educational to me than what it was to them.

From the early days of elementary school to my university years in Greece I was fortunate to be exposed to a series of exceptional teachers. Their influence has established my present foundations. I thank them.

No success is complete enough unless you can share it with your friends, and no obstacle is large enough to stop you if you can fight it with your friends. With some of my friends I go back as many as twenty years. With some others it has been a few quality years that shaped up and tested our friendship. Niko Boura, Eleni Antonopoulou, Petro Mylona, Mari Kosteletoy, Giorgio Potho, Kosti Aggeli, Xari Triantafylloy, Kosta Giavi, Niko Asimopoulo. Thank you for been my friends and tolerating me. Throughout time for better or for worse friends are forever.

How can you express your gratitude for the greatest gift ever. Thank you Theoni and Panagiotti Boura for giving me your love and Maria. Thank you for supporting us all the way.

Last and foremost I thank my family. A solid indestructible foundation on top of which I was fortunate enough to start building. Marousa, Olga and Niko Kollia... giving me so much love that I do not deserve. My wife to be, Maria. My parents Theoni and Polychroni. So much support, effort, self-sacrifice that words fail to express. Never let me down; never let me stop or settle. They give meaning and value to my life..

In Greece we use to say: "saying less is philosophical" and I have said too much already. A "thank you" is not enough. It is only up to time and actions to really show the level of my gratitude. I hope I will be able to meet that challenge.

*«Τά Πάντα Ρεΐ»*

*“All matter Flows”*

*(Hraklitos)*

# Table of Contents

<b>After thoughts...instead of a preface</b>	<b>vi</b>
<i>Acknowledgements</i>	<b>x</b>
<b>Table of Contents</b>	<b>xiv</b>
<b>Table of Figures</b>	<b>xviii</b>
<b>Table of Animations</b>	<b>xxviii</b>
<b>Table of Tables</b>	<b>xxxiv</b>
<b>CHAPTER 1</b>	<b>1</b>
<b>Introduction</b>	<b>1</b>
Motivation	1
Outline	5
<b>CHAPTER 2</b>	<b>7</b>
<b>Facilities Instrumentation and Methods of Investigation</b>	<b>7</b>
ESM Fluid Mechanics Laboratory Water Tunnel	7
Velocity Measurement Techniques.	11
Laser Doppler Velocimetry	11
Component-Based, Mirror-Directed LDV system	11
Two-Velocity Component Fiber-Optic-Delivered LDV System	13
LDV Signal Processing and Data Acquisition	15

Particle Image Velocimetry (PIV)_____	16
A system for high speed Digital PIV Cinematography (DPIVC)_____	16
Hardware description _____	17
Digital Particle Image Velocimetry Evaluation Software_____	21
Data Analysis, Error and Uncertainty _____	25
Image Processing Tools and Particle Tracking Velocimetry _____	27
High-Speed High-Particle-Density Particle-Tracking Velocimetry _____	27
Introduction_____	27
Particle Tracking Algorithm _____	28
Results_____	32
<b>CHAPTER 3 _____</b>	<b>36</b>
<b>On The Wake Of A Circular Cylinder Near The Free Surface. _____</b>	<b>36</b>
Spanwise Vorticity Distribution in the Near Wake Region _____	36
Introduction_____	36
Experimental details _____	41
Facilities and Experimental Setup_____	41
DPIV Software and Data Analysis _____	44
Mean and Turbulent Characteristics of Spanwise Vorticity near the Free Surface _____	48
Results and Discussion _____	48
Unsteady and Instantaneous Flow Characteristics _____	76
Results and Discussion _____	79
Conclusions_____	95
Three-Dimensional Streamwise Vortical Structures of a Turbulent Wake near the Free Surface. _____	97
Introduction_____	97
Experimental details _____	99
Results and discussion_____	102
Conclusions_____	103
<b>CHAPTER 4 _____</b>	<b>111</b>

<b>The Effect Of Free-Surface and Inclination on the Vortex Shedding Behind Circular Cylinders</b>	<b>111</b>
Introduction	111
Experimental details	114
Hydrogen Bubble Flow Visualizations	114
Particle Flow Visualizations	116
LDV Measurements	116
Results and Discussion	120
Hydrogen-Bubble Flow Visualization	120
Particle Flow Visualizations	123
LDV Frequency Measurements	124
Conclusions	127
<b>CHAPTER 5</b>	<b>155</b>
<b>Flow characteristics of the separated region over a surface mounted prism</b>	<b>155</b>
Introduction	155
Experimental Setup	158
Mean and Turbulent Characteristics	164
Results and Discussion	164
Unsteady and Instantaneous Flow Characteristics	182
Particle Flow Visualization	182
Instantaneous Velocity and Vorticity Measurements	186
Conclusions	202
<b>CHAPTER 6</b>	<b>205</b>
<b>Control of separated shear layers over sharp edges</b>	<b>205</b>
Introduction	205
Facilities and Instrumentation	208
Results and Discussion	209
Conclusions	211

<b>CHAPTER 7</b>	<b>226</b>
Conclusions	226
References	231
<b>APPENDIX I</b>	<b>243</b>
<b>On The Wake Of A Circular Cylinder Near The Free Surface. Additional Data</b>	<b>243</b>
Effect of the asymmetry boundary conditions on the vorticity distribution.	243

# Table of Figures

<b>CHAPTER 1</b>	<b>1</b>
<b>CHAPTER 2</b>	<b>7</b>
<i>Figure 1:</i> Schematic representation of the ESM Water tunnel facility.	8
<i>Figure 2:</i> Water tunnel calibration chart for different settings of the DC motor and different elevations.	9
<i>Figure 3:</i> TSI Fiber Optic LDV system layout schematic. (Schematic provided from the system manual.)	14
<i>Figure 4:</i> Schematic layout of the IACL45 laser head configuration.	20
<i>Figure 4-1:</i> Schematic of the Magnetic Pulse Compression unit located in the front end of the laser head (see previous figure: HEAD CAPACITORS)	20
<i>Figure 5:</i> Gray-scale sample image that demonstrates the high particle concentration.	29
<i>Figure 6:</i> Sample image after the application of the threshold.	30
<i>Figure 7:</i> Sample image after the erode procedure.	30
<i>Figure 8:</i> Sample image of the “OR” procedure resulted within a sequence of 10 frames.	31
<i>Figure 9:</i> Particle trajectories traced within a sequence of ten frames. A unique identity (16-bit color) is assigned to each particle.	33
<i>Figure 10:</i> Particle trajectories within a sequence of 10 frames corresponding to 380 vectors.	34
<i>Figure 11:</i> Velocity vectors resulting from a commercial cross-correlation PIV software, corresponding to the same instance of the flow field. From the top, vectors	

calculated with 32x32 interrogation window with 0% overlapping, with 16x16 window with 0% overlapping, and with 16x16 window with 50% overlapping. \_\_\_\_\_ 35

**CHAPTER 3 \_\_\_\_\_ 36**

**Figure 1:** A view of the experimental setup with the laser sheet in the wake of cylinder and parallel to the free surface. \_\_\_\_\_ 43

**Figure 1-1:** PIV planes located with respect to the flow and the cylinder for measurements parallel to the free surface. \_\_\_\_\_ 44

**Figure 2:** Graphical representation of the accuracy of the method with respect to the number of particles for a window of interrogation of  $16^2$  pixels for an artificial flow field with a displacement dynamic range from 0.5 pixels to 7 pixels \_\_\_\_\_ 46

**Figure 3:** Set of figures for the velocity magnitude. \_\_\_\_\_ 52

**Figure 3-1:** Color contours of Velocity Magnitude distribution for plane 1. \_\_\_\_\_ 52

**Figure 3-2:** Color contours of Velocity Magnitude distribution for plane 2 \_\_\_\_\_ 52

**Figure 3-3:** Color contours of Velocity Magnitude distribution for plane 3. \_\_\_\_\_ 53

**Figure 3-4:** Color contours of Velocity Magnitude distribution for plane 4. \_\_\_\_\_ 53

**Figure 3-5:** Color contours of Velocity Magnitude distribution for plane 5. \_\_\_\_\_ 54

**Figure 3-6:** Color contours of Velocity Magnitude distribution for plane 6. \_\_\_\_\_ 54

**Figure 3-7:** Color contours of Velocity Magnitude distribution for plane 7. \_\_\_\_\_ 55

**Figure 4:** Set of figures for the vorticity distribution \_\_\_\_\_ 56

**Figure 4-1:** Color contours of Vorticity distribution for plane 1. \_\_\_\_\_ 56

**Figure 4-2:** Color contours of Vorticity distribution for plane 2. \_\_\_\_\_ 56

**Figure 4-3:** Color contours of Vorticity distribution for plane 3. \_\_\_\_\_ 57

**Figure 4-4:** Color contours of Vorticity distribution for plane 4. \_\_\_\_\_ 57

**Figure 4-5:** Color contours of Vorticity distribution for plane 5. \_\_\_\_\_ 58

**Figure 4-6:** Color contours of Vorticity distribution for plane 6. \_\_\_\_\_ 58

**Figure 4-7:** Color contours of Vorticity distribution for plane 7. \_\_\_\_\_ 59

**Figure 5:** Set of figures for U-RMS distribution \_\_\_\_\_ 60

**Figure 5-1:** Color contours of U-RMS distribution for plane 1 \_\_\_\_\_ 60

**Figure 5-2:** Color contours of U-RMS distribution for plane 2. \_\_\_\_\_ 60

**Figure 5-3:** Color contours of U-RMS distribution for plane 3. \_\_\_\_\_ 61

<b>Figure 5-4:</b>	Color contours of U-RMS distribution for plane 4.	61
<b>Figure 5-5:</b>	Color contours of U-RMS distribution for plane 5.	62
<b>Figure 5-6:</b>	Color contours of U-RMS distribution for plane 6.	62
<b>Figure 5-7:</b>	Color contours of U-RMS distribution for plane 7.	63
<b>Figure 6:</b>	Set of figures for the V-RMS distribution.	64
<b>Figure 6-1:</b>	Color contours of V-RMS distribution for plane 1.	64
<b>Figure 6-2:</b>	Color contours of V-RMS distribution for plane 2.	64
<b>Figure 6-3:</b>	Color contours of V-RMS distribution for plane 3.	65
<b>Figure 6-4:</b>	Color contours of V-RMS distribution for plane 4.	65
<b>Figure 6-5:</b>	Color contours of V-RMS distribution for plane 5.	66
<b>Figure 6-6:</b>	Color contours of V-RMS distribution for plane 6.	66
<b>Figure 6-7:</b>	Color contours of V-RMS distribution for plane 7.	67
<b>Figure 7:</b>	Set of figures for Turbulent Kinetic Energy distribution.	68
<b>Figure 7-1:</b>	Color contours of TKE distribution for plane 1.	68
<b>Figure 7-2:</b>	Color contours of TKE distribution for plane 2.	68
<b>Figure 7-3:</b>	Color contours of TKE distribution for plane 3.	69
<b>Figure 7-4:</b>	Color contours of TKE distribution for plane 4.	69
<b>Figure 7-5:</b>	Color contours of TKE distribution for plane 5.	70
<b>Figure 7-6:</b>	Color contours of TKE distribution for plane 6.	70
<b>Figure 7-7:</b>	Color contours of TKE distribution for plane 7.	71
<b>Figure 8:</b>	Set of figures for $U^iV^j$ distribution.	72
<b>Figure 8-1:</b>	Color contours of $U^iV^j$ distribution for plane 1.	72
<b>Figure 8-2:</b>	Color contours of $U^iV^j$ distribution for plane 2.	72
<b>Figure 8-3:</b>	Color contours of $U^iV^j$ distribution for plane 3.	73
<b>Figure 8-4:</b>	Color contours of $U^iV^j$ distribution for plane 4.	73
<b>Figure 8-5:</b>	Color contours of $U^iV^j$ distribution for plane 5.	74
<b>Figure 8-6:</b>	Color contours of $U^iV^j$ distribution for plane 6.	74
<b>Figure 8-7:</b>	Color contours of $U^iV^j$ distribution for plane 7.	75
<b>Figure 9:</b>	Original LDV signals with the mean value subtracted	77
<b>Figure 10:</b>	Comparison of filtered and unfiltered LDV signals	78
<b>Figure 11:</b>	Shifted filtered signal by an estimate time delay	78

**Figure 12:** Three-dimensional representation of the vorticity distribution for the planes of interrogation after been shifted on the same reference time. Plane 7 is made transparent and projected on the right side for clarity. \_\_\_\_\_ 90

**Figure 12-1:** Three-dimensional representation of the planes of interrogation at  $t/T=0$  90

**Figure 12-2:** Three-dimensional representation of the planes of interrogation at  $t/T=0.5$  91

**Figure 12-3:** Three-dimensional representation of the planes of interrogation at  $t/T=1.0$  92

**Figure 12-4:** Three-dimensional representation of the planes of interrogation at  $t/T=1.5$  93

**Figure 12-5:** Three-dimensional representation of the planes of interrogation at  $t/T=2.0$  94

**Figure 1:** Schematic representation of the placement of the interrogation planes with respect to the free-stream velocity and the passing of the primary Von-Karman vortex through the planes. The projection on the right demonstrates the intersection of the vortex core with the field of view. At this instant, the domains of the flow field on either side of the core will be directing the flow to opposite directions, thus indicating the vortex shedding mechanism. \_\_\_\_\_ 100

**Figure 1-1:** Schematic representation of the placement of the spanwise interrogation planes with respect to the streamwise planes and the passing of the primary Von-Karman vortex through the planes. Blue color corresponds to the flow, red to the spanwise planes and green to the streamwise ones. \_\_\_\_\_ 101

**Figure 2:** Vorticity contours and velocity vectors for the second plane at  $t=0$  seconds 104

**Figure 3:** Vorticity contours and velocity vectors for the second plane at  $t=0.08$  seconds 104

**Figure 4:** Vorticity contours and velocity vectors for the second plane at  $t=0.16$  seconds 105

**Figure 5:** Vorticity contours and velocity vectors for the second plane at  $t=0.24$ seconds \_\_\_\_\_ 105

- Figure 6:** Vorticity contours and velocity vectors for the second plane at  $t=0.32$  seconds 106
- Figure 7:** Vorticity contours and velocity vectors for the second plane at  $t=0.4$  seconds 106
- Figure 8:** Vorticity contours and velocity vectors for the fourth plane at  $t=0.8$  seconds 107
- Figure 9:** Vorticity contours and velocity vectors for the fourth plane at  $t=0.16$  seconds 107
- Figure 10:** Vorticity contours and velocity vectors for the fourth plane at  $t=0.24$  seconds 108
- Figure 11:** Vorticity contours and velocity vectors for the fourth plane at  $t=0.32$  seconds 108
- Figure 12:** Vorticity contours and velocity vectors for the fourth plane at  $t=0.40$  seconds 109
- Figure 13:** Vorticity contours and velocity vectors for the fourth plane at  $t=0.48$  seconds 109
- Figure 14:** Iso-surface representation of the vorticity distribution in the space-time domain for the first period of the flow. Blue color corresponds to negative vorticity and red color to positive. X-Y plane corresponds to the physical two-dimensional plane and Z is the time axis. The free surface is approximately located at  $y/L=1.5$  \_\_\_\_\_ 110

## CHAPTER 4 \_\_\_\_\_ 111

- Figure 1:** : Inclination of the cylinder with respect to the free stream velocity \_\_ 118
- Figure 1-1:** Schematic representation of the position of the hydrogen bubble wire and the fiber optic LDV probe with respect to the cylinder axis. The location of the area of interrogation for the particle flow visualizations is also shown. (All dimensions are in mm.) 118
- Figure 1-2:** Schematic representation of the intersection of the interrogation fields (hydrogen bubbles –particles) with the corresponding laser sheets and the shed vortices. 119

<b>Figure 2:</b> Power Spectra contours as a function of the elevation. Inclination $\alpha=0$ degrees, $Re=1700$ .	146
<b>Figure 3:</b> Power Spectra contours as a function of the elevation. Inclination $\alpha=0$ degrees, $Re=3700$ .	147
<b>Figure 4:</b> Power Spectra contours as a function of the elevation. Inclination $\alpha=0$ degrees, $Re=6000$ .	148
<b>Figure 5:</b> Power Spectra contours as a function of the elevation. Inclination $\alpha=30$ degrees, $Re=1700$ .	149
<b>Figure 6:</b> Power Spectra contours as a function of the elevation. Inclination $\alpha=30$ degrees, $Re=3700$ .	150
<b>Figure 7:</b> Power Spectra contours as a function of the elevation. Inclination $\alpha=30$ degrees, $Re=6000$ .	151
<b>Figure 8:</b> Power Spectra contours as a function of the elevation. Inclination $\alpha=-30$ deg., $Re=1700$ .	152
<b>Figure 9:</b> Power Spectra contours as a function of the elevation. Inclination $\alpha=-30$ deg., $Re=3700$ .	153
<b>Figure 10:</b> Power Spectra contours as a function of the elevation. Inclination $\alpha=-30$ deg., $Re=6000$	154

## **CHAPTER 5** \_\_\_\_\_ **155**

<b>Figure 1:</b> View of the prism geometry	158
<b>Figure 2:</b> View of the experimental setup, showing the arrangement of the DPIV system.	163
<b>Figure 3:</b> Set of figures for the velocity vectors	168
<b>Figure 3-1:</b> Velocity vectors for the first case of $Re=2500$ .	168
<b>Figure 3-2:</b> Velocity vectors for the second case of $Re=9000$ .	168
<b>Figure 3-3:</b> Velocity vectors for the third case of $Re=16500$ .	169
<b>Figure 4:</b> Set of figures for the velocity magnitude	170
<b>Figure 4-1:</b> Color contours of Velocity Magnitude for the first case of $Re=2500$ .	170
<b>Figure 4-2:</b> Color contours of Velocity Magnitude for the second case of $Re=9000$ .	170

<b>Figure 4-3:</b>	Color contours of Velocity Magnitude for the third case of Re=16500.	171
<b>Figure 5:</b>	Set of figures presenting the reverse coefficient.	172
<b>Figure 5-1:</b>	Color contours of reverse coefficient for the first case of Re=2500.	172
<b>Figure 5-2:</b>	Color contours of reverse coefficient for the second case of Re=9000.	172
<b>Figure 5-3:</b>	Color contours of reverse coefficient for the third case of Re=16500.	173
<b>Figure 6:</b>	Set of figures for the vorticity distribution.	174
<b>Figure 6-1:</b>	Color contours of Vorticity for the first case of Re=2500.	174
<b>Figure 6-2:</b>	Color contours of Vorticity for the second case of Re=9000.	174
<b>Figure 6-3:</b>	Color contours of Vorticity for the third case of Re=16500.	175
<b>Figure 7:</b>	Set of figures for $u'_{rms}$ .	176
<b>Figure 7-1:</b>	Color contours of $u'_{rms}$ for the first case of Re=2500.	176
<b>Figure 7-2:</b>	Color contours of $u'_{rms}$ for the second case of Re=9000.	176
<b>Figure 7-3:</b>	Color contours of $u'_{rms}$ for the third case of Re=16500.	177
<b>Figure 8:</b>	Set of figures for $v'_{rms}$	178
<b>Figure 8-1:</b>	Color contours of $v'_{rms}$ for the first case of Re=2500.	178
<b>Figure 8-2:</b>	Color contours of $v'_{rms}$ for the second case of Re=9000.	178
<b>Figure 8-3:</b>	Color contours of $v'_{rms}$ for the third case of Re=16500.	179
<b>Figure 9:</b>	Set of figures for the TKE.	180
<b>Figure 9-1:</b>	Color contours of TKE for the first case of Re=2500.	180
<b>Figure 9-2:</b>	Color contours of TKE for the second case of Re=9000.	180
<b>Figure 9-3:</b>	Color contours of TKE for the third case of Re=16500.	181
<b>Figure 10:</b>	Schematic representation of the flow over the prism, the formation of the horseshoe vortex, the separation and reattachment regions.	184
<b>CHAPTER 6</b>		<b>205</b>
<b>Figure 1:</b>	Schematic of experimental setup	211
<b>Figure 2:</b>	Sharp edged airfoil dimensions(all dimensions in inches)	212
<b>Figure 3:</b>	Average Vector Field, 20° AOA, Reference Airfoil	212
<b>Figure 4:</b>	Average Vector Field, 20° AOA, 2 Hz Actuation	213

<b>Figure 5:</b>	Vorticity 10° AOA, Reference Airfoil _____	213
<b>Figure 6:</b>	Vorticity 10° AOA, 0 Hz Actuation _____	214
<b>Figure 7:</b>	Vorticity 10° AOA, 2 Hz Actuation _____	214
<b>Figure 8:</b>	Vorticity 10° AOA, 4 Hz Actuation _____	215
<b>Figure 9:</b>	Vorticity 10° AOA, 8 Hz Actuation _____	215
<b>Figure 10:</b>	Vorticity 20° AOA, Reference Airfoil _____	216
<b>Figure 11:</b>	Vorticity 20° AOA, 0 Hz Actuation _____	216
<b>Figure 12:</b>	Vorticity 20° AOA, 2 Hz Actuation _____	217
<b>Figure 13:</b>	Vorticity 20° AOA, 4 Hz Actuation _____	217
<b>Figure 14:</b>	Vorticity 20° AOA, 8 Hz Actuation _____	218
<b>Figure 15:</b>	Vorticity 30° AOA, Reference Airfoil _____	218
<b>Figure 16:</b>	Vorticity 30° AOA, 0 Hz Actuation _____	219
<b>Figure 17:</b>	Vorticity 30° AOA, 2 Hz Actuation _____	219
<b>Figure 18:</b>	Vorticity 30° AOA, 4 Hz Actuation _____	220
<b>Figure 19:</b>	Vorticity 30° AOA, 8 Hz Actuation _____	220
<b>Figure 20:</b>	Streamlines, Time Averaged flow field 20° AOA, Reference Airfoil	221
<b>Figure 21:</b>	Streamlines, Time Averaged flow field 20° AOA, 0 Hz Actuation _	221
<b>Figure 22:</b>	Streamlines, Time Averaged flow field 20° AOA, 2 Hz Actuation _	222
<b>Figure 23:</b>	Streamlines, Time Averaged flow field 20° AOA, 4 Hz Actuation _	222
<b>Figure 24:</b>	Streamlines, Time Averaged flow field 20° AOA, 8 Hz Actuation _	223
<b>Figure 25:</b>	Streamlines, Time Averaged flow field 30° AOA, Reference Airfoil	223
<b>Figure 26:</b>	Streamlines, Time Averaged flow field 30° AOA, 0 Hz Actuation _	224
<b>Figure 27:</b>	Streamlines, Time Averaged flow field 30° AOA, 2 Hz Actuation _	224
<b>Figure 28:</b>	Streamlines, Time Averaged flow field 30° AOA, 4 Hz Actuation _	225
<b>Figure 29:</b>	Streamlines, Time Averaged flow field 30° AOA, 8 Hz Actuation _	225
<b>CHAPTER 7</b>	_____	<b>226</b>
<b>APPENDIX I</b>	_____	<b>243</b>
<b>Figure 1:</b>	Time averaged velocity distributions _____	245

<b>Figure 1-1:</b>	Time averaged velocity vectors for the first plane at the free surface.	245
<b>Figure 1-2:</b>	Time averaged velocity vectors for the first plane at the base of the cylinder	245
<b>Figure 1-3:</b>	Time averaged velocity vectors for the second plane at the free surface.	246
<b>Figure 1-4:</b>	Time averaged velocity vectors for the second plane at the base of the cylinder	246
<b>Figure 1-5:</b>	Time averaged velocity vectors for the second plane at the free surface.	247
<b>Figure 1-6:</b>	Time averaged velocity vectors for the second plane at the base of the cylinder	247
<b>Figure 2:</b>	Time averaged vorticity distributions _____	248
<b>Figure 2-1:</b>	Time averaged vorticity for the first plane at the free surface. _____	248
<b>Figure 2-2:</b>	Time averaged vorticity for the first plane at the base of the cylinder	248
<b>Figure 2-3:</b>	Time averaged vorticity for the second plane at the free surface. _____	249
<b>Figure 2-4:</b>	Time averaged vorticity for the second plane at the base of the cylinder	249
<b>Figure 2-5:</b>	Time averaged vorticity for the second plane at the free surface. _____	250
<b>Figure 2-6:</b>	Time averaged vorticity for the second plane at the base of the cylinder	250
<b>Figure 3:</b>	Time averaged in plane turbulent kinetic energy distributions _____	251
<b>Figure 3-1:</b>	Time averaged in plane turbulent kinetic energy for the first plane at the free surface.	251
<b>Figure 3-2:</b>	Time averaged turbulent kinetic energy for the first plane at the base of the cylinder	252
<b>Figure 3-3:</b>	Time averaged turbulent kinetic energy for the second plane at the free surface.	252
<b>Figure 3-4:</b>	Time averaged turbulent kinetic energy for the second plane at the base of the cylinder	253
<b>Figure 3-5:</b>	Time averaged turbulent kinetic energy for the second plane at the free surface.	253

**Figure 3-6:** Time averaged turbulent kinetic energy for the second plane at the base of the cylinder 254

# Table of Animations

<b>CHAPTER 1</b>	<b>1</b>
<b>CHAPTER 2</b>	<b>7</b>
<b>CHAPTER 3</b>	<b>36</b>
<i>Animation 1:</i> Animation of velocity vectors and vorticity contours for the first plane of elevation.	83
<i>Animation 2:</i> Animation of velocity vectors and vorticity contours for the second plane of elevation.	84
<i>Animation 3:</i> Animation of velocity vectors and vorticity contours for the third plane of elevation.	85
<i>Animation 4:</i> Animation of velocity vectors and vorticity contours for the fourth plane of elevation.	86
<i>Animation 5:</i> Animation of velocity vectors and vorticity contours for the fifth plane of elevation.	87
<i>Animation 6:</i> Animation of velocity vectors and vorticity contours for the sixth plane of elevation.	88
<i>Animation 7:</i> Animation of velocity vectors and vorticity contours for the seventh plane of elevation.	89
<b>CHAPTER 4</b>	<b>111</b>
<i>Animation 8:</i> First, set of hydrogen bubbles animation for cylinder inclination 0 degrees.	128

<b>Animation 8-1:</b> Hydrogen Bubbles. Inclination $\alpha=0$ degrees, $Re=1700$ , $Fr=0.3$	128
<b>Animation 8-2:</b> Hydrogen Bubbles. Inclination $\alpha=0$ degrees, $Re=3700$ , $Fr=0.65$	129
<b>Animation 8-3:</b> Hydrogen Bubbles. Inclination $\alpha=0$ degrees, $Re=6000$ , $Fr=1.06$	130
<b>Animation 9:</b> Second set of of hydrogen bubbles animation for cylinder inclination 30 degrees	131
<b>Animation 9-1:</b> Hydrogen Bubbles. Inclination $\alpha=30$ deg., $Re=1700$ , $Fr=0.3$	131
<b>Animation 9-2:</b> Hydrogen Bubbles. Inclination $\alpha=30$ deg., $Re=3700$ , $Fr=0.65$	132
<b>Animation 9-3:</b> Hydrogen Bubbles. Inclination $\alpha=30$ deg., $Re=6000$ , $Fr=1.06$	133
<b>Animation 10:</b> Third set of hydrogen bubbles animation for cylinder inclination -30 degrees	134
<b>Animation 10-1:</b> Hydrogen Bubbles. Inclination $\alpha=-30$ deg., $Re=1700$ , $Fr=0.3$	134
<b>Animation 10-2:</b> Hydrogen Bubbles. Inclination $\alpha=-30$ deg., $Re=3700$ , $Fr=0.65$	135
<b>Animation 10-3:</b> Hydrogen Bubbles. Inclination $\alpha=-30$ deg., $Re=6000$ , $Fr=1.06$	136
<b>Animation 11:</b> First set of particle flow visualization for $Re=1700$ .	137
<b>Animation 11-1:</b> Particle Visualization. Inclination $\alpha=0$ degrees, $Re=1700$ , $Fr=0.3$	137
<b>Animation 11-2:</b> Particle Visualization. Inclination $\alpha=30$ degrees, $Re=1700$ , $Fr=0.3$	138
<b>Animation 11-3:</b> Particle Visualization. Inclination $\alpha=-30$ degrees, $Re=1700$ , $Fr=0.3$	139
<b>Animation 12:</b> Second set of particle flow visualization for $Re=3700$ .	140
<b>Animation 12-1:</b> Particle Visualization. Inclination $\alpha=0$ degrees, $Re=3700$ , $Fr=0.65$	140
<b>Animation 12-2:</b> Particle Visualization. Inclination $\alpha=30$ degrees, $Re=3700$ , $Fr=0.65$	141
<b>Animation 12-3:</b> Particle Visualization. Inclination $\alpha=-30$ degrees, $Re=3700$ , $Fr=0.65$	142
<b>Animation 13:</b> Third set of particle flow visualization for $Re=6000$	143
<b>Animation 13-1:</b> Particle Visualization. Inclination $\alpha=0$ degrees, $Re=6000$ , $Fr=1.06$	143
<b>Animation 13-2:</b> Particle Visualization. Inclination $\alpha=30$ degrees, $Re=6000$ , $Fr=1.06$	144
<b>Animation 13-3:</b> Particle Visualization. Inclination $\alpha=-30$ degrees, $Re=6000$ , $Fr=1.06$	145

**CHAPTER 5** \_\_\_\_\_ **155**

*Animation 1:* Still image corresponding to particle flow visualization for  $Re=2500$  184

*Animation 2:* Still image corresponding to particle flow visualization for  $Re=9000$  185

*Animation 3:* Still image corresponding to particle flow visualization for  $Re=16500$   
\_\_\_\_\_ 185

*Animation 4:* Animation of the flow over the prism for duration of 8 secs at  $Re=2500$ .  
Total number of frames 2048. Animated 400 frames. Speed 5 fps \_\_\_\_\_ 189

*Animation 4-1:* Instantaneous velocity field and vorticity distribution at relative  $t=0.0$   
sec,  $Re=2500$ . \_\_\_\_\_ 190

*Animation 4-2:* Instantaneous velocity field and vorticity distribution at relative  $t=0.04$   
sec,  $Re=2500$ . \_\_\_\_\_ 190

*Animation 4-3:* Instantaneous velocity field and vorticity distribution at relative  $t=0.08$   
sec,  $Re=2500$ . \_\_\_\_\_ 190

*Animation 4-4:* Instantaneous velocity field and vorticity distribution at relative  $t=0.12$   
sec,  $Re=2500$ . \_\_\_\_\_ 190

*Animation 4-5:* Instantaneous velocity field and vorticity distribution at relative  $t=0.16$   
sec,  $Re=2500$ . \_\_\_\_\_ 191

*Animation 4-6:* Instantaneous velocity field and vorticity distribution at relative  $t=0.2$   
sec,  $Re=2500$ . \_\_\_\_\_ 191

*Animation 4-7:* Instantaneous velocity field and vorticity distribution at relative  $t=0.24$   
sec,  $Re=2500$ . \_\_\_\_\_ 191

*Animation 4-8:* Instantaneous velocity field and vorticity distribution at relative  $t=0.28$   
sec,  $Re=2500$ . \_\_\_\_\_ 191

*Animation 4-9:* Instantaneous velocity field and vorticity distribution at relative  $t=0.32$   
sec,  $Re=2500$ . \_\_\_\_\_ 192

*Animation 4-10:* Instantaneous velocity field and vorticity distribution at relative  
 $t=0.36$  sec,  $Re=2500$ . \_\_\_\_\_ 192

*Animation 4-11:* Instantaneous velocity field and vorticity distribution at relative  $t=0.$   
4 sec,  $Re=2500$ . \_\_\_\_\_ 192

*Animation 4-12:* Instantaneous velocity field and vorticity distribution at relative  
 $t=0.44$  sec,  $Re=2500$ . \_\_\_\_\_ 192

<b>Animation 5:</b> Animation of the flow over the prism for duration of 4 secs at $Re=9000$ . Total number of frames 2048. Animated 400 frames. Speed 5 fps. _____	193
<b>Animation 5-1:</b> Instantaneous velocity field and vorticity distribution at relative $t=0$ sec, $Re=9000$ . _____	194
<b>Animation 5-2:</b> Instantaneous velocity field and vorticity distribution at relative $t=0.02$ sec, $Re=9000$ . _____	194
<b>Animation 5-3:</b> Instantaneous velocity field and vorticity distribution at relative $t=0.04$ sec, $Re=9000$ . _____	194
<b>Animation 5-4:</b> Instantaneous velocity field and vorticity distribution at relative $t=0.06$ sec, $Re=9000$ . _____	194
<b>Animation 5-5:</b> Instantaneous velocity field and vorticity distribution at relative $t=0.08$ sec, $Re=9000$ . _____	195
<b>Animation 5-6:</b> Instantaneous velocity field and vorticity distribution at relative $t=0.1$ sec, $Re=9000$ . _____	195
<b>Animation 5-7:</b> Instantaneous velocity field and vorticity distribution at relative $t=0.12$ sec, $Re=9000$ . _____	195
<b>Animation 5-8:</b> Instantaneous velocity field and vorticity distribution at relative $t=0.14$ sec, $Re=9000$ . _____	195
<b>Animation 5-9:</b> Instantaneous velocity field and vorticity distribution at relative $t=0.16$ sec, $Re=9000$ . _____	196
<b>Animation 5-10:</b> Instantaneous velocity field and vorticity distribution at relative $t=0.18$ sec, $Re=9000$ . _____	196
<b>Animation 5-11:</b> Instantaneous velocity field and vorticity distribution at relative $t=0.2$ sec, $Re=9000$ . _____	196
<b>Animation 5-12:</b> Instantaneous velocity field and vorticity distribution at relative $t=0.22$ sec, $Re=9000$ . _____	196
<b>Animation 6:</b> Animation of the flow over the prism for duration of 4 secs at $Re=16500$ . Total number of frames 2048. Animated 400 frames. Speed 5 fps. _____	197
<b>Animation 6-1:</b> Instantaneous velocity field and vorticity distribution at relative $t=0$ sec, $Re=16500$ . _____	198

<b><i>Animation 6-2:</i></b> Instantaneous velocity field and vorticity distribution at relative $t=0.01$ sec, $Re=16500$ .	198
<b><i>Animation 6-3:</i></b> Instantaneous velocity field and vorticity distribution at relative $t=0.02$ sec, $Re=16500$ .	198
<b><i>Animation 6-4:</i></b> Instantaneous velocity field and vorticity distribution at relative $t=0.03$ sec, $Re=16500$ .	198
<b><i>Animation 6-5:</i></b> Instantaneous velocity field and vorticity distribution at relative $t=0.04$ sec, $Re=16500$ .	199
<b><i>Animation 6-6:</i></b> Instantaneous velocity field and vorticity distribution at relative $t=0.05$ sec, $Re=16500$ .	199
<b><i>Animation 6-7:</i></b> Instantaneous velocity field and vorticity distribution at relative $t=0.06$ sec, $Re=16500$ .	199
<b><i>Animation 6-8:</i></b> Instantaneous velocity field and vorticity distribution at relative $t=0.07$ sec, $Re=16500$ .	199
<b><i>Animation 6-9:</i></b> Instantaneous velocity field and vorticity distribution at relative $t=0.08$ sec, $Re=16500$ .	200
<b><i>Animation 6-10:</i></b> Instantaneous velocity field and vorticity distribution at relative $t=0.09$ sec, $Re=16500$ .	200
<b><i>Animation 6-11:</i></b> Instantaneous velocity field and vorticity distribution at relative $t=0.1$ sec, $Re=16500$ .	200
<b><i>Animation 6-12:</i></b> Instantaneous velocity field and vorticity distribution at relative $t=0.11$ sec, $Re=16500$ .	200
<b><i>Animation 6-13:</i></b> Instantaneous velocity field and vorticity distribution at relative $t=0.12$ sec, $Re=16500$ .	201
<b><i>Animation 6-14:</i></b> Instantaneous velocity field and vorticity distribution at relative $t=0.13$ sec, $Re=16500$ .	201
<b><i>Animation 6-15:</i></b> Instantaneous velocity field and vorticity distribution at relative $t=0.15$ sec, $Re=16500$ .	201
<b><i>Animation 6-16:</i></b> Instantaneous velocity field and vorticity distribution at relative $t=0.16$ sec, $Re=16500$ .	201

**CHAPTER 6** \_\_\_\_\_ **205**

**CHAPTER 7** \_\_\_\_\_ **226**

**APPENDIX I** \_\_\_\_\_ **243**

*Animation 1:* Animation of instantaneous vorticity distributions and velocity vectors at the free surface, for the first plane of interrogation \_\_\_\_\_ 255

*Animation 2:* Animation of instantaneous vorticity distributions and velocity vectors at the cylinder base, for the first plane of interrogation \_\_\_\_\_ 256

*Animation 3:* Animation of instantaneous vorticity distributions and velocity vectors at the free surface, for the second plane of interrogation \_\_\_\_\_ 257

*Animation 4:* Animation of instantaneous vorticity distributions and velocity vectors at the cylinder base for the second plane of interrogation \_\_\_\_\_ 258

*Animation 5:* Animation of instantaneous vorticity distributions and velocity vectors at the free surface, for the third plane of interrogation \_\_\_\_\_ 259

*Animation 6:* Animation of instantaneous vorticity distributions and velocity vectors at the cylinder base, for the third plane of interrogation \_\_\_\_\_ 260

## Table of Tables

<i>Table 1.</i>	<b>Table the free stream velocities for various setting of the water level and the frequency of the DC motor_____</b>	<b>9</b>
<i>Table 2.</i>	<b>Table of basic technical specifications of the ACL45 Laser and the CCD camera _____</b>	<b>18</b>
<i>Table 3.</i>	<b>Operating characteristics of the ACL45 laser after the improvements.</b>	<b>19</b>

# Chapter 1

## Introduction

### Motivation

Since the early days of Prandtl and Von-Karman there has been an enormous amount of research dedicated to the study of flows around bluff bodies. The mechanisms of flow separation, vortex formation the behavior of the wake and fluid-structure interaction constitute some of the most important as well as classical problems in fluid mechanics. Considering the overwhelming number of publications and research hours dedicated to the understanding of the aforementioned problems, any further related research may seem redundant. However, the great practical importance of such flows generates new challenges that require better understanding of the fundamental principles that govern them. In addition, the continuous evolution of experimental, numerical and analytical methods provide us today with new tools to gain a more complete and thorough understanding of such flows.

A very important evolution in the area of experimental fluid mechanics over the past years is the development of particle imaging techniques for instantaneous measurements of a whole flow field in two or three dimensions. Measurements in a space-time domain are now conducted, providing an unprecedented amount and wealth of information. The combination of the continuously increasing computational power, with high-resolution high-speed CCD cameras

(Charged Coupled Device) makes the future look even more promising, especially in the direction of investigating turbulent flows, where we have co-existence of coherent structures of different scales and frequencies (Roshko, 1976). However, these emerging and powerful technologies do not guarantee that they can be directly employed to carry out measurements in complex and unsteady flow fields such as the wakes of bluff bodies. It is our responsibility to merge these new tools in our arsenal and adapt them to our needs. Furthermore, we ought to advance them and lay the ground for further improvements. This was one of the major goals of this research.

In the current research, we investigate flows over bluff-bodies that are commonly encountered in nature and carry great practical importance. The fluid mechanics problems that we chose to attack are all characterized by the separation of a boundary layer, the evolution of the shear layer, its growth and eventually the formation of vortices that are shed in the wake. These are the key features that characterize the flow over a bluff body. By investigating generic flows of practical significance, it is attempted to maintain a high level of engineering relevance and at the same time gain better understanding of the fundamental principles that dominate such flows. All cases studied here share a naturally unsteady character that combines with an inherent three-dimensionality of the flow. The three-dimensionality can be a result of the boundary conditions (free slip no slip boundary conditions in the wake of circular cylinder) or because of the geometry of the body (surface mounted prism) or even both (inclined cylinder piercing the free surface). In addition, a forced unsteadiness interacting with the natural unsteady character of the flow (flow control of separated flows) presents the same characteristics. All these cases are unified by a three-dimensional separation and the formation of shear layers whose instabilities evolve in space and time. Therefore, we are investigating the flow characteristics of spatio-temporally developing flows. This leads us to the second unifying link of the present research, which is discussed below.

So far, in experimental fluid mechanics we were able to perform point measurements with great detail in the time domain or achieve high spatial resolution but in a time average sense. Both approaches have great limitations in the investigation of complex spatio-temporally evolving phenomena. The Particle Image Velocimetry technique (PIV), which is the workhorse of the present study, has enabled us to document the velocity field in space and time.

Nevertheless, so far, the method was constrained by insufficient time resolution. The strong time dependence of such flows and on occasion their intermittency affects drastically their character. Conventional approaches will fail to reveal the underlying principles that govern such flows. This research applies a whole-field, time-accurate measurement technique, illustrates the power of these methods and the need to adopt such an approach in order to improve our understanding of the physics of the flow. This need is further manifested by showing results from different problems sharing similar basic physical principles.

The major contribution of the present research is combining state of the art technology in the form of hardware, software and theoretical background for the development of a to investigate unsteady complex flow phenomena with a spatio-temporal resolution never reported in the past. This method involves the integration of special hardware arrangements, the development and/or the evaluation of software to carry out the task of the velocity calculation, the development of software to manage huge amounts of data and the scientific visualization of the results. A complete, step-by-step method, is developed to allow coherent interpretation of the phenomena under investigation. In addition, during this research we investigate a variety of flows to demonstrate the power and the need of such an approach and we are able to enhance our understanding by revealing underlying physical relations that have not been observed in the past using conventional methods.

At the beginning of this effort, the author was offered the choice between science and engineering or in other words, a choice between fundamental and applied research. Of course, all research aims at eventually reaching a point of maturity that will directly affect the engineering practice. Unfortunately, there are no shortcuts towards this direction. It goes through a one-way road, that of fundamental research. Therefore, it was a conscious choice to focus primarily on the scientific aspect and not on the application perspective. Nevertheless, the results that are presented here have engineering significance that will have an indirect impact on the lives of everyday people. More specifically, our understanding of the physics related to the interaction of a body submerged but piercing a water free surface may lead among other things to improvements of the design of ships and offshore structures. The simulation of flow around low-rise structures using a surface mounted prism will enhance our understanding of such flow fields under extreme wind conditions, hence increase the safety.

## *Chapter 1. Introduction*

---

Finally, we offer one last paragraph that may help define the author's motivation and drive throughout the course of this research. It is not only the complexity of nature itself and more specifically the complexity of the fluid mechanics phenomena this research is addressing that make our lives complicated. What makes our lives complicated is our human nature, which is by far more complex, our human curiosity that continuously drives us to seek new challenges and obstacles to overcome, new questions to answer and new problems to solve. We have reached such a level of understanding of the world surrounding us and yet it is still appropriate to quote the ancient Greek philosopher Aristotelis who once said: "*...the more I understand the more I realize how little I know*". In addition, the Greek poet Kavafis also said that: "*...is the trip that matters and not the destination*". Any scientific research will end up posing new questions and problems in order for the process to continue. There is also no doubt that a dissertation represents an in-depth study that gives answers to the problems under investigation. However, it would be arrogant to claim or expect that our work will provide complete solutions to these problems. In view of the above, the major objective and personal ambition was to develop versatility, broad understanding of the relevant physics, and problem solving abilities. This of course, is an endless process, but laying the ground and the foundation upon which one can build and evolve these skills is an indisputable part of a dissertation.

## **Outline**

The structure of this dissertation is somewhat unusual. Because of the versatility of the topics addressed, it was decided that each chapter should stand alone outside the context of the whole. This serves two purposes. First, it is anticipated that a reader may be interested only in the physics and the results of one chapter. Considering the fact that it is hard to flip page in the electronics medium, stand-alone chapters will prove more reader-friendly. Moreover, we should consider the size of the files included in this dissertation in combination with the requirements of electronic submission and making the content of this text available over the Internet. A huge amount of data in the form of animations of time sequences is included. Downloading the whole document over a network would be prohibitive for an interested reader. Accessing only the individual chapters or sections of interest would be the only viable solution. This fact makes imperative the organization of each chapter as a stand-alone document. The second reason serves the convenience of the author. With this organization it will be much easier to submit individual chapters for publication.

Within this structure of the dissertation, the literature review, the exact details of the experimental setup, and the conclusions are presented locally for every chapter. However, for completeness, one chapter (Chapter 2) is included to provide a more detailed discussion of the facilities and the instrumentation. In this chapter, a more comprehensive view of the method developed is presented. It is inevitable that parts of this chapter will appear in the subsequent sections as well.

In Chapter 3 the wake of a circular cylinder, piercing a free surface is investigated. Time resolved Digital Particle Image Velocimetry (DPIV) is employed for the analysis of both the spanwise and streamwise flow structures. The focus is on the effect of the free surface and the asymmetry of the boundary conditions on the vortex formation and the character of the wake. Chapter 4 is adding one more feature by introducing also a geometrical three-dimensionality emerging from inclining the cylinder with respect to the flow. The effect of inclination in combination with the free surface on the vortex shedding is investigated.

## *Chapter 1. Introduction*

---

Chapter 5 changes the scene, focusing on the characteristics of a shear layer emanating from a sharp corner. Because of the three-dimensional geometry of the model used (prism) the shear layers are shed from planes not parallel to each other. Thus they intersect and interact, forming a massive three-dimensional separation. Chapter 6 presents a study of flow control of the separated shear layer using unsteady excitation. In the final chapter (Chapter 7), a summary of the conclusions from the previous chapters is presented. This chapter will be redundant and overlapping with the conclusions presented in the individual sections, however, its existence is necessary for the completeness of this text.

## **Chapter 2**

# **Facilities Instrumentation and Methods of Investigation**

### **ESM Fluid Mechanics Laboratory Water Tunnel**

The water tunnel facility used was designed and manufactured by Engineering Laboratory Design. This facility is fabricated of a composite lamination of fiberglass-reinforced plastic. Clear acrylic plexiglass is used for the test section and the downstream viewing window in order to allow optical access for the various velocity measurement techniques. The water tunnel consists of a closed loop design with the loop plane arranged in the vertical direction. The facility has the return below the test section to allow operation with a free surface. A schematic is shown in figure 1. The overall dimensions are: length, 8.74m; height, 2.00m; width, 2.74m. Water flow is generated by a 20hp, single-stage, axial flow propeller pump, capable of delivering 4500 GPM. A variable speed drive assembly controls an induction motor that drives the axial pump. This is regulated by a potentiometer that allows precise adjustment of test section velocity. The volume of the tunnel when full is approximately 2500 gallons.

Flow velocity in the test section can be varied continuously between 0.05 m/s and 1 m/s. The maximum freestream velocity and the corresponding turbulence intensity that the water

tunnel delivers vary for different volume levels. The settling chamber contains a set of screens, each with a fine mesh for turbulence reduction and flow straightening. They consist of round cell polycarbonate honeycombs. A three-dimensional contraction with a 6:1 ratio precedes the test section. The test section interior dimensions measure 0.61m wide x 0.61m high x 1.81m long. It is constructed of 0.03m acrylic plexiglass on the top, bottom, sides and flanges and is supported by a steel frame. Testing performed with the tunnel full showed turbulence levels to be about 2%. Rubber couplings join the piping to the flow sections in order to isolate the pump from the flow sections and reduce any possible vibrations. A turning vane system within the return plenum acts to divide and direct the flow leaving the test section. A perforated cylinder distributes flow to the inlet plenum. For the current study, the water tunnel is operated always partially full and with the upper water surface free. Although for each experiment during this study the freestream velocity and the corresponding turbulence intensities were accurately measured, a preliminary calibration of the tunnel was performed, in order to determine the gross operational characteristics for various levels of volume and speed settings of the motor. The calibration is carried out using the TSI Fiber Optic LDV system (described later). Table 1 shows of the results of this calibration, while in figure 2 the corresponding curves are presented.

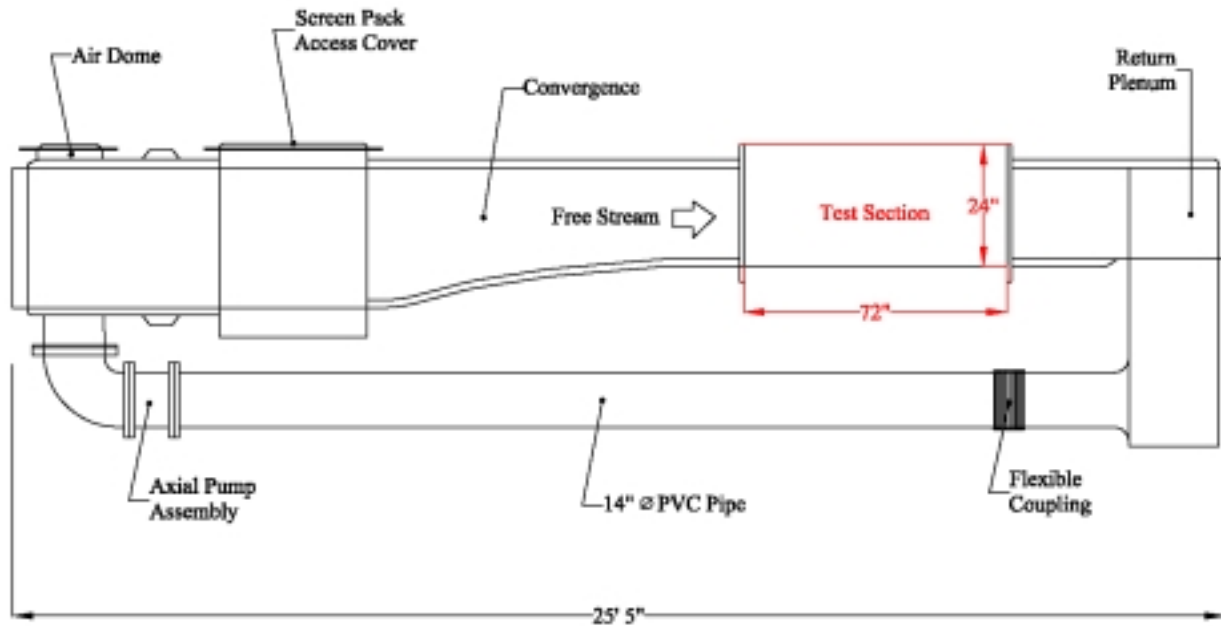


**Figure 1:** Schematic representation of the ESM Water tunnel facility.

**Table 1.** Table the free stream velocities for various setting of the water level and the frequency of the DC motor

Water Level (inches)	Full	13.5"	10.5"	5.5"
Motor Freq. (Hz)	Velocity in cm/s			
3	4.5	6	7	14
6	9	12	14	21
9	14	19	22	35
12	19	26	31	
15	24	34	42	
18	29	42	53	
22	36	53	68	
26	43	65	83	
30	50	78	98	

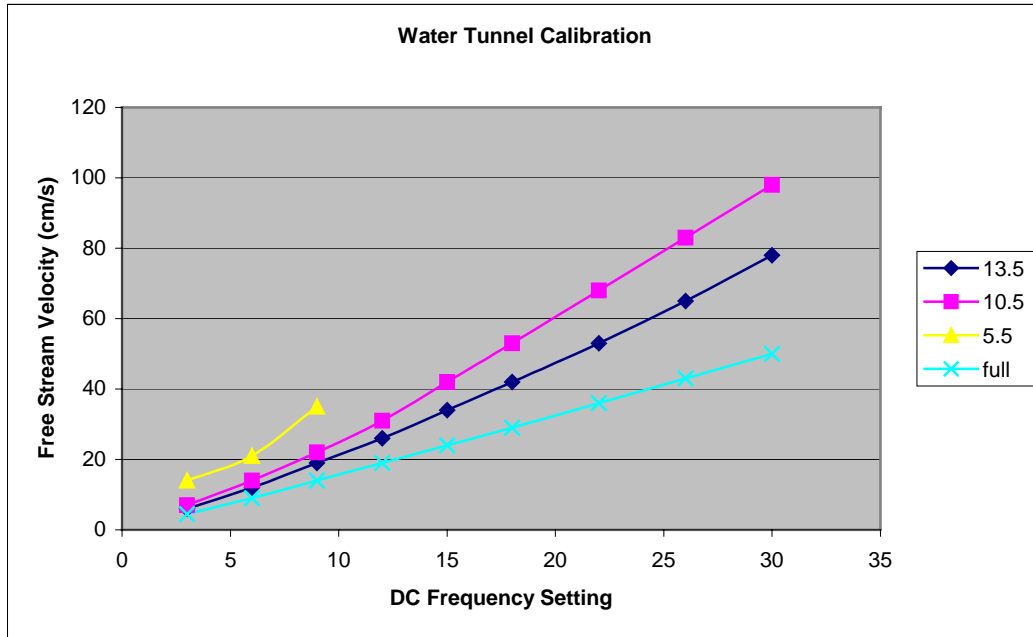


**Figure 2:** Water tunnel calibration chart for different settings of the DC motor and different elevations.

From figure 2 it can be observed that the free-stream velocity varies almost linearly for all cases. No attempt is made to document the flow quality in detail since this is a factor of many parameters such as the condition of screens, the exact water level, and the experimental setup employed in the test section. However, these measurements showed freestream turbulence levels ranging from less than 1% for the tunnel full and running at moderate velocities, to 6% for a water depth of 10.5” and free stream velocities higher than 0.5 m/s. In the table, the bold characters correspond to settings for which the flow quality is extremely poor due to free surface waves and free stream turbulence rendering these setting prohibitives for any measurements. In addition, for frequency settings of the DC motor in the order of 3Hz it is observed that the tunnel could not maintain a steady free stream. Finally, for the water depth of 5.5” (strikethrough characters) a limited number of measurements were performed because the flow is highly distorted.

This preliminary characterization of the performance of the water tunnel served only as a reference of conditions in order to enable us to select the desired conditions for each experiment. However, during the experiment, these conditions were varied appropriately to meet requirements imposed by other components of the experimental setup. When these settings were finalized, additional measurements of the free stream velocity and turbulence intensity were performed for each case.

## **Velocity Measurement Techniques.**

The focus of the current research effort is on the used and application of quantitative flow visualization techniques, namely Digital Particle Image Velocimetry (DPIV). However, the need of better understanding of the physical phenomena under investigation required the complementary use of other measurement methods. Among them, we have to focus on laser-Doppler velocimetry (LDV) which is employed in several occasions to verify flow characteristics observed or measured with flow visualization or even to provide quantitative information in cases where the “workhorse” of the present study (DPIV) failed to deliver. Although there is no effort made to improve or stretch the limits of the method beyond the basics it is necessary for the completeness of this text to provide a brief discussion of the LDV systems used.

### **Laser Doppler Velocimetry**

#### **Component-Based, Mirror-Directed LDV system**

A component-based mirror-directed He-Ne LDV system from TSI Inc. system is used only for real time monitoring of the freestream velocity and turbulence levels. A 60 mW He-Ne laser with a wavelength, of 632.8 nm is used as the light source. Components of the optical train included a beam collimator, two polarization axis rotators, a pair of beam splitters (prism type), two Bragg cells, beam steering wedges (for fine tuning the beam alignment), a single photodetector and a beam expansion unit with a 2.27 expansion ratio. The beam expander reduces the measuring volume length by 5 times, the diameter by 2.27 times and improves the signal-to-noise ratio by 5 times. The optics train splits the single input beam into three separate beams of equal intensity and same polarity. The beams are shifted in frequency using Bragg cells. The system can measure two components of velocity, sharing one of the beams to generate two distinct fringe patterns. The three laser beams are delivered to the test section via a pair of optical mirrors ( $\lambda/20$ ) and focused into a measurement volume by a 250 mm f/4 lens. The mirrors and focusing lens are mounted on an automated, two-dimensional traversing mechanism.

This setup allows automated and accurate positioning of the measurement volume in the area of interest. The measuring volume has a length of 1.26 mm, a diameter of 0.089 mm and a fringe spacing of 4.5  $\mu\text{m}$ . Signals are collected in backscatter mode with the transmitting optics also serving as the receiving optics. This greatly simplifies traversing the measuring volume since the transmission and receiving optics move in unison. However, because back-scattered light is nearly 100 times weaker than forward-scattered light, seeding the flow is necessary. Silicon carbide seeding particles (TSI Model 10081) were used as tracer particles. These particles have an irregular shape with a mean diameter of 1.5  $\mu\text{m}$ , a density of 3.2 g/cm<sup>3</sup>, and a refractive index of 2.65.

Usually, multi-colored laser beams are utilized in multi-component LDV work. Individual signals then are separated with color (optical) filters. The system used here employs instead a single-color laser and frequency shifting linked with electronic filtering to separate the scattered light signals. The laser beam from a 35 mW He-Ne Spectra Physics laser is split into three equal-intensity beams. Two of the beams are frequency shifted by the Bragg cells; one beam is shifted by 40 MHz the other by 60 MHz. The three beams are arranged to form the vertices of a 45°, 45°, 90° triangle. Each beam pair is sensitive to a component of the velocity, however, only two are linearly independent. The two components measured are orthogonal to one another. One velocity component is measured with the 40 MHz-60 MHz beam pair and has a no-flow frequency of +/-20 MHz. The other component uses the 40 MHz-unshifted beam pair. Its no-flow frequency is +/-40MHz. Both signals are received with the same photodetector and are electronically separated with band-pass filters. After separating the signals, the Bragg cell frequencies are subtracted by electronic down-mixing. Flow reversals are detected by adding an additional frequency shift to the laser beams. This frequency is typically selected to be approximately twice the mean Doppler frequency of the flow, and is not down-mixed from the signals. A particle with zero velocity will produce a signal frequency equal to the shift frequency. This down-mixed or separated frequency signal, which is proportional to the velocity, is provided to two TSI frequency counters which will be described in a following paragraph. The frequency counters report a voltage proportional to the frequency of the input signal.

## **Two-Velocity Component Fiber-Optic-Delivered LDV System**

The second of the two laser-Doppler velocimetry systems was employed in carrying out point velocity measurements in order to perform spectral analysis. This is also a component-based system but differs primarily by the fact that the laser beams are delivered to the test section with a fiber-optic probe. Focusing of the beams into a measurement volume is done with a 100 mm focusing lens, which is part of the probe. Both the focusing and the receiving optics are built-in inside the probe. This short focal length limits the usefulness of this probe in the larger water tunnel facility. However, the fiber-optic delivery system provides for much greater flexibility in placing and traversing the measurement volume.

A 3.5 W Argon Ion laser is used as the light source for this multi-color system. The additional power is necessary for this system, as the beam is split into five colors, from which only the two most powerful, blue and green, are used. In addition, significant power losses can occur when the beams are coupled with their fibers. This system now uses 4 beams, 2 different colored pairs to measure two components of velocity. A schematic of the system layout is shown in figure 3 (from the system manual). The beam separation process takes place in the part 9105. From that point, the same type of components as in the previous system are employed to the point where the fiber optic coupling takes place (parts 9259 9262). The two pairs of beams are coupled to a five-fiber, 30 ft long fiber optic cable and are delivered into the probe where the focusing and receiving optics are aligned. The probe diameter is 25mm; with the use of two different focusing lenses, the focal distance can be 102mm or 135mm. For the 102 focal length lens the corresponding fringe spacing is 2.8  $\mu\text{m}$  for the green beam and 2.4  $\mu\text{m}$  for the blue. A color separator is used to separate the scattered light, transmitting 85% of the green wavelength and 95% of the blue wavelength. Two band-pass color filters are used, with width of 6.1nm and 6.4nm for the green and the blue beam respectively and two photo-detectors then measure the back-scattered light from the measurement volume. The same TSI frequency counters and seeding particles as above are used with this system.

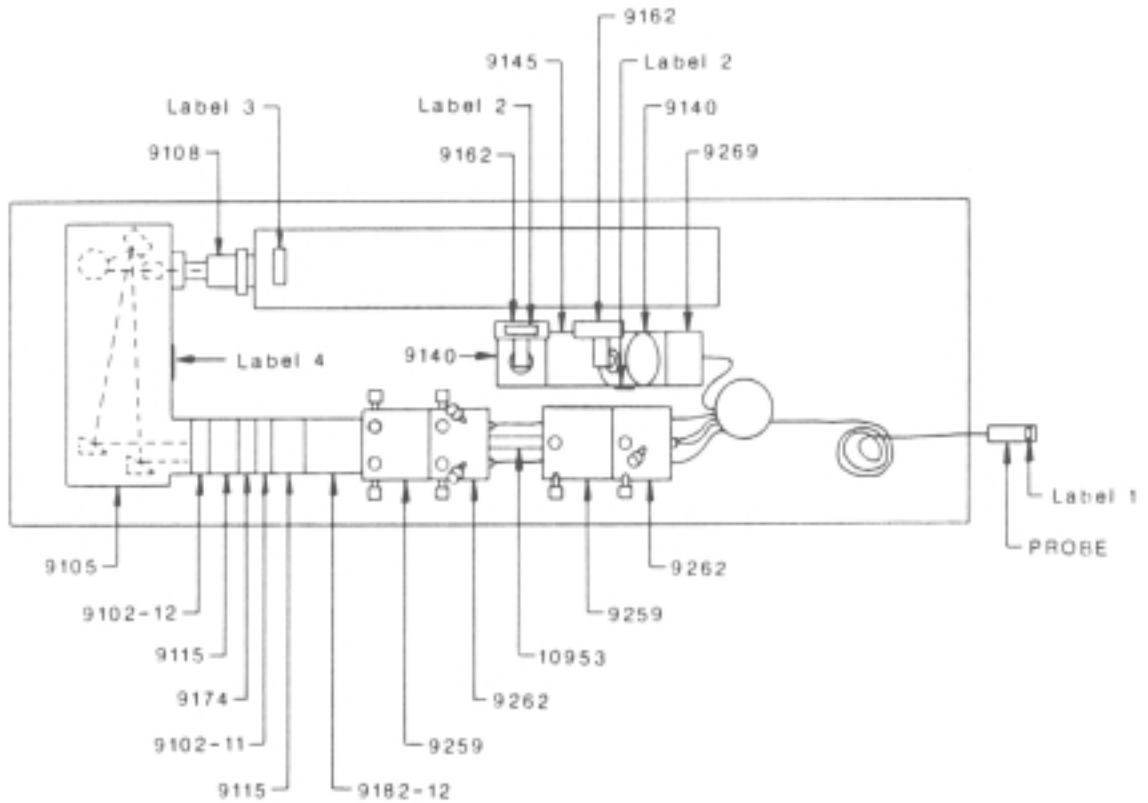


**Figure 3:** TSI Fiber Optic LDV system layout schematic. (Schematic provided from the system manual.)

## **LDV Signal Processing and Data Acquisition**

Two counting signal processors were used with both the TSI LDV systems employed in the ESM Water Tunnel. These processors measure the time between cycles of the Doppler signal. The inverse of this time is the Doppler frequency. Two TSI counters, a TSI Model 1980 and a TSI model 1990 were employed; one for each velocity component. The two counters are essentially alike and are operated in the N-cycle mode with  $N=8$ . This means that the counter times eight cycles of the Doppler signal. To help eliminate spurious signals, the counter also measures the time for four cycles and compares twice the four cycle time with the eight-cycle time. If the two are within a certain percentage of each other (the comparison percentage is set to 5% here) then the signal is considered valid. In addition, each cycle must exceed a preset amplitude limit. A hysteresis limit is used in conjunction with the amplitude limit to avoid timing turbulent fluctuations rather than cycles of the signal.

The TSI counters have two analog outputs: one outputs a voltage that is proportional to the measured time, the other output is proportional to the Doppler frequency, and is simply the inverse of the time output. The voltage output of the LDV signal processors is proportional to the Doppler frequency. A tabulated conversion factor is provided with the TSI counters. The factor is determined by front panel adjustments on the counter and has the units Hz/volt.

A fully automated data acquisition system was developed in the ESM laboratory consisting of an IBM PS/2 Model 55 computer and an analog-to-digital (A/D) and digital-to-analog (D/A) converter board (DT 2905). The A/D converter converts the analog output of the signal processors to digital information for manipulation and storage. The D/A converter controls the stepping motors that traverse the measurement volume. The D/A board has a resolution of 12-bit with a range of  $\pm 10$  Volts resulting into a bit-resolution of 48mVolts. Later, this data acquisition system was replaced with a more up to date unit based on a Pentium 200 PC computer and a D/A board from National Instrument. This board is also with 12-bit resolution but with programmable IO range from  $\pm 10$  Volts down to  $\pm 1.0$  Volt. These, in conjunction with built-in filters and input channel isolators provided superior resolution and signal to noise ratio.

## **Particle Image Velocimetry (PIV)**

### **A system for high speed Digital PIV Cinematography (DPIVC)**

Particle Image Velocimetry is a state of the art experimental method that provides two-dimensional whole-field measurements of the velocity and subsequently the one-component vorticity distribution in the area under investigation. The origin of the method goes back to traditional qualitative particle flow-visualizations, however the early work of Meynard (1983) established the foundations of its present form. During the past two decades numerous publications have appeared presenting improvements on the technique as well as applications of the method to a wide range of flows, from low-speed liquid and two phase flows to supersonic gas flows. The interested reader can refer to Adrian (1991) (1996) and Grant (1994), (1997). Particle Image Velocimetry is the workhorse of the current research.

The most common implementation of the method (currently commercially available) integrates a laser light sheet generated by Nd:YAG pulsing lasers that illuminates the interrogation area and a high-resolution cross-correlation CCD camera. A typical configuration provides 15 instants of the flow field per second and over 900 independent vectors. The advantages of this approach can be summarized in the following. The use of the YAG lasers provides high energy/pulse ( $>100\text{mJoules/pulse}$ ) light source with good coherence and intensity profile. The CCD camera has superior signal to noise ratio than the standard photographic film, eliminates the intermediate digitization step, and takes advantage of a fully computer-based data acquisition system. Recently developed digital image processing techniques are used to accelerate the evaluation and validation of the flow field. However, the photographic film still delivers unsurpassed spatial resolution, able to cover up to three decades of the turbulence spectrum (Adrian, 1996) A typical resolution is about 1 mm with an accuracy of 0.1 of the pixel size. In the digital implementation of PIV the so-called “cross-correlation” CCD cameras have enhanced the ability to investigate, high-speed flow fields, by acquiring two fields per frame, separated only by a few nanoseconds ( $<100\text{ns}$ ). Thus, an approach of dual frame single exposure cross-correlation of two consecutive frames became the most popular approach to carry out PIV measurements.

A major disadvantage of this approach is the inability to provide sufficient time resolution, which is necessary, in order to investigate any high frequency phenomena that occur in turbulent flows. The current research presents an alternative configuration towards the investigation of turbulent flows such as the wakes of bluff-bodies. The success of this approach primarily depends on the integration of a Cu-Vapor laser with a high speed CCD camera.

### **Hardware description**

Using a set of optics in a telescopic arrangement, a laser sheet is delivered into the test section. The light source is a copper vapor 45Watt pulsing laser, delivering approximately 5.5mJ/pulse at its optimum operation. The laser is synchronized with a high-speed CCD camera (EG&G MD4256) using a timer board (Real Time Devices, TC524). The maximum possible number of images is 1000 images/sec with a resolution of 256x256 pixels. Digital images were automatically stored in the image buffer of an SB4001 Adaptive Optics frame grabber. The frame grabber has a built-in image buffer of 256 MB allowing a transfer rate of 80MB/sec. Furthermore, integrated on the board Look-Up-Tables (LUT's) carry out the task of correcting the acquired images by removing electronic noise and equalizing the intensity of the four quadrants of the sensor. A C++ program that accesses the frame grabber and the timer board controls the data acquisition process. The process is fully automated and digital, eliminating the tedious and time consuming tasks of film digitization and allowing the real time observation of the flow field. A summary of the main technical specifications of the laser and the camera is shown in table 2.

Three different types of lenses are used with the CCD camera: (1) A 55mm Nikon lens with  $f\#$  of 1.2 is used to allow more light on the sensor during the limited exposure time of 1/1000 secs. (2) A Schneider 25mm wide-angle lens is used with a continuously variable  $f\#$  down to 0.95. This lens allows even more light on the sensor and is also able to focus at a very small distance from the field of view (<6 in). It is a wide-angle lens therefore it can increase the size of the field of view significantly. The use of this lens can be limited from other parameter of the experimental setup. Finally, a Nikon 80-300mm telephoto lens is used when there is need to acquire data from the downstream window. The smallest possible  $f\#$  is 2.8. This lens cannot

focus inside 1m but at 2m away from the area of the interrogation it can zoom down to an area of almost 0.5 in<sup>2</sup>

**Table 2.** Table of basic technical specifications of the ACL45 Laser and the CCD camera

Cu-Vapor laser	Average Power	Energy/Pulse	Pulse Frequency	Beam Diameter
	36 W	<10mJ	5-7 kHz	42mm
CCD Camera	Frame Rate	Pixel Resolution	Dynamic Range	
	1-1000 fps	256x256	8-bit gray-scale	

The high sampling rate of the data acquisition process introduces significant problems in the adequate illumination of the flow field. In order to synchronize the laser with the camera it requires a light source capable of matching the frame rate of the camera. Standard YAG laser cannot perform at such high pulsing frequencies. Copper vapor lasers can deliver repetition rates up to 30KHz. However, the light coherence is poor and most importantly, the range of operation is very limited and is centered at an optimum frequency of 6-8 KHz. In addition, the mean output power of the laser drops drastically as we reduce the pulsing frequency, subsequently delivering lower energy per pulse. Small bursts of the laser pulsing frequency result in cooling down the laser, which in effect results also in reduction of the output power. In order to compensate for the energy losses and deliver sufficient illumination in the area under investigation, a set of optics specially coated for the exact wavelength of the laser was employed. This resulted into decreasing the losses through the optics from approximately 40% to less than 10%. These improvements allowed us to acquire data up to 1000 frames/sec, which otherwise wouldn't have been feasible.

In addition to the improvements of the laser sheet forming optics there was need to improve the actual performance of the laser. This was done by addressing the following issues. Losses from the optics inside the plasma tube were 30% of the original configuration. (A schematic of the plasma tube is shown in figure 4.) The cavity optics were replaced, and by using the so called "plain cavity optics" the efficiency of the plasma tube reached 99% with a peak power of 45Watts. The price we have to pay for that is that the beam cannot be focused and collimated –with conventional optics- in less than 1mm diameter. However, if there is need to do

so, the optics can be changed back to their original configuration. The next issue that needed to be addressed was that of the limited range of the repetition rate of the laser. The standard configuration of capacitors allowed a range of frequencies from 5 to 8 KHz. When these limits are violated the performance of the laser deteriorates, the output power drops drastically and eventually the laser shuts down. This limitation was overcome by replacing the configuration of the capacitors of the laser head. The use of different combinations of capacitors (Magnetic Pulse Compression Unit, Figure 4-1) allows the adjustments of the optimum running frequency from 3 to 20 KHz. A trial and error approach of combining different sizes of capacitors can optimize the laser to operate at a desired frequency. Of course, in such a case, more adjustments are necessary but these are beyond the scope of this text. Furthermore, a side effect of that process was an additional increase of the output power by 40%. Representative tests of the performance of the laser for at different nominal frequencies and burst frequencies are shown in Table 3. This table illustrates how the improvements enhanced the flexibility and the performance of the laser.

**Table 3.** Operating characteristics of the ACL45 laser after the improvements.

<b>Mean Power (W)</b>	<b>Energy/Pulse (mJ/pulse)</b>	<b>Burst Frequency (Hz)</b>	<b>Burst Energy/Pulse (mJ/pulse)</b>
49.7 @ 10 KHz	4.97	1000	8.68
49.7 @ 10 KHz	4.97	5000	21.7
47.9 @ 8 KHz	5.97	1000	9
34.4 @ 6 KHz	5.73	1000	10.45
22.0 @ 3.5 KHz	6.28	1000	8.16

One final feature of the laser that needs to be mentioned here is the duration of the pulse. Regardless of the operating frequency, the pulse of the laser lasts 20 nsecs at almost constant peak energy and about 20 nsecs of drop duration. This means that the CCD sensor for each exposure to a pulse of the laser has practically less than 40 nsecs to integrate the scattered light into a distinguishable signal. This parameter illustrates how crucial is the optimization of all the aforementioned parameters in order to get an image with high signal to noise ratio.

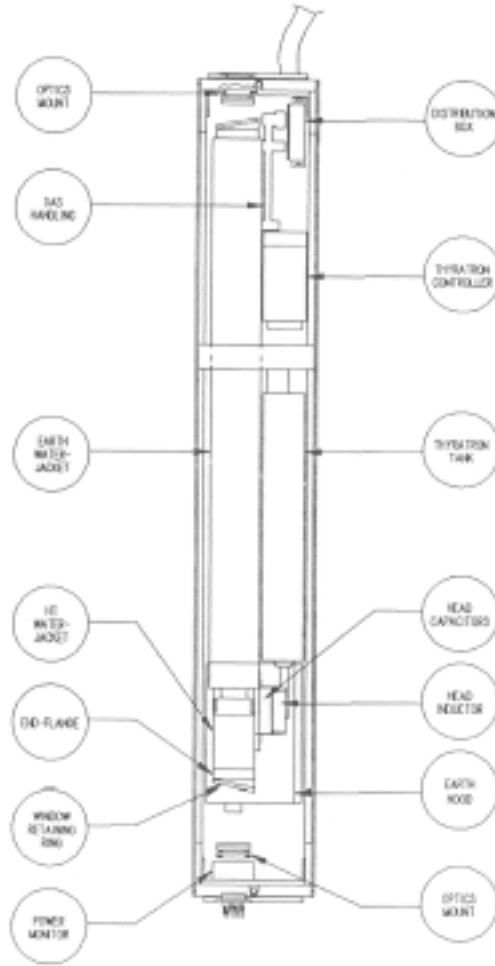


Figure 4: Schematic layout of the IACL45 laser head configuration.

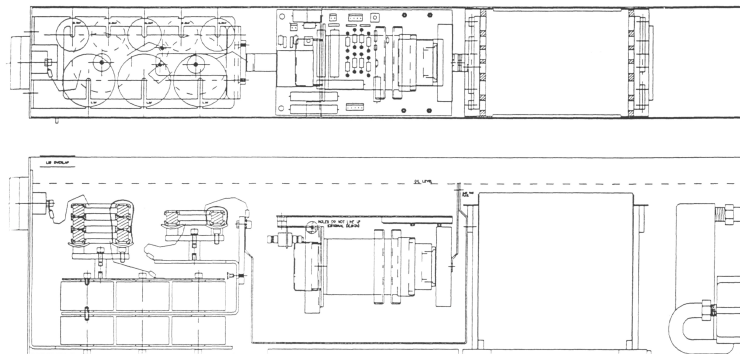


Figure 4-1: Schematic of the Magnetic Pulse Compression unit located in the front end of the laser head (see previous figure: HEAD CAPACITORS)

## **Digital Particle Image Velocimetry Evaluation Software**

The ground of Particle Image Velocimetry was laid in the early eighties (reviews by Hasselinc (1989) and Adrian (1991) provide a detailed discussion) but it was the work of Willert and Gharib (1991), Westerweel (1993a, 1993b) and Huang and Gharib (1993) that established the digital implementation of PIV. Their work, as well as many other studies that followed, focus on a single exposure double-frame digital cross correlation approach. In addition, they focus on high-resolution (1Kx1K pixels) cameras that sample with up to 30 fps resulting to a sampling frequency of the flow field of only 15Hz. These cameras are also called dual field or cross correlation cameras because of their ability to acquire two consecutive fields in the same frame separated by a very small –adjustable-  $dt$  (in the order of 50 to 100 nsecs). There is very limited work addressing the issues rising from the use of high-speed CCD cameras (above 500 fps). These cameras are somewhat different. The time interval between two consecutive frames is fixed as well as the transfer rate (millions of pixels per minute) and these two parameters effectively establish the feasible frame rate. Subsequently, the maximum possible frame rate affects the maximum velocities that can be measured. On the other hand, the increase of the frame rate results in significant decrease of the exposure of the sensor, which limits the density of particles in the acquired images. Adrian (1996,1997) provided an analysis of different approaches to adjust the speed and the resolution of a PIV system. However, even though this study analyses both analog and digital media, it does not treat such high-speed cameras as the one employed in the current research.

The image-processing task for the PIV images is carried out with different programs. First, Visiflow, software developed by AEA©, on a Pentium II 450 based PC, processing one frame every almost 10.secs. The second program was developed by the author based on the basic implementation by Willert and Gharib (1991). This version is more flexible and can be easily customized, however, it is less computationally efficient, requiring 30sec per frame. The dynamic range of the images is 8-bit, resulting in 256 shades of gray. For all the cases considered in this text, the maximum window of interrogation for the digital evaluation is  $16^2$  and the overlapping is 75%, resulting in a minimum number of 61x61 vectors. This choice of interrogation window with high overlapping is essential in order to achieve high spatial

resolution. Willert and Gharib (1991) argued that although overlapping is a form of interpolation the fact that within each interrogation region exist a different number and pattern of particles justifies this as a choice. For both programs, a three-point Gaussian estimator for the correlation peak is used, achieving sub-pixel accuracy of 0.1 pixels for the peak detection process. The vector validation process employs limiting criteria about the velocity magnitude the continuity of the calculated vectors, and a quality factor of the estimated cross-correlation peak point considering the existence of multiple peaks in the interrogation window. Interpolation is carried out using a local weighted average approach. Finally, the data were smoothed using a 5x5 Gaussian filter. In addition, for the tasks of the velocity validation and interpolations, alternative approaches are integrated, namely the Adaptive Gaussian Window method (Agui and Jimenez, 1987) the Inverse Distance Method and two dimensional Local Least Squares. These alternative techniques provide flexibility, which is essential for different applications, since none of them demonstrated to outperform the others in all cases. However, the computational time increases significantly with respect to the basic nearest ballpark approach. Since the CCD camera outputs directly in a digital format, any error resulting from the digitization is considered negligible.

The use for all applications of 10-30 micron neutrally buoyant particles as flow tracers eliminates any errors due to the seeding-lag of the particles to accurately follow the flow. Considering the error from the vector validation and interpolation process, the overall uncertainty of the velocity is estimated to less than 1%FS (full scale) with respect to a maximum displacement of eight pixels.

In order to achieve the spatial resolution of four pixels the size for the interrogation window is set to  $16^2$  pixels. The optimum performance for cross-correlation evaluation of the velocities is well established for windows of interrogation of  $32^2$  and larger (Willert and Gharib (1991) and Huang and Gharib (1997), Keane and Adrian (1990, 1991)). The minimum number of particle pairs required is five, while the mean particle image diameter, is 2.5 pixels. Very little information exists in literature for smaller sizes of the interrogation window, primarily due to the fact that the most popular digital cameras used provide significantly higher resolution but at frame rates up to 30 fps. In addition, these studies were preformed using artificially generated images. Therefore, there is the need to optimize our system (hardware-software combination) to perform under the specific requirements. Initially, artificial images were generated using the

approach described by Raffel et al.(1998) to simulate the effect of electronic noise of the camera, and Gaussian distribution of the laser sheet thickness and the scattered light from the particles. The particles were displaced using a Couette flow with a minimum displacement of 0.5 pixels and maximum of 7 pixels. For displacements larger than eight pixels would be prohibitive to use an interrogation window of  $16^2$  pixels, because of the Nyquist frequency thus it is not considered. By performing these tests, it was observed that the validation quality of the cross-correlation evaluation of the velocities reaches almost 100% for 10 particles per window. This is the same conclusion that previous researches have reached but for larger size windows. However, it is worth mentioning that with a mean particle image diameter of 2.5 pixels and 10 particles for every  $16^2$  pixels this results in a number of 6400 particles in our flow field. Considering a realistic situation where we have out of plane motion of the particles, relatively high background noise, and electronic noise from the sensors, this number indicates that the interrogated image will be very close to be saturated in order to have the required number of distinct particles in the flow. Therefore, during an experiment, extreme care needs to be taken to achieve the appropriate amount of seeding without saturating the flow.

Any other sources of error resulting from the digitization of the images or from the seeding particles (Agui and Jimenez, 1987) are not considered. The digitization error is eliminated by the use of the digital camera, while the use of particles that are small in diameter and neutrally buoyant practically eliminates them as a source of error. The errors from the interpolation and the filtering procedure are embedded in the overall error evaluation and there is no need to treat them independently.

In order to increase the signal to noise ratio of the acquired images and the maximum resolvable speeds a different approach is adopted. Because of the use of a high repetition rate, pulsing laser with pulse duration of 40 nsec the energy per pulse delivered on the sensor is significantly reduced. More importantly synchronizing the laser with the camera at i.e. 500 Hz for 4 secs is impossible since the repetition rate affects the temperature in the plasma tube therefore in effect determines the output power. Such an attempt will cause the laser to cool down rapidly and during the first 0.5 secs will be forced to shut down. In order to overcome these difficulties a multi-exposure approach was adopted. Once the desired frame rate of the camera is determined, an optimization procedure of the laser is preformed using a trial and error

approach in order to determine the optimum number of exposures per frame that will continuously allow the laser to run a certain frequency that will deliver high energy per frame. Multiple exposures per frame for the auto-correlation implementation of PIV have been studied extensively (Keane and Adrian, 1990 and 1991) and a procedure for optimizing the pulse separation has been proposed (Boilot and Prasad, 1996). The only paradigm of multiple exposures per frame cross-correlation approach was performed by Cenedese and Paglialuga (1990). In their approach, however they used photographic film, and instead of performing cross correlation of the particle patterns to determine the displacement, they initially determined the centroids of the particles and then cross-correlated the projections of these centroids in each direction.

In the present approach, we perform multiple exposures per frame and we evaluate the vectors using digital cross-correlation of two consecutive frames in a way similar to the double frame single exposure method. In order to achieve the desired time and spatial resolution we carry out a set of optimization steps based on the findings of previous researchers. The first step requires the adjustment of the field of view in such a way that the entire domain of interest is contained and the mean particle image diameter is in the order of 1.5 pixels. In addition, the image density needs to be about five particles per  $16^2$ -pixel window. The image diameter is determined by performing a sequence of basic image processing techniques to identify each particle find its centroid and measure the diameter and the particle concentration. The optimization of the particle image diameter and the seeding density increase the signal to noise ratio during the cross-correlation evaluation of the velocities (Willert and Gharib (1991), Keane and Adrian (1990, 1991)). By optimizing the particle diameter, we determine the pixel size. This allows calculating the minimum required frame rate, such that the particle maximum displacement between two consecutive frames will not exceed eight pixels. Same as in the previous approach, because of the limited resolution of our CCD sensor the use of a  $16^2$  window is needed in order to increase the spatial resolution of the interrogation. The laser pulse frequency is adjusted next. This is performed by changing the number of exposures per frame in such a way that the running frequency of the laser remains inside the operational limits of the laser but also avoiding the appearance of long streaks in the images. Once this step is completed, estimation of the error is carried out either by evaluating the velocities of a free stream or a

quasiest flow field, or by comparing with LDV measurements. Extensive tests for different applications demonstrated a performance similar to the standard cross-correlation with errors of the same order. In effect, the multiple exposures per frame may result into multiple images of the same particle to appear as different particles. Therefore the signal to noise ratio increases, without compromising the accuracy of the method.

## **Data Analysis, Error and Uncertainty**

The present DPIV system implementation is limited only to the investigation of low speed liquid flows. This drawback results from two hardware limitations. The minimum possible time interval between two consecutive frames is 1 milisc while the moderate pixel resolution of the sensor limits the maximum field of view. All cases presented in this text correspond to liquid low speed applications. The maximum in plane displacement between two consecutive frames is constrained to be less than 8 pixels. The uncertainty of the velocity estimation can be quantified as:

$$\left(\frac{\sigma_u}{u^2}\right)^2 = \left(\frac{\sigma_{\Delta X}}{\Delta X^2}\right)^2 + \left(\frac{\sigma_{dt}}{dt^2}\right)^2$$

Where  $\sigma$  denotes the rms of the fluctuation of the subscripted quantity. For such low velocities and by using a digital interrogation procedure the uncertainty of the time separation is negligible. Thus the only error source will be introduced by the displacement estimation. Considering a typical particle image diameter of 2 pixels in order to optimize the correlation peak detection algorithm, then the uncertainty of the velocity estimation will in the order of 1%

Once the velocity vectors are evaluated, we obtain the spatial velocity distribution for a sequence of about 2000 instants of the flow. From this point, data analysis tools are employed in order to extract information about the physical phenomena involved. Various flow properties are calculated namely: vorticity, stream function, U and V rms, the in plane turbulent kinetic energy resulting from the two measured velocity components, the in-plane Reynolds stresses, the coefficient of flow reversal, and the circulation integral at certain domains of the flow field. All these are employed in a manner appropriate to the case under investigation.

The statistical uncertainty of the estimation of a fluctuating quantity is inversely proportional to the square root of the number of samples used. Therefore, for a typical experiment with 2000 time records, the uncertainty of the estimation of the velocity rms is of the order of 2% of the mean value. However in the case of the in plane turbulent kinetic energy one has to consider the fact that there is no contribution to the estimation of the third velocity component.

Special care is taken for the computation of vorticity. The vorticity calculation is performed by applying fourth order compact schemes (Lele, 1992) to reduce the contribution of the truncation error to the overall error of the calculation. In most cases, vorticity is calculated from experimental results using explicit second order schemes or is calculated from the circulation. Comparisons with artificial data were carried out and it is shown that the compact implicit schemes are more accurate, paying a small price of computational time.

By performing extensive overlapping to increase the spatial resolution of the flow field a typical number of 61x61 vectors with a step size of four pixels can be achieved. In order to meet the Nyquist criterion the maximum characteristic length scale  $L$  for the flow cannot exceed one half of the field of view. This results to a grid step size of 3%  $L$ . Comparing this spatial resolution with the Kolmogorov microscale for a typical step size in the order of 1mm we realize that we can resolve scales that are approximately one order of magnitude larger than the finest turbulent scales.

In addition, the cross-correlation procedure allows us to resolve only linear displacements of a certain pattern of particles. Thus it is immediately understood that any fluctuations within the interrogation window cannot be resolved. The latter combined with the fact that because of the overlapping process same particle images correlate with each other results to a bias and over smoothing of the velocity estimation. This problem is more important in cases where high velocity gradients are present in the flow.

## **Image Processing Tools and Particle Tracking Velocimetry**

### **High-Speed High-Particle-Density Particle-Tracking Velocimetry**

#### **Introduction**

Particle Image Velocimetry (PIV) and Particle Tracking Velocimetry (PTV) fall in the general category of particle based techniques using a pulsed light source. Adrian (1991) gives a very detailed discussion in a review article. Both are limited to two-dimensional velocity measurements in their standard form, but they can be extended to three dimensions (Dracos and Gruen, 1998; Hinsch and Hinrichs, 1996; Adrian et. al., 1993; Prasad and Adrian, 1993; Adrian, 1996). Evolutions of the two-dimensional PIV are DPIV (Digital Particle Image Velocimetry) (Willert and Gharib, 1991; Huang and Gharib, 1997) where the photographic film is replaced by a CCD, and PIVC (PIV Cinematography) for resolving unsteady flows. A color-coded particle tracking velocimetry method is proposed (Wung and Tseng, 1992; Wung, 1997) for resolving in real time two and three-dimensional flows.

PIV and PTV are complementary methods as they are both based on the same principle. Velocity is determined from the displacement of particles within a fixed time interval. Their basic differences are: a) in PIV the time step is determined by the pulsing frequency of the illumination source while in PTV it is determined either by the frame rate of the camera used or for single frame particle tracking by the number of pulses per frame; b) most importantly PTV requires low particle concentration so that there is no overlapping between particle images (Dalziel SB, 1993; RJ Perkins and JCR Hunt, 1989). These two considerations are limiting PTV to lower flow speeds and result in a smaller density of velocity vectors in comparison with PIV. Furthermore, by using multiple exposures per frame for single frame particle tracking the directional ambiguity needs to be resolved.

Most standard PIV or PTV systems use 30Hz CCD Cameras. This can be prohibitive for any turbulence measurements where the range of frequencies that need to be resolved can be much higher. Moreover, the most commonly used version of PIV, DPIV and PIVC, is based on cross correlating two sequential frames, which requires the application of an interrogation

window on each image. This can be an additional limiting factor, because it results in reduction of the minimum size of the length scales in the flow field that can be resolved.

An improved particle tracking technique applied to liquid flows is presented in this section. The limitations of PTV mentioned above are overcome by implementing a smart particle-tracking algorithm, which allows to accurately trace the trajectories of a large number of particles in a sequence of high particle density images. The images are acquired with a sampling frequency of 1000Hz providing sufficient time resolution to resolve the high frequency phenomena that occur in turbulent flows.

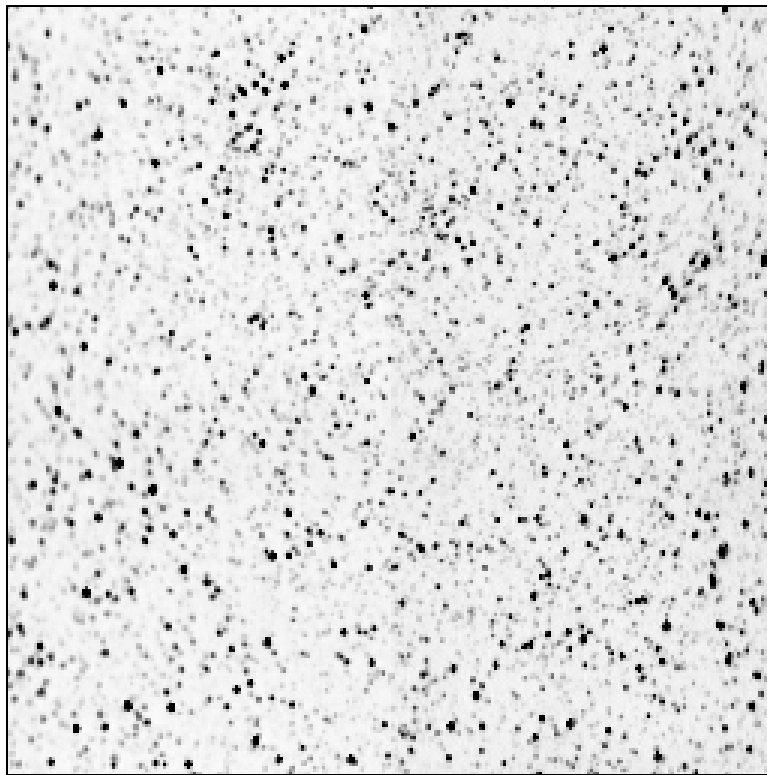
### **Particle Tracking Algorithm**

Fig 1 shows a sample image of an instance of the flow field interrogated with the system described, with a sampling frequency of 1000fps. The particle density is high and no precautions were taken to avoid overlapping of the particle images. The effectiveness of the method is depends on successfully tracking a large number of particles within a sequence of frames, so that a large number of vectors can be produced. In order to achieve this, image-processing techniques are used to remove background noise and speckles are reduced using a “center-of-gravity” approach.

Initially, a small threshold value is applied on the image in order to remove the low-level background noise. Furthermore, in many instances, the mean local intensity of the pixels does not have a uniform value throughout the field of view. This can be attributed to uneven illumination or to insufficient calibration of the CCD camera. In order to overcome this problem and achieve uniform intensity, we apply on the images “locally adaptive thresholds”, which are dynamically adjusted based on the mean local intensity of every area under consideration. The size of the processed areas depends upon the quality of the images and is determined by a trial and error procedure. Figure 6 shows an image after the thresholds have been applied. Thus, a relatively uniform intensity is achieved as well as a constant concentration of particles for all the regions of the field of view.

In the majority of the cases when an image is acquired using a CCD camera a particle is not represented by a single pixel, but is occupying more than one pixel. In order to determine the

exact position of the particle with sub-pixel accuracy we smooth the edges of its image. Jahne (1991) describes the purpose of the smoothing and how it establishes sub-pixel accuracy. Subsequently we perform an “erosion” procedure. Recursive erosions of the speckle particle constitute this procedure, until a single pixel remains to represent the particle. If the procedure fails to a speckle geometry that no further erosion can be performed, then the centroid of the geometry is calculated using a weighted averaging approach based on the relative intensities of the pixels that construct the speckle. The erosion process is preformed in multiple passes. Figure 7 demonstrates the result of the erosion process.



**Figure 5:** Gray-scale sample image that demonstrates the high particle concentration.

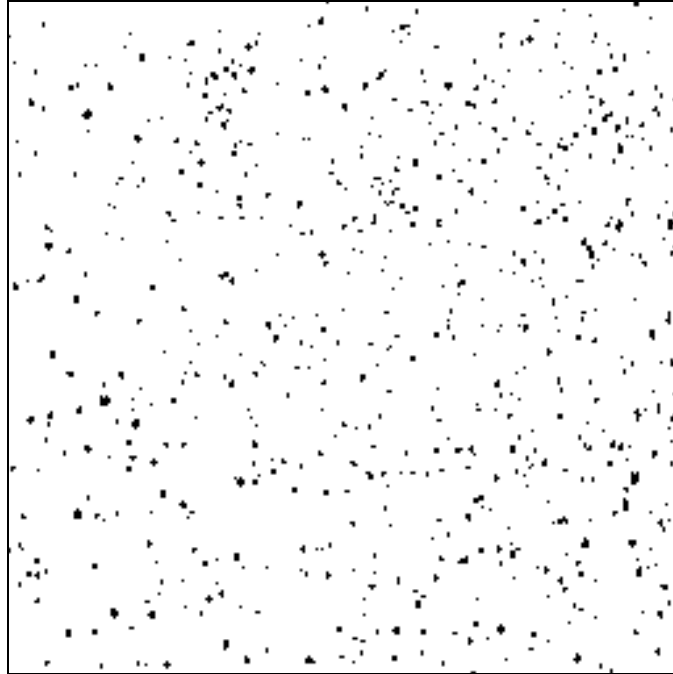


**Figure 6:** Sample image after the application of the threshold.

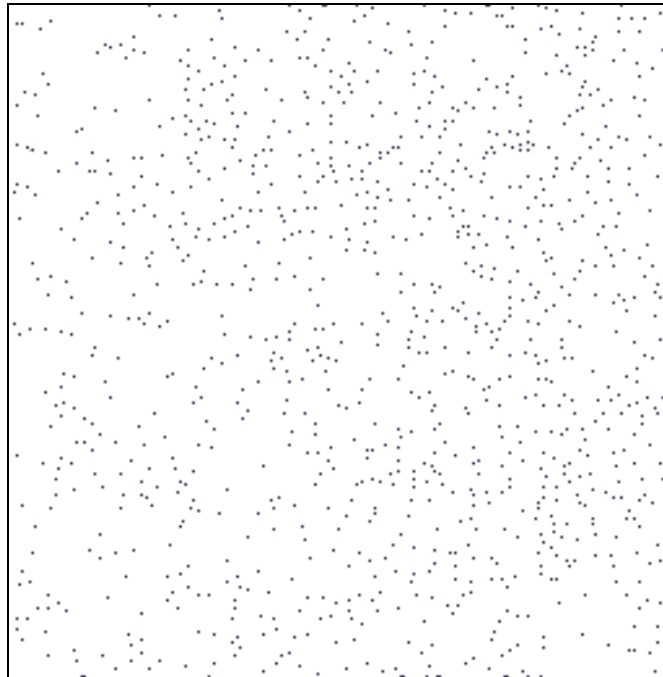


**Figure 7:** Sample image after the erode procedure.

A logical OR operation is applied on the sequence of the frames producing the streaks of each individual particle that resulted from the erosion procedure. These streaks are shown in figure 8 and they correspond to an accurate visualization of the flow. Assigning a decreasing grayscale intensity value on each pixel of the streak (the last pixel of each streak will always be black) provides directional information for the flow.

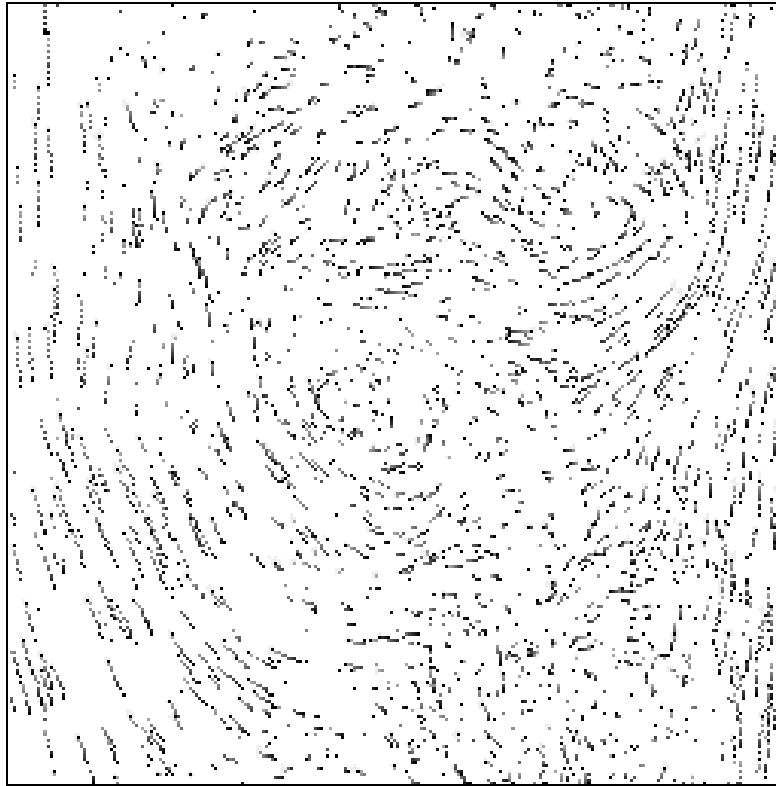


**Figure 8:** Sample image of the “OR” procedure resulted within a sequence of 10 frames.

The final step of the method is to calculate the velocity vector field for every instance of the flow by tracing particles within a short sequence of frames (i.e 5 frames). An implementation of a simple “nearest neighborhood” method is used. We perform three passes for each frame in order to determine the optimum match for each particle. Each pass corresponds to three different search radii, which are defined based on the free stream velocity of the particles. If a pass fails, the next one will use larger search radius. The optimum match will be selected among a number of candidate pixels by meeting dynamically pre-specified conditions for each particle. These conditions are defined based on the previous established direction of the particle and its intensity.

An increase in accuracy is achieved by keeping only the particles that are consistently traced during a sequence of 5 frames. The rest of the particles are ignored if they correspond to random noise or if they move out of the interrogation plane. Each traced particle is assigned a random 16-bit number as a “color identity”. This color identity will be the same for every instant of the flow field that the particle remains in the flow. Thus, if the time sequence is animated, the trajectory of the particle will be evident, providing visual proof of the accuracy of the tracking algorithm. Tracking within a sequence of frames resolves the problem of directional ambiguity automatically. Moreover, by tracking the particles within five frames, 200 realizations of the flow field per sec, can be obtained providing enough sampling frequency to investigate turbulence phenomena. This sampling frequency can be increased up to 1000Hz by using two overlapping images for each flow field analysis. The resulting streaks from a particle tracking within a sequence of ten frames are shown in figure 9.

## **Results**

In figure 10 the velocity vectors that correspond to the streaks of figure 9 are shown. Figure 11 represent the velocity vector fields at the same instant, as it is calculated using commercial cross-correlation PIV software. For the first plot of figure 11 an interrogation window of 32 by 32 pixels is used without overlapping, resulting in 64 independent vectors. The middle plot shows the same instant of the flow field processed with a window of 16 by 16 pixels with zero overlapping, producing 256 independent vectors. Finally, the last plot uses a 16 by 16 window where 50% overlap is used to interpolate the vectors, resulting in a total number of 961 vectors. The particle-tracking algorithm for this instant of the flow field produced a total number of 380 independent vectors, while by processing a series of 100 instances of the flow field using 10 frame sequences an average of 435 vectors are calculated.

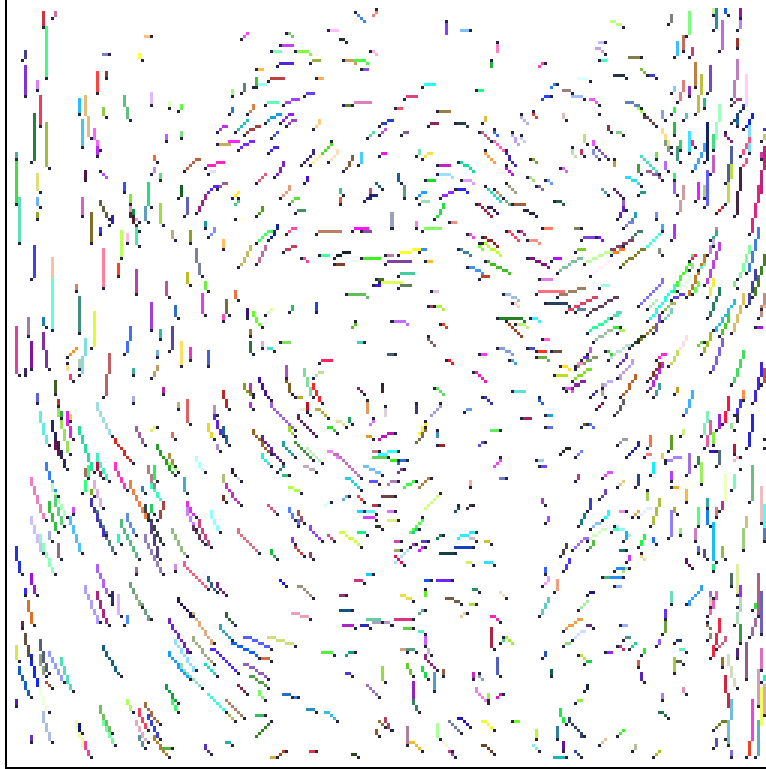


**Figure 9:** Particle trajectories traced within a sequence of ten frames. A unique identity (16-bit color) is assigned to each particle.

A direct comparison of these plots with the visualization plot of figure 8 shows that the particle-tracking algorithm describes the flow more accurately. Furthermore, the larger number of independent vectors provides more details for the coherent structures in the flow, for a wider range of length scales. Because of aliasing, the cross-correlation will not be able to resolve any structures smaller than the double of the Nyquist wave number, which is determined by the size of the interrogation window. Such a limitation does not apply on the particle-tracking algorithm. The use of smaller threshold values will result in increase of the calculated vectors increasing the mean wave number that can be resolved, at the expense though of decreasing the signal to noise ratio. In turbulent flows, high frequency structures correspond to smaller length scales therefore it is necessary to be able to resolve a broad wave number spectrum in order to be able to investigate the flow.

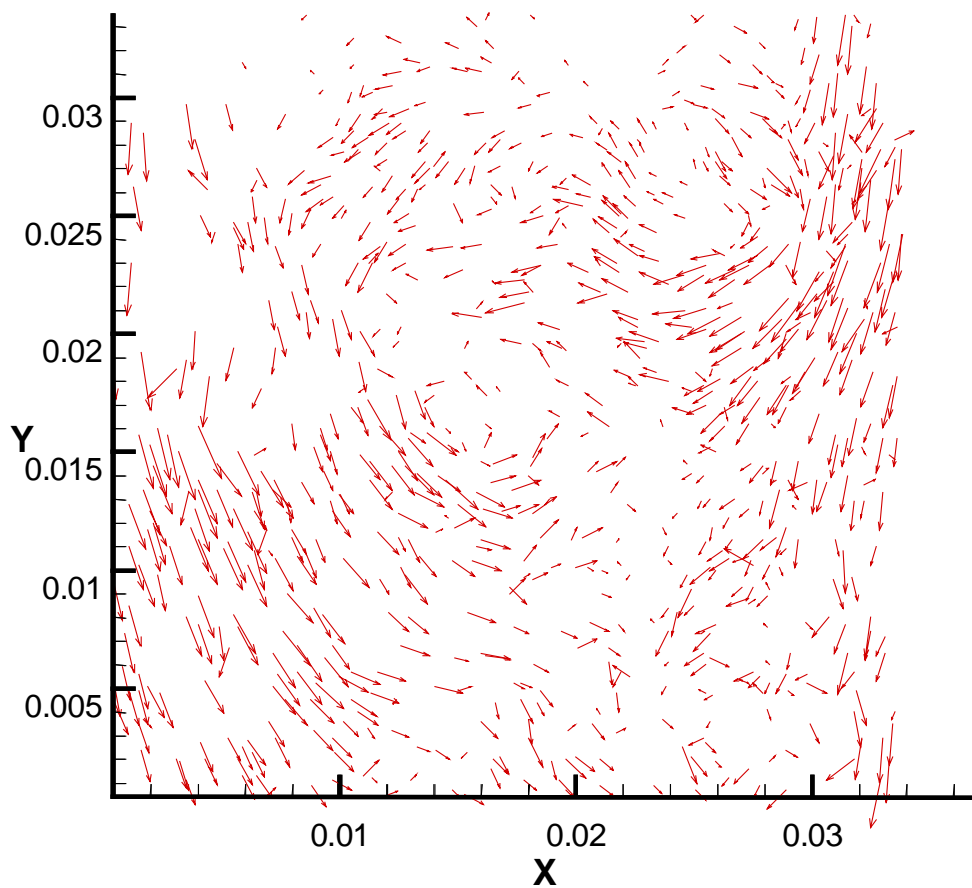


*Figure 10:* Particle trajectories within a sequence of 10 frames corresponding to 380 vectors.

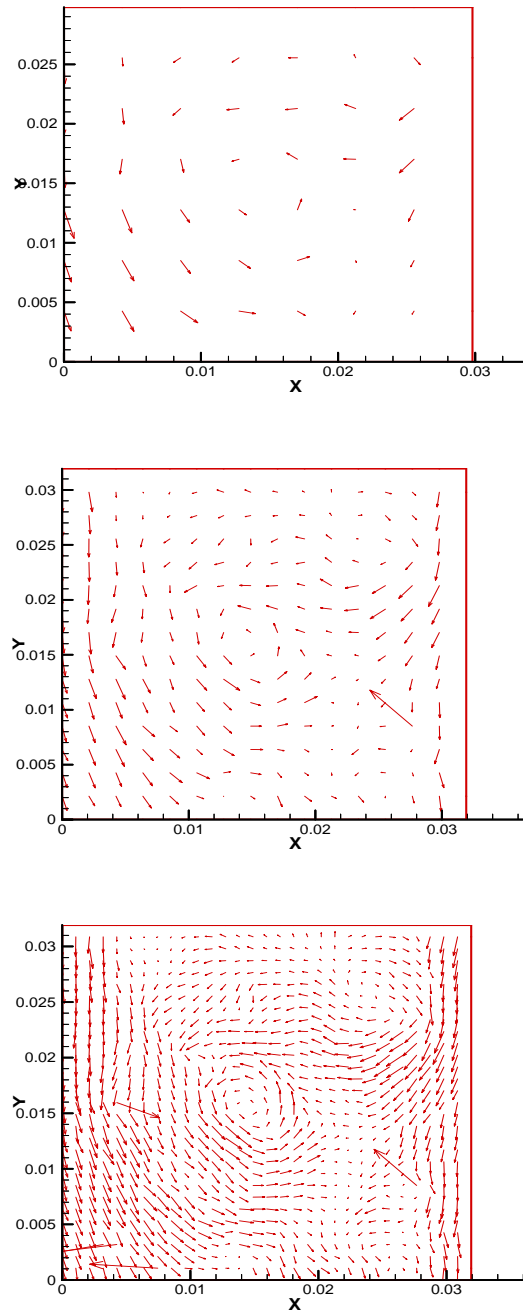


**Figure 11:** Velocity vectors resulting from a commercial cross-correlation PIV software, corresponding to the same instance of the flow field. From the top, vectors calculated with 32x32 interrogation window with 0% overlapping, with 16x16 window with 0% overlapping, and with 16x16 window with 50% overlapping.

## **Chapter 3**

# **On The Wake Of A Circular Cylinder Near The Free Surface.**

### **Spanwise Vorticity Distribution in the Near Wake Region**

#### **Introduction**

The flow over bluff-bodies and especially the wake of a circular cylinder has produced an endless number of publications (see reviews by Williamson 1995, 1996). The complexity of the flow lies on the fact that the upcoming free stream interacts with boundary layer formed at the forward side of the cylinder, the separated shear layer and finally the vortices that shed in the wake. Initially, it appears that the flow develops in a two-dimensional fashion but a more careful observation reveals three-dimensional patterns as for example the streamwise vortical instabilities which ride the separated vortex sheets (Wei and Smith 1986) (Bernal and Roshko, 1986). The three-dimensional effects on the wake of a circular cylinder depend primarily upon the end conditions. This has been demonstrated by several authors in the past, such as Ramberg (1983) and many others. End disturbances in the spanwise direction could trigger oblique shedding and totally violate the two-dimensional character of the flow (Hammache and Gharib 1991).

It has been demonstrated by several authors in the past such as Ramberg(1983), and many others, (see for example the review from Williamson 1996) that three-dimensional effects on the wake of a circular cylinder depend upon the end conditions. In the current study, we focus on the asymmetry of the end conditions introduced by the free surface. For a cylinder piercing a free surface, the free surface represents an end condition more compatible with the two-dimensional character of the flow. This is because on a solid wall, all the vortex lines must bend and align parallel to the wall, whereas on a free surface, vortex lines can terminate at the free surface. Yet, by introducing a free surface boundary condition, the complexity of the problem increases enormously. Free surface is a stress-free interface that constrains the motion of the vortex. As a result, it allows the existence of a vorticity component normal to the free surface and the process of vortex “reconnection” takes places. As an additional consequence, we can assume that the free surface acts as rigid image plane for the parallel vorticity component and thus inducing velocities that propel the vortex. If we take, also under consideration the effect of surface deformation, then we have to account for generation of secondary vorticity and vorticity flux. Deviations from the two-dimensional motion will develop when a free surface depression and surface turbulence characterize the core of the vortex. All this complexities constitute a behavior of the vorticity that is not observed in flows with no-slip boundaries. For a more detailed description of the mathematical boundary conditions, the reader is referred to Rood (1994a, 1994b, 1995).

The spanwise three-dimensionality in the wake of a circular cylinder has received much attention over the past years. The interaction of a separated shear layer with the forming vortices and the free stream triggers three-dimensional instabilities and vortex dislocations (Williamson 1992). Until recently, the major part of the related research was carried out using qualitative flow visualization. The existence of streamwise vortices was observed in plane mixing layers (Bernal and Roshko, 1986) and in the wake of a circular cylinder for a wide range of Reynolds numbers. (Gerrard 1978, Wei and Smith 1986, Williamson 1988). Particle Image Velocimetry has been employed by Lin et al (1995,1996) who studied the spanwise vortical structures in the near wake of a circular cylinder and documented the existence of large scale vortical structures with vorticity concentrations almost one-third of the streamwise vorticity and wavelength in the order

of one cylinder diameter. The relation of the length scales and the vorticity concentration of spanwise vortices (rollers) with the streamwise vortical structures (braids) are intrinsically related to the conservation of vorticity and the mechanism of vortex stretching. Furthermore, for  $Re > 1000$  the flow is affected mostly by the shear layer instabilities developing from both sides of the body introducing in the wake frequencies that are almost one order of magnitude higher than the vortex shedding frequency. Castro and Haque (1988) established that depending on the level of the oncoming free-stream turbulence the shear layer entrainment is enhanced. If the time scales of the free stream turbulence are of the same order of magnitude as that of the shear layer, the evolving instabilities will be enhanced and they will act in favor of the formation of a large-scale spanwise vortex. However, near the free surface we have a quasi two-dimensional turbulent flow field that is effected by the three-dimensional turbulence beneath it and as a result, reversing the energy cascade (Sarpkaya et al, 1994). Thus, it is reasonable to expect a variation of the streamwise vorticity with respect to the spanwise direction as we approach the free surface.

An extensive amount of work has been carried out so far to understand bluff-body wakes as well as the behavior of free surface vorticity. However, research combining the two problems is generally lacking. To this point, the author is not aware of many publications or reports on the fluid mechanics of a cylinder wake near a free-surface when the cylinder is piercing the free surface, despite the great importance of such a problem to engineering applications (offshore structures, ship wakes, risers) and understanding fundamental of fluid mechanics. Lang and Gharib (1998) have investigated the problem but with focus on the effect of varying free surface conditions. In their case, the free surface is contaminated by surfactants and is no longer a stress-free interface. As a result, the free-surface vorticity has the tendency to align with the free surface. Stern et al (1994) have studied the interaction of a flat plate piercing a free surface, however the flat plate was aligned with the free stream and the main objective was the understanding of the boundary layer development. Noca et al. 1998 investigated the wake of a circular cylinder piercing a free surface for a range of  $Re\ 300 < Re < 4,000$  using DPIV, but the focus of this investigation was the variation of the vortex formation length with respect to the Re number and not the effect of the free surface. The DPIV data were acquired in the region of the

mid-span of the cylinder. An important feature they reported was the great influence of the aspect ratio to the vortex formation length but they noted that the diameter of the cylinder plays an important role. However, they did not expand their work in the effect of the spanwise position and the free surface. Inoue et al.(1993) studied the problem numerically and experimentally. Their experimental measurements were performed for Reynolds numbers of 27,000 and 29,000 and corresponding Froude numbers of 0.8 and 1.0 in a towing tank facility. They conducted point velocity measurements using hot film anemometry. Their results suggest a quasi-periodic vortex shedding below the free surface but higher frequencies and more organized structures near the free surface. However, they reported suppression of the vortex shedding mechanisms near the free surface due to the interaction of the shear layers with the free surface waves. Their numerical calculations were limited to laminar cases thus they reproduce only large-scale features of the flow. More detailed and accurate computations using LES and RANS were performed by Kawamura. These computations confirmed the suppression of the vortex shedding near the free surface. For a Froude number of 0.8 the effect of the free surface extended almost one diameter below. These results suggested that the three-dimensional flow pattern near the free surface and the interaction with the free surface waves causes the separated shear layers to stay stable preventing the vortices from rolling and subsequently shedding.

To detect the effect of the free surface and the variations in the spanwise direction, we carried out two-dimensional velocity measurements at many elevations using Digital Particle Image Velocimetry (DPIV). During the past two decades numerous publications have appeared presenting improvements of this technique as well as applications of the method to a wide range of flows, from low-speed liquid and two phase flows to supersonic gas flows. The reader can refer to reviews by Adrian (1991) (1996a and 1996b), and Grant (1994), (1997). The digital implementation of PIV was discussed in detail by Willert and Gharib (1991) and Huang and Gharib (1997). In the present study, we employ a high time-resolution DPIV system overcoming a major disadvantage of standard commercial DPIV systems. Most conventional systems provide a sampling frequency up to 30Hz, which is not adequate to resolve turbulence fluctuations in a flow. In other cases high sampling frequency can be reached but for a very limited duration of time, resulting to a period much smaller than the time scale of the phenomena under

investigation. By reaching a sampling frequency of 1000Hz, the current study provides sufficient time and space resolution to investigate turbulent phenomena. Simultaneously with PIV data that are obtained along different elevations, a single fixed-point LDV record is obtained to provide a reference for the proper stacking of events. In this way, a direct comparison of the individual planes as they overlay on top of each other, can be achieved.

The main thrust of the work presented here is to explore the flow over a free-surface piercing circular cylinder. We focus on the influence of the free surface on the three-dimensional character of the flow and on the asymmetry of the end conditions introduced by replacing one of the boundaries with a free surface. Practical applications of the flow under examination here can be found in offshore structure designs. However, the Fr number is kept very small ( $Fr=0.3$ ), essentially representing a free-slip surface with almost no deformation.

Digital Particle Image Velocimetry measurements are employed to investigate the turbulent characteristics of the wake of a circular cylinder in the vicinity of the free surface for  $Re=1700$  and  $Fr=0.3$ . Time averaged plane distributions of the mean velocity magnitude, vorticity,  $u'_{rms}$ ,  $v'_{rms}$  mean turbulent kinetic energy, and  $u'v'$  are presented. We found that the vortex formation length increases as we approach the free surface extending up to 3.4 diameters downstream, while the width of the wake practically doubles to approximately two diameters. Vorticity is increasing as we move to higher elevations but is decreasing to a minimum at the last elevation corresponding to the free surface, thus indicating a vortex shedding suppression. Turbulent kinetic energy is primarily dominated by the fluctuations of the transverse velocity component but as we reach the free surface the turbulent intensity decreases and the fluctuations of the streamwise component are contributing to a greater extent. The instantaneous unsteady characteristics of the flow are investigated by employing a new approach to stack properly planes of PIV data, using the LDV signal as a guide for elimination of the phase difference. The results indicate larger structures away from the free surface. Very near the free surface evidence is presented of motion in the vertical direction, which may have the character of upwelling

## **Experimental details**

### **Facilities and Experimental Setup**

The wake of a circular cylinder piercing the water free surface for a  $Re_D=1700$  based on the diameter was investigated. DPIV data were obtained along different elevations. The aspect ratio of the cylinder was 12.8. By translating the sheet-forming optics, we were able to interrogate seven different planes. The first plane was located 8.4 diameters from the base of the cylinder and the elevation increment for the next five planes was set to be 0.8D (cylinder diameters). The last (7th) plane was placed at 0.005m below the free surface corresponding to a step increment of 0.08D. The field of view was one diameter downstream from the center of the cylinder. A fully automated traversing system with feedback using linear variable displacement transducers was employed in order to assure accuracy in the positioning.

The present study was conducted in a 2'x2', low-speed and low-turbulence water tunnel, operated with a free surface. The tunnel was set to run at a free stream velocity of 0.12 m/sec. Figure 1 shows the arrangement of the experimental setup, while figure 1-1 gives a schematic of the placement of the planes of interrogation with respect to the cylinder

The model is a rigid 15.875mm in diameter PVC cylinder mounted vertically in the test section. Precautions to limit flow-induced vibrations were taken. There was no attempt made to polish the cylinder beyond its manufacturing smoothness, since it is proven that moderate roughness does not affect the flow at low Re number.

For the PIV laser sheet, the light source was a copper vapor 45Watt pulsing laser, delivering approximately 5.5mJ/pulse at its optimum operation. Using a set of set optics in a telescopic arrangement, a laser sheet was delivered into the test section. The laser was synchronized with a high-speed CCD camera (EG&G MD4256) using a timer board (Real Time Devices, TC524). The number of images acquired was 1000/sec with a resolution of 256x256 pixels. Digital images were automatically stored in the image buffer of an SB4001 Adaptive Optics frame grabber. The viewing area was adjusted to 0.001 m<sup>2</sup>. Hollow glass silver coated

spheres of 10-30 microns average diameter were used as flow tracers. The data acquisition process is digital eliminating the tedious and time consuming tasks of film digitization and allowing the real time observation of the flow field.

The high sampling rate of the data acquisition process introduces significant requirements on the illumination of the flow field. In order to synchronize the laser with the camera, a light source matching the frame rate of the camera is required. Standard YAG lasers cannot perform at such high pulsing frequencies. Copper vapor lasers can deliver repetition rates up to 30KHz. However, the light coherence is poor and, more importantly, the range of operation is very limited and is centered on an optimum frequency of 6-8 KHz. In addition to that, the mean output power of the laser drops drastically as we reduce the pulsing frequency, subsequently delivering lower energy per pulse. Small bursts of the laser pulsing frequency result in cooling down the laser, which in effect results also in reduction of the output power. In order to compensate for the energy losses and deliver sufficient illumination in the area under investigation, a set of optics specially coated for the exact wavelength of the laser was employed. This resulted in decreasing the losses through the optics from approximately 40% to less than 10%. Additionally, the camera was equipped with a 55mm Nikon lens with  $f\#$  of 1.2, to allow more light on the sensor during the limited exposure time of 1/1000 secs. These improvements allowed us to acquire data up to 1000 frames/sec, which otherwise wouldn't have been feasible.

A two-dimensional fiber-optic LDV system was used to take fixed-point velocity measurements. In order to avoid background noise in the PIV images no LDV particles were added to the flow. The measurement point was located two and a half diameters downstream of the cylinder axis and one and a half diameters across its axis. The elevation of the fixed LDV point is  $8.4D$ . A view of the experimental setup is shown in Fig.1. Both systems, PIV and PDV, were triggered simultaneously and recorded data for a period of 2 secs. This time corresponds approximately to four periods of the phenomenon. Hardware limitations deprived us from the ability to acquire data for longer times. A HP Signal Analyzer was also used for real time monitoring of the spectra of the fixed-point velocity, to ensure the repeatability of the experiment. A small amount of LDV seeding (1 micron diameter particles) was added in the flow

to improve the signal-to-noise ratio but in order to avoid increasing the background noise levels of the acquired images we primarily relied on the PIV seeding particles for the LDV measurements as well. The LDV data rate was above 1000 Hz and a “sample and hold” approach was used to reconstruct the signal. Because of the improper seeding, the noise levels of the LDV signal were significant. But since the goal of the approach was only to estimate the time delay of realizations of periodic phenomenon and not to perform accurate LDV measurements, no further attempt to improve the quality of the signal was made.

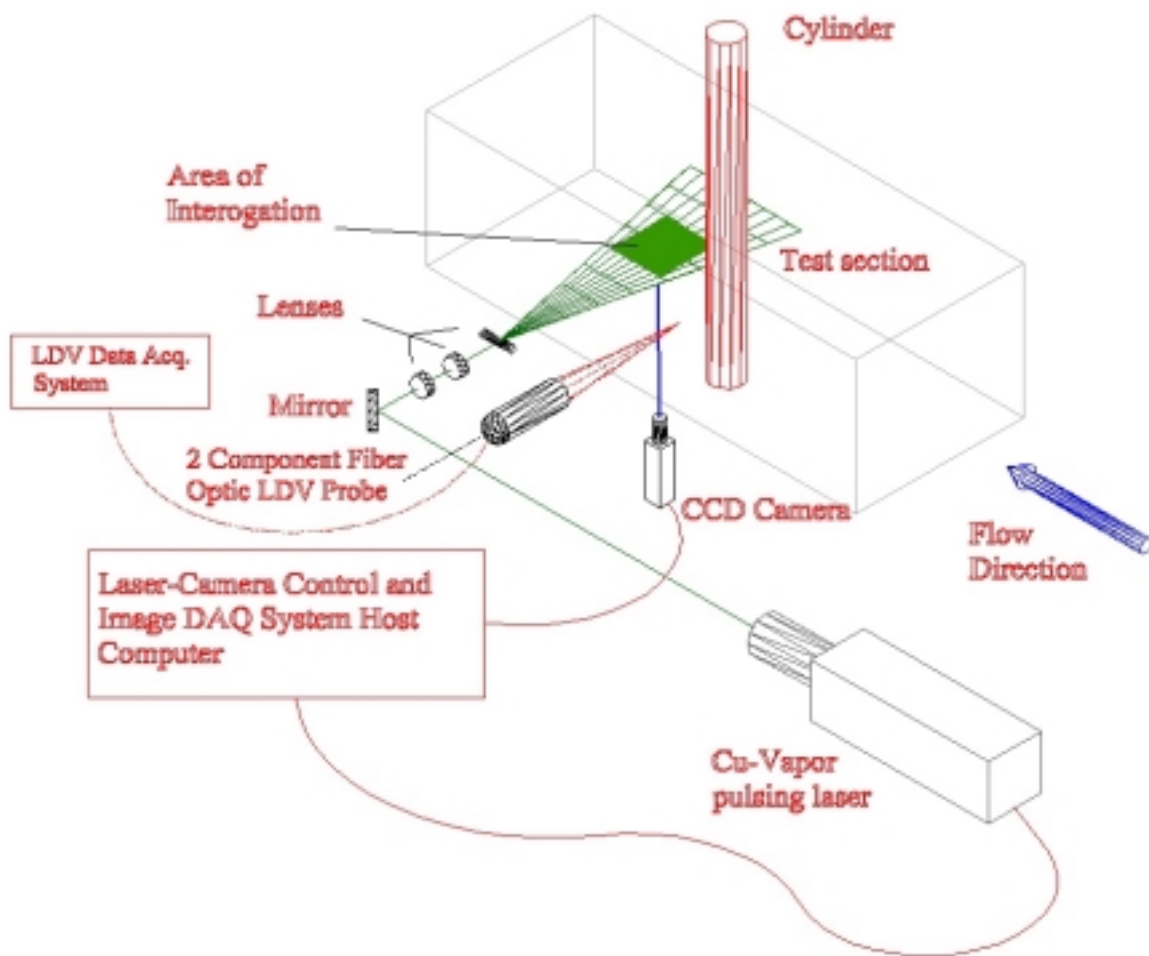


**Figure 1:** A view of the experimental setup with the laser sheet in the wake of cylinder and parallel to the free surface.

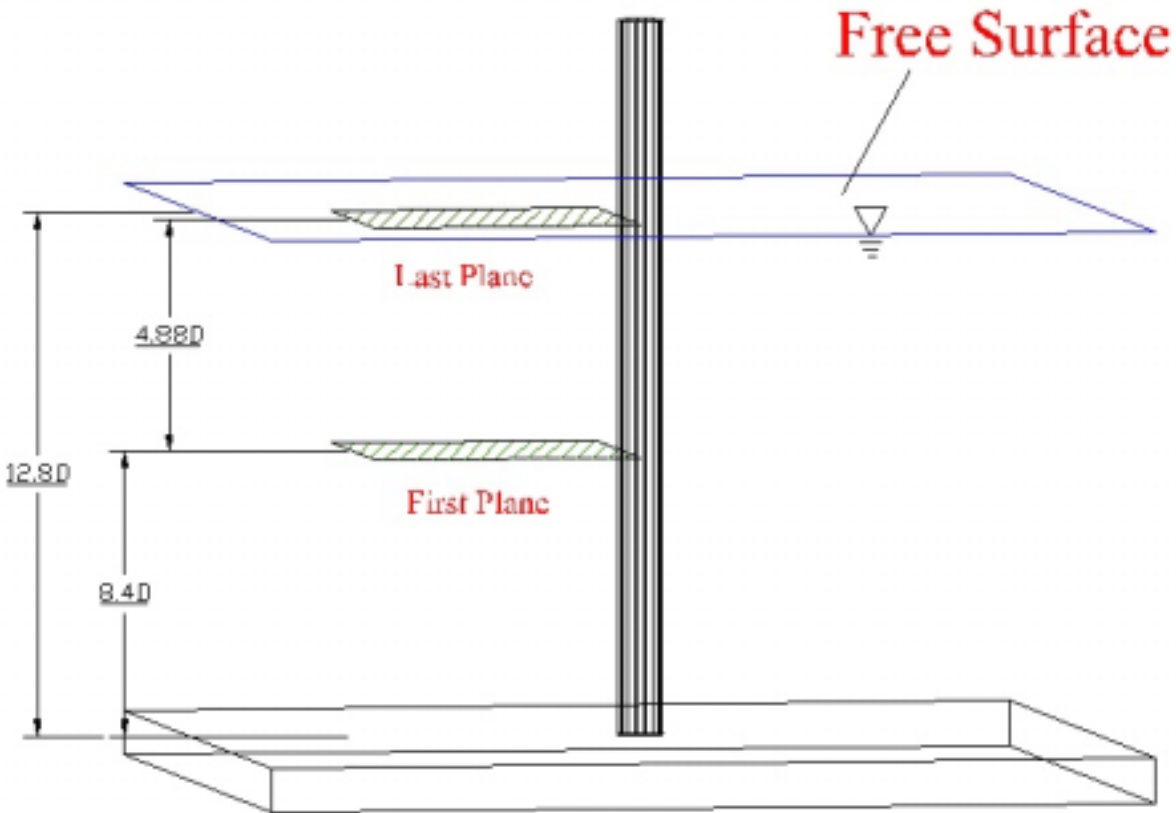


**Figure 1-1:** PIV planes located with respect to the flow and the cylinder for measurements parallel to the free surface.

### **DPIV Software and Data Analysis**

The image-processing task for the PIV images was carried out with Visiflow on a Pentium II 450 based PC, processing one frame every 4.secs. For each plane of interrogation, 2000 frames were acquired with a sampling frequency of 1000fps. The image dynamic range was 8-bit, resulting in 256 shades of gray. As the elevation increased, the field of view expanded from  $1.85D$  at the first elevation, to  $2.35D$  at the last one. Standard dual-frame single-exposure cross-correlation was used to extract the velocities resulting in  $61 \times 61$  vectors placed in a uniform grid. Based on the dimensions of the field of view, the minimum step size is 1.6% of the cylinder diameter. Since the CCD camera outputs directly in digital format, any error resulting from the digitization is considered negligible. The use of 10-micron, neutrally buoyant particles as flow

tracers eliminates any errors due to the seeding. The mean particle density is estimated at 3000 particles per frame, with a particle image diameter of approximately 2.5 pixels, thus optimizing the performance of the cross-correlation. A tree-point Gaussian estimator for the correlation peak is used, achieving sub-pixel accuracy of 0.1 pixel for the peak detection process and considering the error from the vector validation and interpolation process, the overall uncertainty of the velocity is estimated to less than 0.1%FS (full scale with respect to the free stream velocity). The vector validation process employed criteria about the velocity magnitude the continuity of the calculated vectors, and a quality factor of the estimated cross-correlation peak point considering the existence of multiple peaks in the interrogation window. Interpolation was carried out using a local weighted average approach. Finally, the data were smoothed using a 5x5 Gaussian filter.

In order to achieve the spatial resolution of 0.0016D the size for the interrogation window was set to  $16^2$  pixels. The optimum performance for cross-correlation evaluation of the velocities is well established for windows of interrogation of  $32^2$  and larger (Willert and Gharib (1991) and Huang and Gharib (1997), Keane and Adrian (1990, 1991)). The minimum number of particle pairs required is five, while the mean particle image diameter, is 2.5 pixels. Very little information exists in literature for smaller sizes of the interrogation window, primarily due to the fact that the most popular digital cameras used provide significantly higher resolution but at frame rates up to only 30 fps. In addition, these studies were performed using artificially generated images. Therefore, there was the need to optimize our system (hardware-software combination) to perform under the specific requirements.

Artificial images were generated using the approach described by Raffel et al.(1998) to simulate the effect of electronic noise of the camera and Gaussian distribution across the thickness of the laser sheet and the corresponding intensity of the scattered light from the particles. The particles were displaced according to an exact analytical solution, namely Couette flow, with a minimum displacement of 0.5 pixels and maximum of 7 pixels. Any displacements larger than eight pixels would be prohibitive to use an interrogation window of  $16^2$  pixels because of the Nyquist frequency and thus it was not considered. Figure 2 shows that the validation quality of the cross-correlation evaluation of the velocities reaches almost 100% for a

number of 10 particles per window. This is the same conclusion that previous studies have reached but for larger size windows. However, it is worth mentioning that with a mean particle image diameter of 2.5 pixels and 10 particles for every  $16^2$  pixels this results to 6400 particles in our flow field. Considering a realistic situation where we have out of plane motion of the particles and relatively high background noise from the flow field and electronic noise from the sensors, this number indicates that the interrogated image will be very close to be saturated in order to have the required number of distinct particles in the flow. Therefore, extreme care was taken to achieve the appropriate amount of seeding without saturating the flow. Once the condition was set, an estimation of the error was carried out by acquiring a set of images of a quiescent flow field (zero velocity). The mean calculated velocities should be zero. By performing this test, the resulting error was less that 0.01. Of course, the particle displacement and the flow conditions will increase the error by almost an order of magnitude reach the 0.1 of the full scale that was previously mentioned.

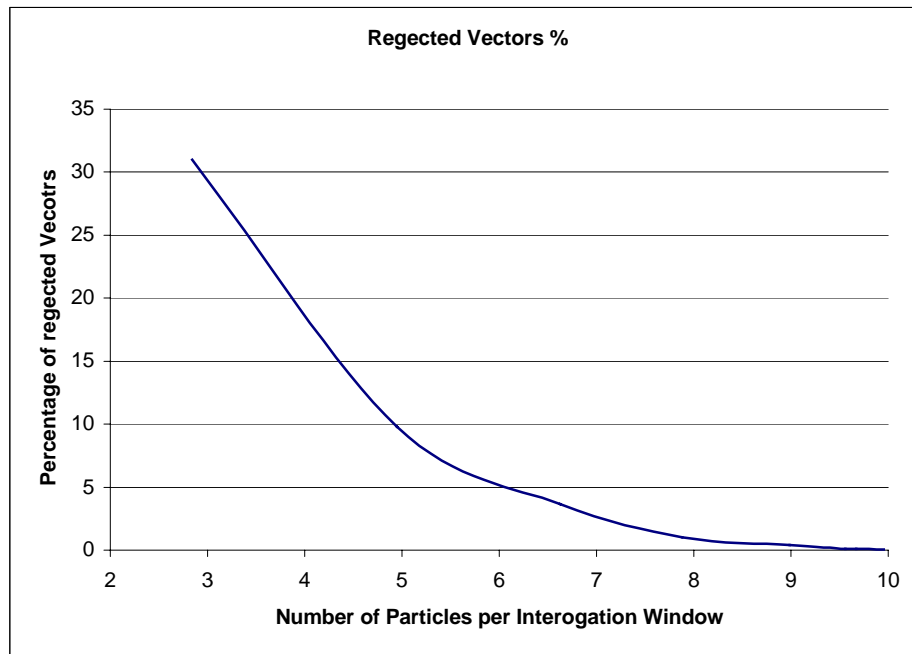


**Figure 2:** Graphical representation of the accuracy of the method with respect to the number of particles for a window of interrogation of  $16^2$  pixels for an artificial flow field with a displacement dynamic range from 0.5 pixels to 7 pixels

Any other sources of error resulting from the digitization of the images or from the seeding of particles (Agui and Jimenez, 1987) are not considered. The digitization error is eliminated by the use of the digital camera, while the use of particles that are small in diameter and neutrally buoyant practically eliminates them as a source of error. The errors from the interpolation and the filtering procedure are embedded in the overall error evaluation and there is no need to treat them independently.

The vorticity calculation was performed by applying fourth-order compact schemes (Lele, 1992) to reduce the contribution of the truncation error to the overall error of the calculation. In most cases, vorticity is calculated from experimental results using explicit second order schemes or is calculated from the circulation. Comparisons with artificial data were carried out and it was shown that the compact implicit schemes are more accurate, paying only a small price of computational time. Turbulent characteristics of the flow were calculated, namely mean velocity magnitude, turbulent kinetic energy, the two-dimensional Reynolds stress tensor, and the RMS values of the velocity components throughout the flow field. The time-average data presented correspond to a period of 2secs from a sequence of 2000 instants of the flow field. With a vortex shedding frequency of approximately 2 Hz, four periods of the phenomenon are taken into account.

## **Mean and Turbulent Characteristics of Spanwise Vorticity near the Free Surface**

### **Results and Discussion**

The first set of figures (3-1 to 3-7) presents contours of the mean velocity magnitude, overlapped with mean streamlines. The mean quantities were calculated by averaging the entire time series over time. The location of zero velocity corresponds to the mean closure point of the wake, namely the vortex formation length. We observe a variation of the location of the saddle point as we approach the free surface. Initially (figure 3-1) is located at approximately 2.4 diameters downstream. Noca et al studied the position of the vortex formation for different diameters, aspect ratios and Reynolds numbers at the mid-span of the cylinder using DPIV. For the same cylinder diameter,  $L/D = 29$  and within a range of Reynolds numbers  $1,000 < Re < 4,000$ , they reported a vortex formation position that ranged from 2.2 to 2.7. The difference can be primarily attributed to the fact that our first plane is not placed at the mid-span of the cylinder but at approximately 65% of its span. In the next plane, (figure 3-2) the vortex formation position shifts upstream to a region close to 2 diameters. From plane 3 and up, it starts extending downstream to a position of about 2.8 diameters (figure 3-3), 3 diameters (figure 3-4) and as we move closer to the free surface it extends outside our field of view, by more than 3.4 diameters away from the center of the cylinder. The region of the wake with zero mean velocity expands.

Time average of the periodic unsteady flow of the wake of a circular cylinder results in a vortex pair “bubble”, representing the primary alternate vortices that propagate through this region. However, the time average removes any feature related to the alternate vortex shedding. One interesting feature is the existence of this vortex bubble for the first three planes. Extended time averages of PIV data for larger aspect ratio cylinder and symmetric boundary conditions (Lourenco, 1996) present the same topology of the mean flow field. On the following three elevations, the flow structure exhibits a less organized behavior and finally the vortex bubble recovers at the free surface.

For planes 4-6, the elongation of the wake results in a zero mean velocity region with very strong velocity gradients, resulting in turn to strong shear layers. This can be clearly seen in figures 4-1 to 4-7 presenting the mean vorticity. The acceleration of the flow in planes 4-6 (figures 3-4, 3-5, 3-6) is of the order of 1.8 of the free stream while on the last plane, at the free surface, only 5mm above the previous elevation, this magnitude drops down to 1.2 of the free stream. Finally, we note the fact that the effective width of the wake on the first plane is one cylinder diameter –as expected- but at the free surface expands to approximately two diameters.

The above-mentioned features of the variation of the shear layer with respect to the spanwise direction are shown clearly in the next set of figures (4-1 to 4-7) representing the vorticity contours. Between planes one and two, the length of the shear layer decreases, thus agreeing with the corresponding decrease of the vortex formation length observed in the previous set of figures. On the following planes, the variation of the vortex formation length is in agreement with the length and thickness of the formed shear layers. However, we note a sharp decrease of the vorticity levels between the sixth and seventh plane were the values of maximum vorticity drop by almost 50%. In order to meet the kinematic boundary condition the vortex is forced to reconnect normal to the free surface. Therefore, we would expect the vortex axis to be normal to the plane of interrogation, showing increase of the in-plane vorticity. In addition to the fact that the vortex pair structure recovers at the free surface, we conclude that the free surface partially suppresses the vortex shedding, resulting in a weak vorticity field.

Conclusions for the mean closure point of the wake can also be reached from the distributions of  $u'_{rms}$   $v'_{rms}$ . Initially in figures 5-1 to 5-7, we in the first three planes a mild increase of the rms values of the transverse velocity component. But from the fourth plane and as we approach the free surface, the values of the turbulent fluctuations drop significantly reaching a level of about 50% at the free surface. Based on the definition by Bloor and Gerrard (1966), the vortex formation length will coincide with peak rms value of the transverse velocity component along the centerline. Therefore, we can attribute this decrease of the  $u'_{rms}$  to the fact that the mean closure point is displaced by 3.4 diameters downstream as we have already observed from the previous plots. As a result we obtain a statistically zero fluctuation of the transverse velocity

component from planes five and six. As we reach the last plane, we note a significant increase of the vorticity with respect to the previous plane. This is attributed to the free surface turbulence. The region near the free surface will not be turbulent free, even if the flow field below is. This is because of the existence of upwellings and downdrafts while small eddies are forced to alternate the orientation of their axis in order to reconnect normal to the free surface.

A different behavior is observed for the fluctuations of the streamwise velocity component presented in figures 6-1, to 6-7. Initially the rms level increases for the first three planes (6-1, 6-3), and slightly decreases for the next two (4-5). As we reach very close to the free surface (planes 6-7), however, the values increase significantly. In addition, we note that throughout the flow field, the maximum levels of  $u'_{rms}$  are smaller than the corresponding  $v'_{rms}$  but this is reversed in the vicinity of the free surface. In two-dimensional flow the increase of the turbulent intensity will result in increase of both  $u'_{rms}$  and  $v'_{rms}$ , indicating the existence of eddies with their axis normal to the x-y plane. However, in the present case we have a three-dimensional field which we are investigating using a two-dimensional measurement technique. We have no information of the behavior of the  $w'_{rms}$  component. Furthermore, in the vicinity of the free surface, the flow is constrained by the interface. Since velocity component fluctuations are essentially due to disturbance vortices, the decrease of one component should imply the increase of another. In the present case if  $v'_{rms}$  increases but  $u'_{rms}$  decreases, implies that  $w'_{rms}$  must be increasing. This indicates a turning of the individual disturbance vortex vectors towards the direction parallel to the free surface. This at first appears to be contradicting the mathematical boundary condition at the free surface that dictates that the vorticity vector should be normal to the free surface. Apparently, the vorticity vectors turn upwards and the vorticity lines reconnect with the free surface only in the immediate vicinity of the free surface. This explains the free surface visual observations of wavy streaks that are broken in distinct cells. We interpret this to mean that vortices with their axis parallel to the free stream reach the interface and then break up in small cells that turn individually up to reconnect with the free surface. The evidence collected here in terms of vorticity content combined with the velocity fluctuations distributions, indicate that axial vortices, i.e. vortices close to the direction of the free stream and therefore parallel to the free surface get reinforced as we approach the free surface.

The next set of figures (7-1 to 7-7) presents the distribution of turbulent kinetic energy. The first observation here is that plane-by-plane comparison of the  $v'_{rms}$  with the turbulent kinetic energy, shows a qualitative agreement, indicating that the turbulent kinetic energy is dominated by the fluctuations of the transverse velocity component. However, as we approach the free surface, this agreement is degrading and on the free surface plane where the levels of turbulent kinetic energy have reduced by approximately 50%, the contribution is coming primarily from the fluctuations of the streamwise component. In addition, for the first three planes, the peak values of the turbulent kinetic energy coincide with the location of the mean closure point of the wake, therefore the turbulent kinetic energy can serve as an additional criterion to determine the position of the vortex formation length.

The final set of figures demonstrates the contours of the mean  $u'v'$  component of the Reynolds stress tensor. The general structure of two symmetric “islands” of opposite sign corresponding to the alternate vortex shedding mechanism is noted. In plane four however, the negative sign stresses are reduced with respect to the positive indicating an asymmetry in the vortex shedding in a time mean sense. This asymmetry is in agreement with the asymmetry of the topology of the flow observed in figures 3-4 and 3-6. In plane 5 the levels are almost zero due to the fact that the vortex formation location has shifted outside the field of view. In the next plane, which is very close to the free surface, the stresses present a sudden increase, followed by a subsequent drop in the last plane which in combination with the previous observations about the vorticity distribution at the same elevation leads us to the conclusion that the vortex shedding is being suppressed near the free surface.

Figure 3: Set of figures for the velocity magnitude.

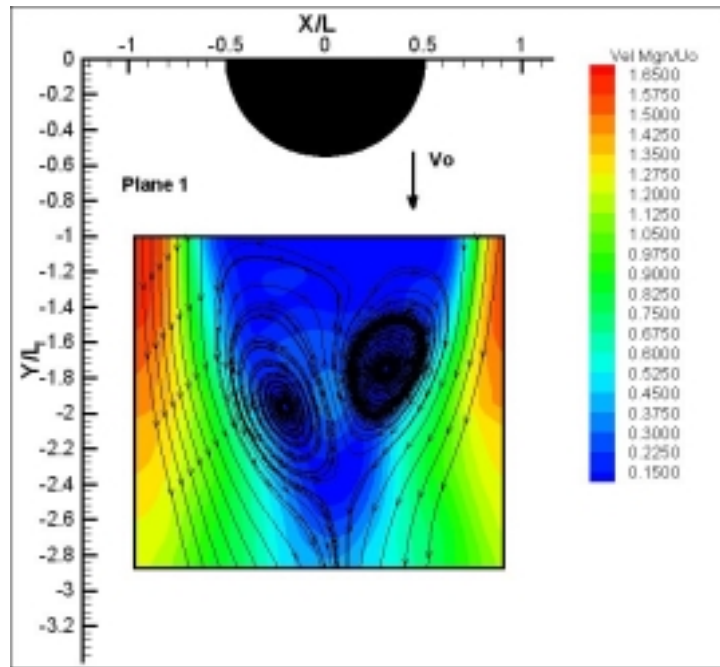


Figure 3-1: Color contours of Velocity Magnitude distribution for plane 1.

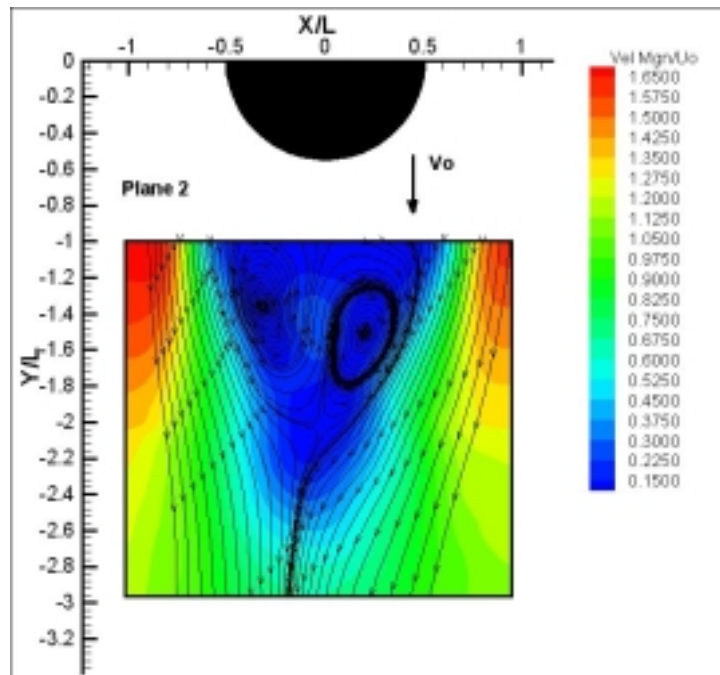


Figure 3-2: Color contours of Velocity Magnitude distribution for plane 2

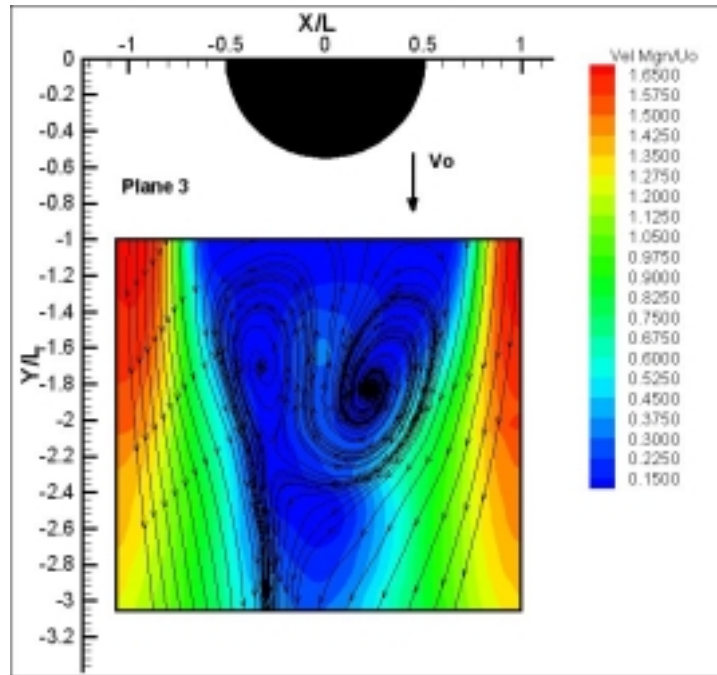


Figure 3-3: Color contours of Velocity Magnitude distribution for plane 3.

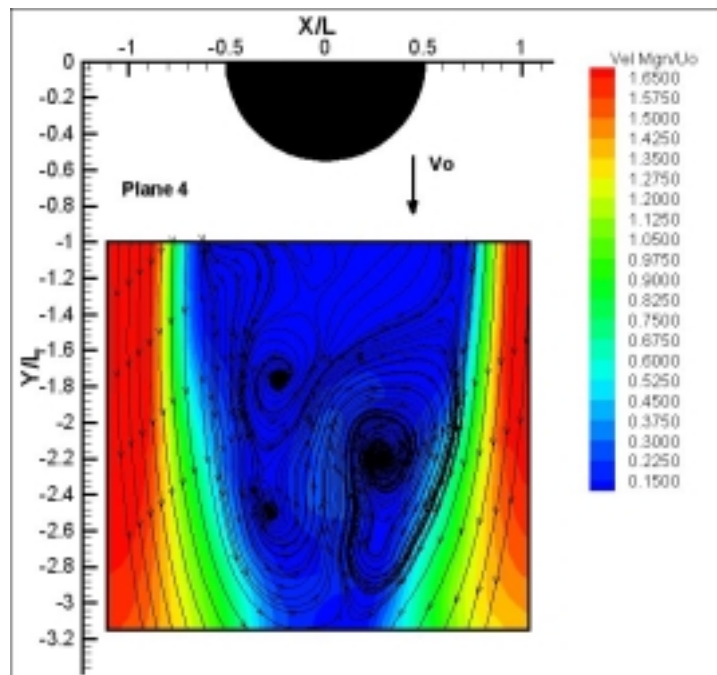


Figure 3-4: Color contours of Velocity Magnitude distribution for plane 4.

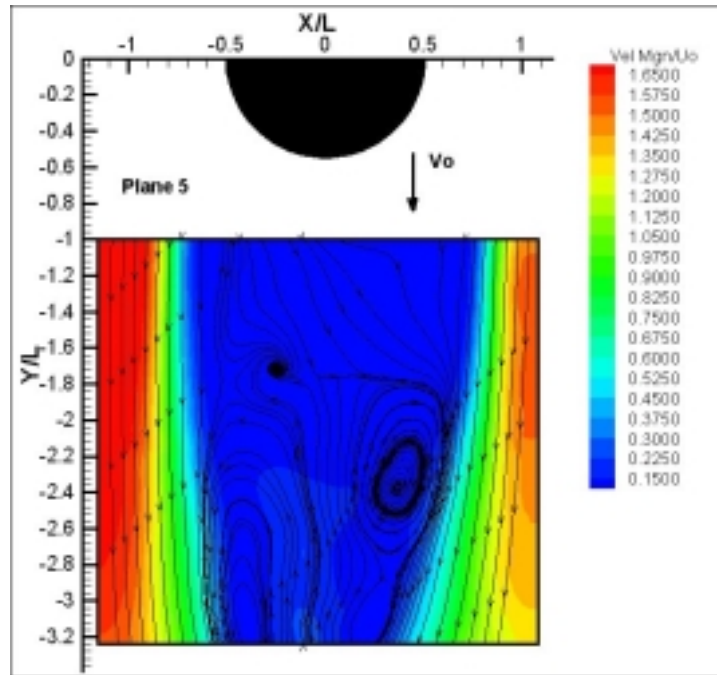


Figure 3-5: Color contours of Velocity Magnitude distribution for plane 5.

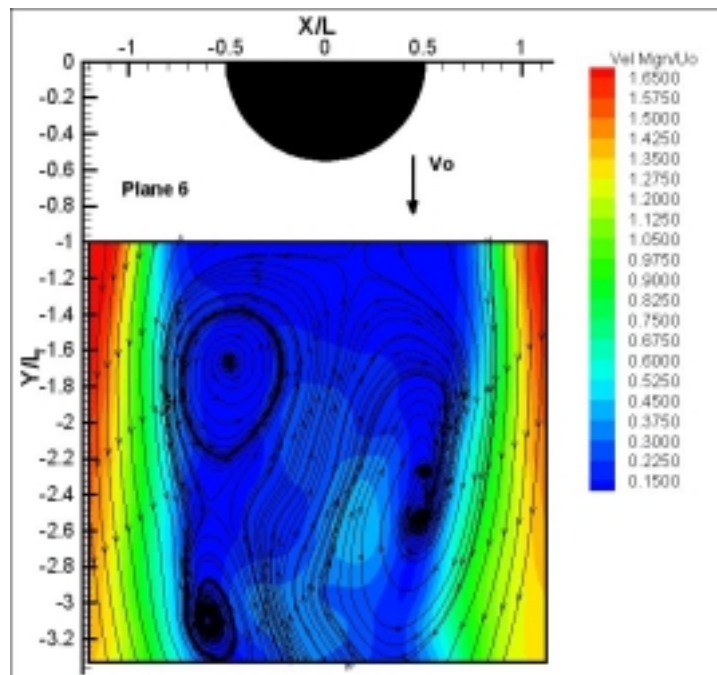
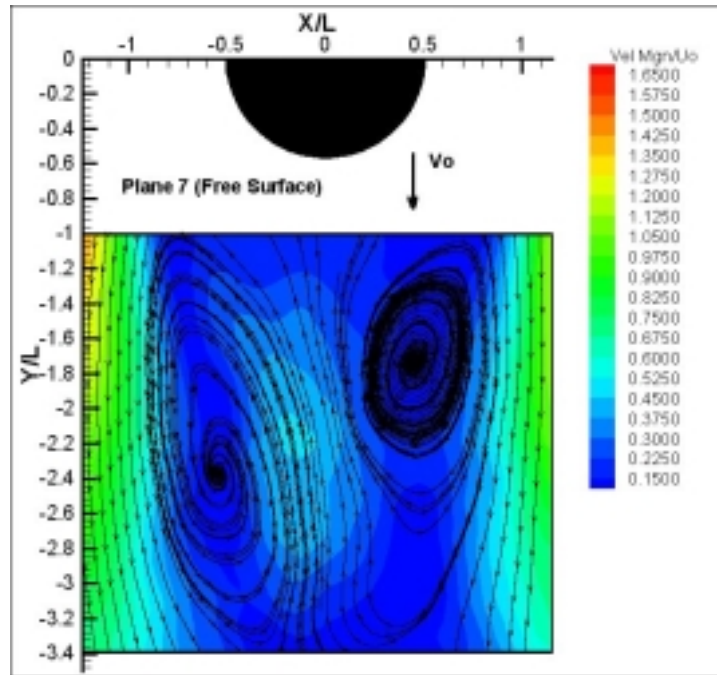


Figure 3-6: Color contours of Velocity Magnitude distribution for plane 6.



**Figure 3-7:** Color contours of Velocity Magnitude distribution for plane 7.

Figure 4: Set of figures for the vorticity distribution

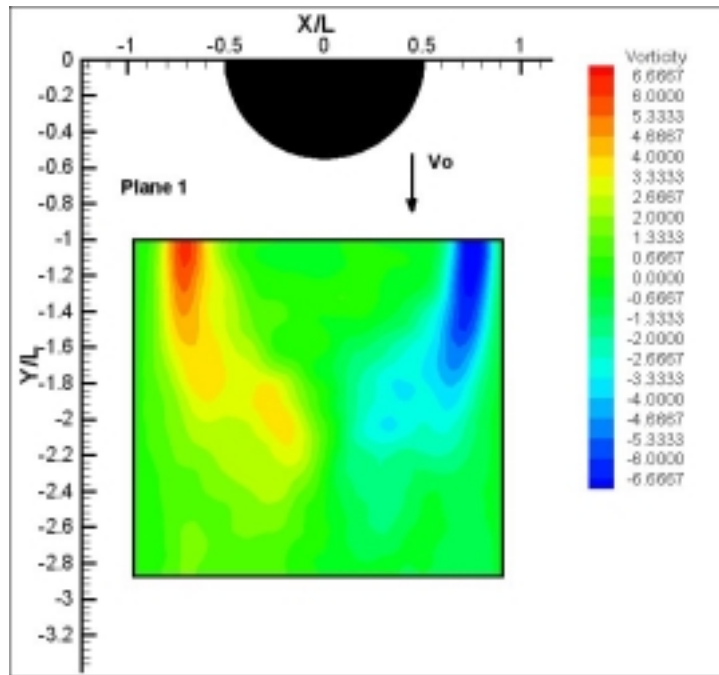


Figure 4-1: Color contours of Vorticity distribution for plane 1.

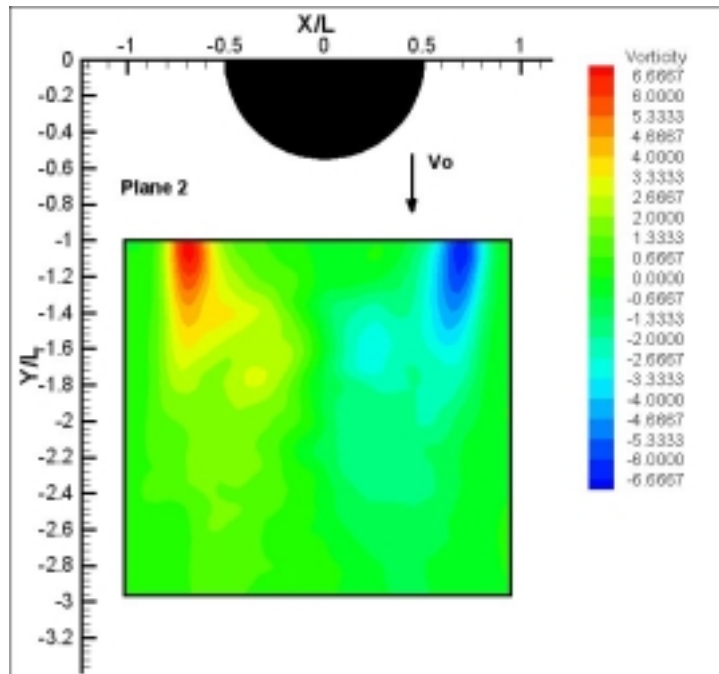


Figure 4-2: Color contours of Vorticity distribution for plane 2.

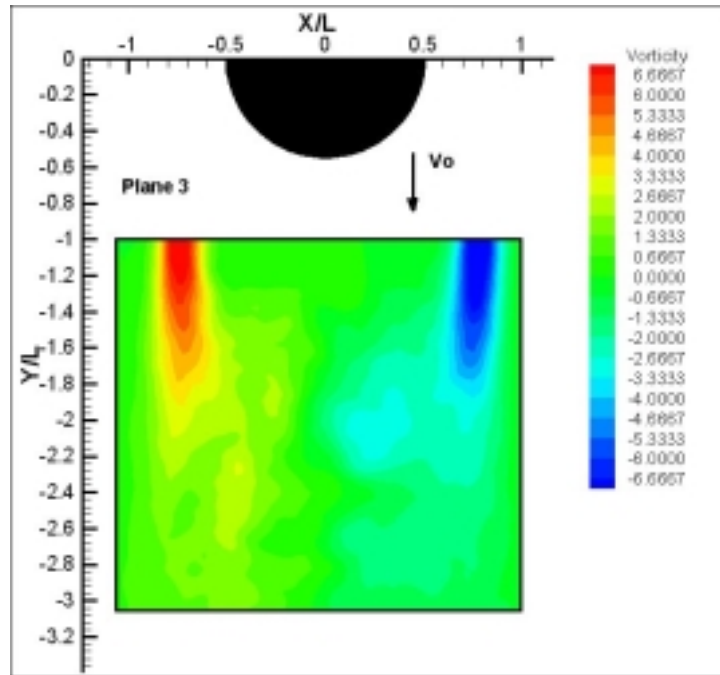


Figure 4-3: Color contours of Vorticity distribution for plane 3.

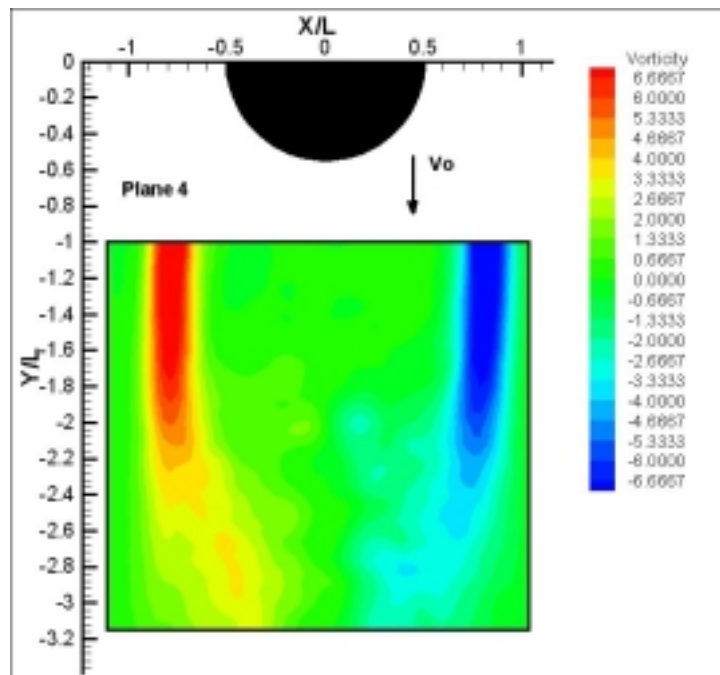


Figure 4-4: Color contours of Vorticity distribution for plane 4.

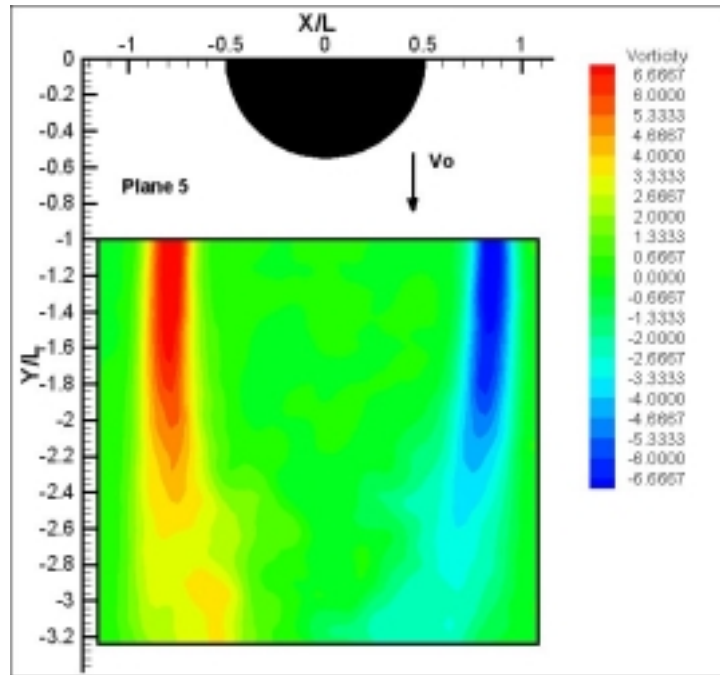


Figure 4-5: Color contours of Vorticity distribution for plane 5.

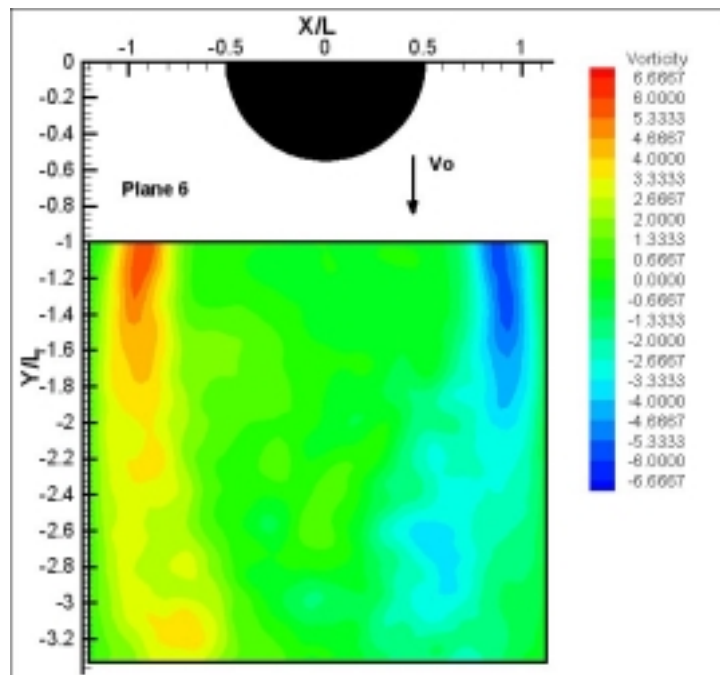
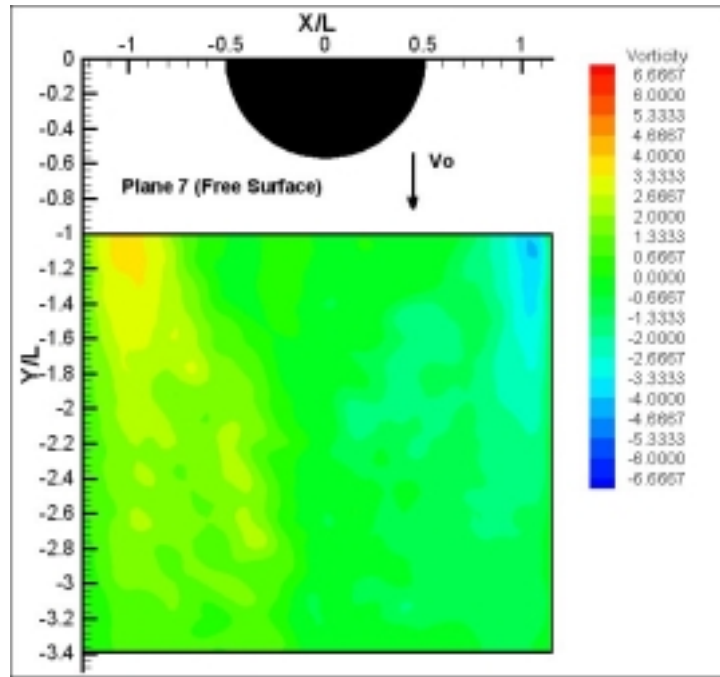


Figure 4-6: Color contours of Vorticity distribution for plane 6.



**Figure 4-7:** Color contours of Vorticity distribution for plane 7.

Figure 5: Set of figures for U-RMS distribution

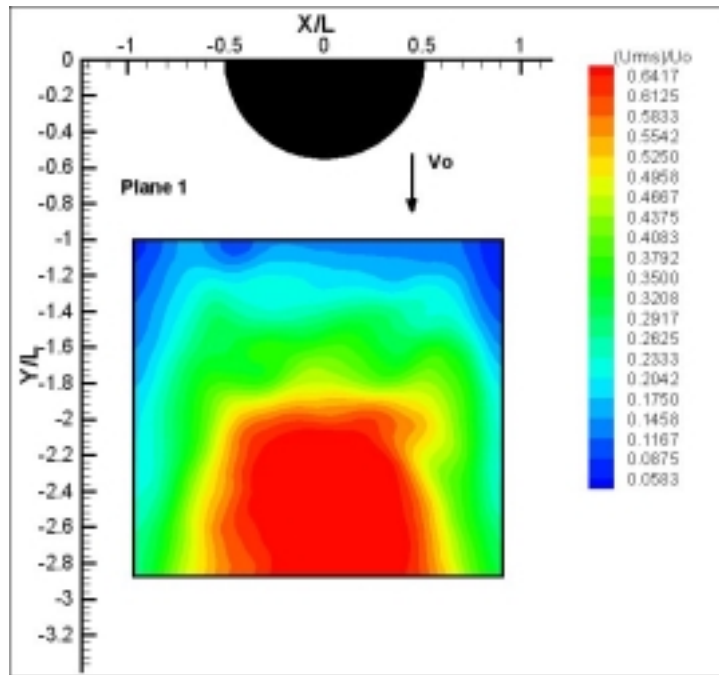


Figure 5-1: Color contours of U-RMS distribution for plane 1

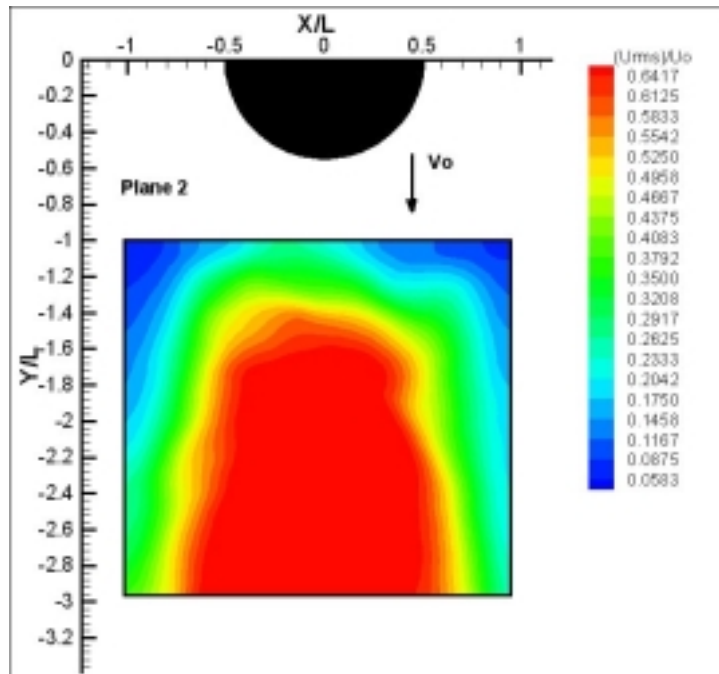


Figure 5-2: Color contours of U-RMS distribution for plane 2.

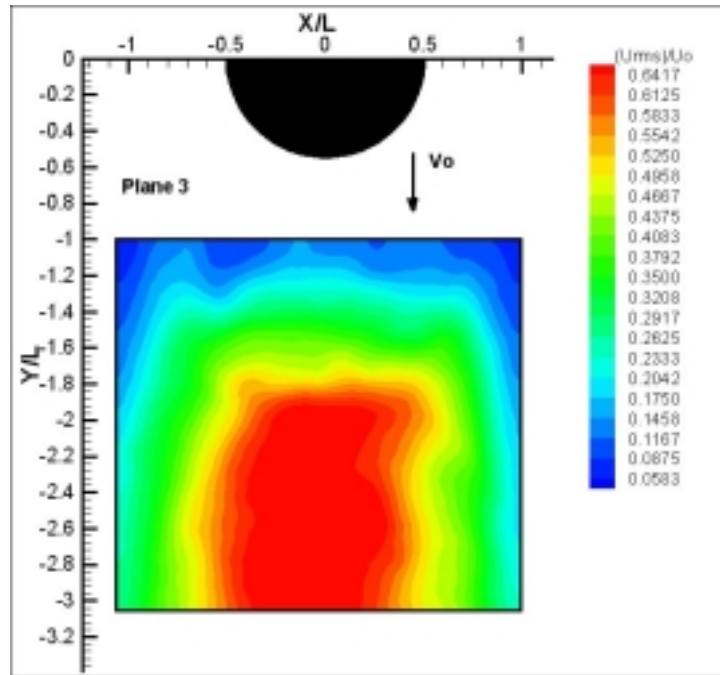


Figure 5-3: Color contours of U-RMS distribution for plane 3.

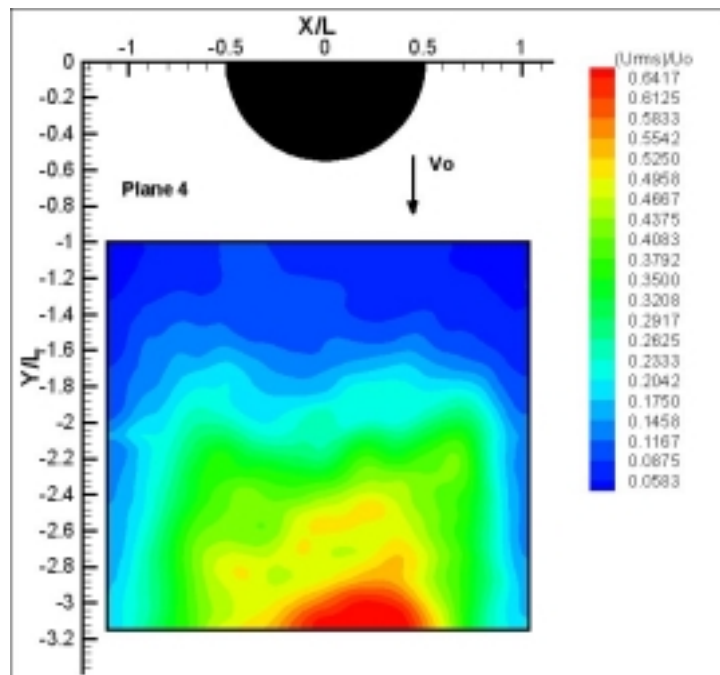


Figure 5-4: Color contours of U-RMS distribution for plane 4.

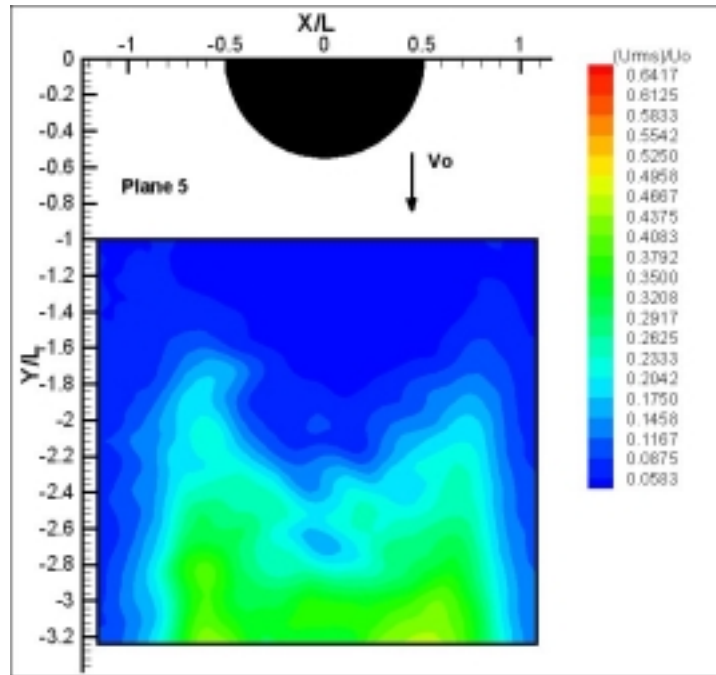


Figure 5-5: Color contours of U-RMS distribution for plane 5.

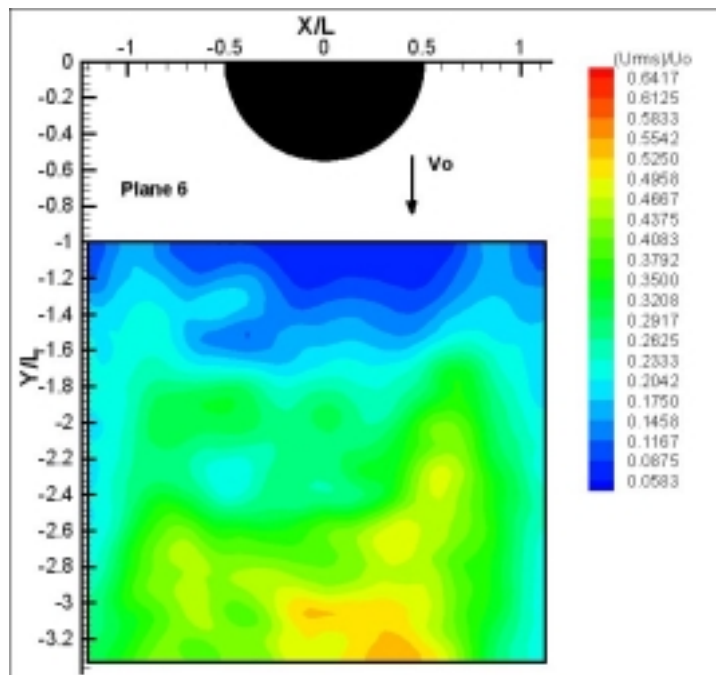
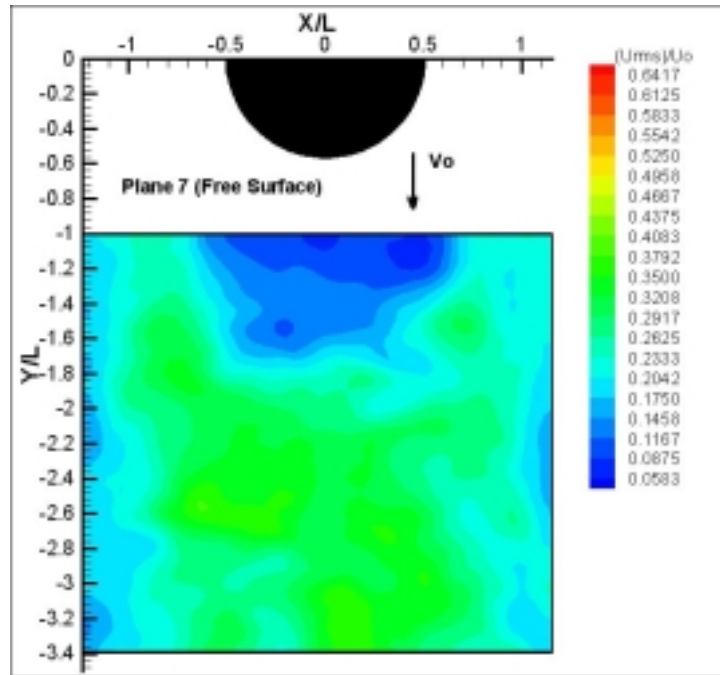


Figure 5-6: Color contours of U-RMS distribution for plane 6.



**Figure 5-7:** Color contours of U-RMS distribution for plane 7.

Figure 6: Set of figures for the V-RMS distribution.

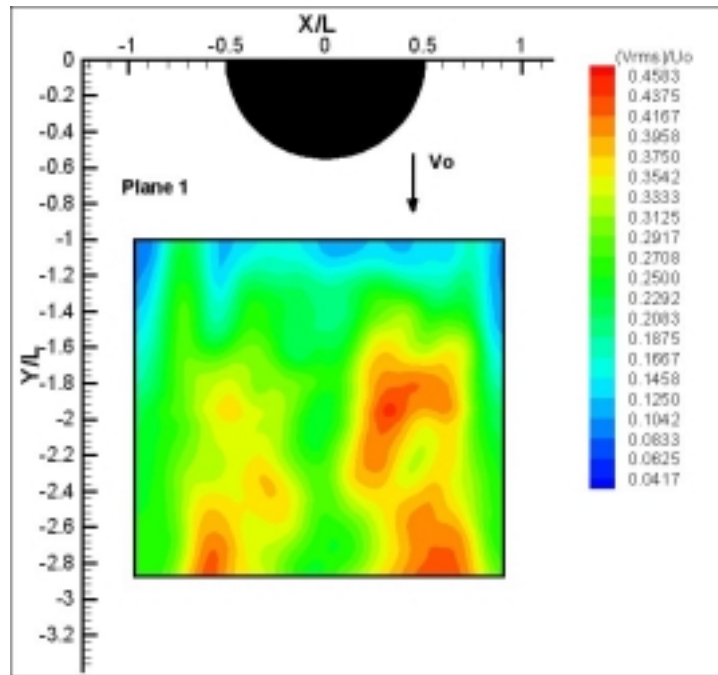


Figure 6-1: Color contours of V-RMS distribution for plane 1.

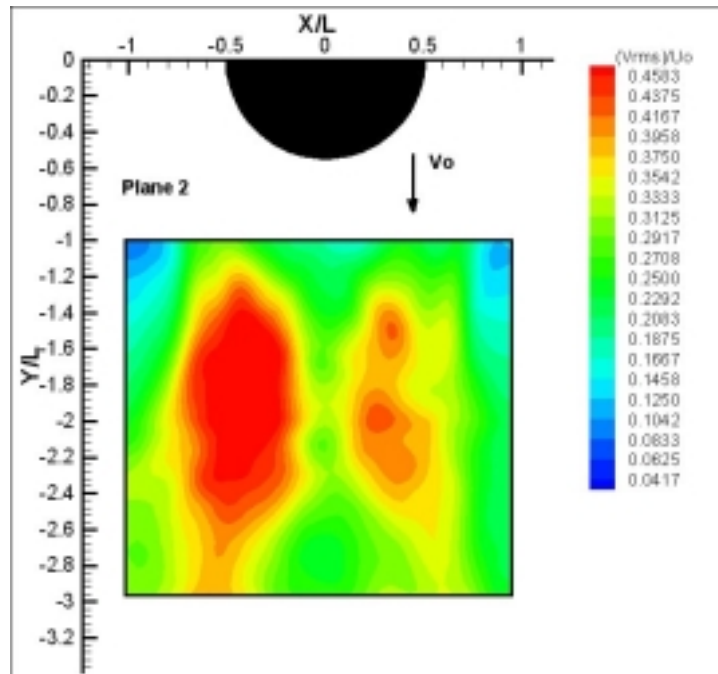


Figure 6-2: Color contours of V-RMS distribution for plane 2.

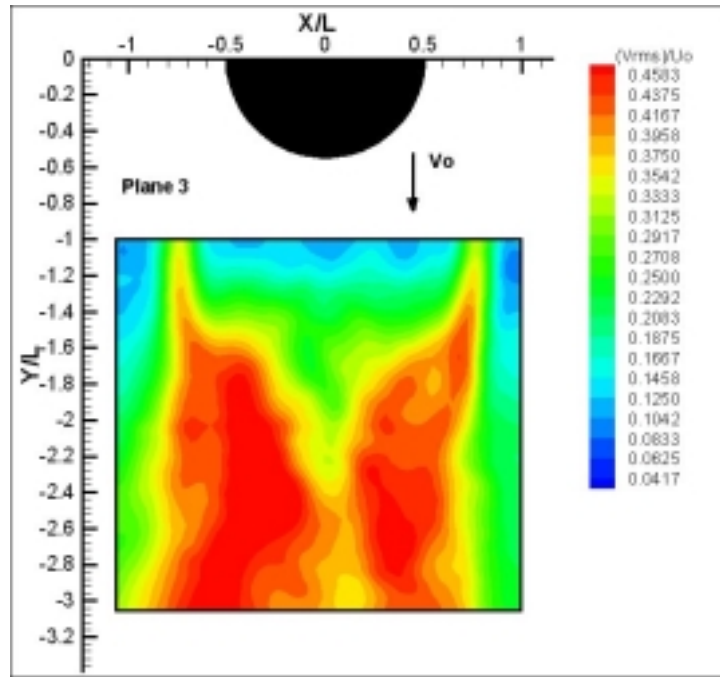


Figure 6-3: Color contours of V-RMS distribution for plane 3.

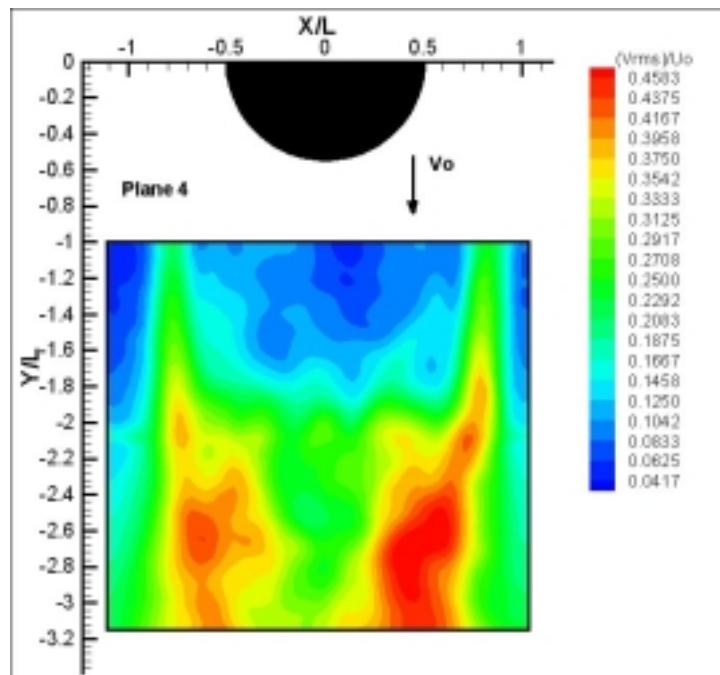


Figure 6-4: Color contours of V-RMS distribution for plane 4.

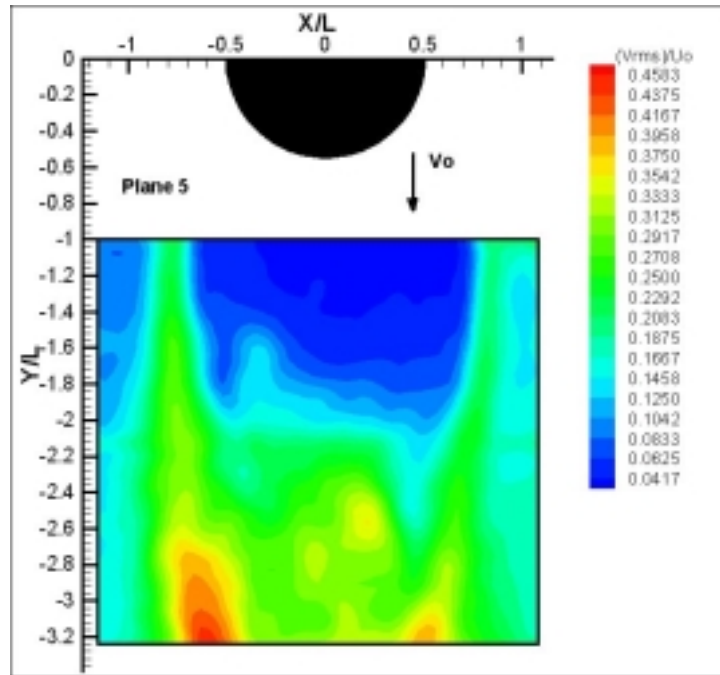


Figure 6-5: Color contours of V-RMS distribution for plane 5.

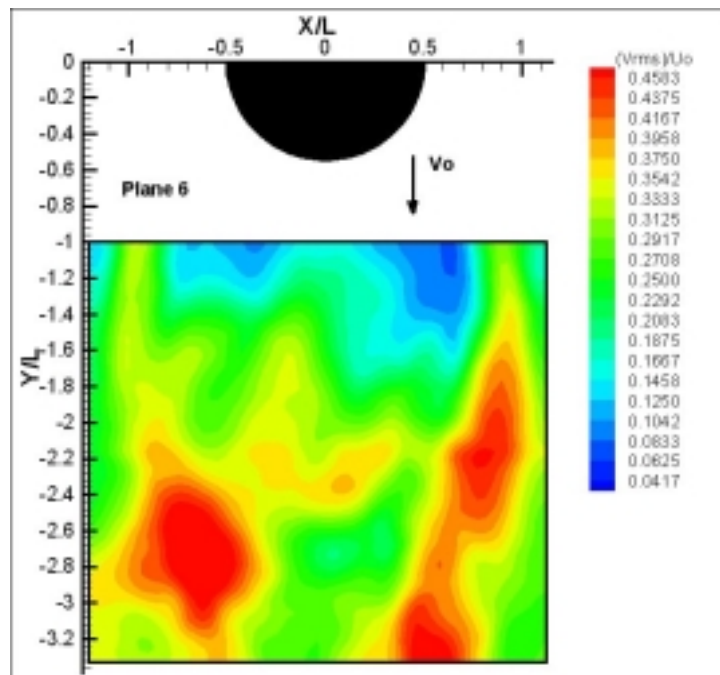


Figure 6-6: Color contours of V-RMS distribution for plane 6.

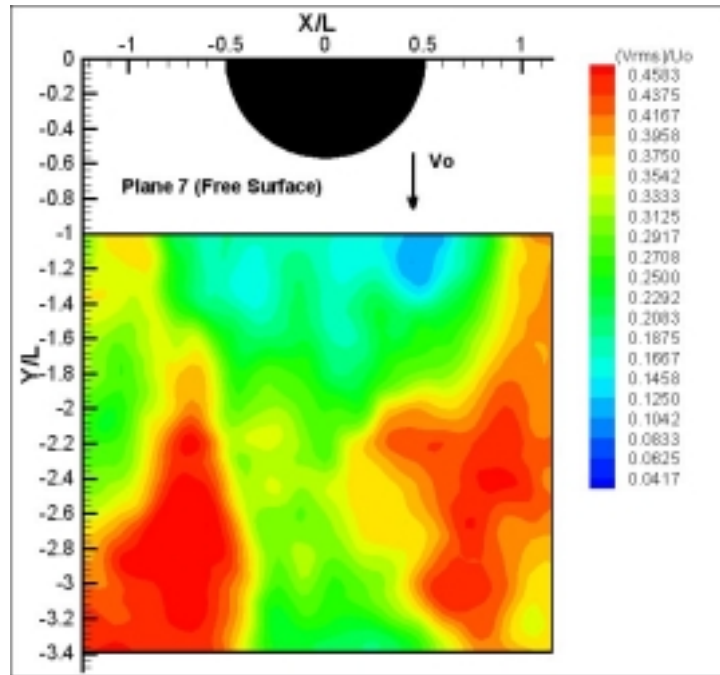


Figure 6-7: Color contours of V-RMS distribution for plane 7.

Figure 7: Set of figures for Turbulent Kinetic Energy distribution.

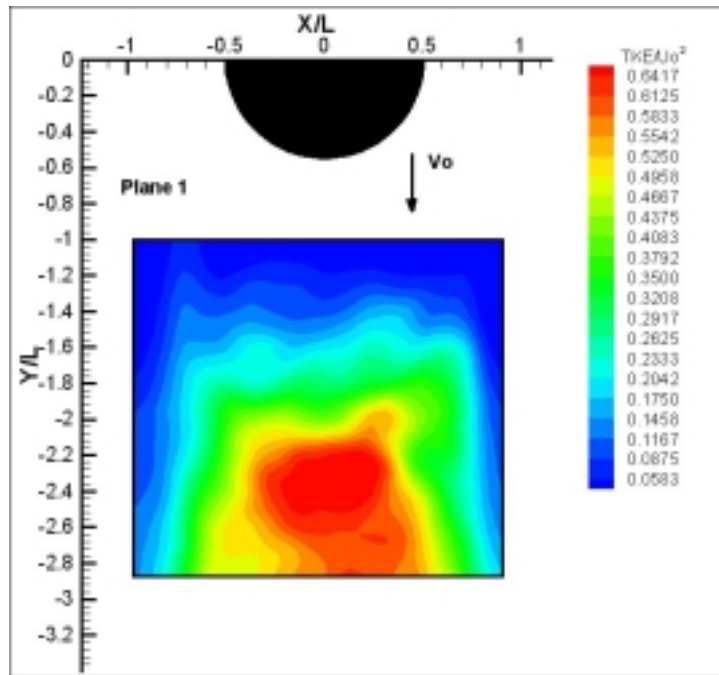


Figure 7-1: Color contours of TKE distribution for plane 1.

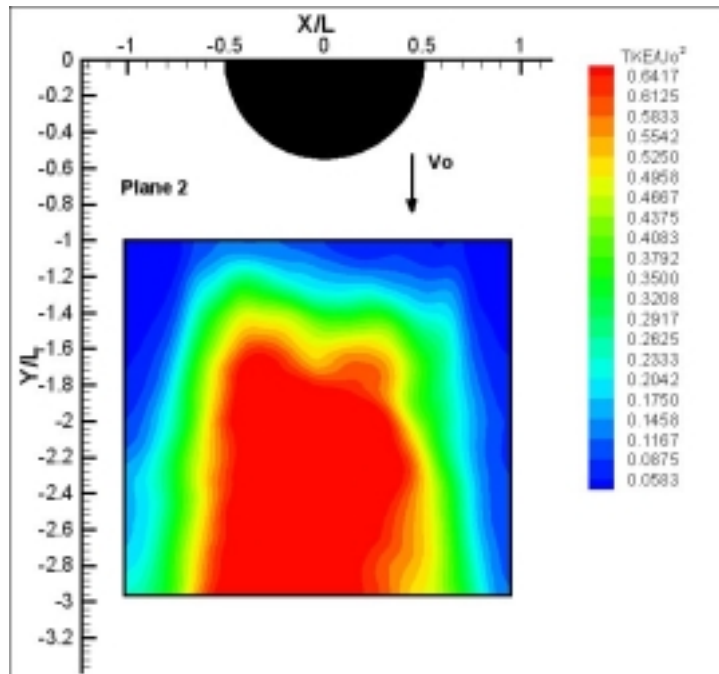


Figure 7-2: Color contours of TKE distribution for plane 2.

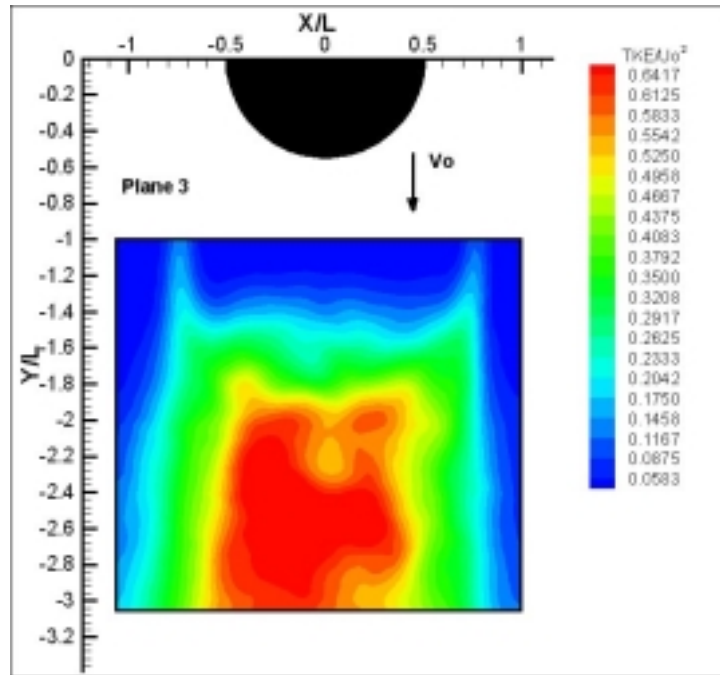


Figure 7-3: Color contours of TKE distribution for plane 3.

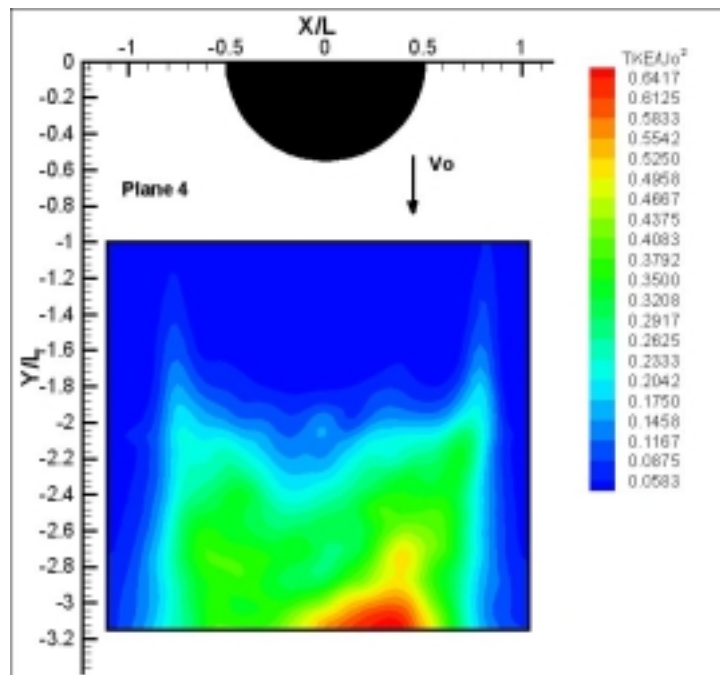


Figure 7-4: Color contours of TKE distribution for plane 4.

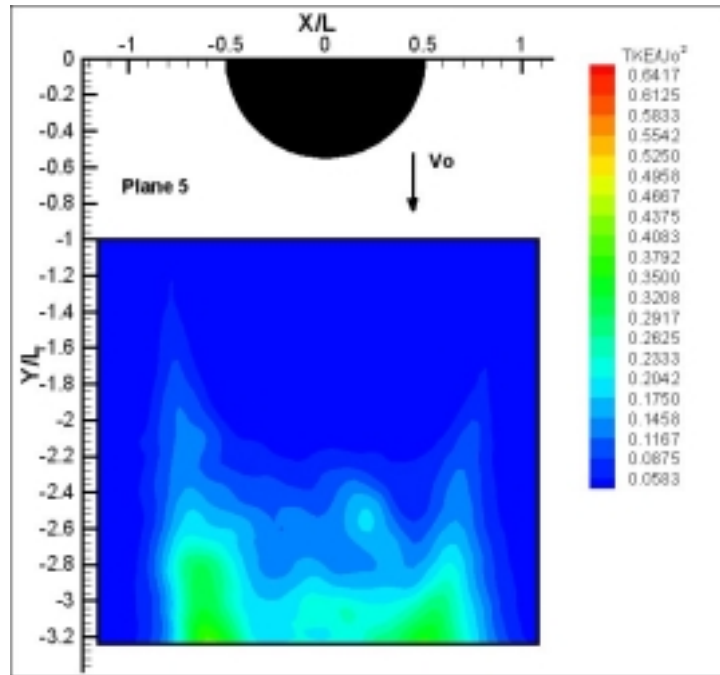


Figure 7-5: Color contours of TKE distribution for plane 5.

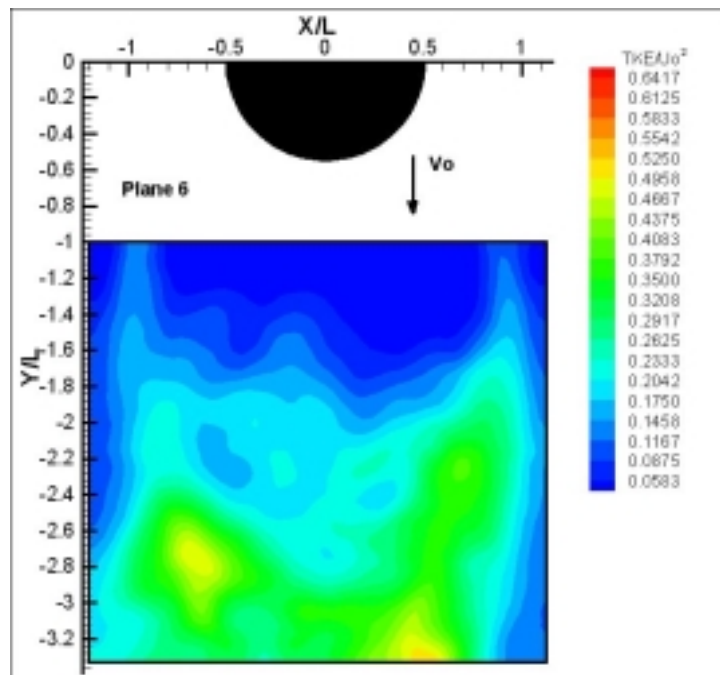
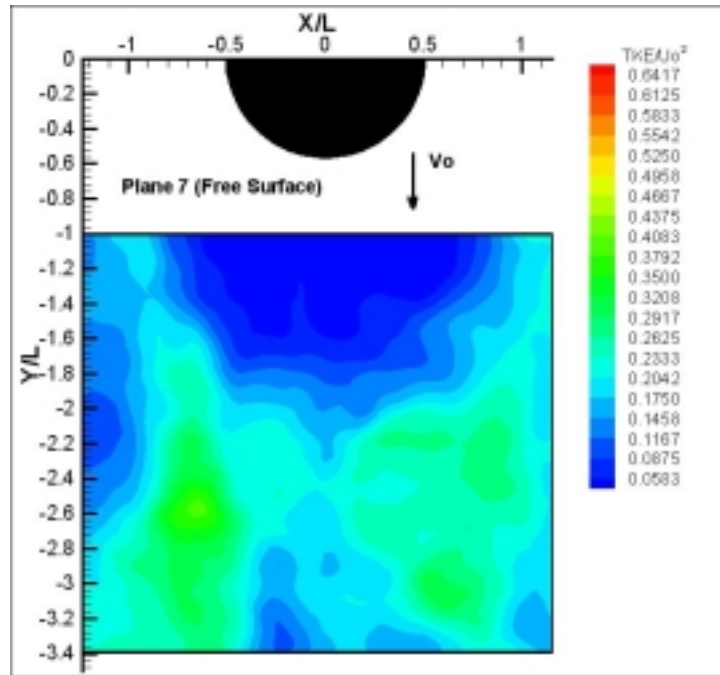


Figure 7-6: Color contours of TKE distribution for plane 6.



**Figure 7-7:** Color contours of TKE distribution for plane 7.

Figure 8: Set of figures for  $U/V'$  distribution.

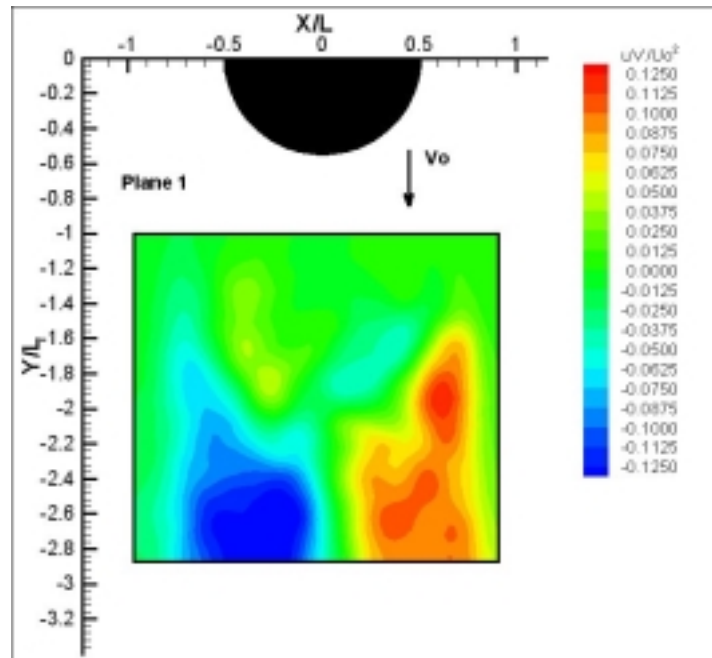


Figure 8-1: Color contours of  $U/V'$  distribution for plane 1.

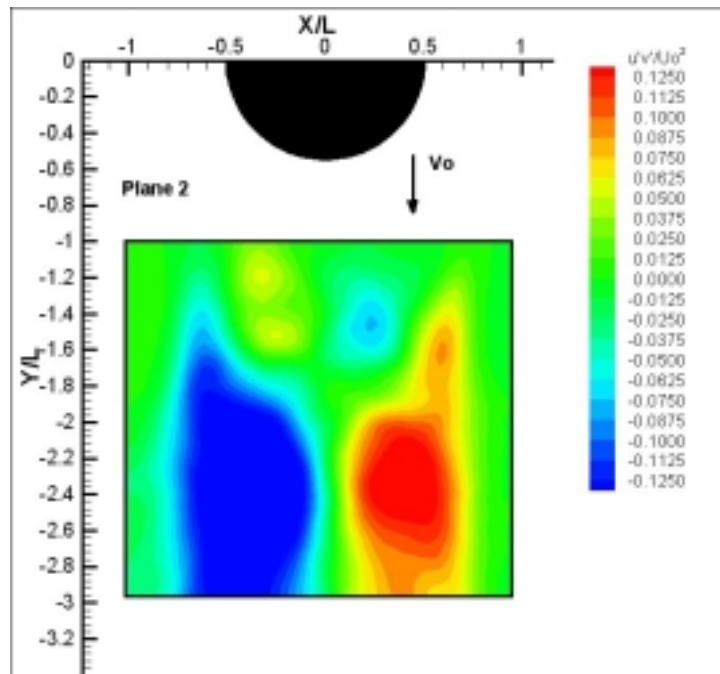


Figure 8-2: Color contours of  $U/V'$  distribution for plane 2.

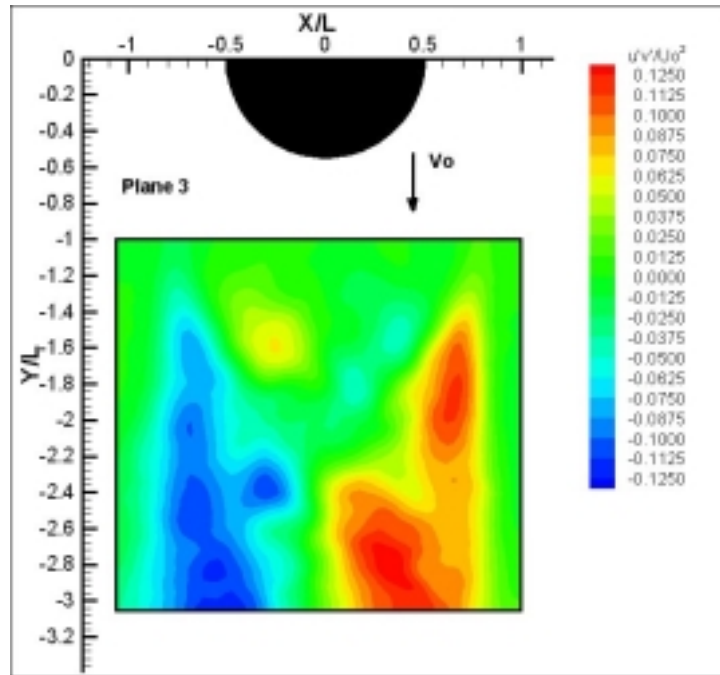


Figure 8-3: Color contours of  $U/V$  distribution for plane 3.

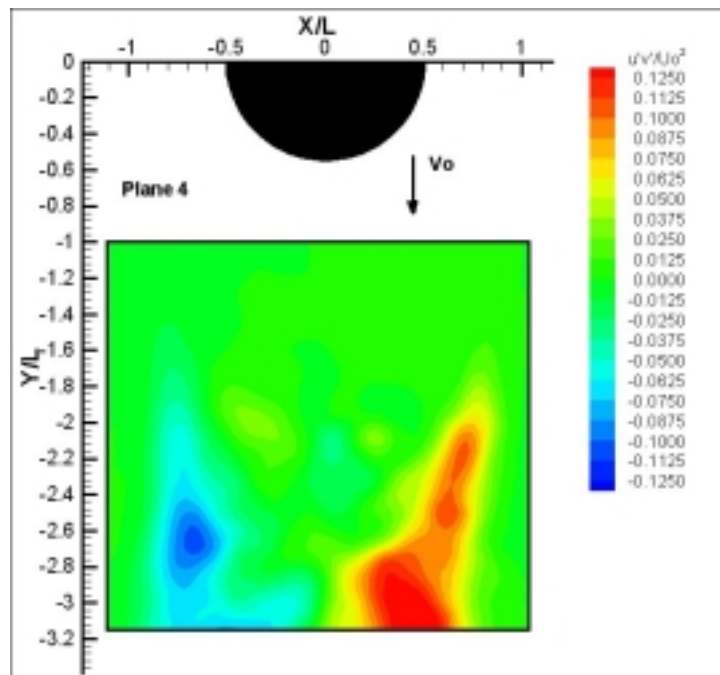


Figure 8-4: Color contours of  $U/V$  distribution for plane 4.

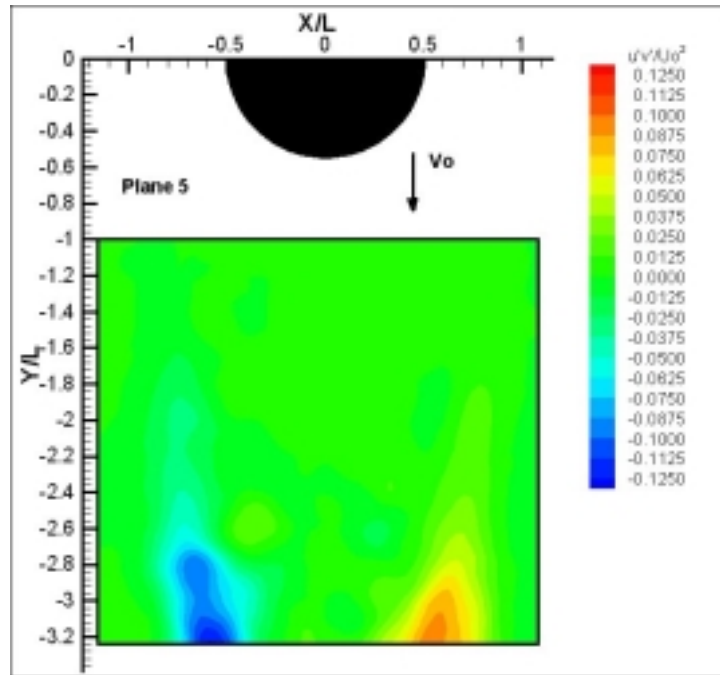


Figure 8-5: Color contours of  $U'V'$  distribution for plane 5.

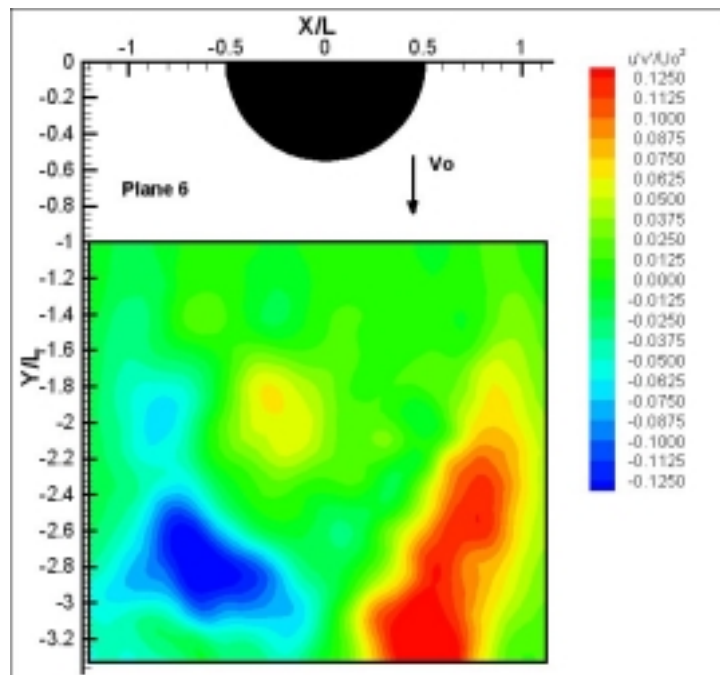
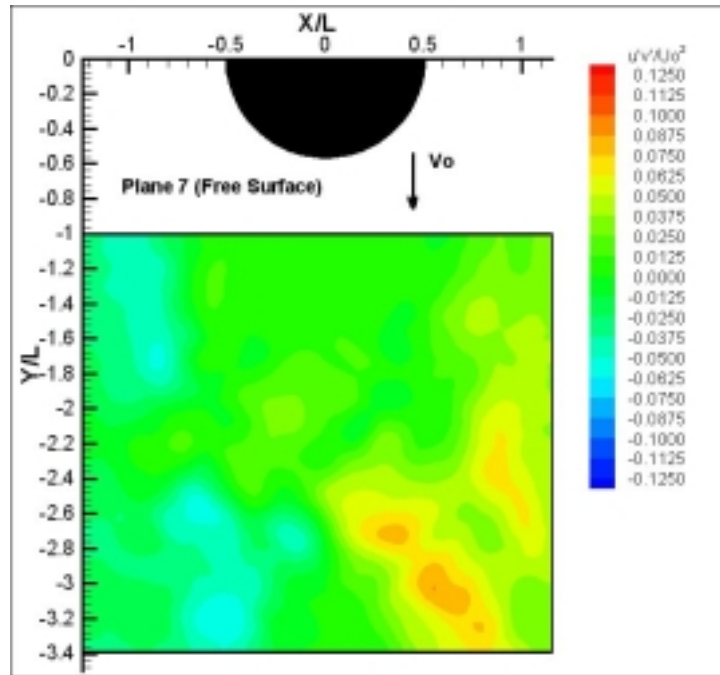


Figure 8-6: Color contours of  $U'V'$  distribution for plane 6.



**Figure 8-7:** Color contours of  $U'/V'$  distribution for plane 7.

## **Unsteady and Instantaneous Flow Characteristics**

The instantaneous characteristics of the flow field and the variation of the vorticity distribution as we approach the free surface are studied in two ways. Initially each plane of data is treated independently and the time-dependent characteristics of the flow for a period of 2 sec are investigated. Subsequently the data along spanwise planes are stacked, using a reference LDV signal to determine the initiation of data acquisition with respect to the period of the vortex shedding. This was achieved as follows. The LDV measuring volume was positioned at a fixed point in space, at  $x = 2.5 D$ ,  $y = 1.5 D$ ,  $z = 8.4 D$ . The LDV signal was used as a reference signal. PIV data were obtained along planes placed at different elevations, which will be referred to as levels 1, 2, 3, 4, 5, 6, and 7 according to the corresponding elevations, with 1 been the 1<sup>st</sup> (at the mid span of the cylinder) and 7 been the last one at the free surface. The PIV data present frames of nearly instantaneous velocity vectors of a field developing in time. Proper stacking of these frames is necessary to reconstruct the three-dimensional field. This requires that each frame corresponds to the same instant within the period of the motion. PIV data is shifted by a calculated time delay. This delay was determined through cross-correlation of the LDV signals, as described later.

The use particles of 10 micron in diameter for the PIV images introduced a great amount of noise in the LDV signal. Based on the fringe spacing of our LDV system the optimum particle diameter would be in the order of 2 microns. The use of such particles would significantly affect the quality of the PIV images, while the use of both kinds would increase the background noise. Thus, a compromise was inevitable. A pair of velocity signals during a period of two seconds is shown in figure. 9 In order to compensate for the aforementioned compromise the use of a band-pass filter was adopted. The filter was centered on an analytical estimate of the vortex shedding frequency and with amplitude of  $\pm 0.5$  Hz. Figure 10 shows the filtering effect for the first signal. Finally a cross correlation between each combination of the first signal with the rest was performed to determine the necessary time shifting. A generalized cross-correlation algorithm (described in Nikias and Petropoulou, 1993) was employed for an adaptive windowing of the

signal; based on the power spectrum of the signals. The outcome of this time shifting over one period is demonstrated in figure 11.

Based on the calculated time delay, the PIV data on each plane was shifted to the same reference time. A sequence of instantaneous vectors fields corresponding to one period of the vortex shedding for each plane are placed on top of each other according to their spanwise position. Thus, underlying features of the flow such the inclination of the vortex or phase differences in the vortex shedding are revealed.

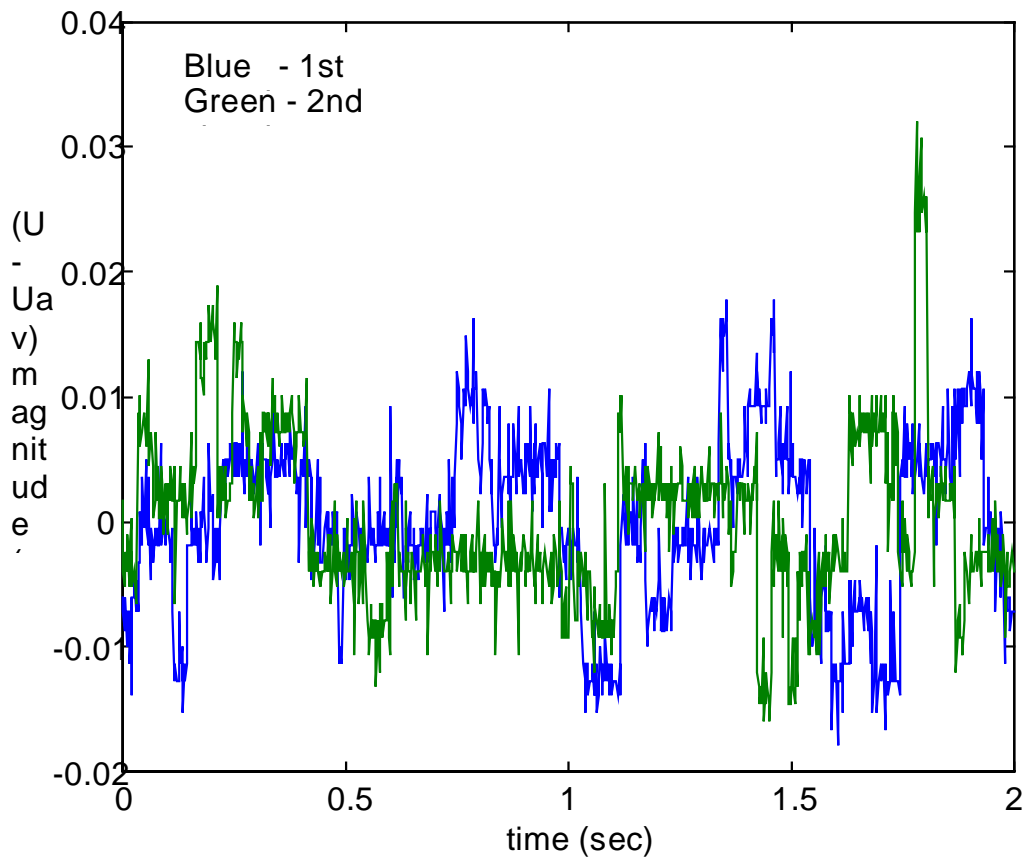


**Figure 9:** Original LDV signals with the mean value subtracted

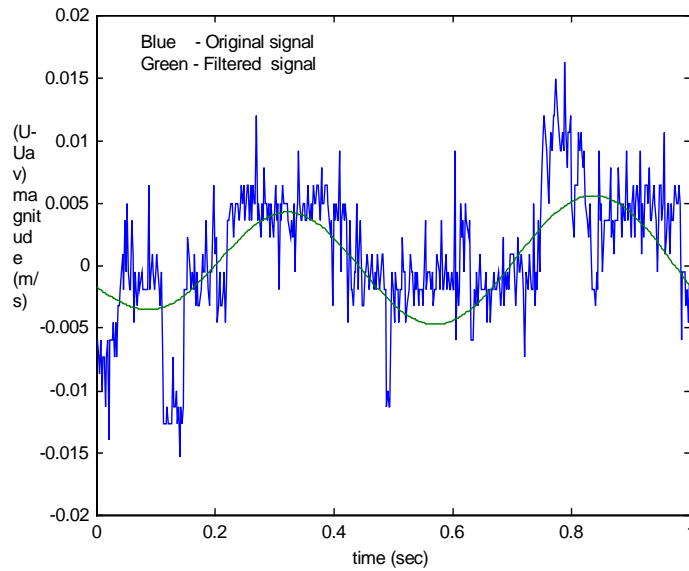


Figure 10: Comparison of filtered and unfiltered LDV signals

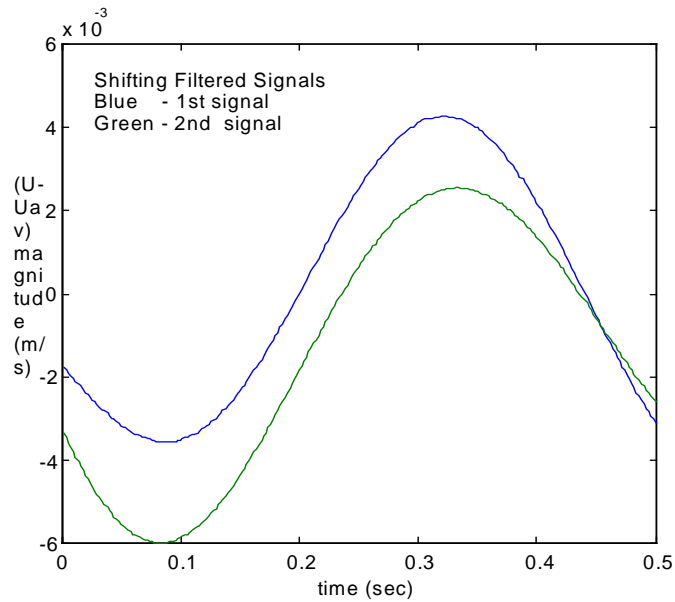


Figure 11: Shifted filtered signal by an estimate time delay

## **Results and Discussion**

The dominating two-dimensional periodic character of the flow under examination implies a repetition of the flow pattern as we move up in the spanwise direction. This expectation is reinforced by the fact that the free surface boundary condition is compatible with the two-dimensional character of the flow. Deviations from the predominant two-dimensional pattern indicate three-dimensional effects. By simple comparison of the mean flow characteristics in the spanwise direction, (shown in previous figures) this deviation is apparent. However, the three-dimensionality of the flow in the wake of the circular cylinder is triggered from streamwise and spanwise instabilities that evolve with time. Therefore, it is imperative that we study the time dependence of the flow field in order to understand the underlying physics.

In the animation for the first plane of interrogation  $z=-4.88D$  below the free surface we view a flow field that does not deviate from the conventional flow patterns of the wake of the circular cylinder observed in so many previous studies. For the Reynolds number under investigation the flow is dominated by the shear layer instabilities (Williamson 1996) that roll to form the primary vortices. The alternate character of the vortex shedding is clearly illustrated. In the second plane  $z=-4.08D$  the general pattern is similar, however, in agreement with the observation made from the mean properties of the flow, the vortices roll earlier shifting the location of vortex formation closer to the cylinder. This can be caused from larger scale instabilities (Noca et al 1998) interacting with the shear layer. When the length scale of upcoming disturbances is of the same order with the shear layer instabilities, the vortex formation will be favored and the primary vortices will roll. From both of the first two animations, it is clearly demonstrated how the opposite sign vortex in each case will penetrate the region dominated by the primary vortex cutting off the supply of vorticity and forcing the vortex to shed in the wake. The third animation changes the scene and the effect of the free surface is becoming noticeable. The shear layers do not roll as close to the cylinder as before. Thus, the point of vortex formation moves downstream and the dead water region increases in size. More importantly, there are instants in the flow where we observe two vortices rolling together. This phenomenon can have one of the following explanations. The mode of vortex

shedding can instantaneously change and the vortices can shed simultaneously (similar to an impulsively started flow) and then shift back to the alternate shedding mode. However, there is no obvious explanation of what could possibly trigger the change of mode. Another, more possible explanation can be based on the stability of the shear layers. The shear layer was able to maintain its stability and grow larger without rolling yet to a big vortex. Therefore, what we observe is the shear layer eddies growing and not shedded vortices. The intermittent appearance of this phenomenon however indicates a departure from the periodicity. These observations are further confirmed from the flow character of the next plane.

The data on the fourth plane demonstrates the same basic trends but significantly intensified. We observe an elongation of the shear layer to approximately 3 diameters downstream, while now the appearance of simultaneously forming pairs of vortices propagating downstream is more consistent. The size of these vortices is less than  $0.5D$  while the VonKarman vortex should be almost of the same size as the cylinder. This observation further validates the conclusion that the vortices seen in the field are not VonKarman vortices but grown shear layer eddies. Finally, the vortex formation length has moved almost outside our field of view. Similar observations are valid for the fifth plane. The most important difference is the size of the dead water region where very small activity of the flow is observed. Inoue et al. (1993) by performing hot film measurements measured a drastic effect on the  $u$ -velocity spectrum along the centerline of the wake. Takanamura (1997) by carrying out numerical computations (LES, RANS) presented a similar instantaneous flow structure. Both attributed the character of the flow to vortex shedding suppression. However, based on our observations from the previous elevations this extended dead water region along the centerline of the wake is attributed to the stability of the shear layers, which allowed them to grow continuously downstream without rolling. Because the kinematic boundary condition at the free surface preserves the two-dimensional character of the flow, the three-dimensional instabilities that are present at lower elevations do not develop therefore the vortices do not form, but further downstream when the size of the shear layer instabilities will grow to a magnitude that will force them to roll.

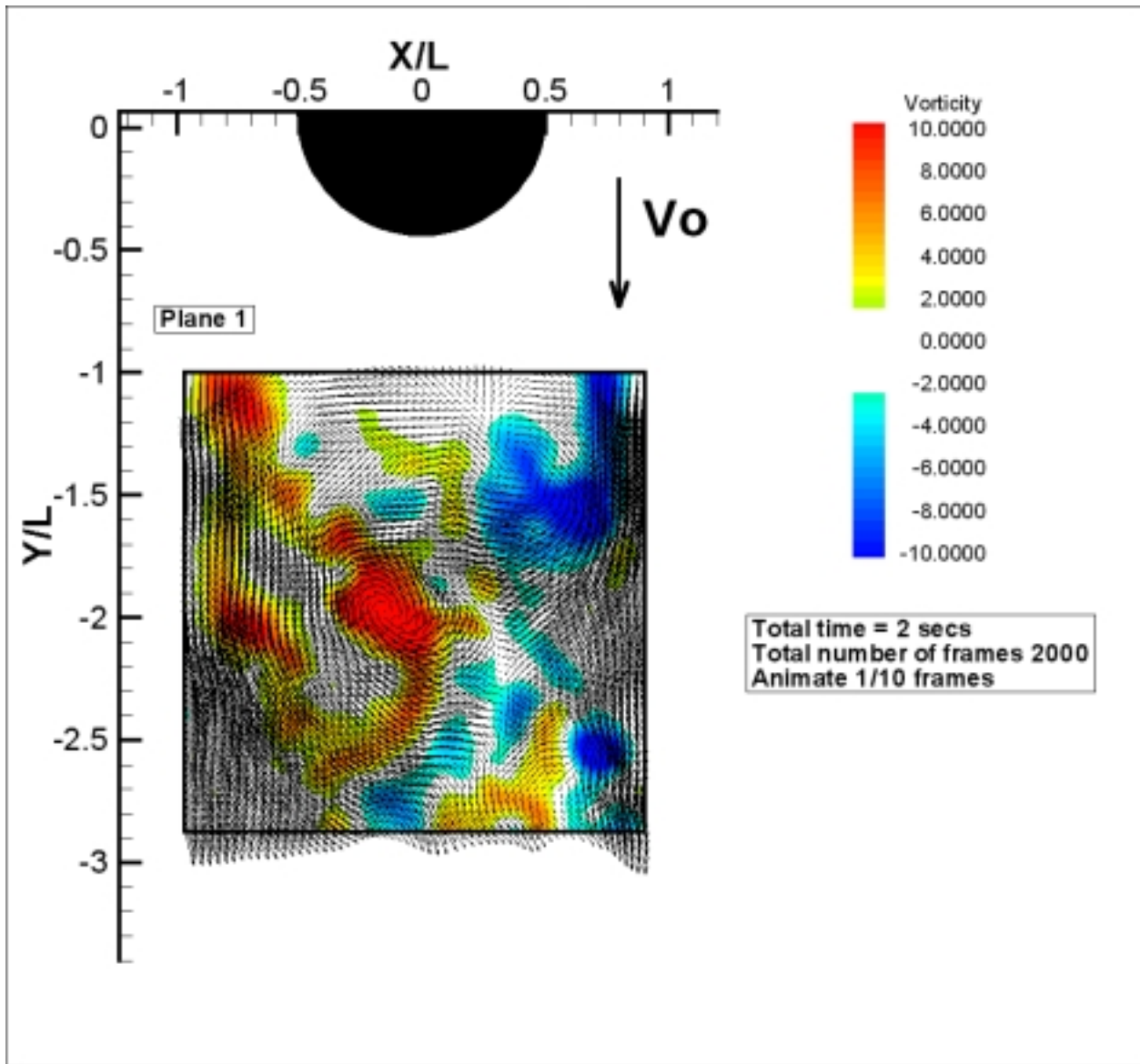
In the last two planes, the general structure of the flow is similar. The shear layers do not roll consistently to form vortices. However, there are instants that we observe the detachment of bulks of vorticity from the shear layers and the formation of pairs of small but not coherent vortical structures. The flow field is characterized by a more random and turbulent behavior. This is due to the free surface turbulence. It is also worth to note the instantaneous appearance of upwellings and downdrafts on the last plane. Evidence for this type of activity is in the form of local sink- source-like velocity patterns. This fact indicates, out of plane velocity components. This vertical motion of the flow is generated from streamwise vortices that break into cells of vorticity and eventually turn their axis to reconnect normal to the free surface.

Subsequently we consider the results from the proper stacking of the PIV planes in a three dimensional volume. All data are shifted to a zero reference time with respect to the vortex shedding. We consider one cycle of the interrogation time (total of 1000 frames) corresponding approximately to two periods of the vortex shedding. The results are presented in figure 12. Only five snapshots of the flow fields are presented here. Animation of such a volume would be difficult to observe and analyze within the context of this text.

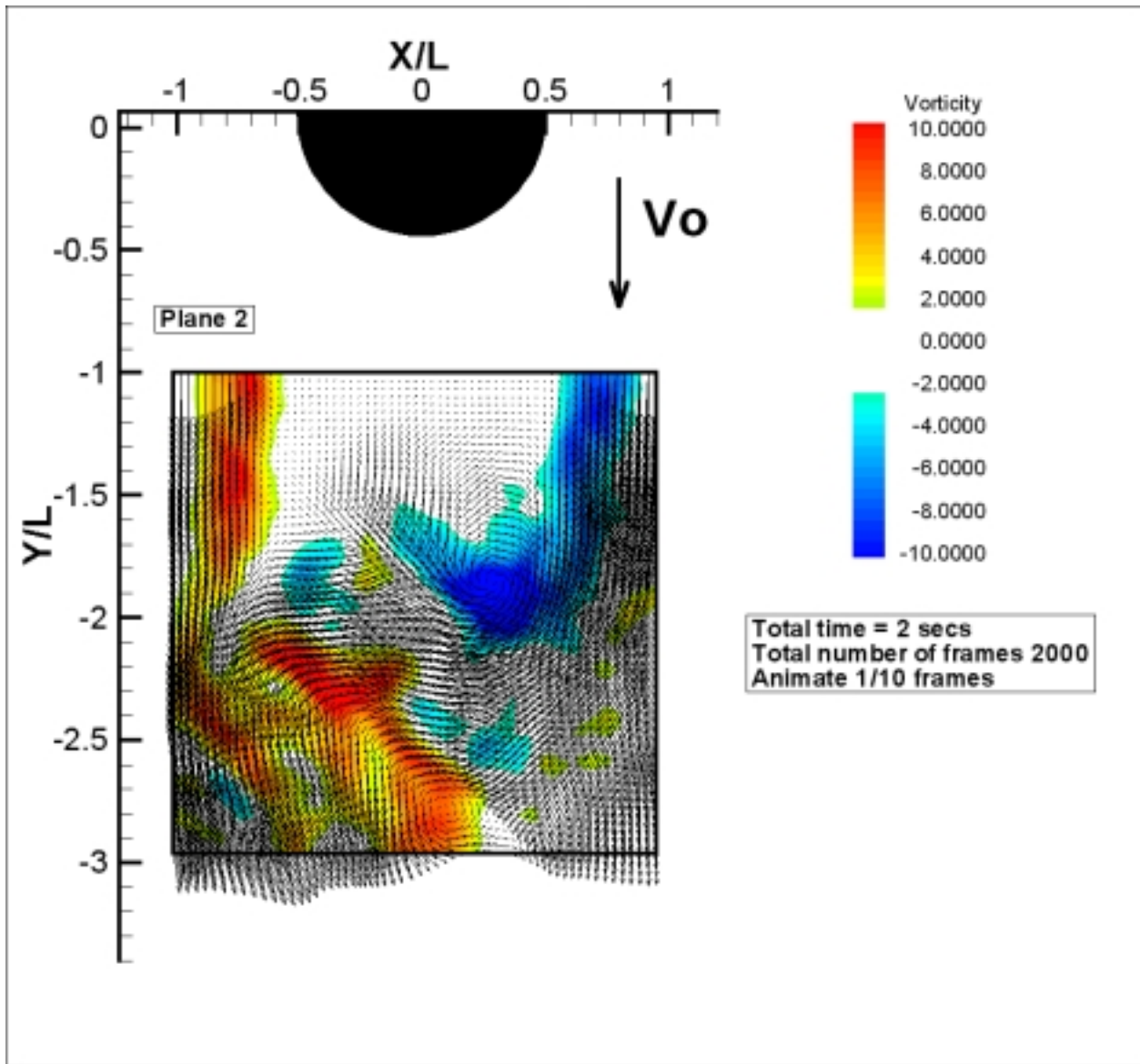
In the first figure –which we mark as the beginning of the cycle- we observe that for the first two planes the positive vortex is the primary von Karman vortex dominating the flow. As we move to the third plane, we notice that the positive vortex is further downstream indicating an inclination of the vortex with respect to the axis of the cylinder. Oblique vortex shedding is associated with the existence of streamwise vorticity and depends strongly upon the boundary conditions and the end effects (Hammache and Charib, 1991). In this case, the asymmetry of the end conditions triggers the oblique vortex shedding, enhancing the three-dimensional character of the flow. However, on the next two planes, which are closer to the free surface, the flow is affected by the two-dimensional character of the boundary condition, stabilizing the shear layers and forming the vortices further downstream. Thus, the inclination is further increasing. In the vicinity of the free surface (planes 6-7) the axis of the vortex is forced to change in order to reconnect normal to the latter. However, this probably occurs outside our field of view, therefore what we are able to observe for the last two planes is a flow field that is more turbulent and

random and not a vortex line extending from the previous planes. The next instant,  $t/T = 0.5$  corresponds to a time half a period away from the initial frame. As expected, the primary vortex sign has changed and for the first two planes, we see the negative von Karman vortex dominating the flow field. Again the effect of the inclination is illustrate in the third plane, where the negative vortex has moved outside from the frame and the positive one is taking its place. The following planes behave according to our previous observations. In the next instant at  $t/T=1.0$  (one complete cycle) we note again the difference of the third plane with respect to the others. In this case, it seems that a pair of vortices has shed almost simultaneously. All the observations made for the first cycle are valid also for the second.

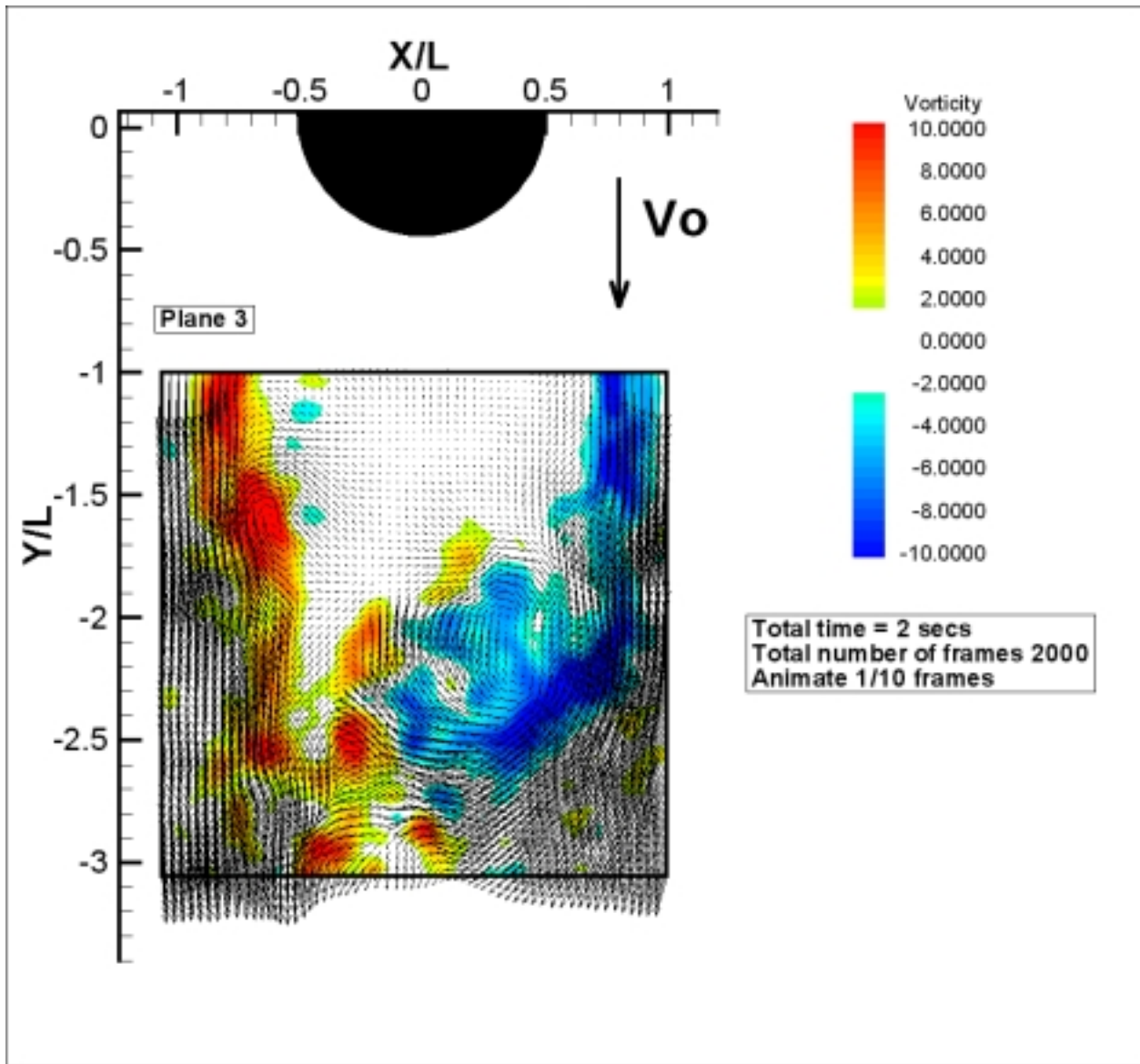
We conclude from the three-dimensional representation of the flow field that the effect of the asymmetric boundary conditions triggers the oblique vortex shedding. However, in the neighborhood of the third plane (about  $3.5D$  below the free surface) the influence of the free surface is becoming more noticeable, drastically altering the character of the flow. The vortex formation length increases as well as the inclination of the shed vortices and finally, at the free surface, no coherent vortical structure related the vortices beneath is found and free surface turbulence dominates the flow.



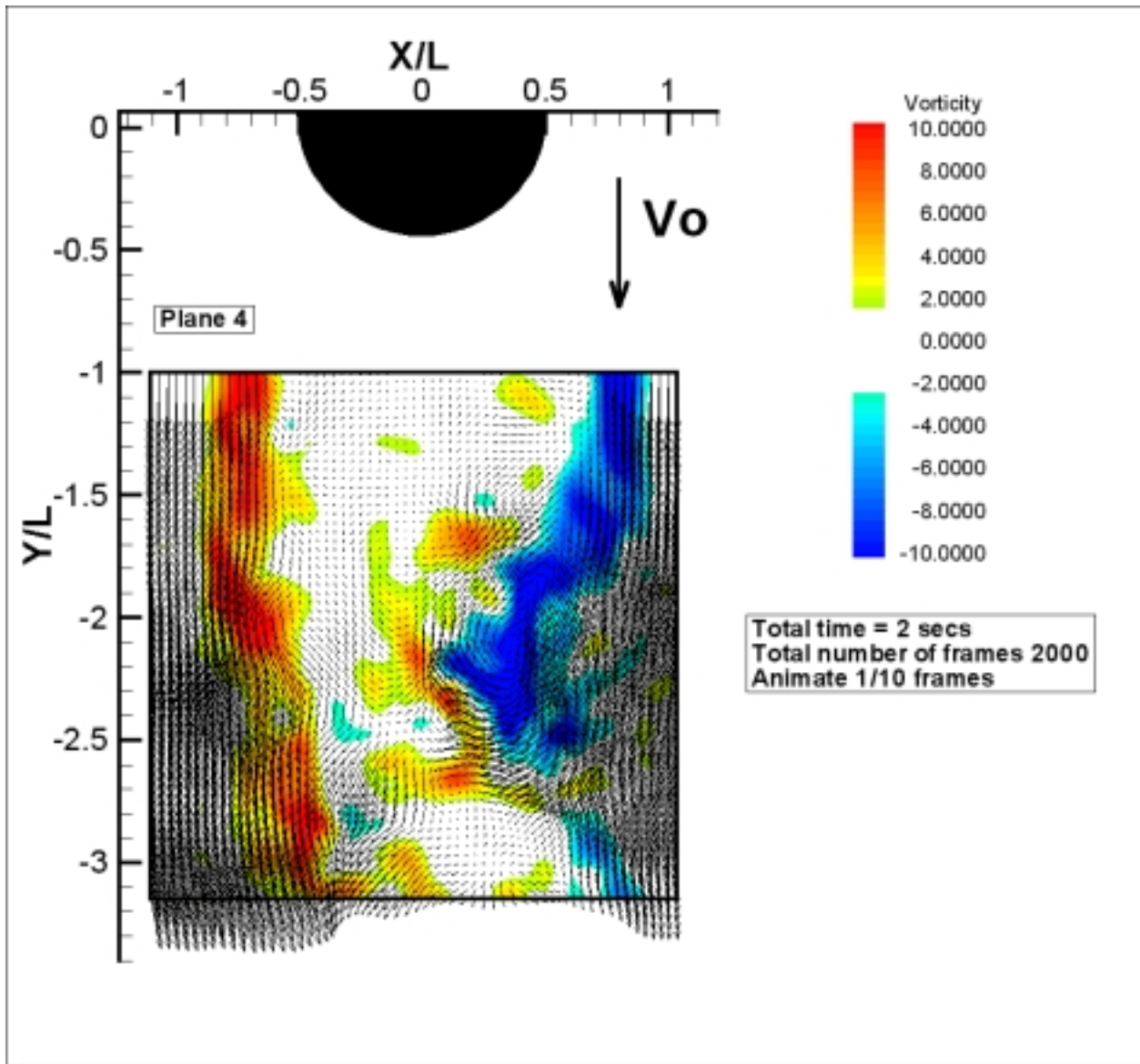
*Animation 1:* Animation of velocity vectors and vorticity contours for the first plane of elevation.



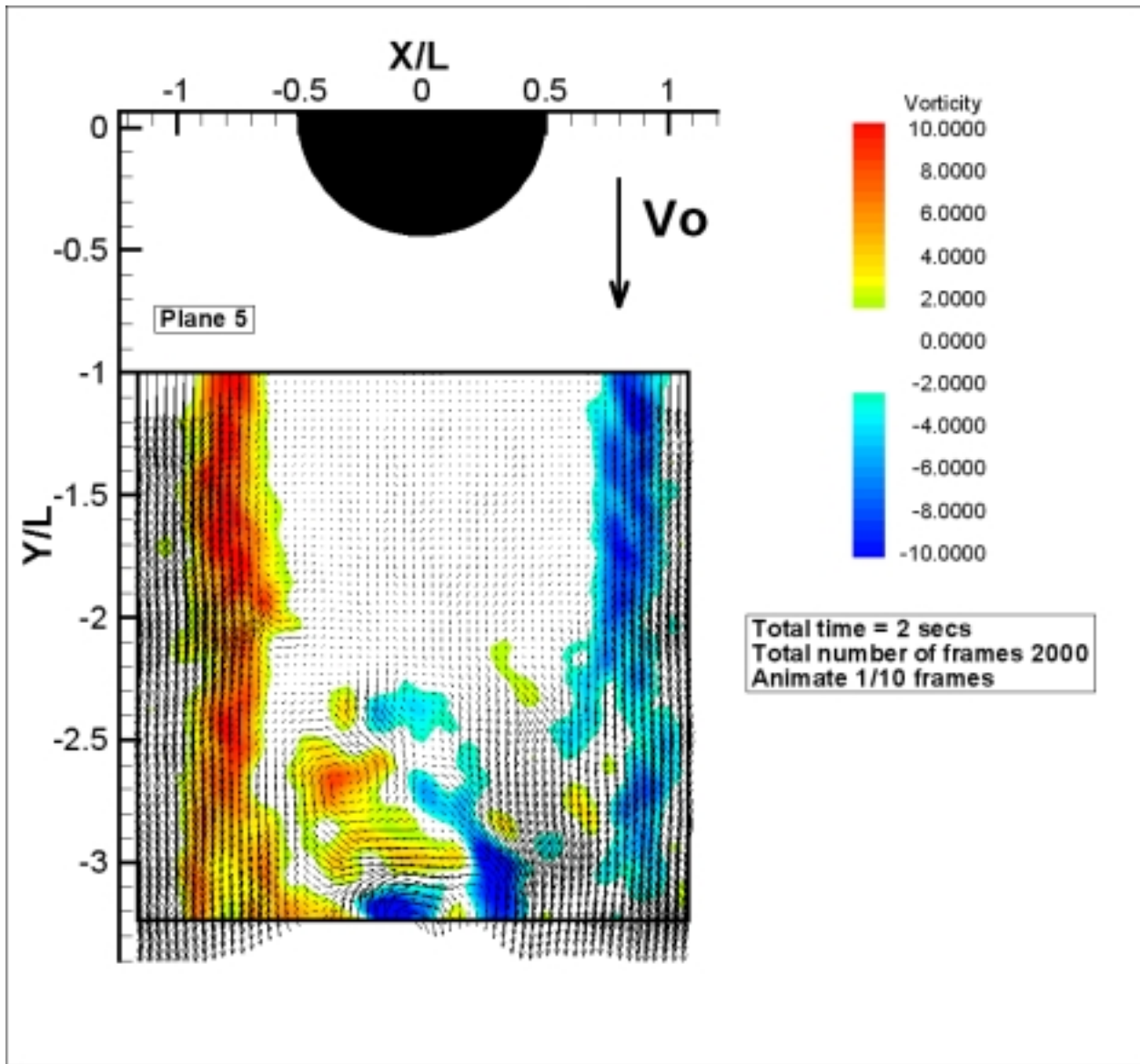
*Animation 2:* Animation of velocity vectors and vorticity contours for the second plane of elevation.



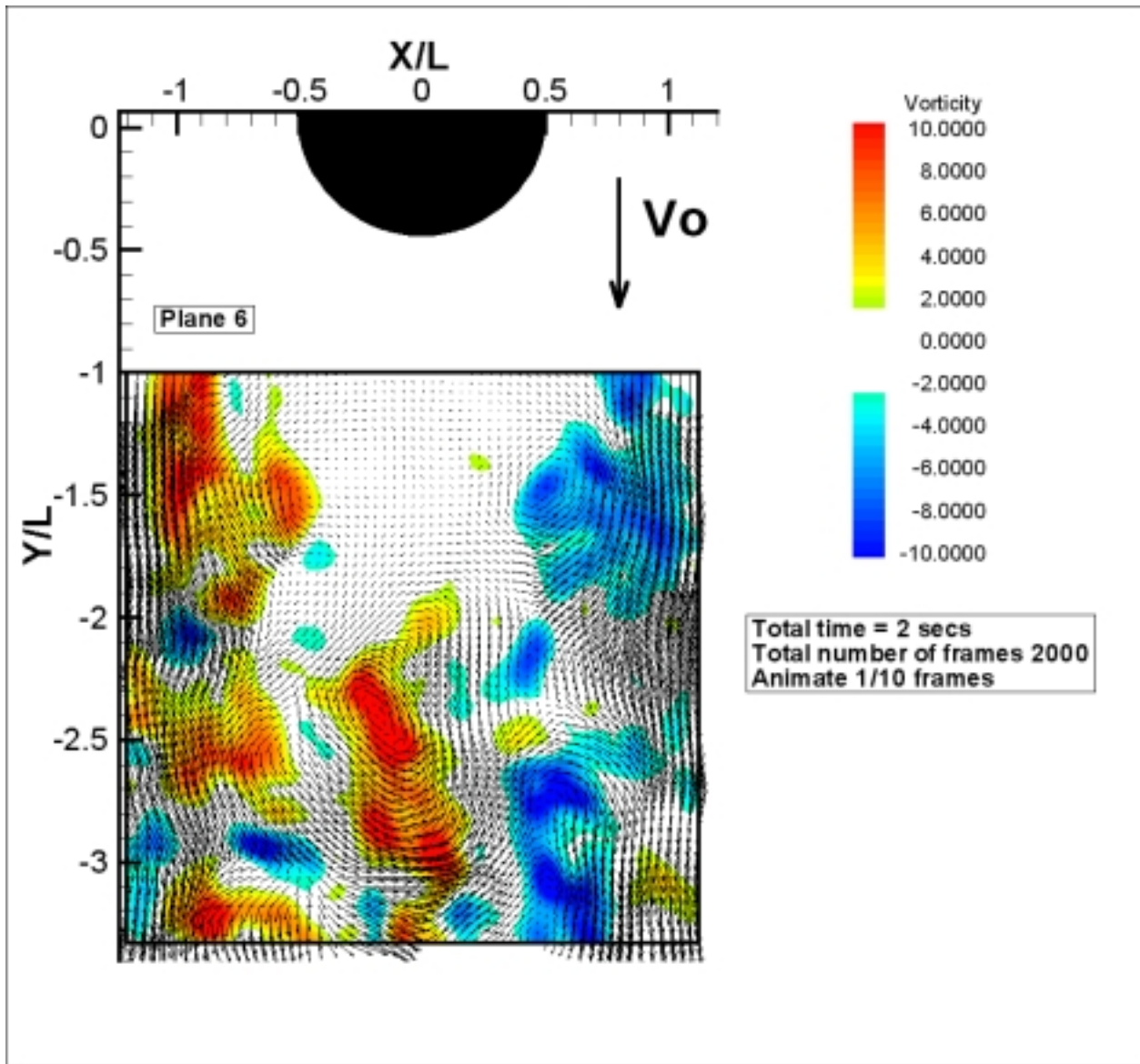
*Animation 3:* Animation of velocity vectors and vorticity contours for the third plane of elevation.



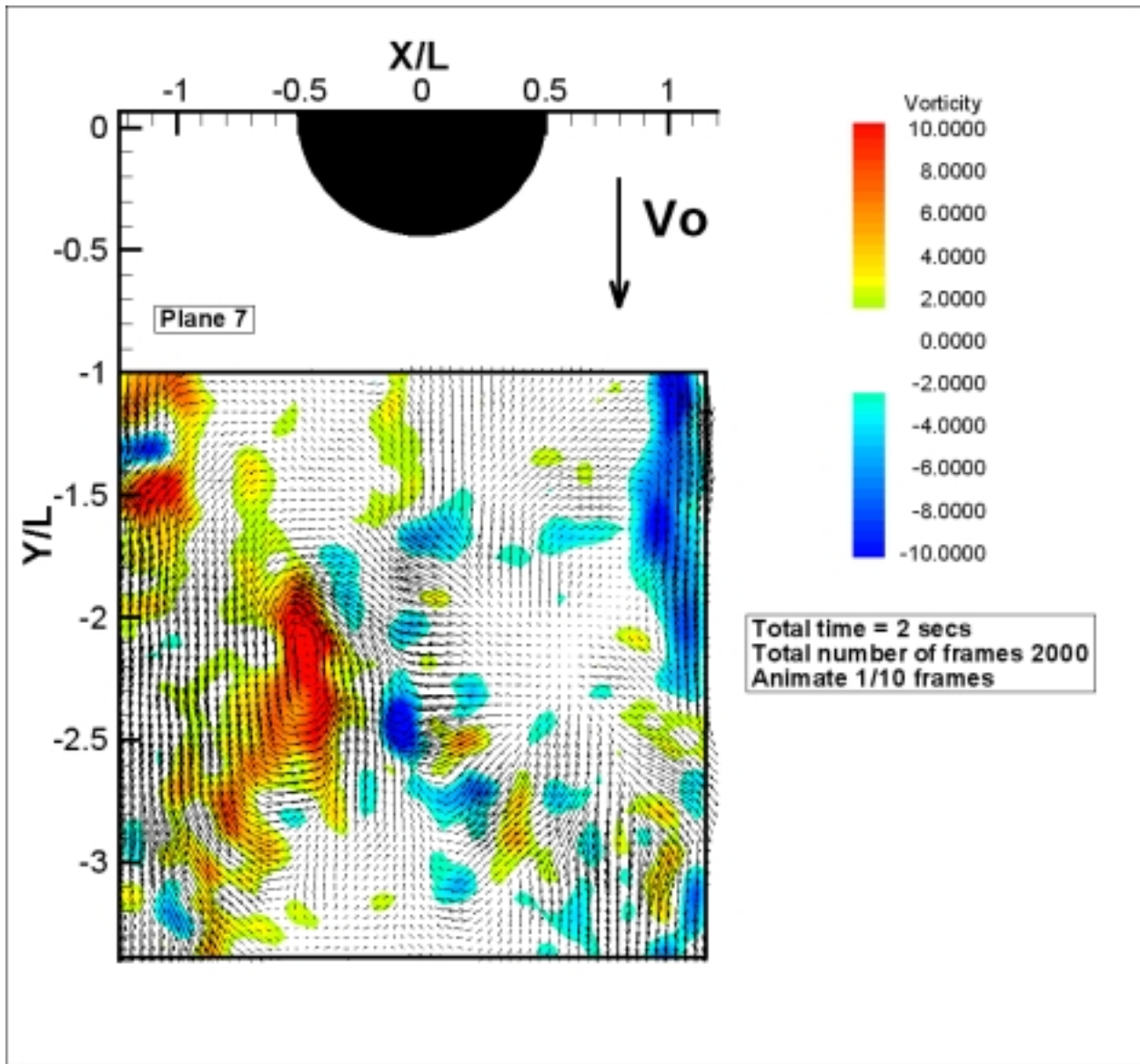
*Animation 4:* Animation of velocity vectors and vorticity contours for the fourth plane of elevation.



*Animation 5:* Animation of velocity vectors and vorticity contours for the fifth plane of elevation.



*Animation 6:* Animation of velocity vectors and vorticity contours for the sixth plane of elevation.



*Animation 7:* Animation of velocity vectors and vorticity contours for the seventh plane of elevation.

**Figure 12:** Three-dimensional representation of the vorticity distribution for the planes of interrogation after been shifted on the same reference time. Plane 7 is made transparent and projected on the right side for clarity.

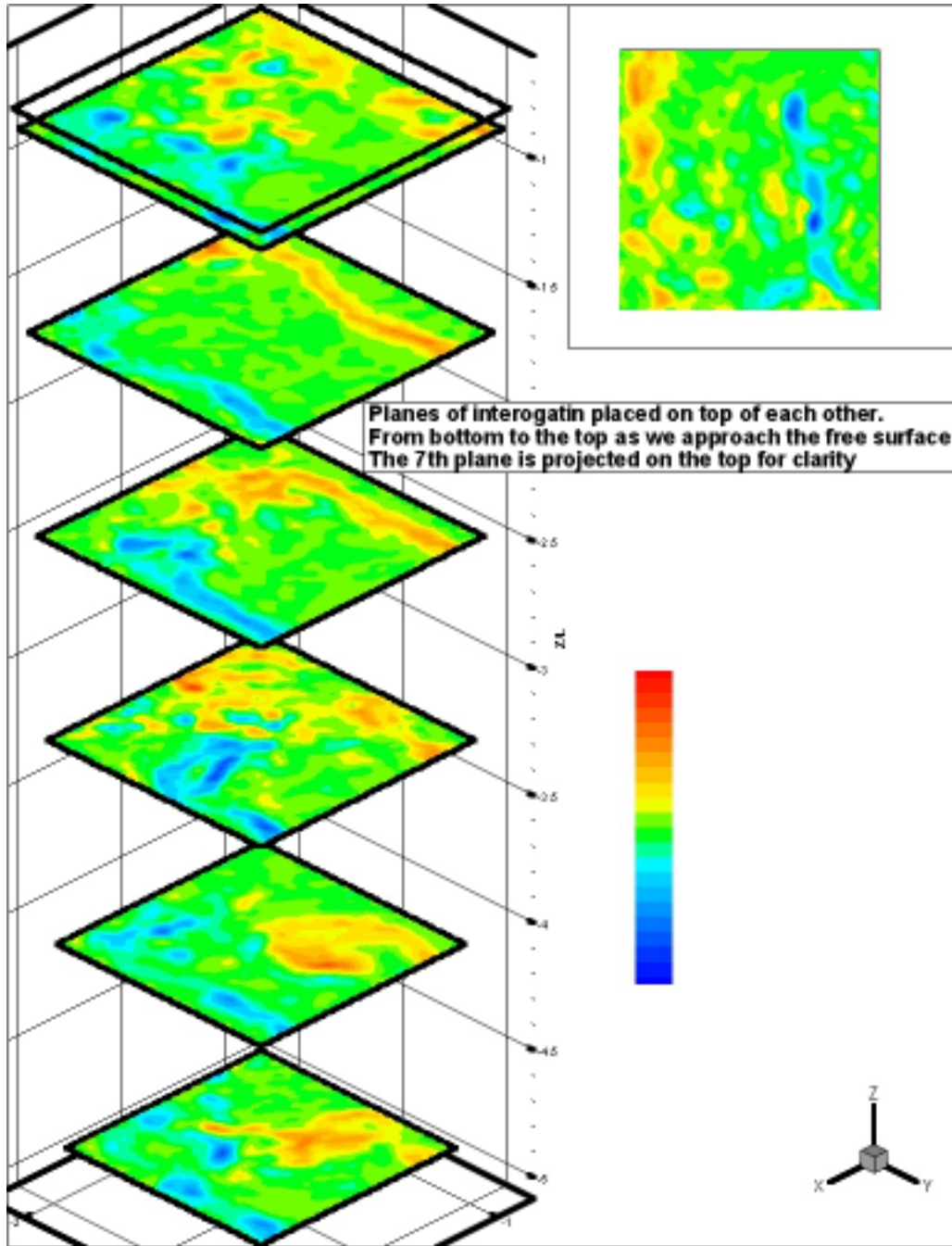


**Figure 12-1:** Three-dimensional representation of the planes of interrogation at  $t/T=0$

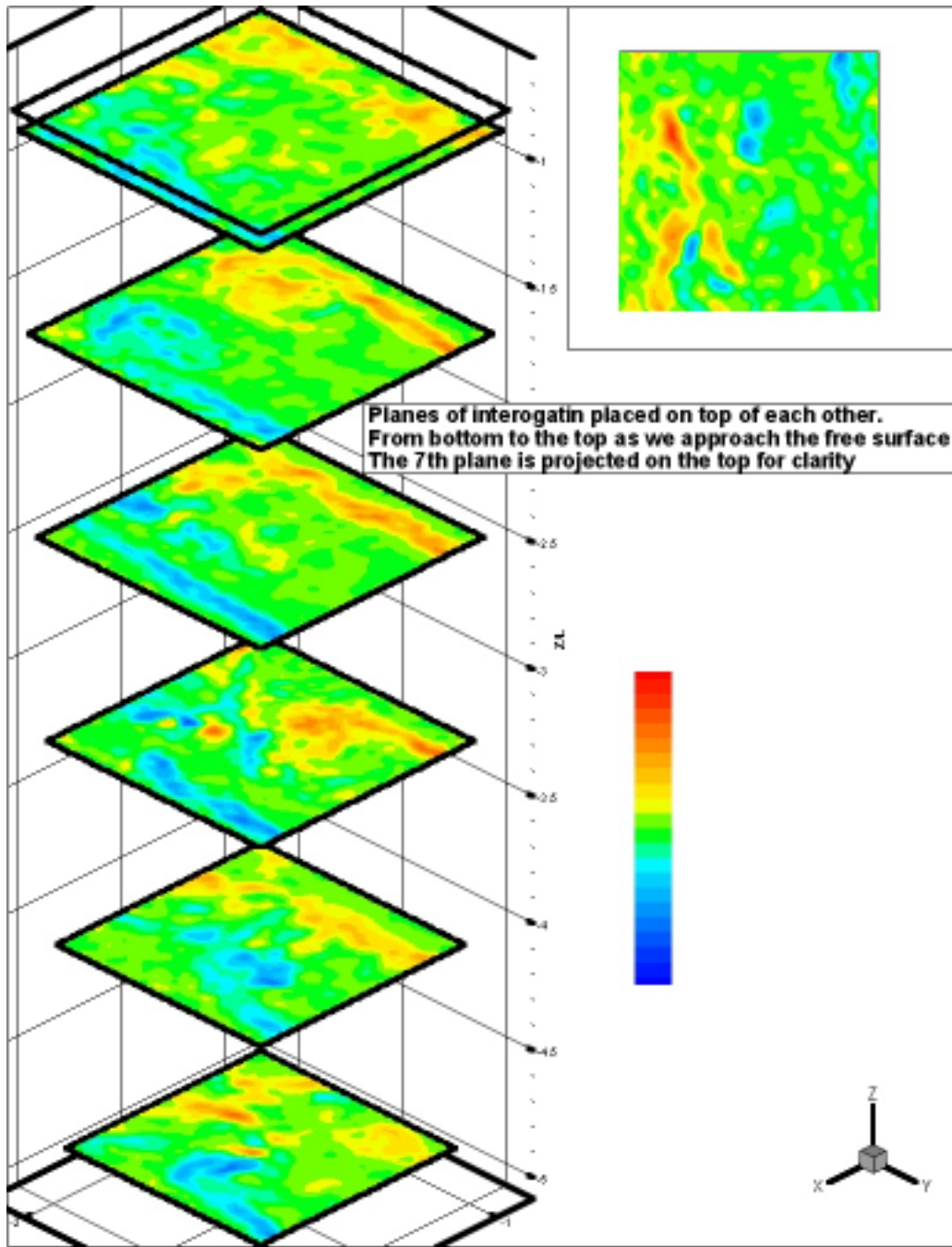


Figure 12-2: Three-dimensional representation of the planes of interrogation at  $t/T=0.5$

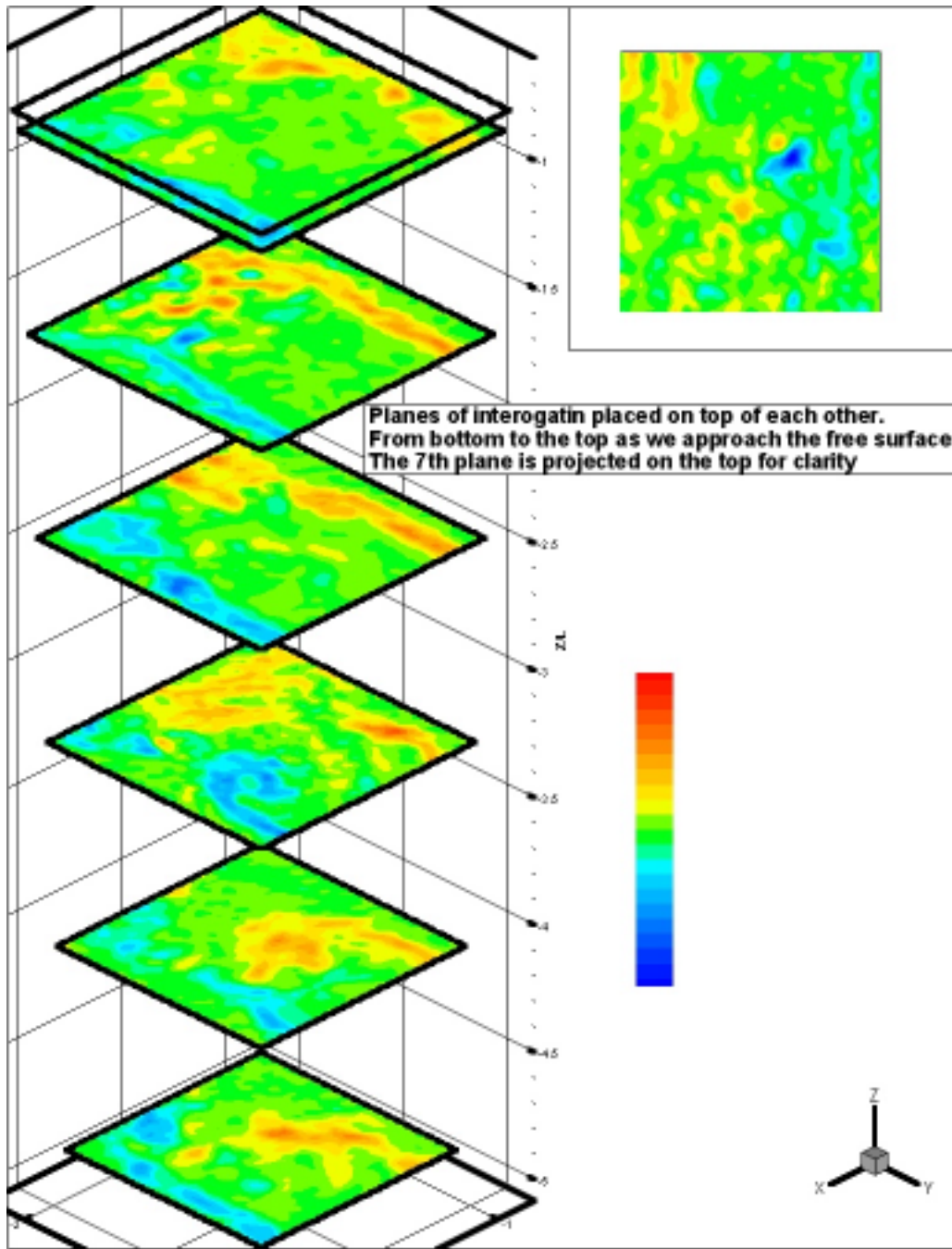


Figure 12-3: Three-dimensional representation of the planes of interrogation at  $t/T=1.0$

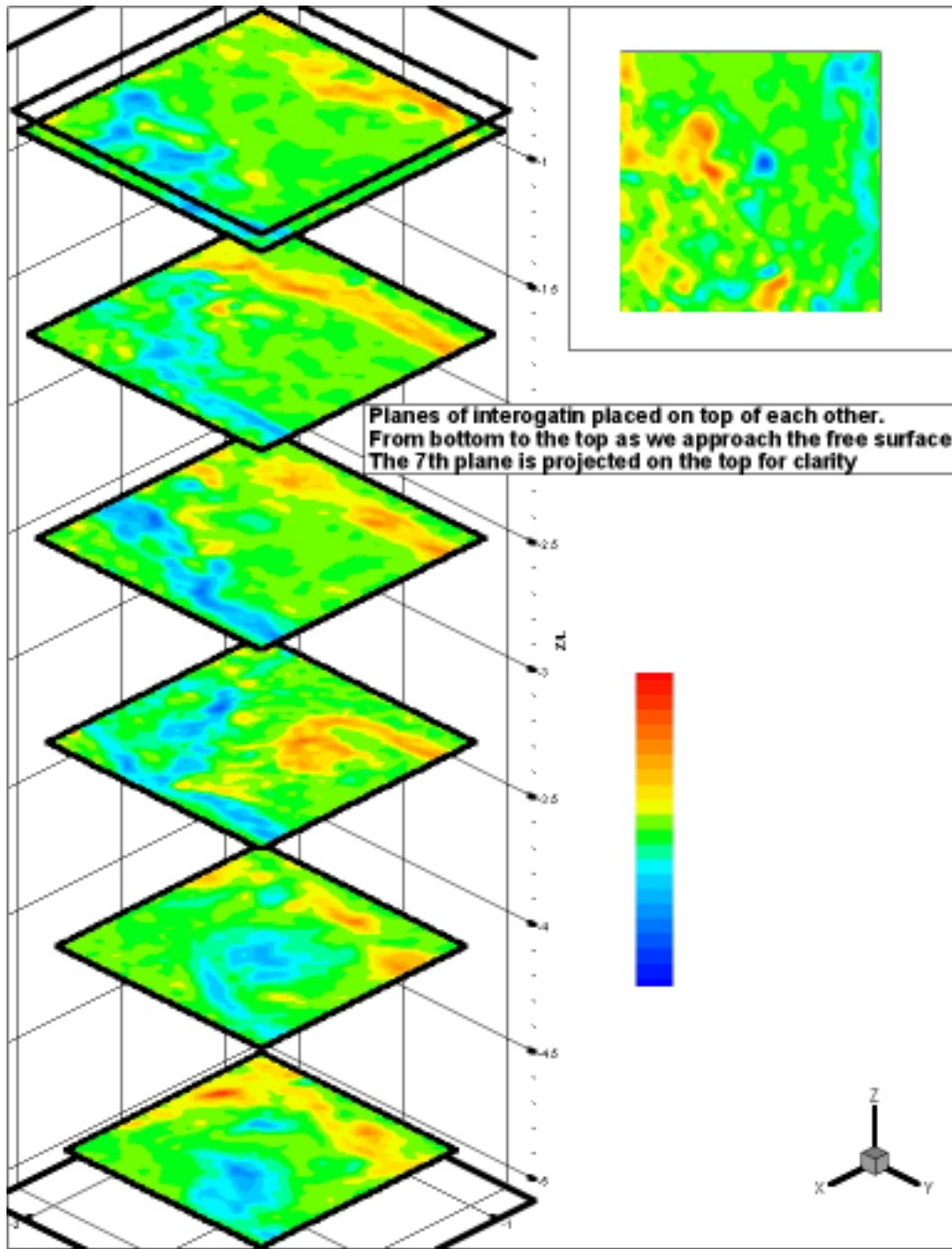


Figure 12-4: Three-dimensional representation of the planes of interrogation at  $t/T=1.5$

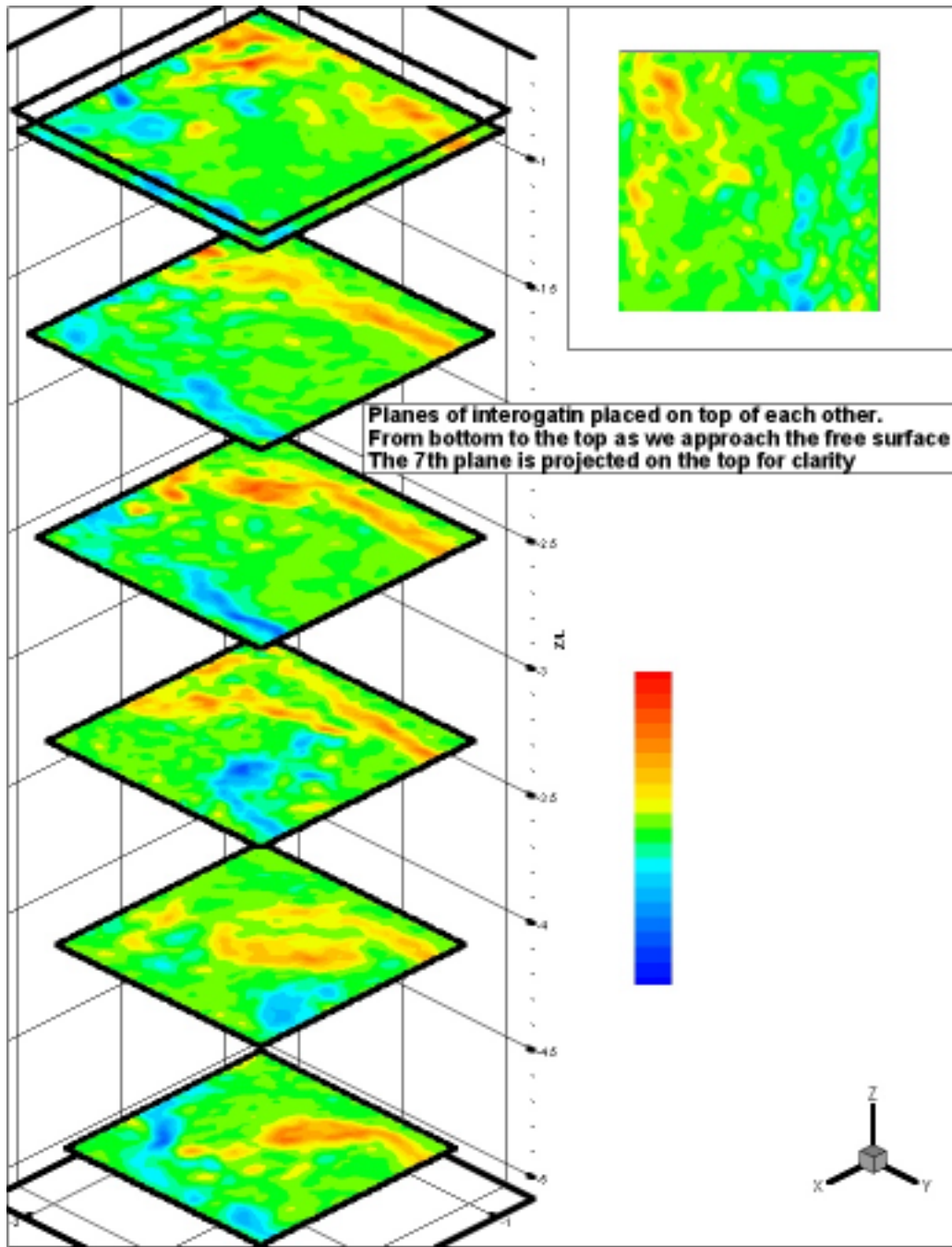


Figure 12-5: Three-dimensional representation of the planes of interrogation at  $t/T=2.0$

## **Conclusions**

Digital Particle Image Velocimetry measurements were used to investigate the characteristics of the wake of a circular cylinder near the free surface. The time mean and the unsteady characteristics of the flow were documented.

Time-averaged plane distributions of the mean velocity magnitude, vorticity,  $u'_{\text{rms}}$ ,  $v'_{\text{rms}}$  turbulent kinetic energy, and  $u/v'$  were presented. The vortex formation length increases as we approach the free surface extending up to 3.4 diameters downstream while the width of the wake practically doubles to approximately two diameters. The vorticity in the shear layers exhibits an increase as we move to higher elevations. Subsequently it reverts and decreases to a minimum when we reach the last elevation, corresponding to the free surface. Turbulent kinetic energy is primarily dominated by the fluctuations of the transverse velocity component but as we approach the free surface, the turbulent intensity decreases and the fluctuations of the streamwise component are contributing a larger portion to it. Finally, the turbulent fluctuations indicate that in the vicinity of the free surface, eddies align with the streamwise direction reducing the normal to the free surface vorticity component. They turn upwards to reconnect, meeting the “stress-free” boundary condition only in the immediate neighborhood of the free surface.

The instantaneous vorticity distributions at different elevations in the wake of the circular cylinder reveal the effect of the free surface. It was observed that as we approach the free surface, the shear layers emanating from the cylinder are becoming more stable and roll to form vortices further downstream. This results in a shift of the vortex formation length away from the cylinder and an increase of the concentration of vorticity inside the shear layers as it was observed from the mean characteristics. At the free surface however, the flow is becoming more turbulent and the shear layers less coherent. This is attributed to the effect of free surface turbulence.

Finally, in this work we were able to reconstruct temporally evolving information of the flow field in a three-dimensional space. This approach allowed us to observe the spanwise

distribution of vorticity as we approach the free surface. The existence of oblique vortex shedding was clearly demonstrated because of shifting of the vortex formation downstream. The onset of the effect of the free surface was determined to be in the neighborhood of 3.5 diameters below the interface. However, the free-slip boundary condition at the interface by forcing the vortex to reattach normal to the free surface causes the axis of the vortex to change again. As a result, vortex lines break into cell of vorticity and generate incoherent structures at the free surface in the form of downdrafts and upwellings.

As a more general conclusion we deduce that by having a free surface interface we imposed a boundary condition that was more compatible to the two dimensional character of the flow, thus not allowing the three-dimensional instabilities of the shear layers to grow and eventually roll into vortices. This demonstrates the great importance of end effects on the wake of the cylinder, and illustrates the significance of the evolution of three-dimensional instabilities in the shear layers.

## **Three-Dimensional Streamwise Vortical Structures of a Turbulent Wake near the Free Surface.**

### **Introduction**

The three-dimensionality in the wake of a circular cylinder has received much attention over the past years. The interaction of a separated shear layer with the forming vortices and the free stream triggers three-dimensional instabilities and vortex dislocations (Williamson 1992, 1995, 1996). Until recently, the major part of the related research was carried out using qualitative flow visualization. The existence of streamwise vortices was observed in plane mixing layers (Bernal and Roshko, 1986) and in the wake of a circular cylinder for a wide range of Reynolds numbers. (Gerrard 1978, Wei and Smith 1986, Williamson 1988). Particle-Image Velocimetry has been employed by Lin et al (1995, 1996) to study the spanwise vortical structures in the near wake of a circular cylinder and documented the existence of large-scale vortical structures with vorticity concentrations almost one-third of the streamwise vorticity and wavelength in the order of one cylinder diameter. Furthermore, for  $Re > 1000$  the flow is affected mostly by the shear layer instabilities developing from both sides of the body introducing in the wake frequencies that are almost one order of magnitude higher than the vortex shedding frequency. Castro and Haque (1988) established that the time scales of the free stream turbulence are of the same order of magnitude as those of the shear layer, the evolving instabilities can be enhanced and act in favor of the formation of a large-scale spanwise vortex.

Near the free surface we have a quasi two-dimensional turbulent flow field that is affected by the three-dimensional turbulence beneath it and as a result, reversing the energy cascade (Sarpkaya et al, 1994). In general, free surfaces have vorticity content even if the underlying flow is vortex-free (Rood, 1994a, 1994b, 1995). In addition, the surface curvature and the zero tangential stress on the interface combine to generate secondary vorticity. The relation of the length scales and the vorticity concentration of spanwise vortices (rollers) with the streamwise vortical structures (braids) are intrinsically related to the conservation of vorticity and the flux of vorticity. Since the free surface allows the existence of non-zero normal velocity component, the total vorticity will be the sum of the normal and the tangential (streamwise)

components and variation of one of the two will affect the other. Thus, it is reasonable to expect a variation of the streamwise vorticity with respect to the spanwise direction as we approach the free surface.

In order to detect the two-dimensional streamwise vortical structures in the spanwise direction, near the free surface, three-dimensional (2-D space and time) velocity measurements using DPIV Cinematography were carried out in planes normal to the free stream velocity. Lin et al (1995,1996) performed similar measurements in the wake of a circular cylinder with symmetric boundary conditions and a sampling frequency of 65Hz, which is sufficient to map the large-scale temporal variations but not the fine scales in the flow.

During the past two decades numerous publications have appeared presenting improvements of the DPIV technique as well as applications of the method to a wide range of flows, from low-speed liquid and two phase flows to supersonic gas flows. The interested reader can refer to reviews by Adrian (1991) (1996a and 1996b), and Grant (1994), (1997). The digital implementation of PIV is discussed in details by Willert and Gharib (1991) and Huang and Gharib (1997). A more elaborate description of the method employed in this studied can be found in chapter 2.

DPIV Cinematography is employed here to carry out spatio-temporal measurements, in the wake of a circular cylinder near a free surface. Results for two independent planes of interrogation normal to the free stream velocity are presented. Sufficient time resolution allowed us to reveal the underlying character of the alternate vortex shedding mechanism. Data analysis shows braid vortices beneath the free surface with size of the same order of the cylinder diameter. Their intensity remains unchanged with respect to the downstream position. High vorticity values exist at the immediate neighborhood of the free surface presenting a more coherent and deterministic distribution in comparison with the vorticity distributions below the free surface.

## **Experimental details**

In order to determine the feasibility of detecting the spanwise variations of the alternated vortex shedding character of the flow based on measurements performed in planes normal to the free stream, two independent experiments were carried out. Originally, DPIV data were obtained at different downstream stations with the interrogation plane normal to the direction of the free-stream as shown in figure 1. The first plane was located 2.5 cylinder diameters downstream and the translation step was set to be 1 diameter. By translating the sheet-forming optics, we were able to interrogate four different planes. However, only a portion of these data will be presented. The Reynolds number was approximately 1700, the aspect ratio ( $L/D$ ) of the cylinder was 12.8D, the Froude number was 0.3 and the shedding frequency was in the order of 1.98 Hz (from our previous work, see Vlachos et al, 1998) resulting a Strouhal number of  $Str=0.24$ . In figure 1-1 we illustrate how the streamwise planes of interrogation relate to the spanwise planes that were investigated in the first part of this chapter.

The same experimental setup was employed for the second experiment where three planes normal to the free stream and intersecting the free surface were interrogated. The planes were positioned at 2.0, 4.0 and 6.0 cylinder diameters downstream. In addition, three more planes were interrogated at the same downstream stations but located approximately 1.0 cylinder diameter below the base of the cylinder. This additional information would be used to compare the effect of the asymmetry of the boundary conditions in the spanwise direction. These data will not be presented in this section but will be included into Appendix I

For the illumination of the field of view a Copper-Vapor pulsing laser was employed delivering 5.5 mJ/pulse. Multi exposed images were acquired using a 1000fps CCD camera with an 8-bit dynamic range and 256x256 pixel resolution. For each plane of interrogation, 2048 frames were acquired with a sampling frequency of 128 Hz providing sufficient time resolution to capture high frequency fluctuations. The velocities were calculated by cross-correlating consecutive frames. The flow field is described by 61x61 vectors placed on a uniform grid.

Vorticity calculations were performed by applying fourth-order compact schemes (Lele, 1992) to reduce the contribution of the truncation error to the overall error of the calculation. The

lengths are non-dimensionalized with the cylinder diameter thus the center of the cylinder is located approximately at point zero. The field of view for the first plane covers almost five diameters intersecting the free surface. As we translate the interrogation plane, the field of view is slightly reduced.

Sufficient time resolution allows us to identify the vortex shedding process in the time domain by inspecting the reversal of the transverse velocity component. Once the first (i.e. positive) vortex intersects the interrogation plane, on either side of the core the flow is directed towards one side, subsequently for the passing of the second (negative) vortex the transverse component of the velocity reverses towards the other side.

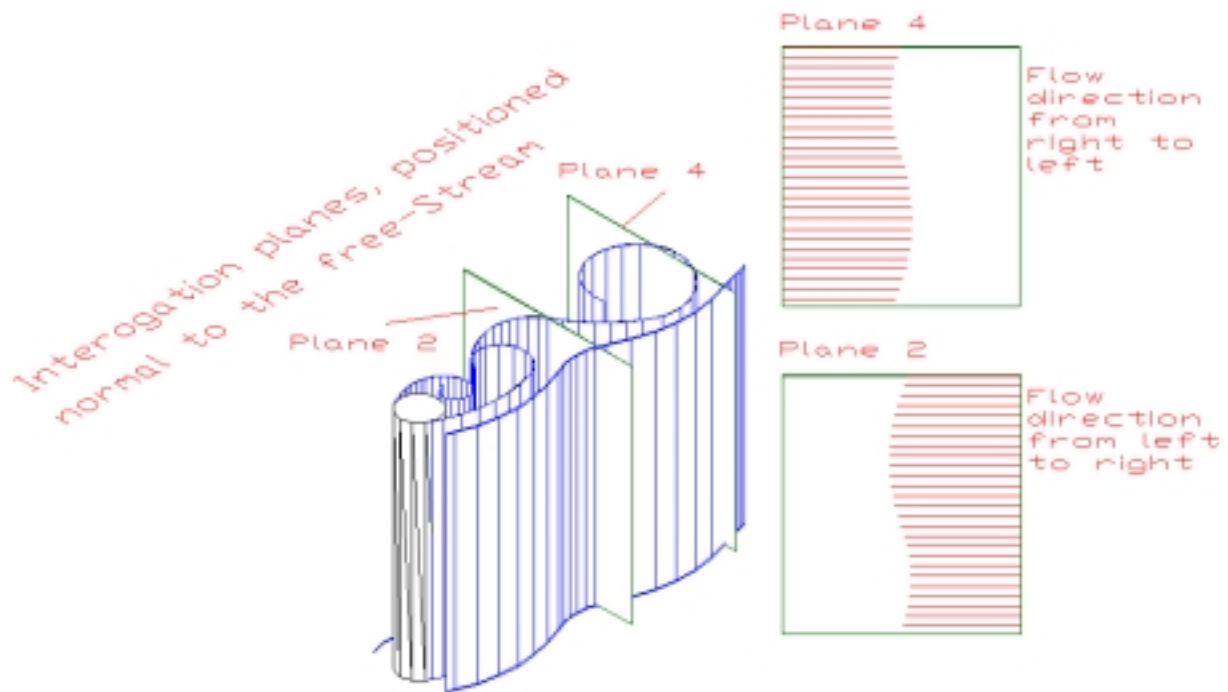


**Figure 1:** Schematic representation of the placement of the interrogation planes with respect to the free-stream velocity and the passing of the primary Von-Karman vortex through the planes.

The projection on the right demonstrates the intersection of the vortex core with the field of view. At this instant, the domains of the flow field on either side of the core will be directing the flow to opposite directions, thus indicating the vortex shedding mechanism.

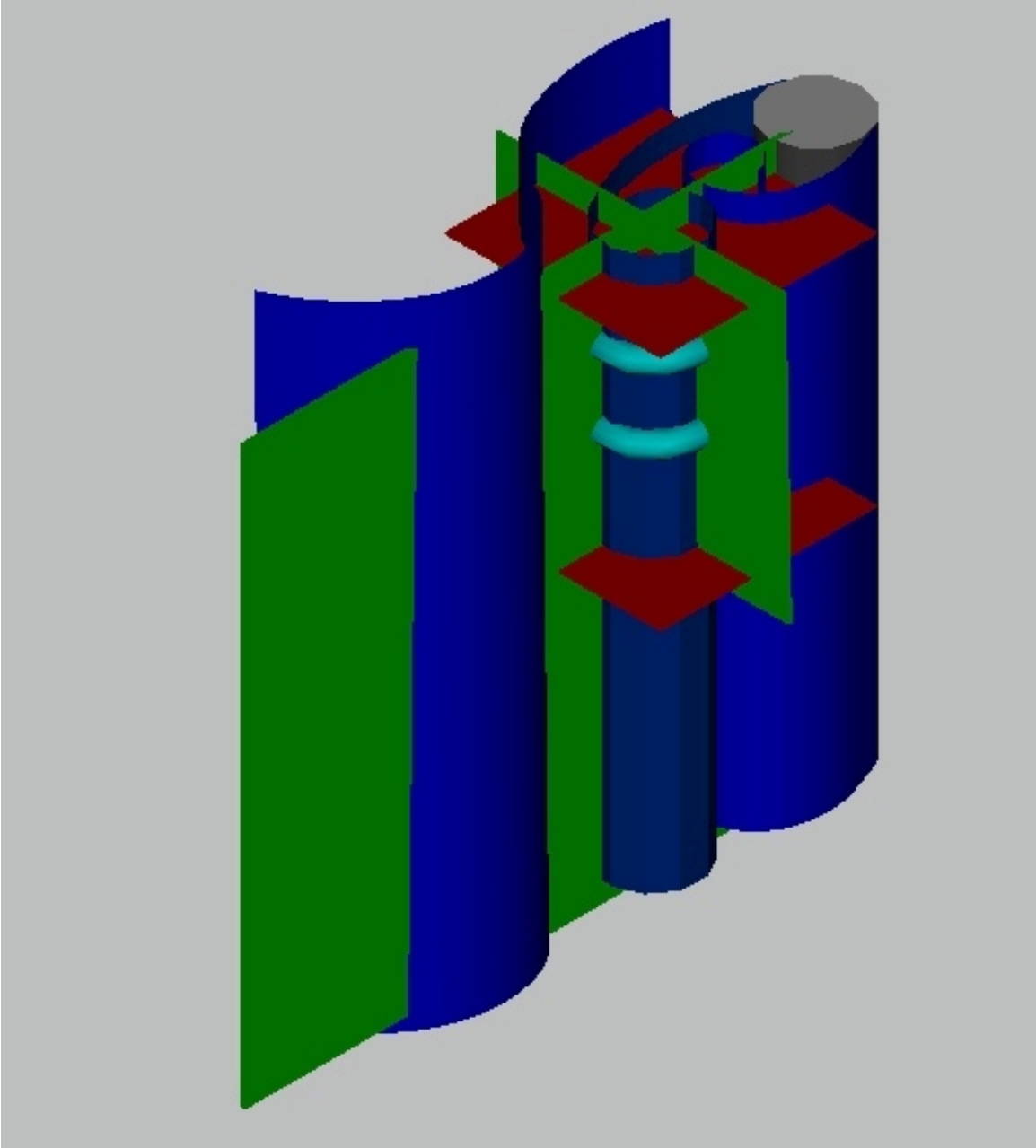


**Figure 1-1:** Schematic representation of the placement of the spanwise interrogation planes with respect to the streamwise planes and the passing of the primary Von-Karman vortex through the planes. Blue color corresponds to the flow, red to the spanwise planes and green to the streamwise ones.

## **Results and discussion**

Instantaneous vorticity contours overlapped with the velocity vectors are presented for the second and fourth plane of interrogation. The time step between two consecutive frames presented here is 0.08 seconds, therefore six instants will correspond to total of 0.48 seconds, almost one period of the vortex shedding. The free surface is located at approximately  $y/L=1.5$ . The first set of figures (2-7) corresponds to the second plane of interrogation located approximately 3.5 diameters downstream of the cylinder. Visual observation of the velocity vector reveals the underlying pattern of the vortex shedding process, namely the passing through the field of view of the primary Von-Karman vortex. In figure 1 we note an asymmetry of the flow field, showing a fairly uniform velocity distribution directing the flow from left to right. This region of the field is disrupted by the existence of pairs of counter-rotating streamwise vortices. In figure 2 the asymmetry of the flow field is decreased presenting a balance between both directions and tending to shift in the opposite way. In figure 3 the flow pattern has reversed. Now the flow is directed from right to left, indicating the passing of the opposite primary von-Karman vortex through our interrogation area. In figure 4 the asymmetry decreases again showing the flow's tendency to reverse direction again, which happens in figures 5 and 6 completing one period of the Von-Karman vortex shedding. Throughout the sequence of frames, braid vortices intersect with the plane of interrogation. Surprisingly the size of these vortices in the vicinity of the free surface is in the order of one diameter. In addition we observe the existence of high vorticity levels in the immediate neighborhood the free surface. These can be attributed to small-scale vortices present in that region as well as the existence of "downdrafts" and "upwellings". In addition, streamwise vortices are forced to reconnect normal to the free surface, thus causing an abrupt change in the direction of their axis. This fact, combined with the generation of vorticity at the free surface due to the free surface deformation contributes to the vorticity present in this region.

In the next set of figures (7-13) the corresponding instants of the flow field for the fourth plane of interrogation are presented. This plane is situated 5.5 cylinder diameters downstream. The same pattern of alternation of the flow direction is observed, providing visual evidence of the vortex shedding process. However, we note that in this case, the velocity magnitude has

decreased, primarily due to the fact that we are further downstream therefore the vortices are getting diffused. Braid vortices are clearly observed in this case as well. Despite the fact that at positions further downstream, the von Karman vortex core is expanding, the size of the braid vortices remain almost constant to one cylinder diameter. Vorticity values of the same order of magnitude with the previously presented plane exist at the edge of the free surface. Throughout figures 2-13 we observe pairs of positive and negative streamwise vorticity. This can be attributed either to independent streamwise vortices or to vortex rings intersecting the field of view.

Finally in figure 14 we present iso-surfaces of the positive (red) and negative (blue) vorticity in the space-time domain, for a total time of approximately one period of the vortex shedding at the second plane of interrogation. A sequence of 128 frames was used to reconstruct the volume of data. The free surface is located at  $y/L=1.5$ . At the vicinity of the free surface we observe extended areas of alternate positive and negative vorticity. Even though the distribution at the free surface is fairly coherent, the distribution of the streamwise vorticity below the free surface is extremely random.

## **Conclusions**

DPIV Cinematography is employed to carry out spatio-temporal measurements, in the wake of a circular cylinder near a free surface. Results for two independent planes of interrogation normal to the free-stream velocity are presented. Data analysis shows braid vortices beneath the free surface with size of the same order of the cylinder diameter. Their intensity remains fairly unaffected with respect to the downstream position. High vorticity values exist on the edge of the free surface, presenting a more coherent and deterministic distribution in comparison with the vorticity distributions below the free surface. Finally, by employing a method with sufficient time resolution, we were able to detect the underlying mechanism of the alternate vortex shedding, even though the interrogation planes were placed normal to the free stream. This eventually will allow us to investigate spanwise variation of the vortex shedding and detect the axis of the vortex core.

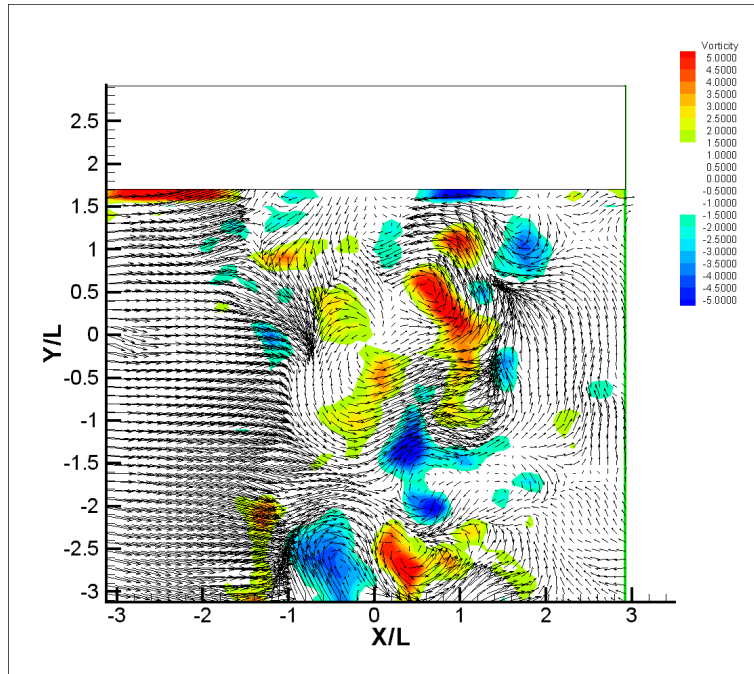


Figure 2: Vorticity contours and velocity vectors for the second plane at  $t=0$  seconds

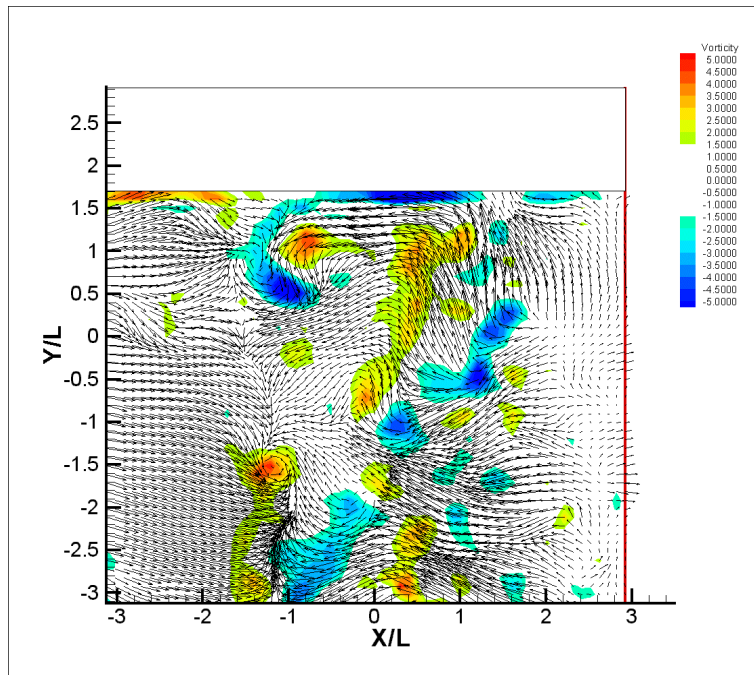


Figure 3: Vorticity contours and velocity vectors for the second plane at  $t=0.08$  seconds

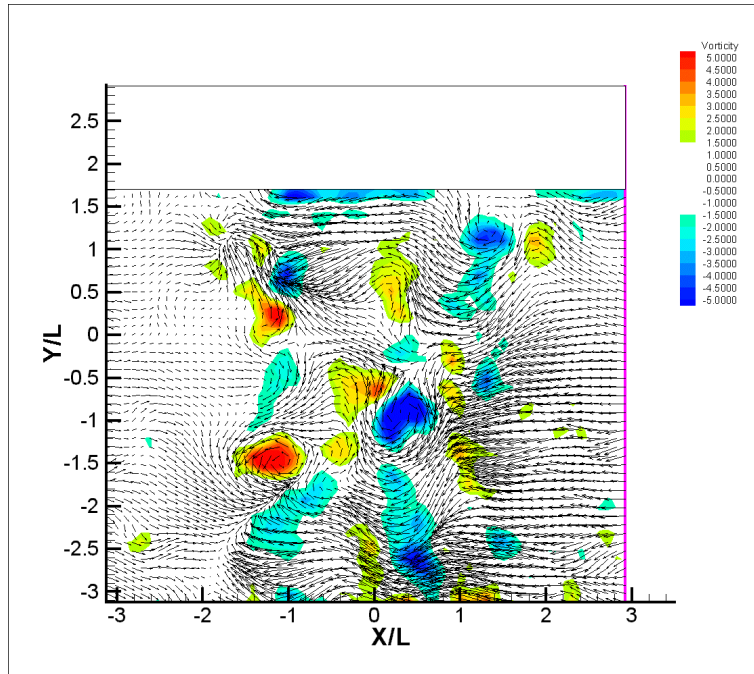


Figure 4: Vorticity contours and velocity vectors for the second plane at  $t=0.16$  seconds

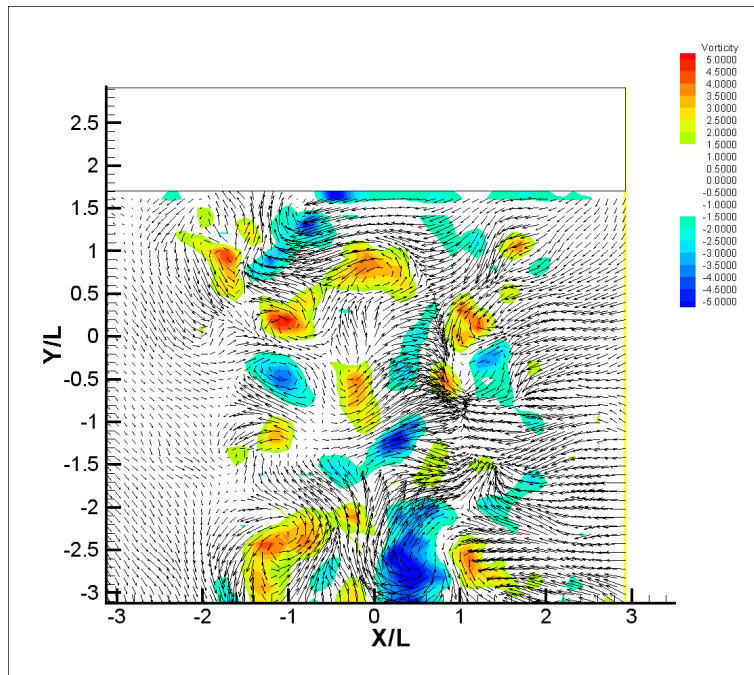


Figure 5: Vorticity contours and velocity vectors for the second plane at  $t=0.24$ seconds

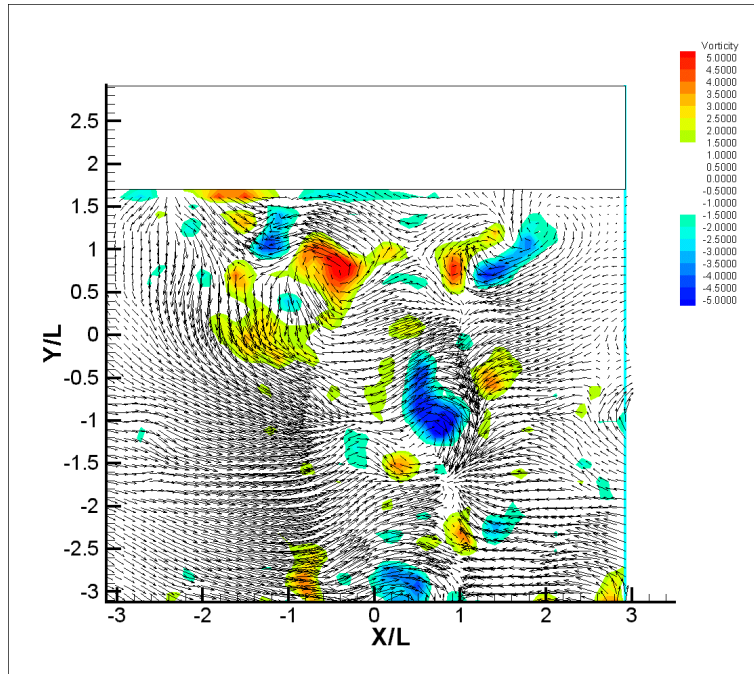


Figure 6: Vorticity contours and velocity vectors for the second plane at  $t=0.32$  seconds

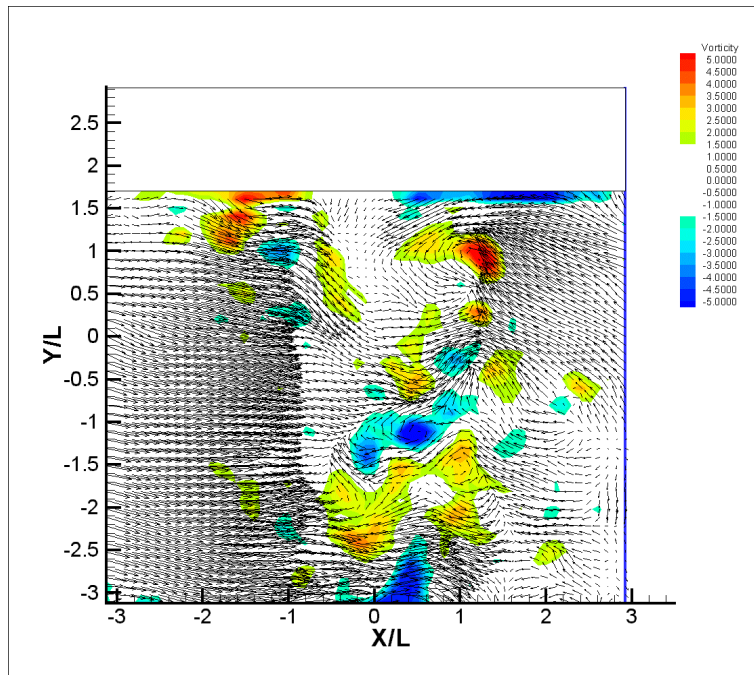


Figure 7: Vorticity contours and velocity vectors for the second plane at  $t=0.4$  seconds

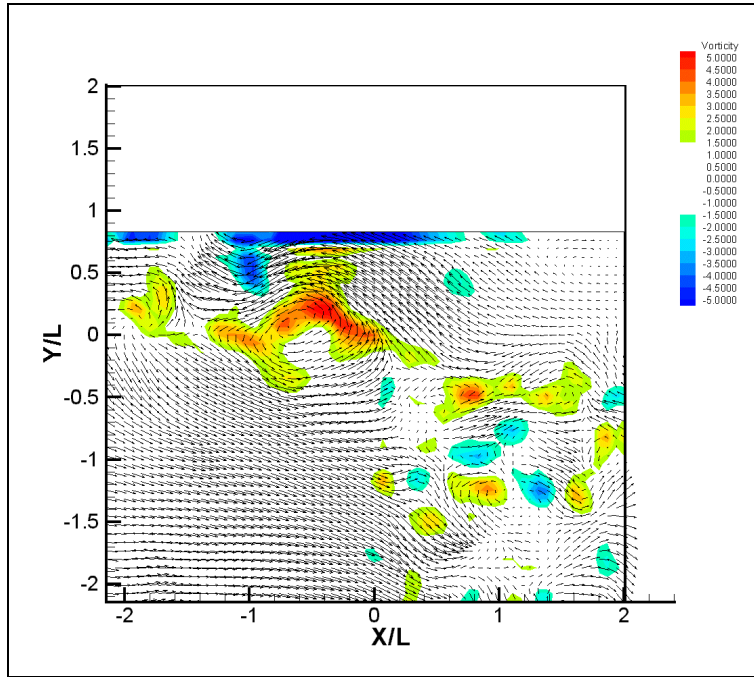


Figure 8: Vorticity contours and velocity vectors for the fourth plane at  $t=0.8$  seconds

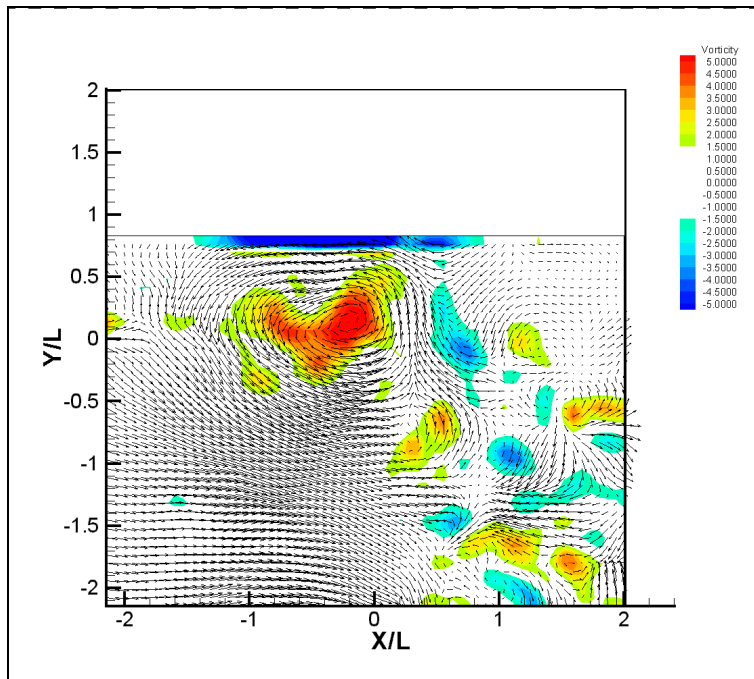


Figure 9: Vorticity contours and velocity vectors for the fourth plane at  $t=0.16$  seconds

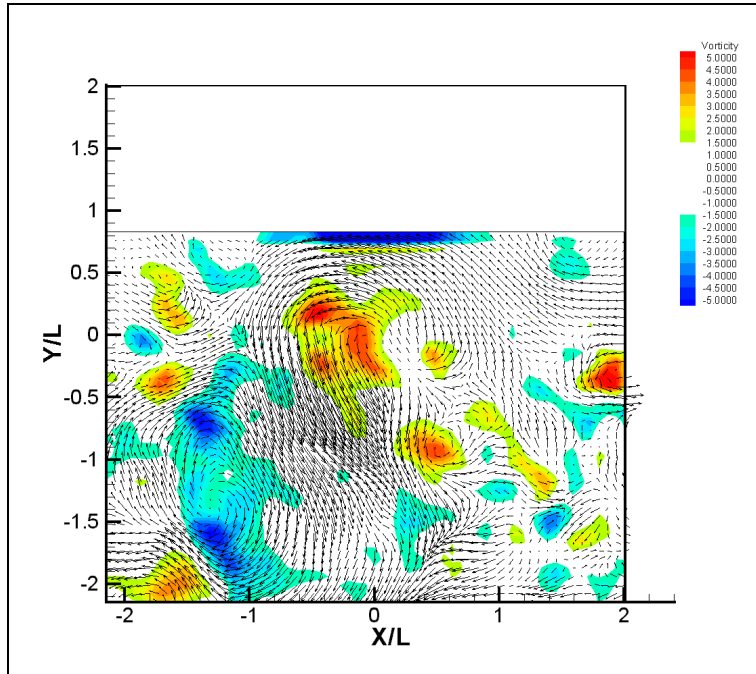


Figure 10: Vorticity contours and velocity vectors for the fourth plane at  $t=0.24$  seconds

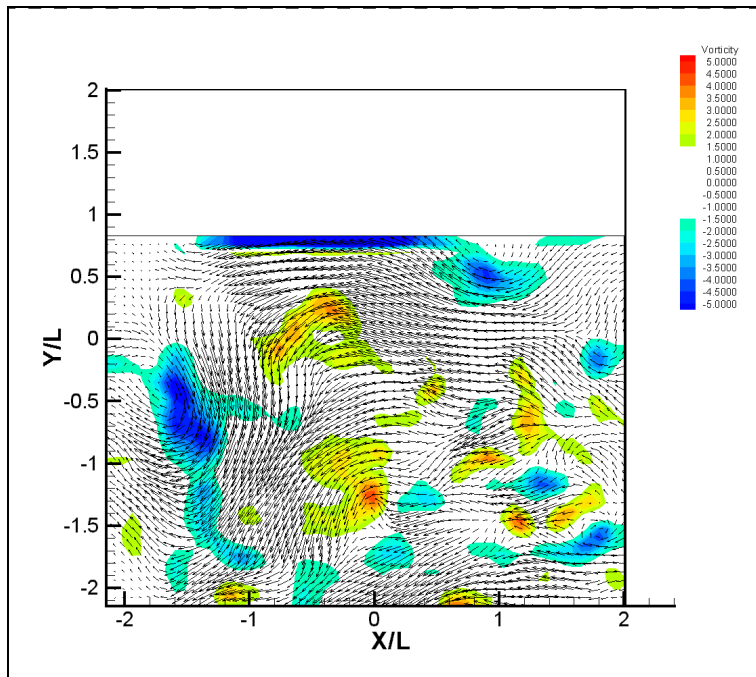


Figure 11: Vorticity contours and velocity vectors for the fourth plane at  $t=0.32$  seconds

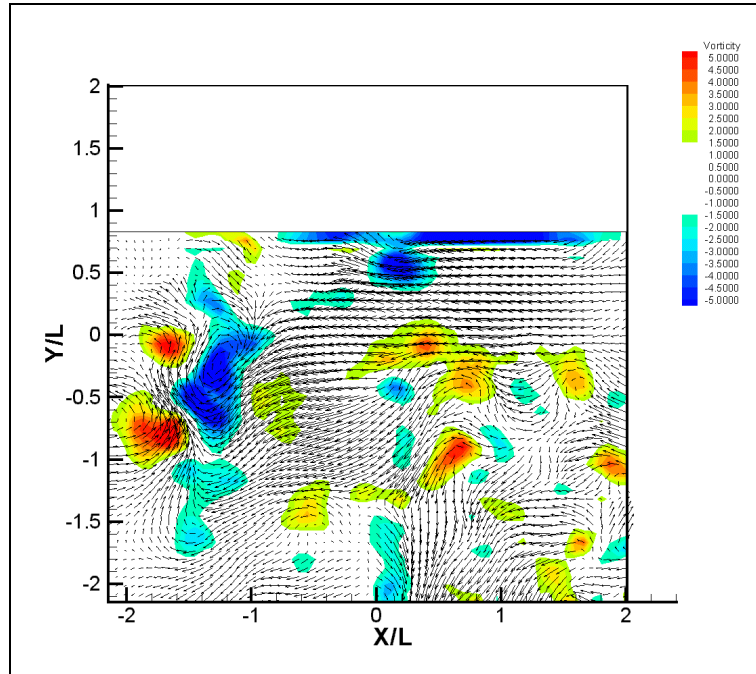


Figure 12: Vorticity contours and velocity vectors for the fourth plane at  $t=0.40$  seconds

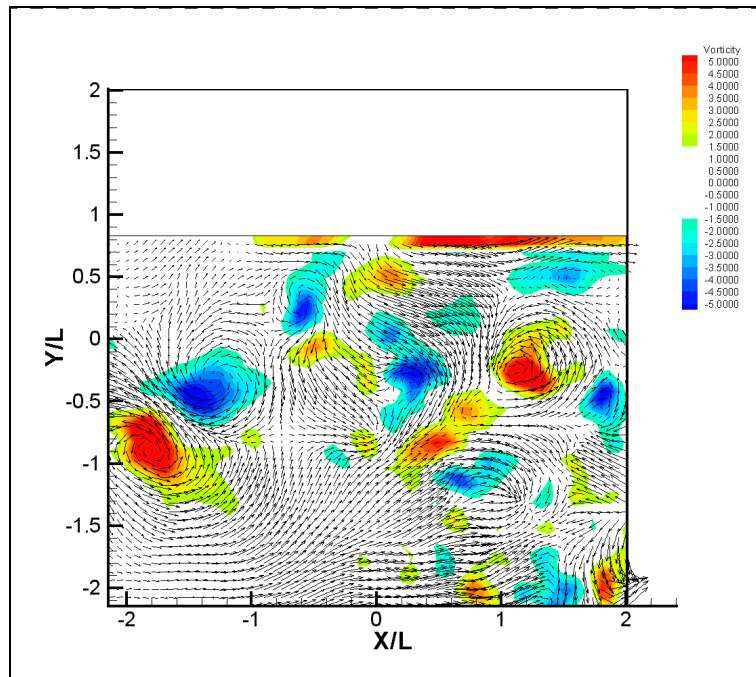
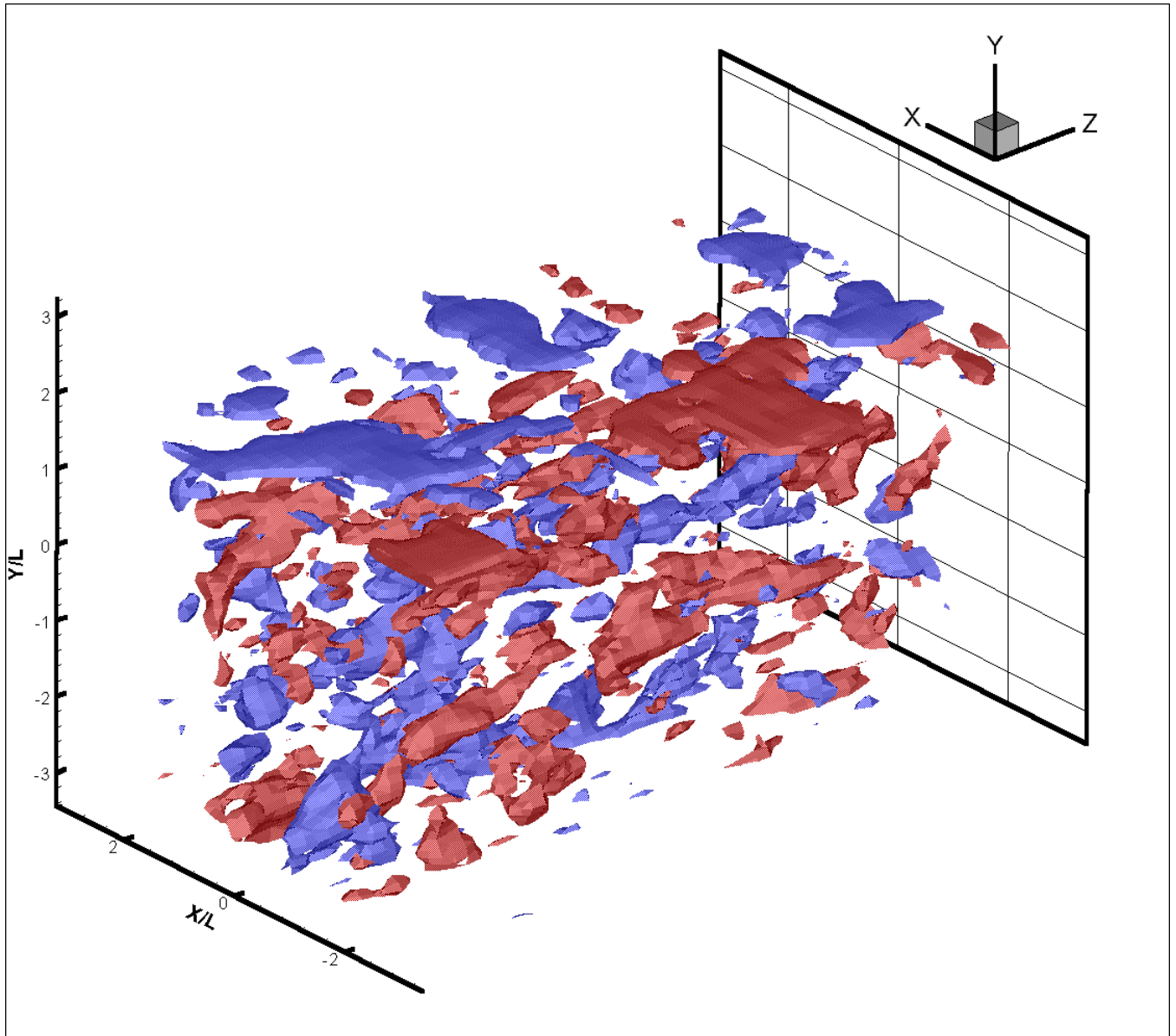


Figure 13: Vorticity contours and velocity vectors for the fourth plane at  $t=0.48$  seconds



**Figure 14:** Iso-surface representation of the vorticity distribution in the space-time domain for the first period of the flow. Blue color corresponds to negative vorticity and red color to positive. X-Y plane corresponds to the physical two-dimensional plane and Z is the time axis. The free surface is approximately located at  $y/L=1.5$

## **Chapter 4**

# **The Effect Of Free-Surface and Inclination on the Vortex Shedding Behind Circular Cylinders**

### **Introduction**

The case of the circular cylinder wake has attracted hundreds of researchers who produced a literally endless list of publications. This is due partly to the simplicity of setting up an experimental or computational investigation of the problem and to the great engineering and practical importance that it presents (see reviews by Williamson 1995, 1996). The flow involves the interactions of the free stream with the boundary layer, the separating shear layer and the vortices that form and shed in the wake. Macroscopically, it appears that the flow develops in a two-dimensional fashion but a closer look reveals some interesting three-dimensional patterns as for example the streamwise vortical instabilities which ride the separated vortex sheets (Wei and Smith 1986) (Bernal and Roshko, 1986). It has been demonstrated by several authors such as Ramberg(1983) and many others, that three-dimensional effects on the wake of a circular cylinder depend upon the end conditions. End disturbances in the spanwise direction could trigger oblique shedding and totally violate the two-dimensional character of the flow

(Hammache and Gharib 1991). In the current study, we focus on the asymmetry of the end conditions introduced by replacing one of the boundaries with a free surface.

Deviations from two-dimensional flow in wake of a circular cylinder have been observed even at low Re numbers. Apart from the formation of vortical structures with their axis aligned with the free stream (braids), the three-dimensional character of the flow is manifested in the form of the oblique shedding process. Hammache and Gharib (1991) showed how the oblique shedding depends upon the end conditions. They were able to control the angle of the vortex shedding by employing two transverse circular cylinders upstream of the main cylinder and therefore reproduce both types of shedding. However, their work was limited in a range of very small Reynolds numbers, Re (40-160) where the onset of the initial wake instabilities are observed. For higher values of the Reynolds number, Re (>1000) the wake is affected by the shear layer instabilities and the upstream turbulence and not only by the end conditions.

In order to understand the three-dimensional character of the flow, the effects of yaw in the vortex shedding mechanism have been studied extensively. Ramberg (1983) investigated the effects of yaw for Re ranging (160-1000) and showed that there exists a relation between the vortex shedding frequency and the angle of the shed vortex filaments. Generally the wake of an inclined cylinder is governed by the so called “Independence Principle” which states that the Strouhal frequency is linked to the component of the free stream velocity normal to the cylinder. This principle relates the Strouhal frequency to the Re number by a universal relation. According to the early work by Roshko(1954) the Strouhal frequency is proportional to  $1/Re$ . This relation is valid for all cases, with and without inclination. More recent studies show better agreement of experimental data for a wider range of the Re number if an expansion of  $\sqrt{1/Re}$  replaces  $1/Re$ . (Williamson and Brown, 1998). Changes in the vortex shedding frequency with respect to the spanwise direction correspond to different shedding modes and subsequently changes in the inclination of the vortex axis thus oblique vortex shedding.

For a cylinder piercing a free surface, the latter represents an end condition more compatible with the two-dimensional character of the flow. This is because on a solid wall, all

the vortex lines must bend and align parallel to the wall, whereas on a free surface, vortex lines can terminate at the free surface. Yet, by introducing a free-surface boundary condition interface, the complexity of the problem increases. Free surface is a stress-free interface that constrains the motion of the vortex. As a result, it allows the existence of a vorticity component normal to the free surface and the process of vortex “reconnection” takes place. Vortices with arbitrary axis direction like braids and rings may cut themselves and reconnect to the free surface. Moreover, the free surface acts as an image plane for the parallel to the free surface vorticity component thus inducing velocities that propel the vortex. If we take also under consideration the effect of surface deformation, then we have to account for the generation of secondary vorticity and vorticity flux. All these complexities constitute a behavior of the vorticity that is not observed in the flow interaction with solid boundaries. For a more detailed description, the reader is referred to Rood (1994a, 1994b, 1995).

An extensive amount of work has been carried out so far to understand bluff-body wakes as well as the behavior of free surface vorticity. However, research combining the two problems is generally lacking, despite the need for the understanding of the fundamentals of fluid mechanics and the great importance of such problem for engineering applications (offshore structures, ship wakes, risers). Lang and Gharib (1998) investigated the problem but with focus on the effect of varying free surface conditions. In their case, the free surface is contaminated by surfactants thus it is no longer a stress-free interface. As a result, the free-surface vorticity has the tendency to align with the free surface. Stern et al (1994) studied the interaction of a flat plate piercing a free surface. However the flat plate was aligned with the free stream and the main objective was the understanding of the boundary layer development and its interaction with the free surface.

The current study presents analysis of hydrogen bubble flow visualization which indicate that free surface affects the vortex shedding more than two to three cylinder diameters below the free surface. Discontinuities of the vortex axis and cells of shedding which induce a phase difference in the vortex shedding mechanism were visually observed. Streamwise vortical structures form along the primary vortex axis. Furthermore, from particle visualizations,

evidence of vortex suppression is found in the region near the free surface for the case of the highest Froude number and zero model inclination. This is confirmed by LDV measurements. Positive model inclination, i.e. a model leaning with the flow, counteracts the effects of the free surface recovering the vortex shedding process, while negative inclination presents a very turbulent broad spectrum in the neighborhood of the free surface. The introduction of asymmetry in the boundary condition of the wake of a circular cylinder in combination with a yaw angle with respect to the free-stream generates a three-dimensional flow field that depends on the respective values of the Re and Fr numbers as well as the position in the spanwise direction.

## **Experimental details**

The effect of the free surface boundary condition to the formation of vortex shedding is the subject of the current work. Flow visualizations and laser-Doppler velocimetry (LDV) are employed. Three model inclination are considered, case (a)  $\theta=0$ , case (b)  $\theta=30$ , case (c)  $\theta=-30$  degrees –as shown in Figure 1-1 and three Reynolds numbers, case I Re=1700, case II Re=3700, case III Re=6000, corresponding to Froude numbers of 0.3, 0.65, 1.06 respectively, based on a diameter of 15.8mm. In order to be able to compare the effect of model inclination, we are going to use a Re number based on the free stream only, and not account for the cosine of the inclination angle. The aspect ratio of the cylinder diameter with respect to the depth of the test section was  $L/D=20$ . The experiments were conducted in the free-surface water tunnel facility of the Engineering Science and Mechanics Dept at Virginia Tech. The tunnel has a 610x610 mm test section and a capacity of 2500 gallons approximately.

## **Hydrogen Bubble Flow Visualizations**

Hydrogen bubble flow visualizations were performed in order to define the time lines of the vortices shed, while particle flow visualizations were used to observe flow topology in planes parallel to the free surface. Hydrogen bubbles generated by thin wires are excellent tracers for monitoring instantaneous characteristics of the flow field since their relative time scale of responding to flow fluctuations is usually less than  $10^{-4}$  seconds. A detailed discussion of the

*Chapter 4: The Effect of Free-Surface and Inclination on the Vortex Shedding Behind  
Circular Cylinders*

---

properties, behavior and applications of hydrogen bubbles in flow visualizations can be found in Lian and Su (1996). Lu and Smith (1985,1991) employed hydrogen bubbles to investigate the bursting characteristics of a turbulent boundary layer while Utami and Ueno (1984) used them to investigate characteristics of a turbulent open channel flow. Hydrogen bubbles were employed by Techet et al (1998) in a way similar to the present study, to visualize the vortex shedding characteristics in the wake of a tapered cylinder in oscillating flow. However in their experiments the bubbles were generated using the lead precipitation method.

The hydrogen bubbles were generated using the method of electrolysis. A platinum wire of about 20micron in diameter was stretched along the span of the cylinder and approximately one diameter away from the center. One issue that needs to be considered is the rising terminal velocity of the bubble. This can be calculated from the balance of the drag forces with the buoyancy forces. Thus, the terminal velocity of a rising bubble can be calculated from the equation:

$$U = gd^2 (\rho - \rho_h) / 12\mu \quad (1)$$

where:  $U$  is bubble terminal velocity,  $d$  is bubble diameter,  $\rho$  is density of water,  $\rho_h$  is density of the bubble,  $\mu$  is dynamic viscosity of water.

For a bubble diameter of 0.1mm, the rising terminal velocity is in the order of 0.8 cm/s, which is less than 6% of the smaller velocities that are under consideration in the present study. Since the objective is to qualitatively determine the time variation of the vortex core inclination and not to perform any accurate velocity measurements the bubble velocity deficit due to the wake of the wire is not taken into account which in addition is going to be laminar and closed affecting the flow even less. Because of the rotational motion of the fluid in the vicinity of the vortex core, the centrifugal acceleration directs the bubbles towards the center (larger bubbles move in the core faster) increasing the bubble concentration in that area. As a result, the intensity of the reflected light increases. In this way the vortex core is easily identified. Further downstream the bubbles are diffused in the turbulent wake thus their intensity gradually deteriorates.

*Chapter 4: The Effect of Free-Surface and Inclination on the Vortex Shedding Behind  
Circular Cylinders*

---

A Cu-Vapor pulsing laser was employed with a mean output power of 36Watts energy/pulse of 5.5 mJ, emanating a green wavelength beam. Specially coated optics were used to form a laser sheet and deliver it in the test section. A gray scale CCD camera able to acquire up to 1000fps with resolution of 256x256 pixels and 8-bit dynamic range (256 shades of gray) was used to acquire the images. For all cases, the camera was in synchronization with the laser at frequencies from 30 to 50 Hz. In all cases, 10 seconds of data were digitally stored. The plane of the laser sheet was aligned with to the axis of the cylinder (Figure-1-2). The field of view was adjusted to fit the full depth of the test section corresponding to a 1.3x1.3mm pixel area.

### **Particle Flow Visualizations**

For the particle flow visualization, the plane of the laser sheet was oriented parallel to the free surface and located one diameter below and half a diameter downstream of the model (Figure 1-2). Attempts to acquire images closer to the free surface were unsuccessful, due to reflections from the free surface that saturated the images. These reflections are visible even one diameter below the surface, especially for the case of the highest Re number. As flow tracers, neutrally buoyant 30-micron hollow glass spheres were used. Because of their diameter and specific gravity, any lag of the particle velocity to respond to velocity accelerations is negligible. The camera field of view was adjusted to 3.65D (cylinder diameters).

### **LDV Measurements**

A TSI fiber-optic LDV was employed to acquire velocity time series at different locations along the spanwise direction of the cylinder, in order to investigate the effect of the inclination and the free surface on the frequency of the vortex shedding. The data rate of the LDV signal was carefully kept above 1000Hz and a “sample-and-hold” approach was used for the reconstruction of the signal. Since the frequencies under consideration do not exceed 15 Hz, the “random arrival” problem of the LDV measurements is not an issue. The sampling frequency was set at 128Hz. The task of the A/D conversion was carried out with a 12-bit  $\pm 10$  Volts D/A board, resulting in accuracy of  $\pm 48$  mili-Volts. Only the U-component (streamwise) of the velocity was acquired, and therefore there was no need to run the measurements in coincidence

*Chapter 4: The Effect of Free-Surface and Inclination on the Vortex Shedding Behind  
Circular Cylinders*

---

mode. Traversing of the LDV probe allowed measurements from one half cylinder diameters above the floor of the tunnel, to one half diameter below the free surface, covering nineteen diameters. Based on the positioning accuracy of the traversing scales and the implemented feedback using Linear Variable Displacement Transducers (LVDT), the overall accuracy of the traversing system is estimated in the order of  $\pm 20$  microns. For all cases, i.e. vertical and inclined cylinders, the axis of translation was carefully kept parallel to the axis of the cylinder. The LDV measurement volume was placed 3.15 diameters downstream and 1.25 diameters away from the center of the cylinder (Figure 1-2). Finally, an HP signal analyzer was employed for real time monitoring of the velocity signals and on-line calculation of power spectra.

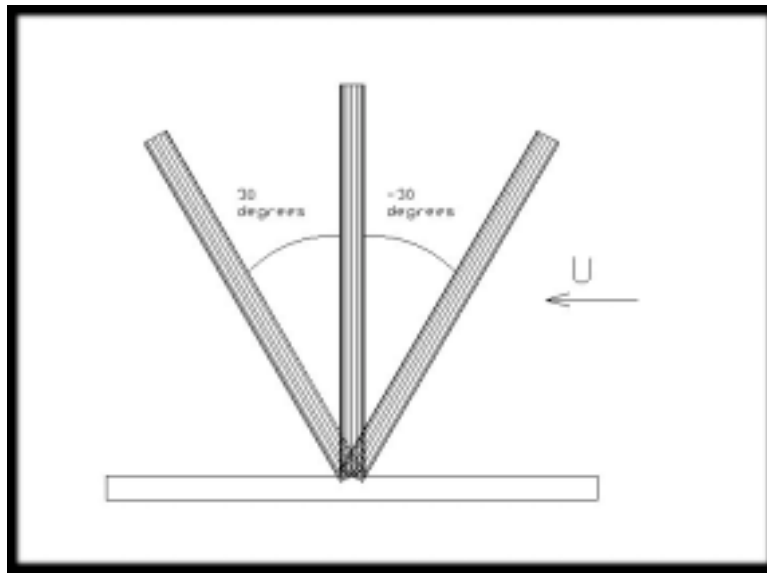


**Figure 1:** : Inclination of the cylinder with respect to the free stream velocity

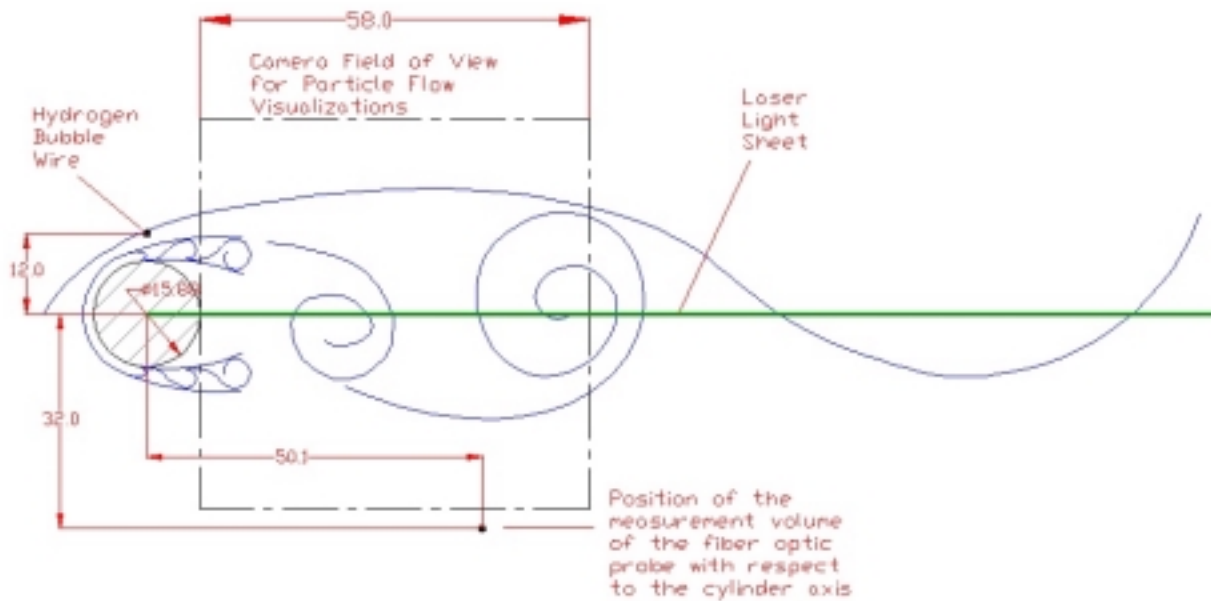


**Figure 1-1:** Schematic representation of the position of the hydrogen bubble wire and the fiber optic LDV probe with respect to the cylinder axis. The location of the area of interrogation for the particle flow visualizations is also shown. (All dimensions are in mm.)

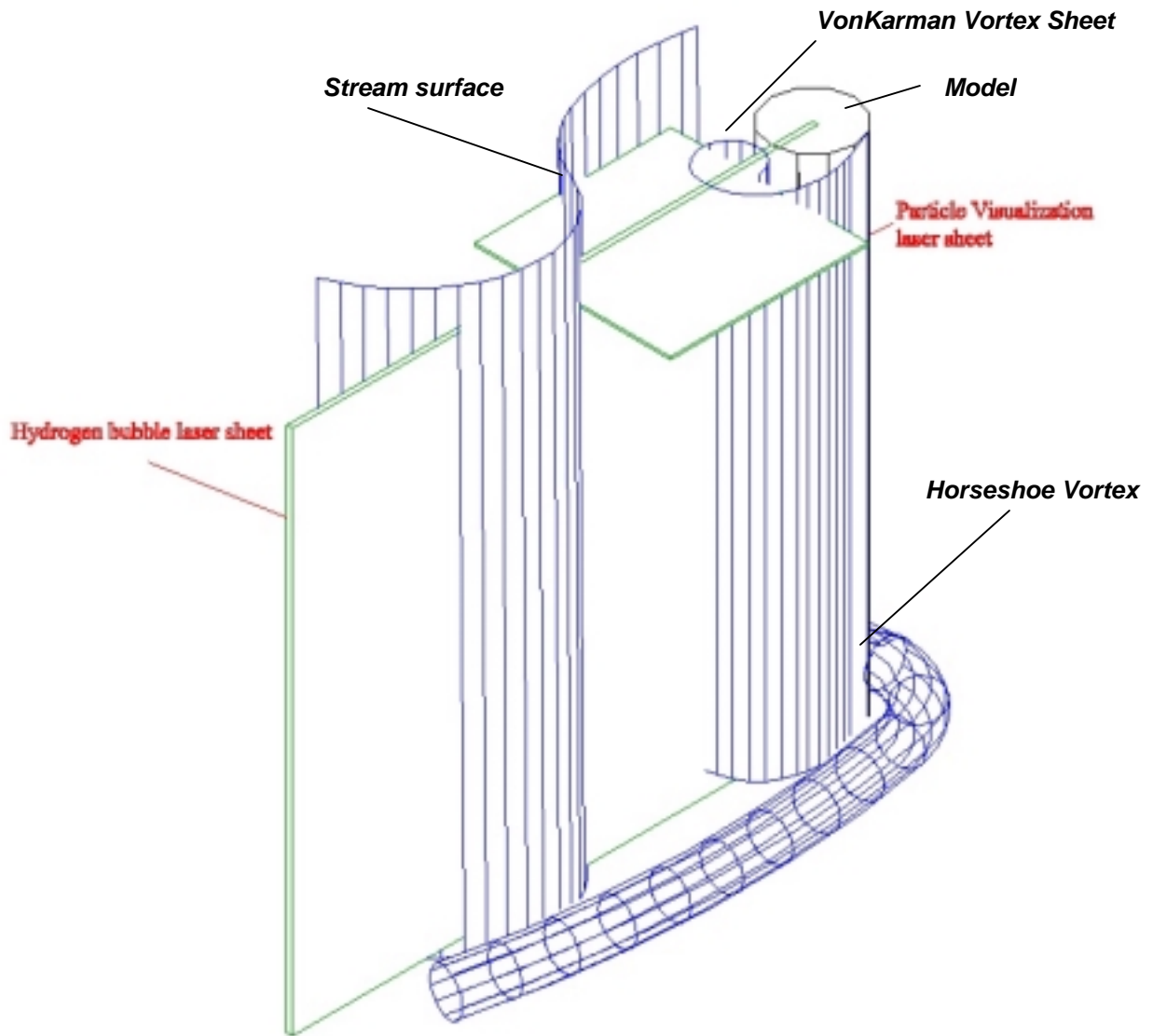


**Figure 1-2:** Schematic representation of the intersection of the interrogation fields (hydrogen bubbles – particles) with the corresponding laser sheets and the shed vortices.

## **Results and Discussion**

### **Hydrogen-Bubble Flow Visualization**

Results from the hydrogen-bubble flow visualizations are presented first. Three distinct cases were considered for the three inclinations. For each case the Reynolds and Froude number were given three distinct values. For all cases, representative independent instantaneous frames of the flow field demonstrate the general characteristics of the vortex shedding process. However, these present a limited view of the phenomena under consideration. A more complete understanding can be achieved only by animating the entire sequence.

For the first case of zero inclination,  $Re=1700$ , and  $Fr=0.3$  the trace of the vortex axis as it intersects with the laser sheet is shown in Animation 1-1. It is observed that the vortex shedding is affected and this can be attributed to the horseshoe vortex forming at the base of the model as it is shown in figure 1-2. As we move up in the spanwise direction, an inclination of the vortex axis with respect to the axis of the cylinder develops, indicating a component of vorticity parallel to the free stream. After the 50% of the span however the inclination of the shed vortex is reduced and the vortex axis becomes almost parallel to the model axis in order to reconnect normal to the free surface. By observing the sequence, we note that the inclination is varying from oblique to almost uniformly parallel to the cylinder axis and the effect of the horseshoe vortex is alternating as well. Almost in all frames, the vortex clearly reconnects normal to the free surface. However oblique shedding can be encountered a few diameters below the free surface. The animation of the complete sequence shows the unsteady character of the flow. Changes of the inclination occur inconsistently and with no repeatable pattern. Furthermore, the existence of “braid” vortices is observed throughout the span of the cylinder but with no obvious periodicity both in time and space.

In the second case of zero inclination, with a  $Re=3700$  and  $Fr=0.65$  (Animation 1-2), the behavior is changing. We attribute this to the stronger effect of the free surface distortion. In the majority of the instants, the inclination of the shed vortex is consistently oblique, emphasizing

the three-dimensional character of the flow. Braid vortices are also present along the span of the cylinder. What is very interesting is the fact that there exists a phase difference in the vortex shedding processes as a function of the span in the form of strong discontinuities of the trace of the vortex. However, because of the fact that the condition at the free surface forces the vortex to reconnect normal, the change of the inclination is sharper in the vicinity of the free surface if compared to the lower Fr number case.

The third case of zero inclination for  $Re=6000$ ,  $Fr=1.06$  is presented in Animation 1-3. The inclination is alternating between different instants, with abrupt changes in the slope, showing discontinuities on a wave pattern of the hydrogen bubble trace. This can be indicative of a variation in the development of the shear layer instabilities with respect to the span, leading to vortex dislocations or three dimensionalities in the Von-Karman scale. An interesting feature is the formation of a steady free-surface depression in the wake, which in the image corresponds to the reflection of the deformed free surface in the neighborhood of the cylinder-free surface juncture. This is due to very low base pressure in the near wake region. This by itself generates three dimensionalities near the free surface. In addition, the free-surface depression behaves as an obstacle with free slip boundary, which accelerates the flow. As a result, there is no distinct trace of the vortex core in the region near the free surface, indicating instantaneous suppression of the vortex shedding or extension of the vortex formation length further downstream. Because of the high free stream velocity, the time scale of the life of the bubbles is reduced, making observation even harder.

A visual comparison of the three cases shows that the intensity of the oblique shedding is increasing as the Re and Fr numbers increase. The boundary conditions imposed by the solid wall (no-slip) and the free surface (free-slip) dictate the character of the shedding in their neighborhood. The asymmetry introduced from the different character of the boundary conditions enhances the three-dimensional effects.

The observations for the zero degrees inclination are mostly valid and for the inclined models cases as well. We will therefore focus the remaining discussion only on additional features and major differences.

The second set of animations (Animation 2) corresponds to the inclination of 30 degrees. The cylinder is inclined away from the flow. For the first case of  $Re=1700$  and  $Fr=0.3$ , (Animations 2-1) vortex shedding occurs almost parallel to the cylinder axis for the major part of the length. However, since the cylinder is inclined and the vortex needs to reconnect normal to the free surface the slope is forced to change and align with the normal direction. This is perhaps the source of discontinuities. Comparison with case 1-1 shows that the effect of the horseshoe vortex extends higher above the floor, affecting the vortex shedding almost up to 5 cylinder diameters from the base. For the case of  $Fr=0.65$ , the existence of a wavy pattern of the vortex axis is observed (Animation 2-2). The third case of  $Fr=1.06$  (Animation 2-3), the size of the free-surface depression in the wake is smaller with respect to the zero degrees inclination, allowing the vortex to reconnect at the free surface. Furthermore, the discontinuities in vortex shedding observed in the previous inclination case are significantly reduced. Instantaneous discontinuities resulted in sharp changes on the inclination but even in such cases, the reconnection occurs perpendicular to the surface. For all the cases of the second set, it can be seen that the vortex shedding process is affected more by the horseshoe vortex, while the influence of the free surface is limited to a few diameters below the interface.

The case of  $-30$  degrees of inclination is presented in the next set of animations (Animation 3). The effect of the boundary conditions is reversed with respect to the previous case and this can be observed for all the  $Fr$  numbers. The region near the base of the cylinder where there is no trace of the vortex core is confined to only one diameter from the solid wall. On the opposite end, the reconnection process affects the change of the slope more significantly, in some instants extending down to the 50% of the span of the cylinder. For a  $Fr=0.3$ , where the intensity of the trace of the core is stronger in comparison with the higher  $Fr$  numbers cases, a change in the phase of the vortex shedding can be clearly observed (Animation 3-1). The intermediate case of  $Fr=0.65$  shows that there is reconnection normal to the free surface,

however the phase differences are intensified (Animation 3-2). Further increase of the Fr number shows a formation of a stronger free-surface depression in the wake, where it seems that the reconnection is suppressed by the free-surface depression since there is no distinct trace of the vortex in the vicinity of the free surface (Animation 3-3).

Summarizing the observation for three Re and Fr numbers and for three inclinations we see that the increase of the Froude numbers results in a suppression of the vortex shedding near the free surface. This suppression is significantly stronger as we change the inclination from +30 to 0 to -30. The existence of braid vortices and cells of shedding causing phase differences is noted for all cases. Finally, the primary -spanwise- vortex in all cases reconnects normal to the free surface with the exception of the cases where a strong free-surface depression suppresses the vortex shedding, or the process of reconnection itself. These observations are not adequately documented from individual snapshots of the flow field, a complete understanding can only be achieved by observing the entire animated sequence.

### **Particle Flow Visualizations**

Particle flow visualizations were performed for all cases of free stream velocity and model inclination. From these animations, general characteristics of the vortex shedding process can be extracted. The location of the vortex formation length can be also determined. Instantaneous snapshots of the flow field do not provide an accurate way to quantify the vortex formation length. However, comparison of the cases clearly identifies the differences.

The first Animation 4-1 corresponds to  $Fr=0.3$   $Re=1700$  and zero degrees of inclination. A clear vortex-shedding pattern is observed with an approximate vortex formation length about 2.4 diameters downstream, which is also valid for the  $Fr=0.65$  case (Animation 4-2). However, for the last case of zero degrees of inclination there is no evidence of vortex shedding, proving that the process is suppressed, even at one diameter below the free surface. Steady wave patterns are generated in the wake near the free surface, forming a Kelvin wedge (Lighthill, 1978) with an angle that varies from 45-55 degrees (Animation 4-3).

In the case of 30 degrees, we note the opposite behavior. For  $Fr=0.3$ , the vortex formation has extended to about three diameters, forming a larger near wake region (Animation 5-1). The increase of the  $Re$  number to 3700 changes again the position of the formation to 2.5 diameters (Animation 5-2). For such a moderate increase in the  $Re$  number, is a significant change therefore it can be only attributed to the effect of the free surface which is most considerable in this case – as it was shown from the hydrogen bubbles. For the last case of  $Re=6000$  the vortex formation location is approximately the same but there is no visible wave pattern. This is because the wedge angle increased, so it was outside from the field of view. The reflection from the free-surface depression is noticeable for all  $Re$  numbers which shows that the size of the free-surface depression increases for the  $-30$  inclination.

Finally, for the case of  $-30$  degrees inclination, the vortex formation position has shifted upstream to approximately one diameter for  $Re=1700$  (Animation 6-1), and 1.5 for  $Re=3700$  (Animation 6-2). A major difference between the 0 degrees inclination and this case is for  $Re=6000$ , where for the latter case we see a vortex shedding pattern and an approximate vortex formation point at 1.5 diameters downstream (Animation 6-3). There is also steady wave pattern reflected from the free surface with an approximate wedge angle of about 40-45 degrees. Therefore, the particle flow visualizations show that the inclination affects the vortex formation length. The influence of the free surface is noticeable for the higher  $Re$  numbers only. In the case of 0 degrees and  $Re=6000$  vortex shedding is entirely suppressed. However, both positive and negative inclinations counteract the effect of the free surface and allow the vortices to be formed.

### **LDV Frequency Measurements**

LDV measurements were performed in order to quantify the variation of the vortex shedding frequency with respect to the elevation, as well as the effect of the model inclination. In the next set of figures, the power spectrum estimation is represented in the form of contours of the amplitude with respect to the reduced frequency (Strouhal number,  $St=fD/U$ ) and the elevation. The logarithm of the power is shown, with the very small values that are attributed to

noise removed. For the power spectrum estimation, the Welch periodogram was employed with the Bartlett windowing function, 75% overlapping and step frequency of 0.5Hz.

In figure-2 the frequency for the case of  $\alpha=0$  degrees inclination and  $Fr=0.3$  is presented. A very distinct dominant frequency at approximately  $St=0.25$  is present, however the amplitude is reduced as the elevation increases suggesting that the free surface affects the strength of the vortices shed but not the frequency. In the region of the horseshoe vortex, a relatively broad band of frequencies extending almost five diameters from the base is present. The region between five and 15 diameters is less effected from the asymmetry of the boundary conditions showing distinct peak values of the vortex shedding frequency, but also significant modes at lower frequencies ( $St=0.05$ ). The increase of the  $Fr$  number to 0.65 (figure-3) demonstrates similar trends. The most dominant mode is in the neighborhood of  $St=0.25$ . The effect of the horseshow vortex is more dominant and a wide range of frequencies is covering that region, extending up to approximately five to six diameters from the base. The energy content has increased by half a decade and as we approach the free surface, the  $St$  number shifts to 0.27. Within three diameters beneath the free surface, the energy content decreases, suggesting fading of the vortex shedding process. For the last  $Fr$  number, 1.06, a very clear shedding frequency at  $St=0.27$  exists throughout the span, but in the region located approximately five diameters below the free surface vanishes providing further evidence of the vortex shedding suppression observed from the flow visualization. For both cases, the horseshow vortex affects the flow three to four diameters from the base of the cylinder, generating a broadband spectrum surrounding the dominant shedding frequency.

The inclination of 30 degrees is considered in the next set of figures. For the  $Fr=0.3$  (figure 5) case the picture is drastically different. The effect of the boundary conditions is inverted. The horseshoe vortex region contains less energy, and the vicinity of the free surface is characterized by a dominant vortex shedding process. The prevailing  $St$  number is around 0.24, however the peaks are broader than the ones observed for the 0 degrees inclination. The increase of the  $Fr=0.65$  results in power spectrum distribution with many dominant frequencies, varying between 0.06 and 0.26. Overall, there is energy content with almost one decade difference in the

*Chapter 4: The Effect of Free-Surface and Inclination on the Vortex Shedding Behind  
Circular Cylinders*

---

power, in frequencies up to  $St=0.75$ . This proves that the positive inclination results in a more turbulent flow field, but enhances the vortex shedding process. The final Fr number for this inclination,  $Fr=1.06$  (figure 7) presents a very distinct peak frequency at 0.22 that spans with very small variation the whole length of the cylinder. About eight diameters from the bottom the energy content is reduced. Generally, the 30 degrees inclination demonstrated a reduction of the energy contained in the area of the horseshoe vortex.

Finally, the power spectra for the case of  $-30$  degrees inclination are presented. The case of  $Fr=0.3$  (figure 8) demonstrates the wider range of frequencies. However, the shedding activity is mostly organized around  $St=0.24$ . An interesting feature is that even though vortex shedding is not suppressed near the free surface, the amplitude is drastically reduced. Furthermore, in the cases of higher Fr numbers we observe a shift towards lower frequencies (figures 9 and 10). Reduction of the vortex shedding frequency indicates increase in the effective width and length of the wake. Even more interesting is the case of  $Fr=0.65$ , where at 16 diameters the effect of the free surface becomes dominant, generating a very broad spectrum with high energy content while for  $Fr=1.06$ , the free surface influences approximately 3 diameters below, shifting the dominant frequencies to values as low as  $St=0.04$ .

The measured St numbers range primarily from 0.22 to 0.27. Equation (2) proposed by Williamson (1998) for the St-Re relation for higher Re numbers: predicts a St number of 0.246, 0.255, 0.258 respectively for the three Re numbers based on the free stream. This shows a very good agreement with the experimental measurements presented.

$$St = 0.2731 - \frac{1.1129}{\sqrt{Re}} + \frac{0.4821}{Re} \quad (2)$$

Summarizing the observations resulting from the LDV frequency measurements, we conclude that the effect of the free surface changes depending on the inclination and the Fr number, ranging from one to five diameters below the free surface. In addition, the no-slip boundary condition at the solid wall affects the flow but in reverse manner. Namely, when the horseshoe vortex is predominant, the free surface influence is reduced and vice versa. The

prevailing mode of vortex shedding is approximately at  $St=0.25$ . However, depending on the yaw angle and the free-stream velocity, values as low as 0.04 and as high as 0.3 were measured. The broadening of the spectrum indicates a more turbulent wake. Finally and more importantly, in the vicinity of the free surface, significant decrease in the energy content of the shed vortices was observed and on occasion, complete suppression of the vortex shedding.

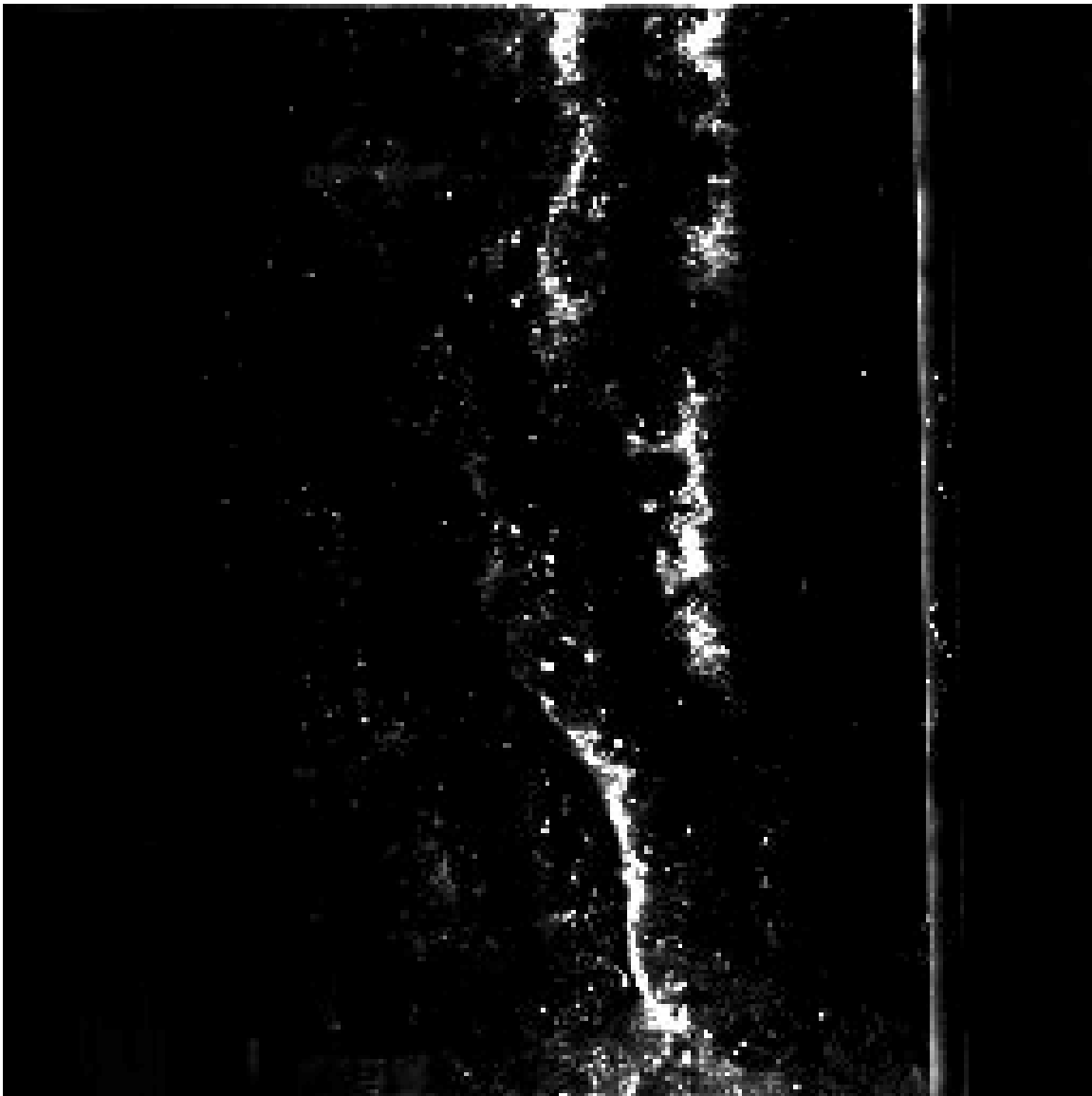
## **Conclusions**

Analysis of hydrogen bubble flow visualization images with frequencies calculated from LDV velocity measurements indicates that free surface affects the vortex shedding more than two to three cylinder diameters below the free surface. Discontinuities of the vortex axis, and cells of shedding which induce a phase difference in the vortex shedding mechanism were visually observed. The streamwise vortical structures form along the primary vortex axis. Furthermore, from particle visualizations, evidence of vortex suppression is found in the region near the free surface for the case of the highest Reynolds/Froude number and zero inclination. This is confirmed from LDV frequency measurements. Moreover, the positive inclination counteracts the effects of the free surface recovering the vortex shedding process, while for the negative inclination, the neighborhood of the free surface presents a turbulent broad spectrum. The introduction of asymmetry in the boundary condition of the wake of a circular cylinder in combination with a yaw angle with respect to the free stream generates a three-dimensional flow field with character strongly dependent on the respective values of the  $Re$  and  $Fr$  numbers as well as the position in the spanwise direction.

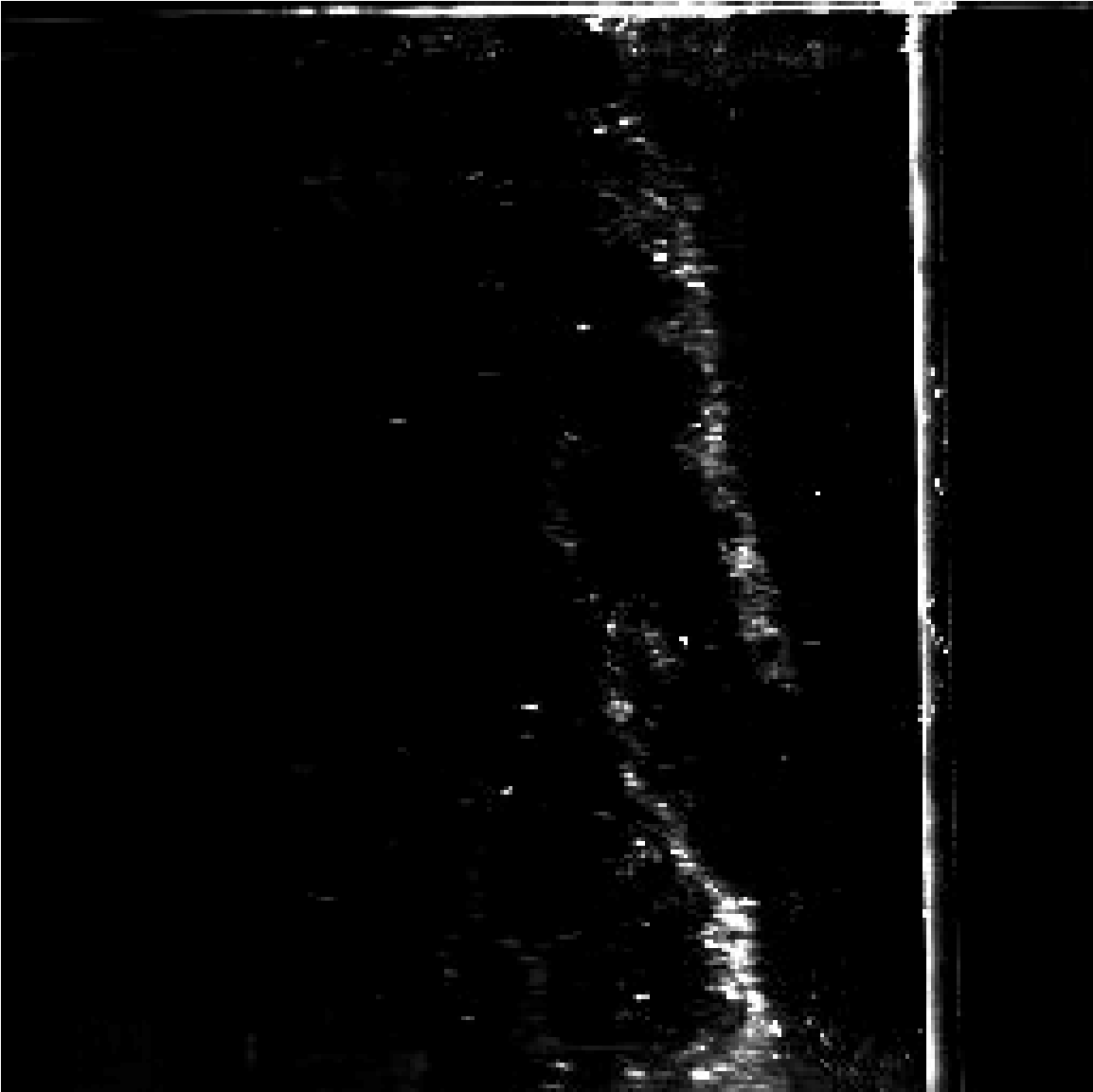
*Chapter 4: The Effect of Free-Surface and Inclination on the Vortex Shedding Behind  
Circular Cylinders*

---

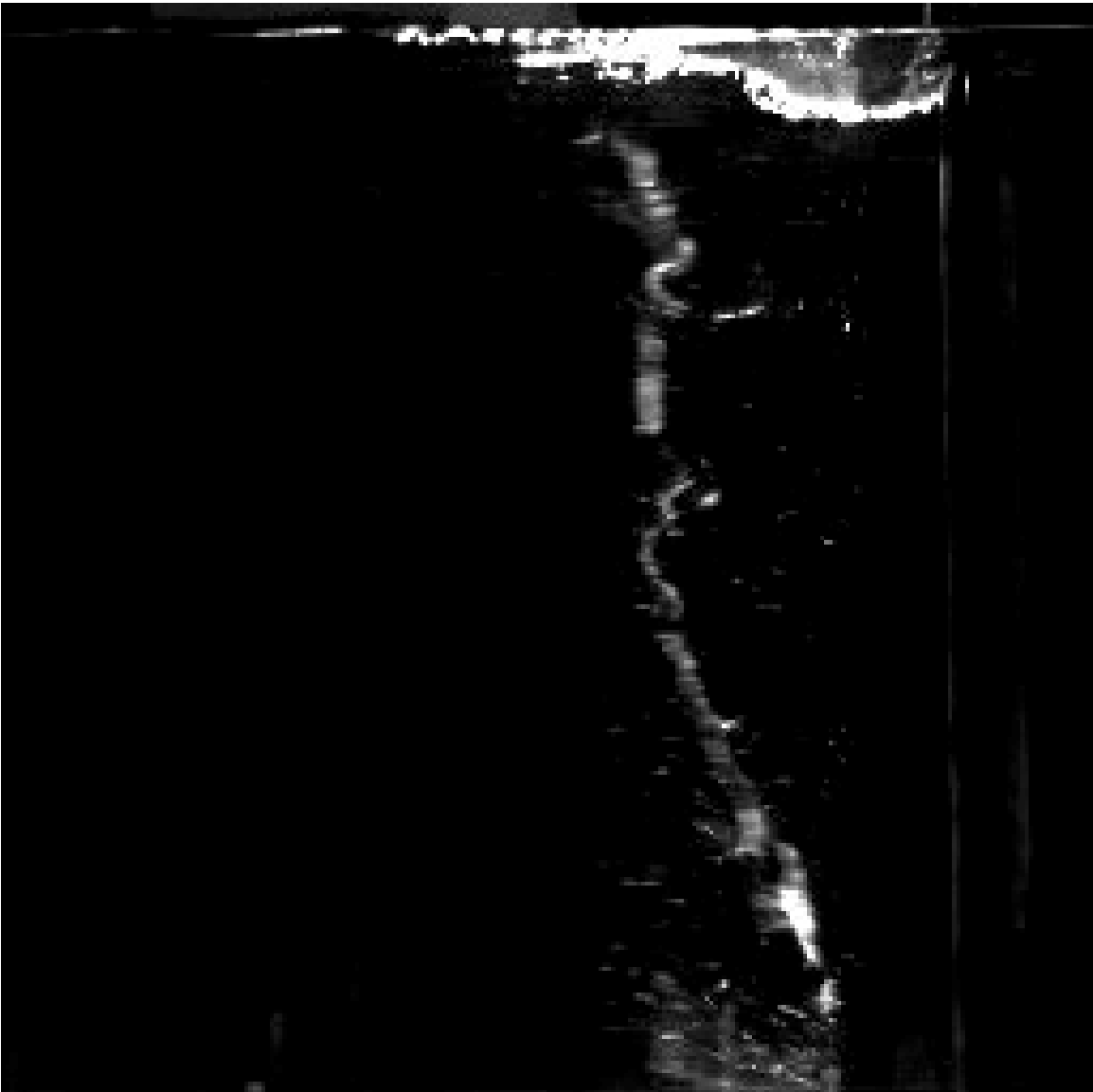
*Animation 8:* First, set of hydrogen bubbles animation for cylinder inclination 0 degrees.



*Animation 8-1:* Hydrogen Bubbles. Inclination  $\alpha=0$  degrees,  $Re=1700$ ,  $Fr=0.3$



*Animation 8-2:* Hydrogen Bubbles. Inclination  $\alpha=0$  degrees,  $Re=3700$ ,  $Fr=0.65$

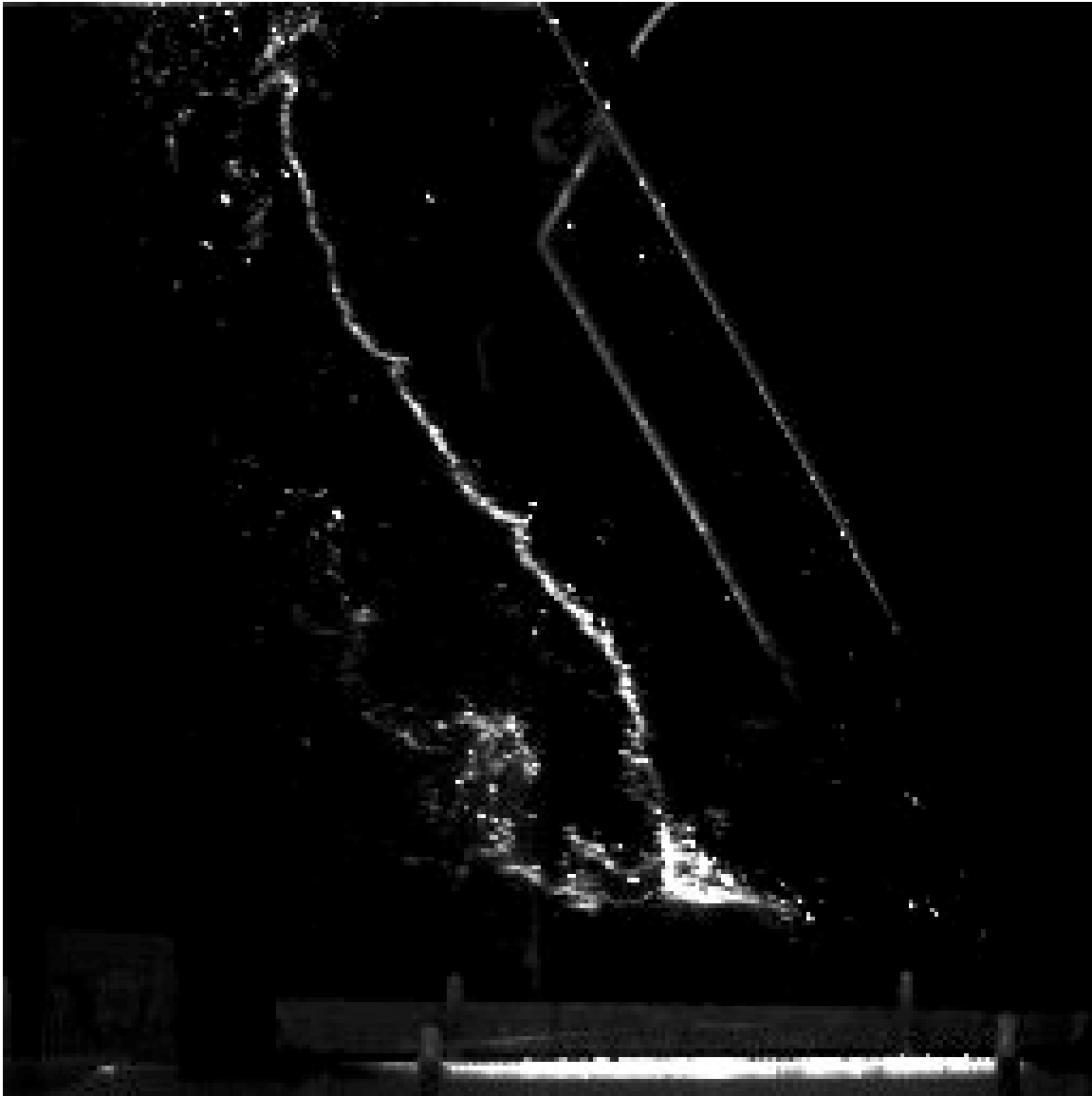


*Animation 8-3:* Hydrogen Bubbles. Inclination  $\alpha=0$  degrees,  $Re=6000$ ,  $Fr=1.06$

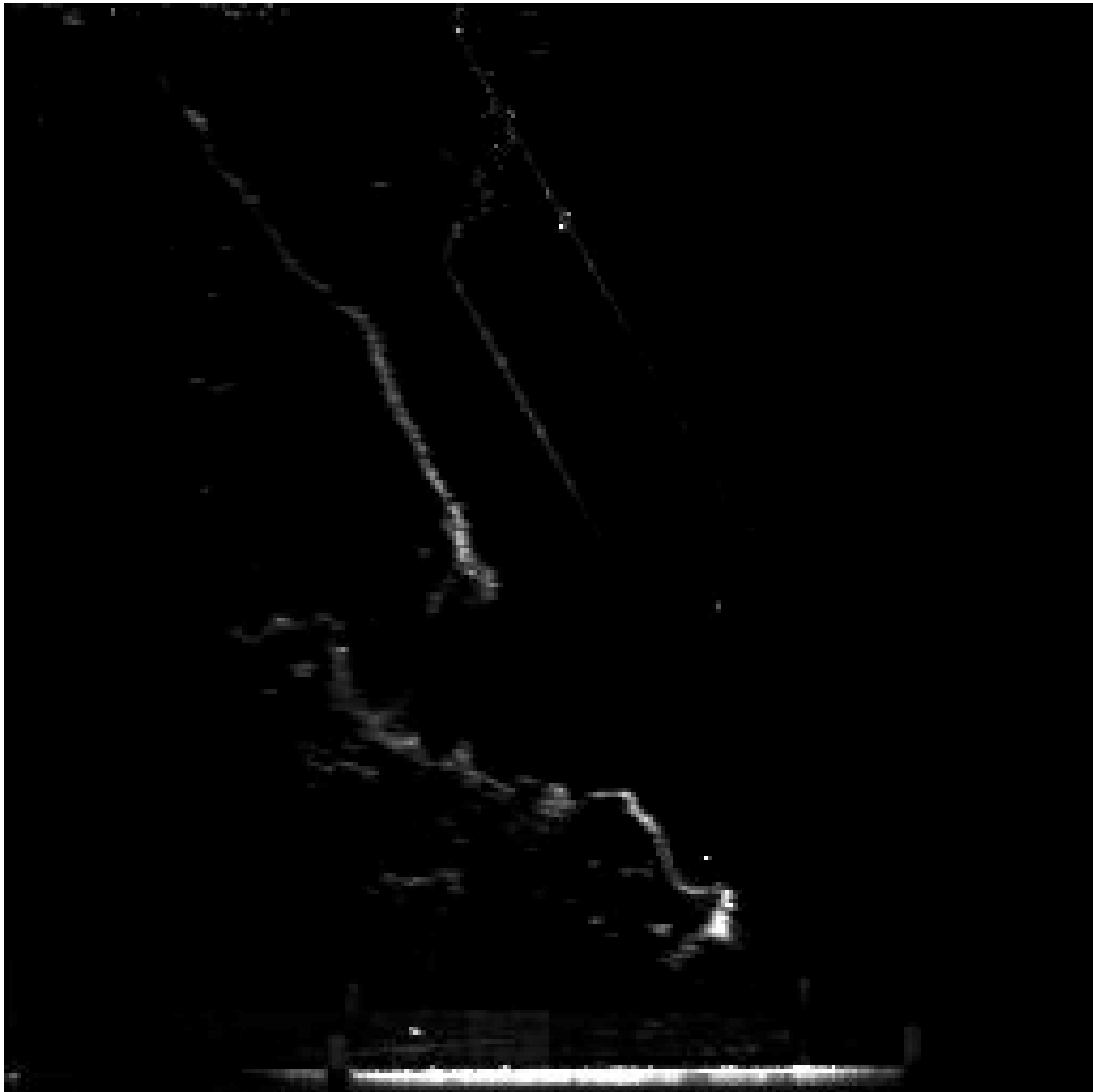
*Chapter 4: The Effect of Free-Surface and Inclination on the Vortex Shedding Behind  
Circular Cylinders*

---

*Animation 9:* Second set of hydrogen bubbles animation for cylinder inclination 30 degrees



*Animation 9-1:* Hydrogen Bubbles. Inclination  $\alpha=30$  deg.,  $Re=1700$ ,  $Fr=0.3$



*Animation 9-2:* Hydrogen Bubbles. Inclination  $\alpha=30$  deg.,  $Re=3700$ ,  $Fr=0.65$

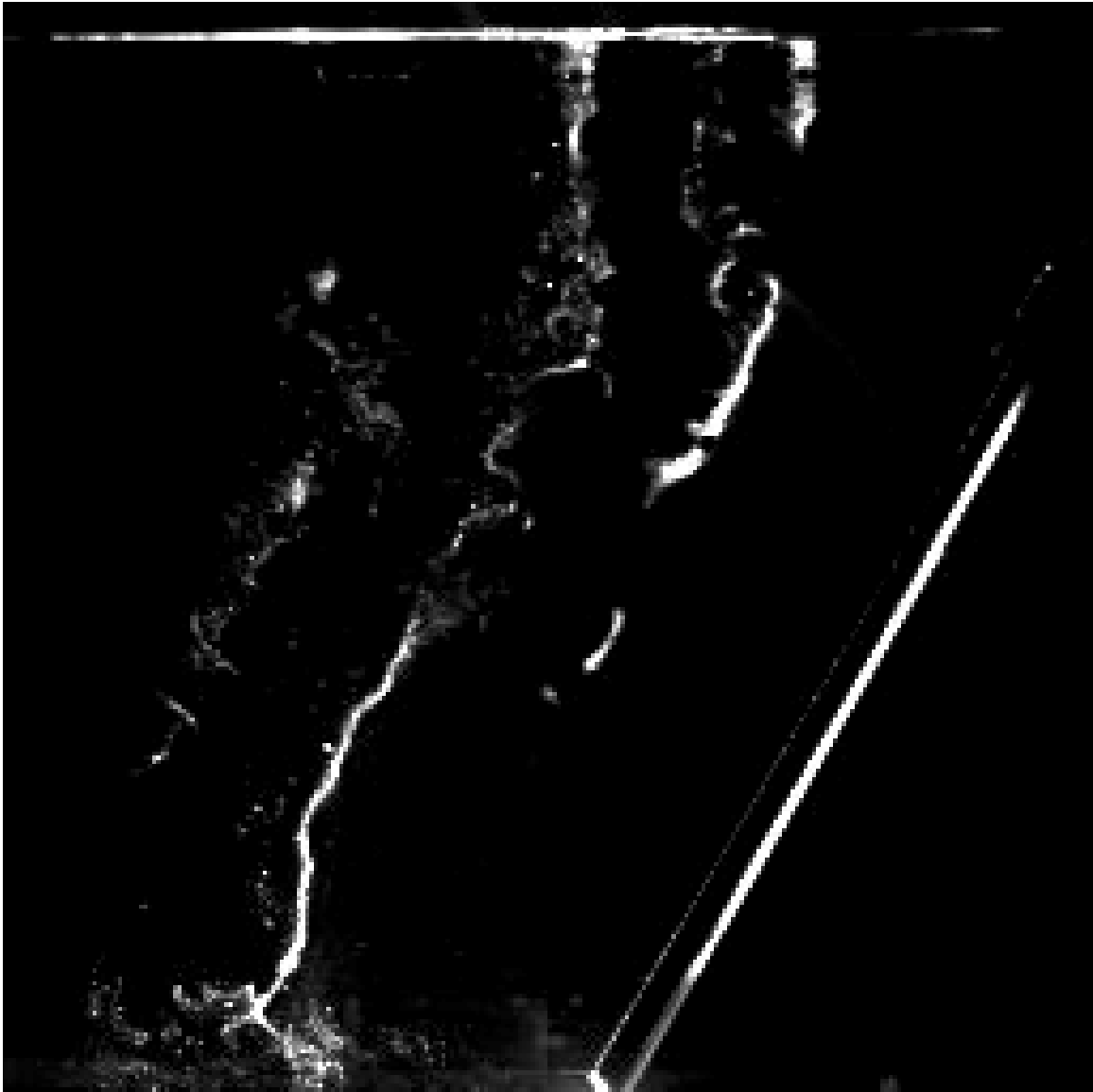


*Animation 9-3:* Hydrogen Bubbles. Inclination  $\alpha=30$  deg.,  $Re=6000$ ,  $Fr=1.06$

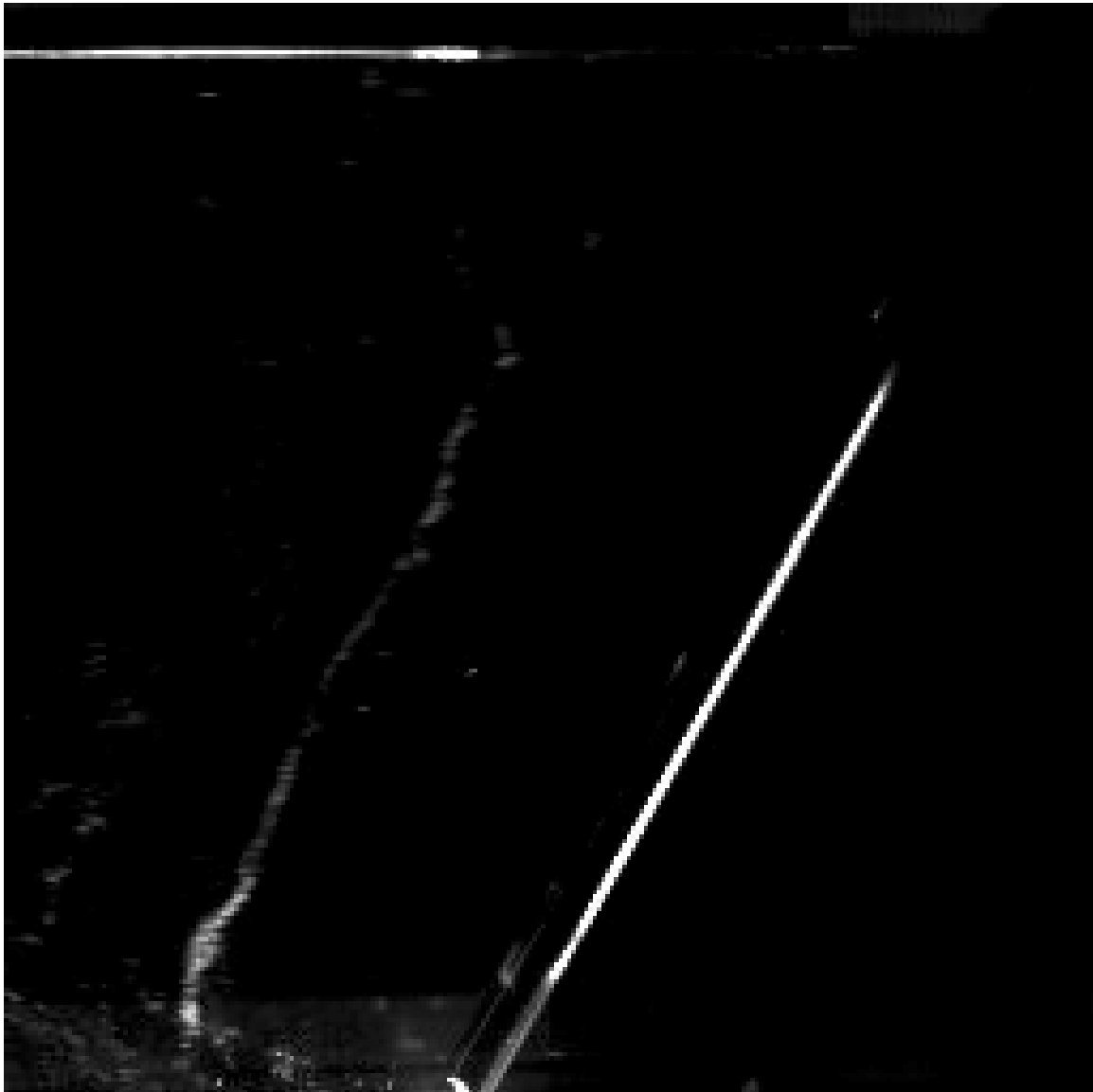
*Chapter 4: The Effect of Free-Surface and Inclination on the Vortex Shedding Behind  
Circular Cylinders*

---

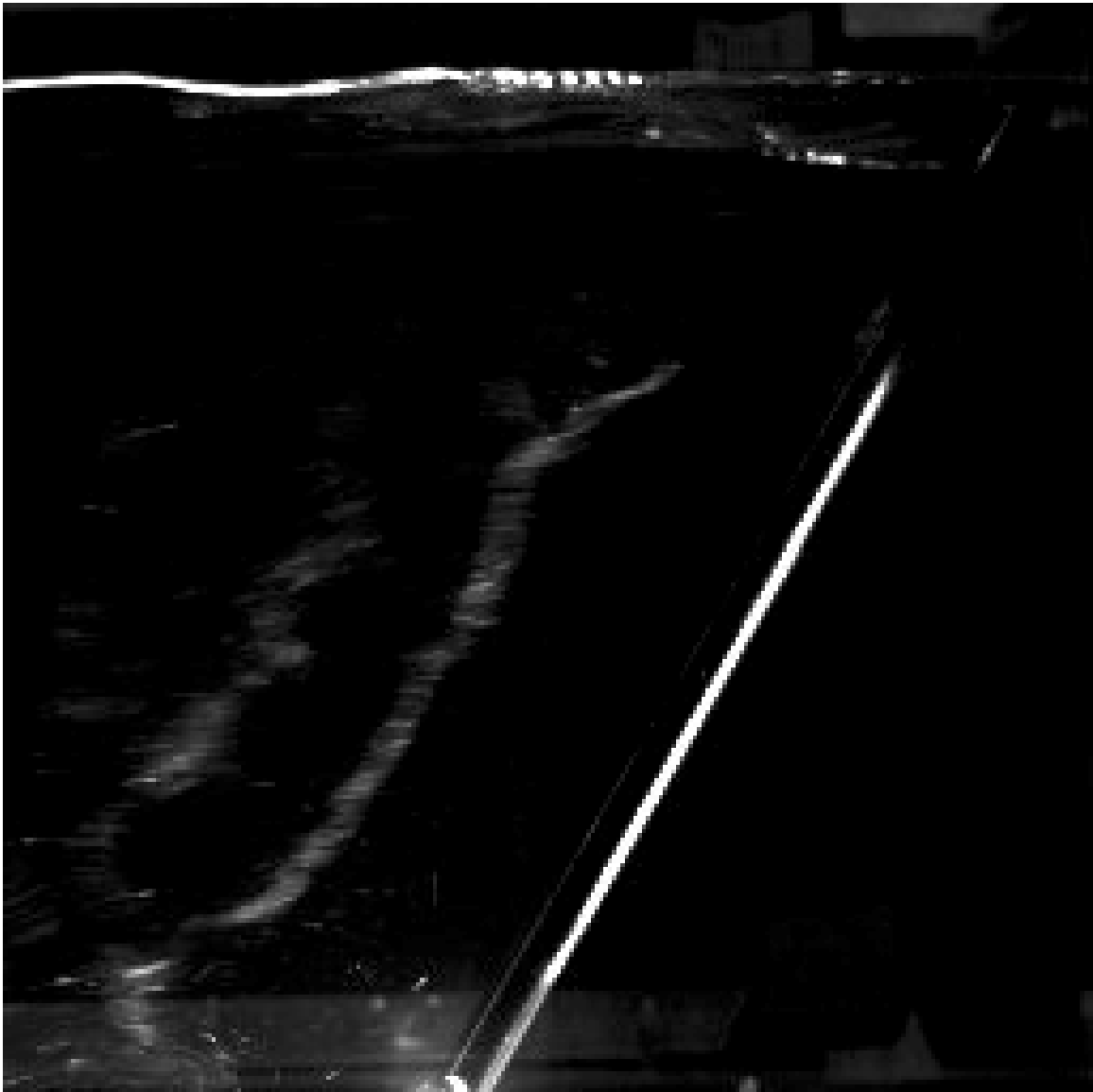
*Animation 10:* Third set of hydrogen bubbles animation for cylinder inclination -30 degrees



*Animation 10-1:* Hydrogen Bubbles. Inclination  $\alpha = -30$  deg.,  $Re = 1700$ ,  $Fr = 0.3$

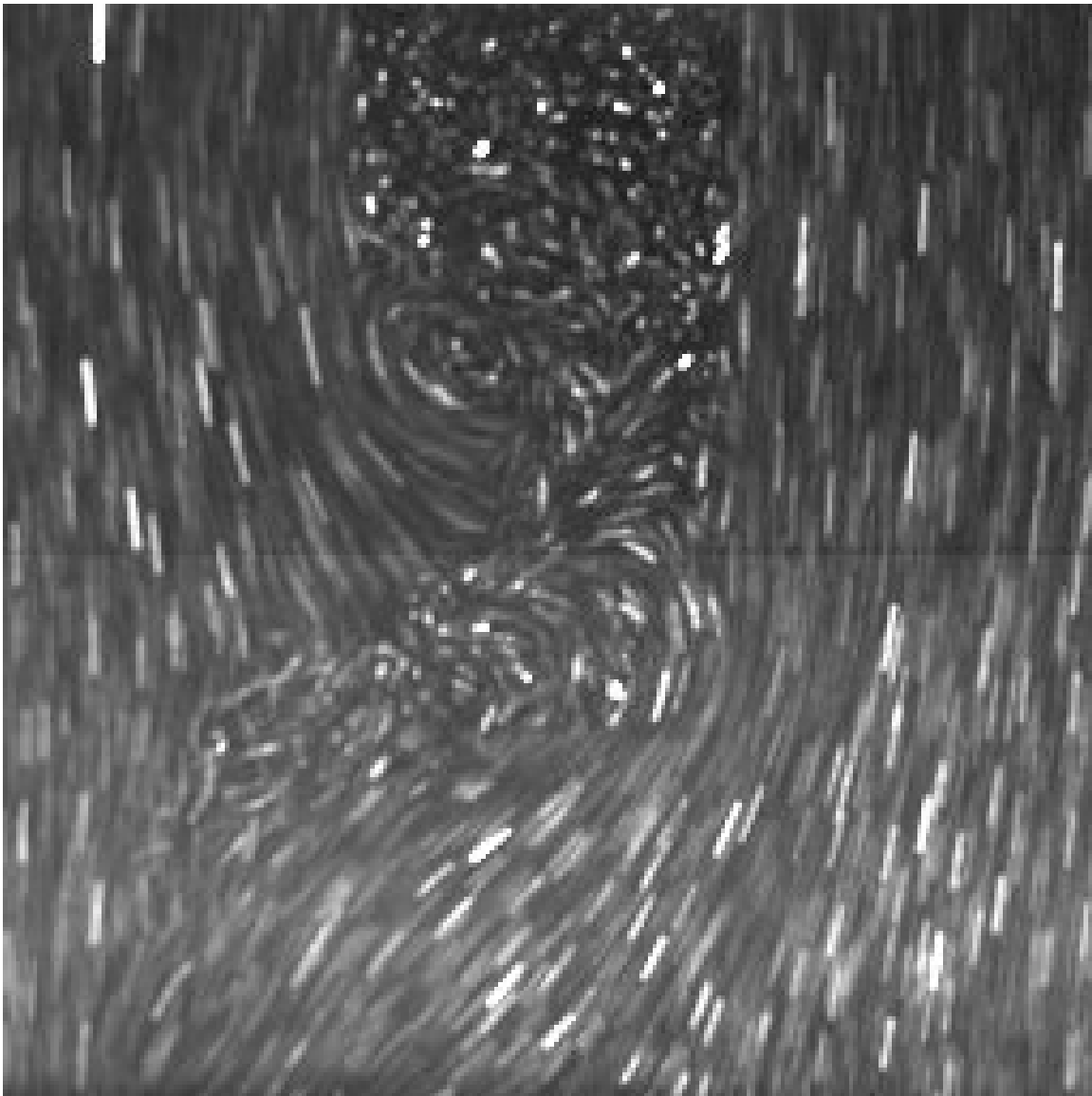


*Animation 10-2:* Hydrogen Bubbles. Inclination  $\alpha = -30$  deg.,  $Re = 3700$ ,  $Fr = 0.65$

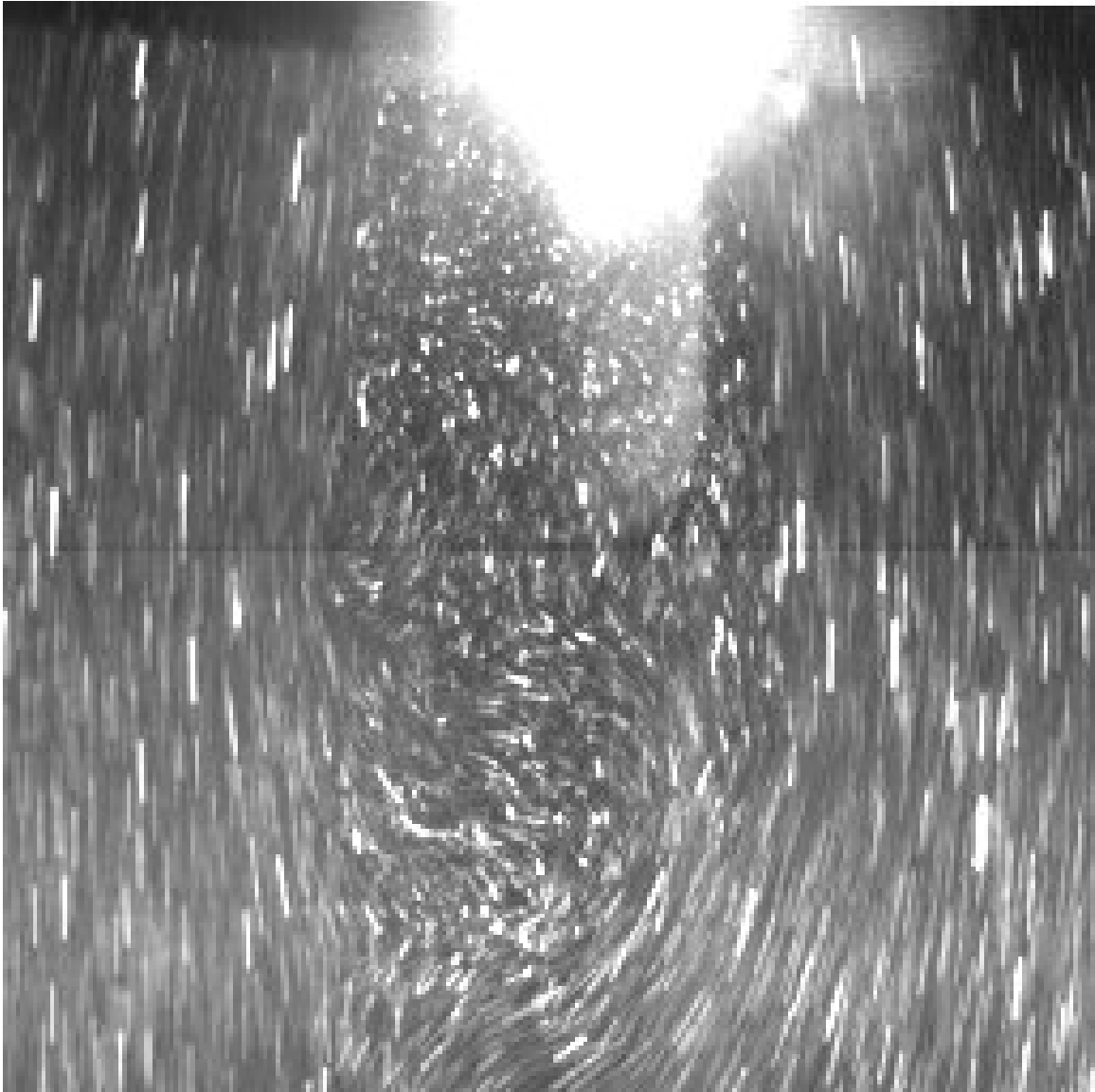


*Animation 10-3:* Hydrogen Bubbles. Inclination  $\alpha = -30$  deg.,  $Re = 6000$ ,  $Fr = 1.06$

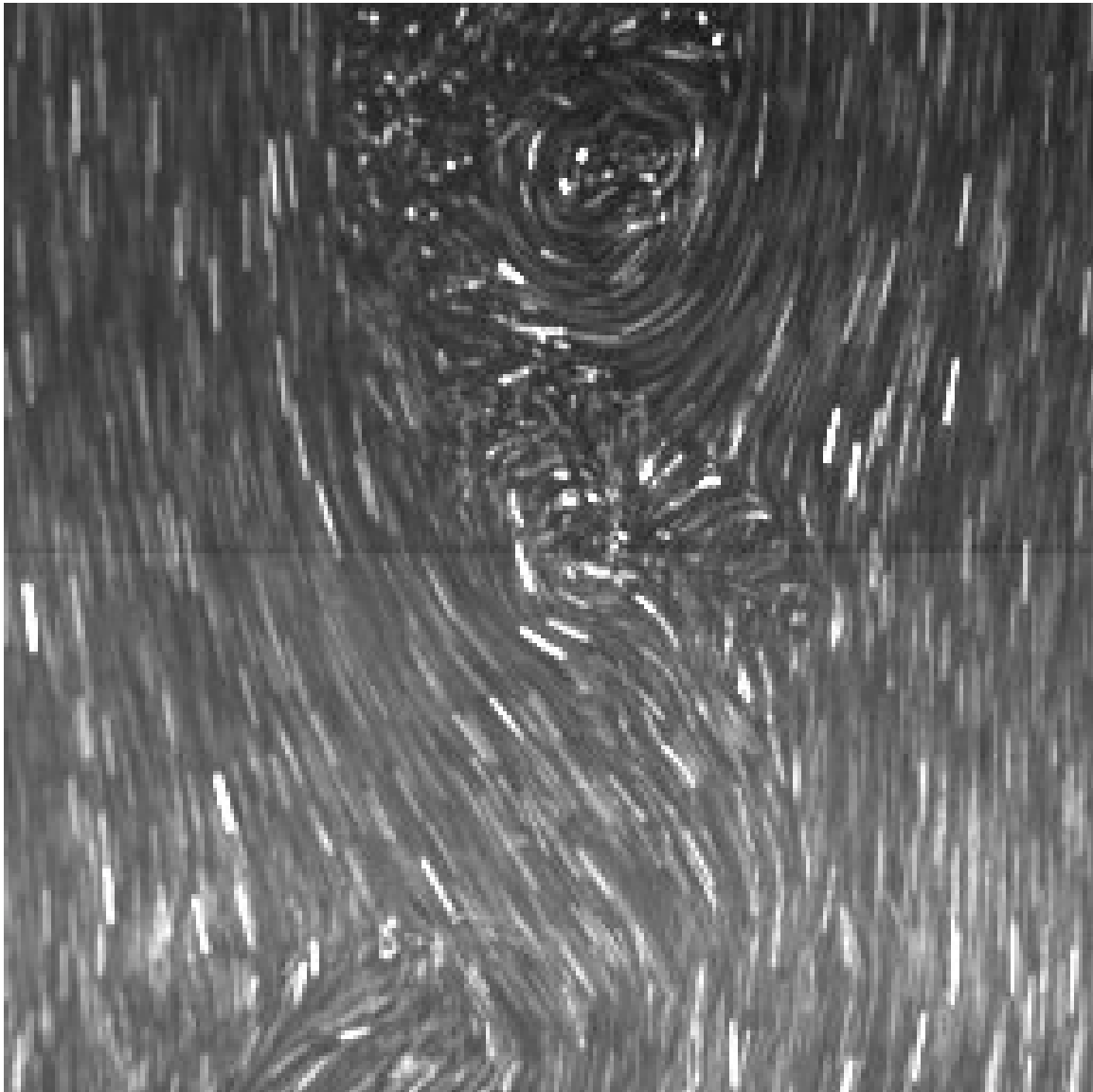
*Animation 11:* First set of particle flow visualization for  $Re=1700$ .



*Animation 11-1:* Particle Visualization. Inclination  $\alpha=0$  degrees,  $Re=1700$ ,  $Fr=0.3$



*Animation 11-2:* Particle Visualization. Inclination  $\alpha=30$  degrees,  $Re=1700$ ,  $Fr=0.3$

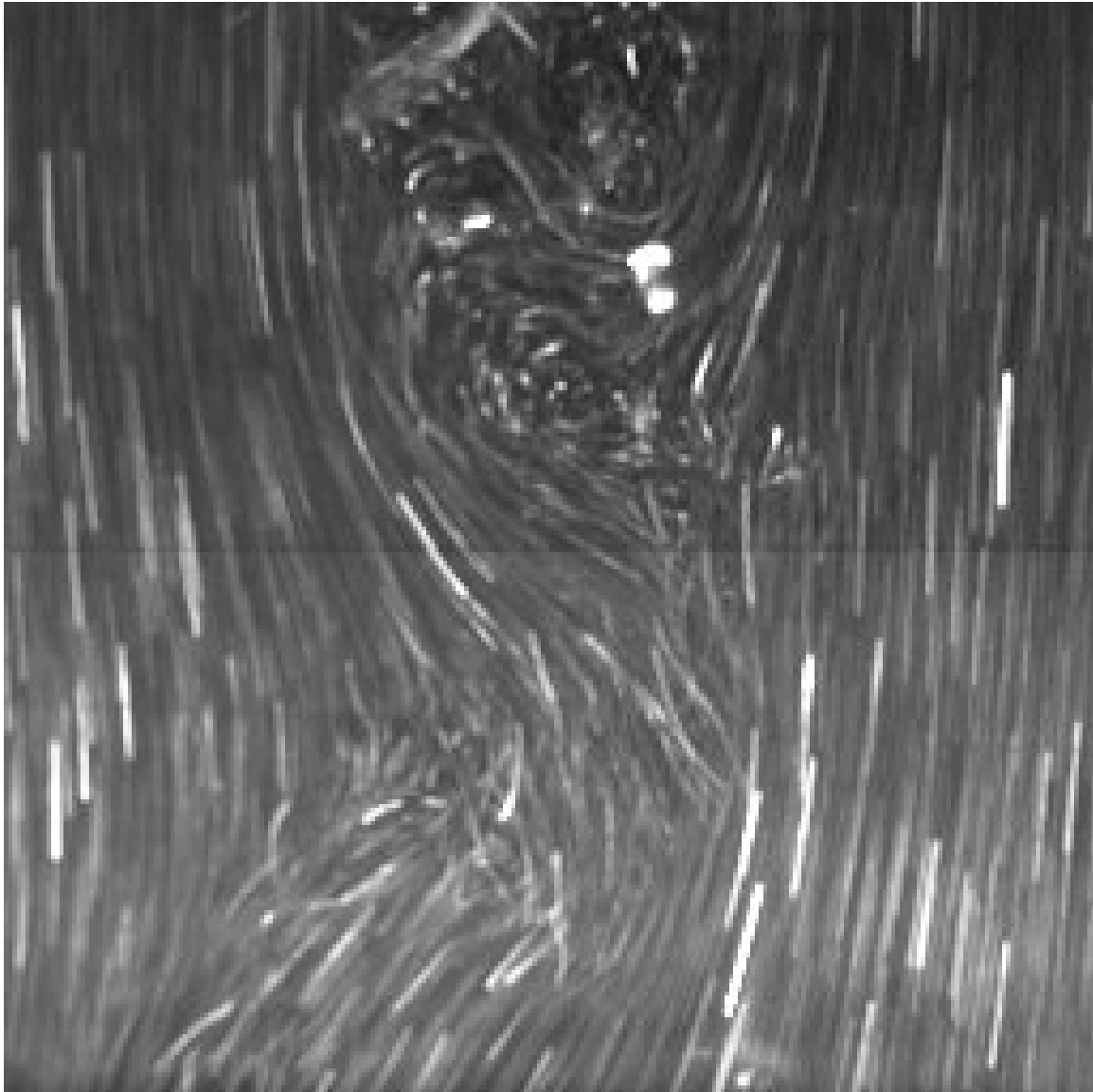


*Animation 11-3:* Particle Visualization. Inclination  $\alpha = -30$  degrees,  $Re = 1700$ ,  $Fr = 0.3$

*Chapter 4: The Effect of Free-Surface and Inclination on the Vortex Shedding Behind  
Circular Cylinders*

---

*Animation 12:* Second set of particle flow visualization for  $Re=3700$ .



*Animation 12-1:* Particle Visualization. Inclination  $\alpha=0$  degrees,  $Re=3700$ ,  $Fr=0.65$



*Animation 12-2:* Particle Visualization. Inclination  $\alpha=30$  degrees,  $Re=3700$ ,  $Fr=0.65$



*Animation 12-3:* Particle Visualization. Inclination  $\alpha = -30$  degrees,  $Re = 3700$ ,  $Fr = 0.65$

*Chapter 4: The Effect of Free-Surface and Inclination on the Vortex Shedding Behind  
Circular Cylinders*

---

*Animation 13:* Third set of particle flow visualization for  $Re=6000$



*Animation 13-1:* Particle Visualization. Inclination  $\alpha=0$  degrees,  $Re=6000$ ,  $Fr=1.06$



*Animation 13-2:* Particle Visualization. Inclination  $\alpha=30$  degrees,  $Re=6000$ ,  $Fr=1.06$



*Animation 13-3:* Particle Visualization. Inclination  $\alpha = -30$  degrees,  $Re = 6000$ ,  $Fr = 1.06$

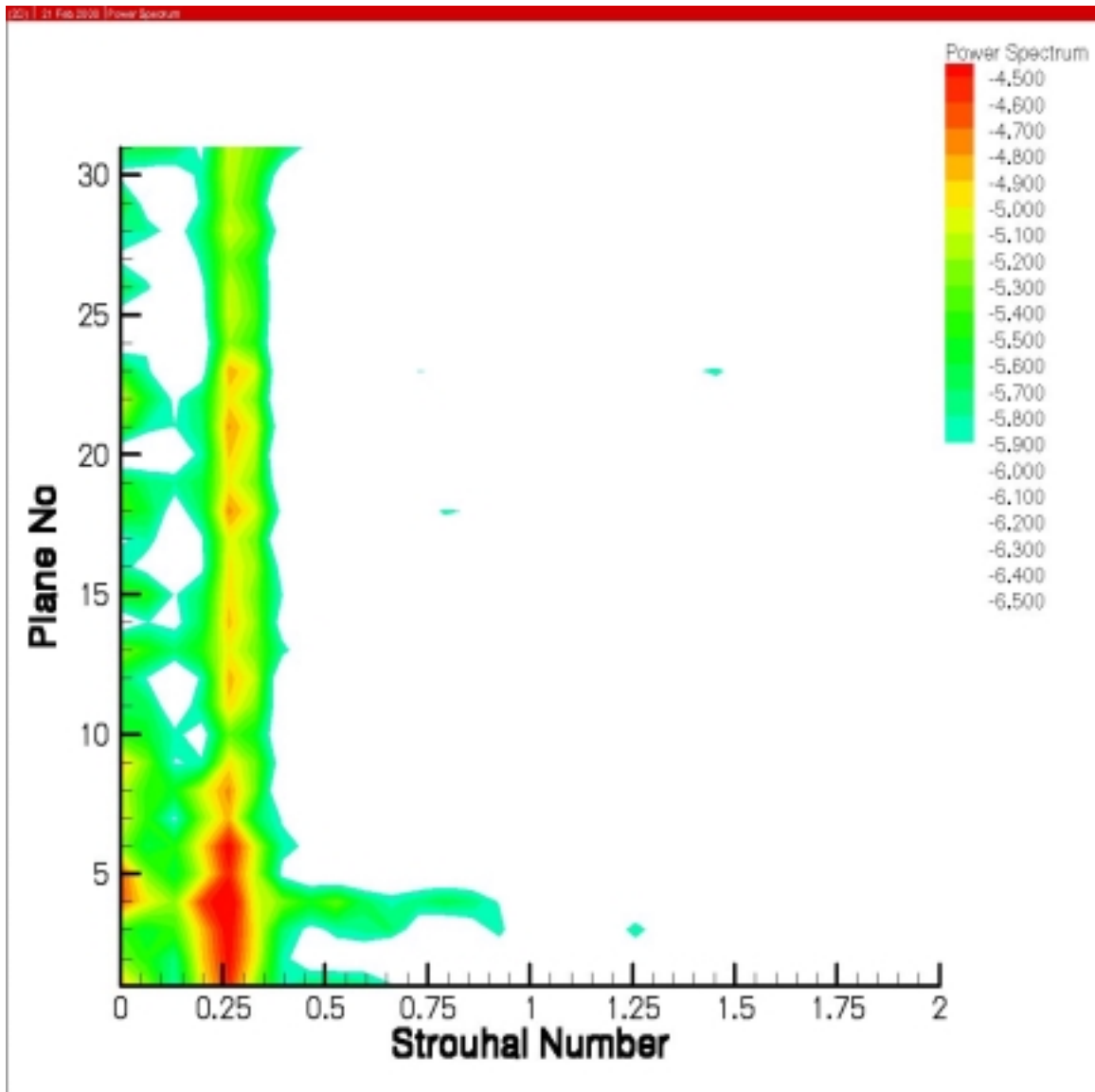


*Figure 2:* Power Spectra contours as a function of the elevation. Inclination  $\alpha=0$  degrees,  $Re=1700$ .

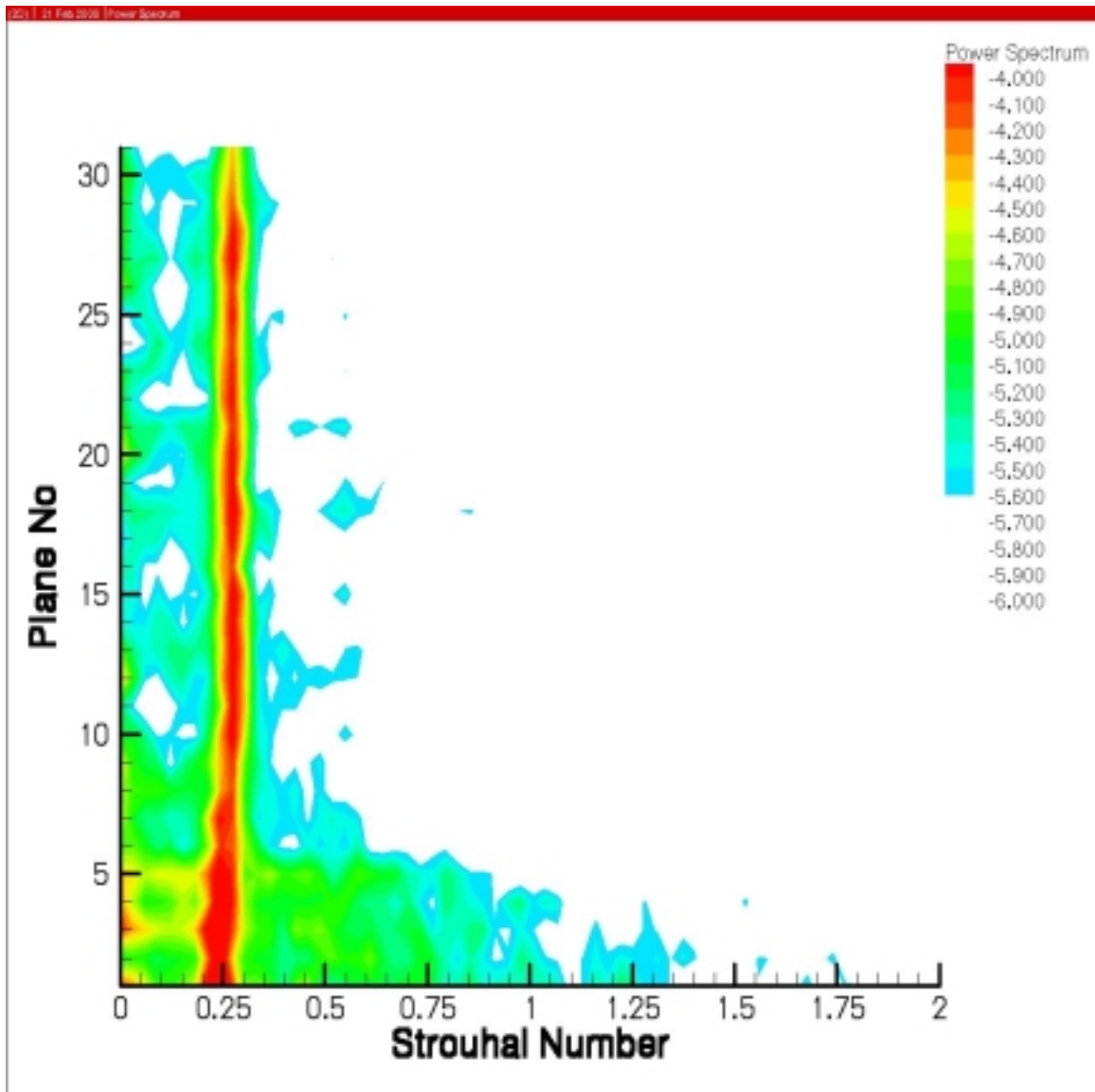


*Figure 3:* Power Spectra contours as a function of the elevation. Inclination  $\alpha=0$  degrees,  $Re=3700$ .

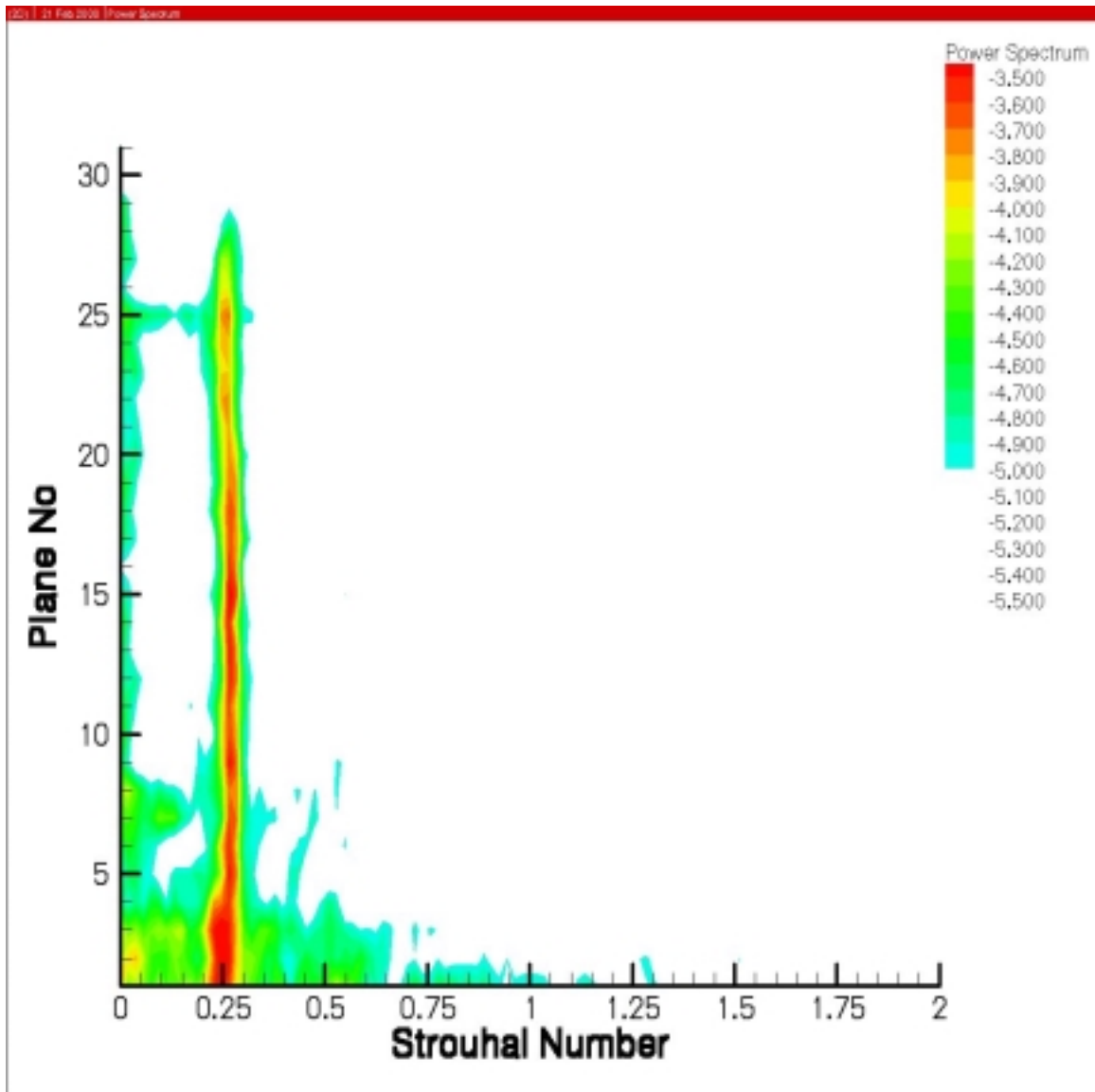


*Figure 4:* Power Spectra contours as a function of the elevation. Inclination  $\alpha=0$  degrees,  $Re=6000$ .

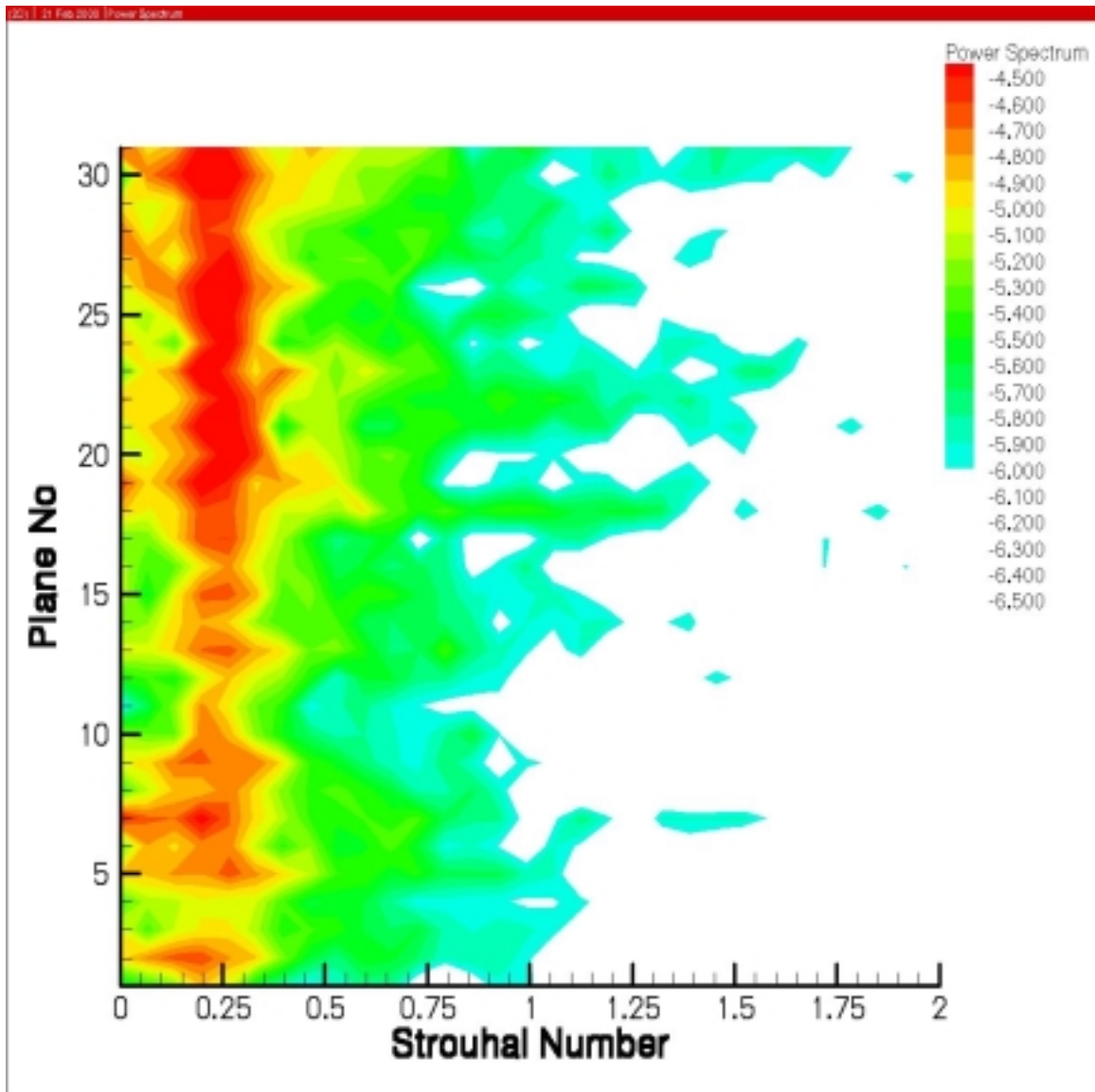


**Figure 5:** Power Spectra contours as a function of the elevation. Inclination  $\alpha=30$  degrees,  $Re=1700$ .

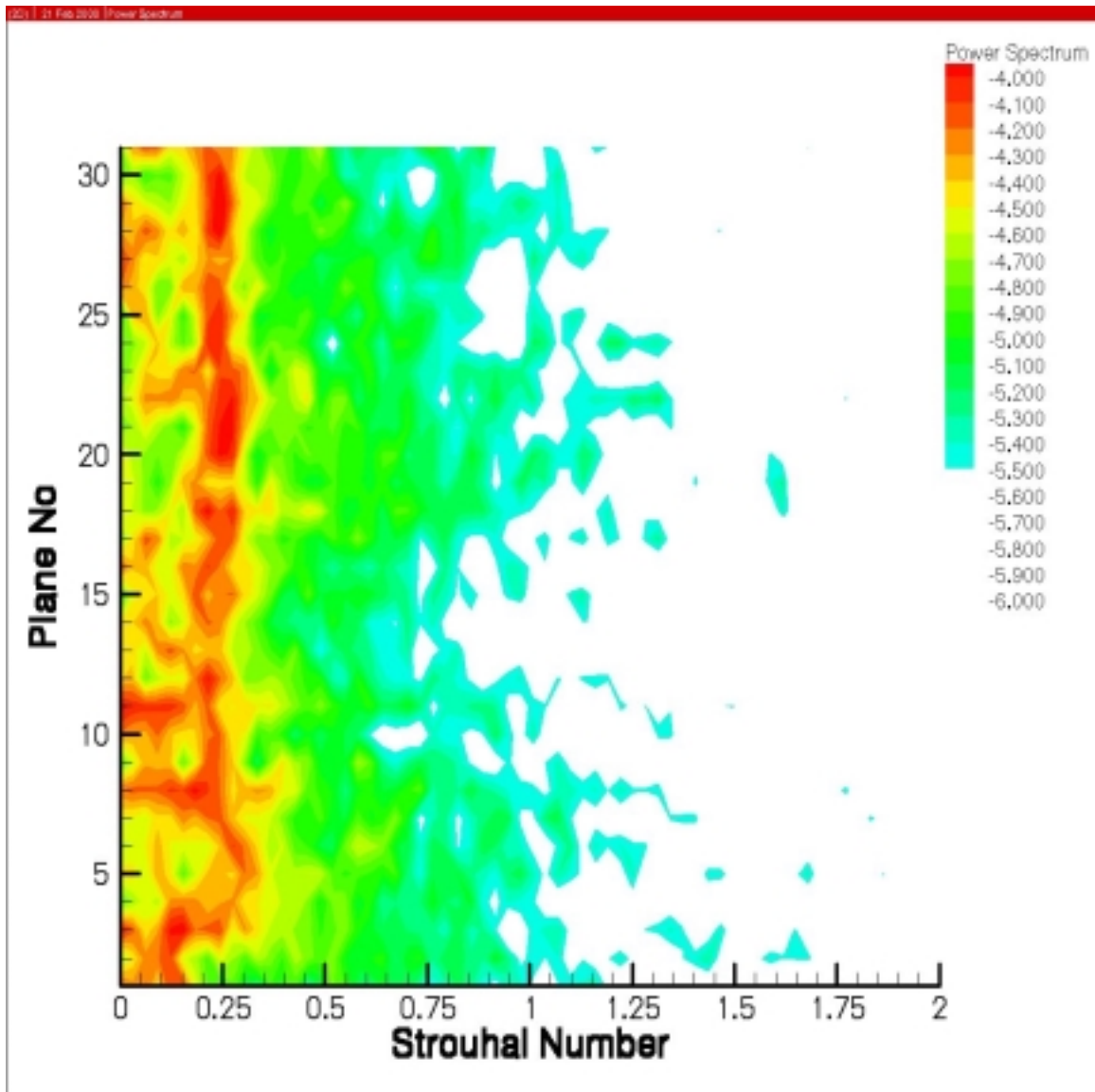


**Figure 6:** Power Spectra contours as a function of the elevation. Inclination  $\alpha=30$  degrees,  $Re=3700$ .

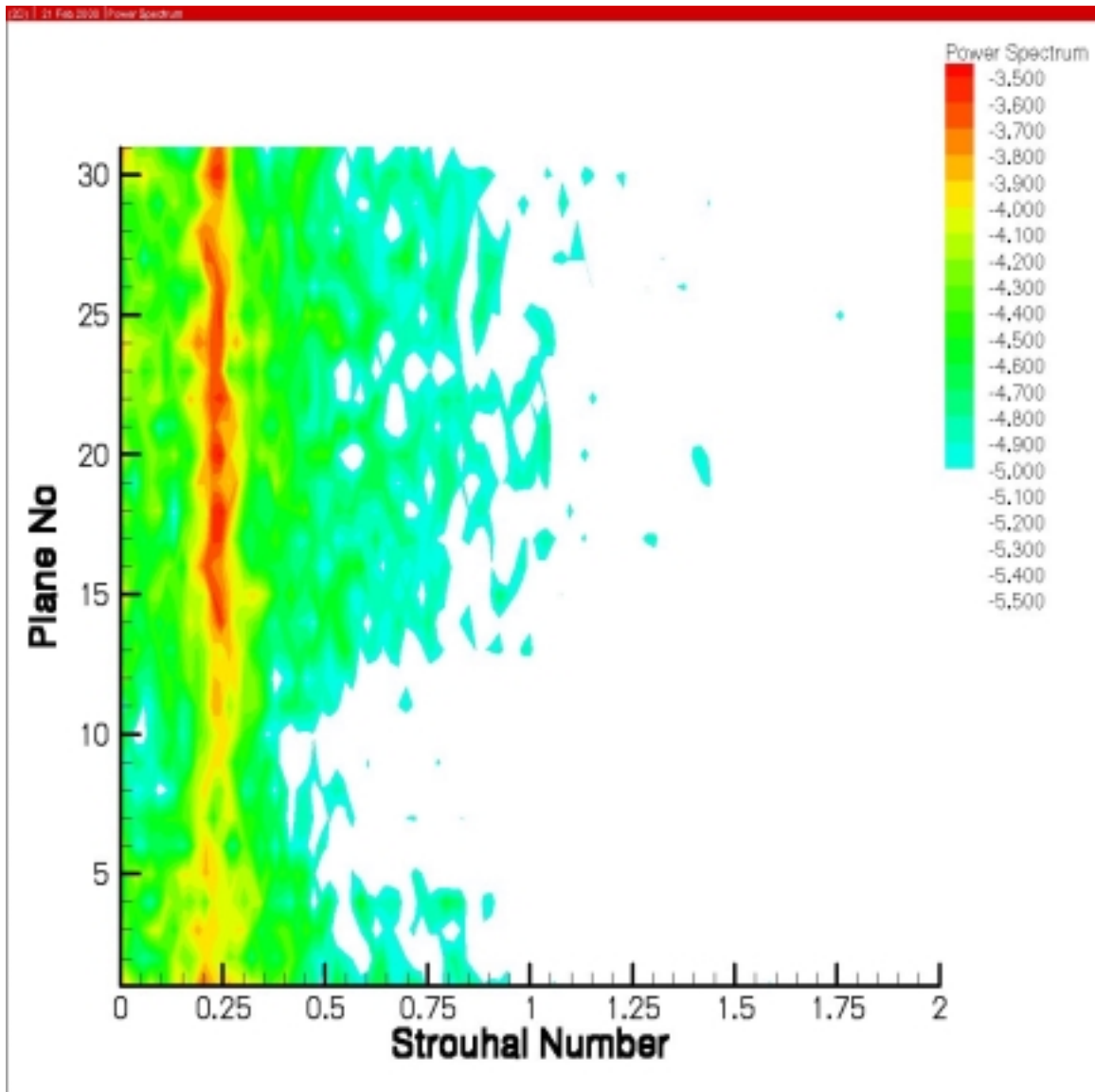


**Figure 7:** Power Spectra contours as a function of the elevation. Inclination  $\alpha=30$  degrees,  $Re=6000$ .

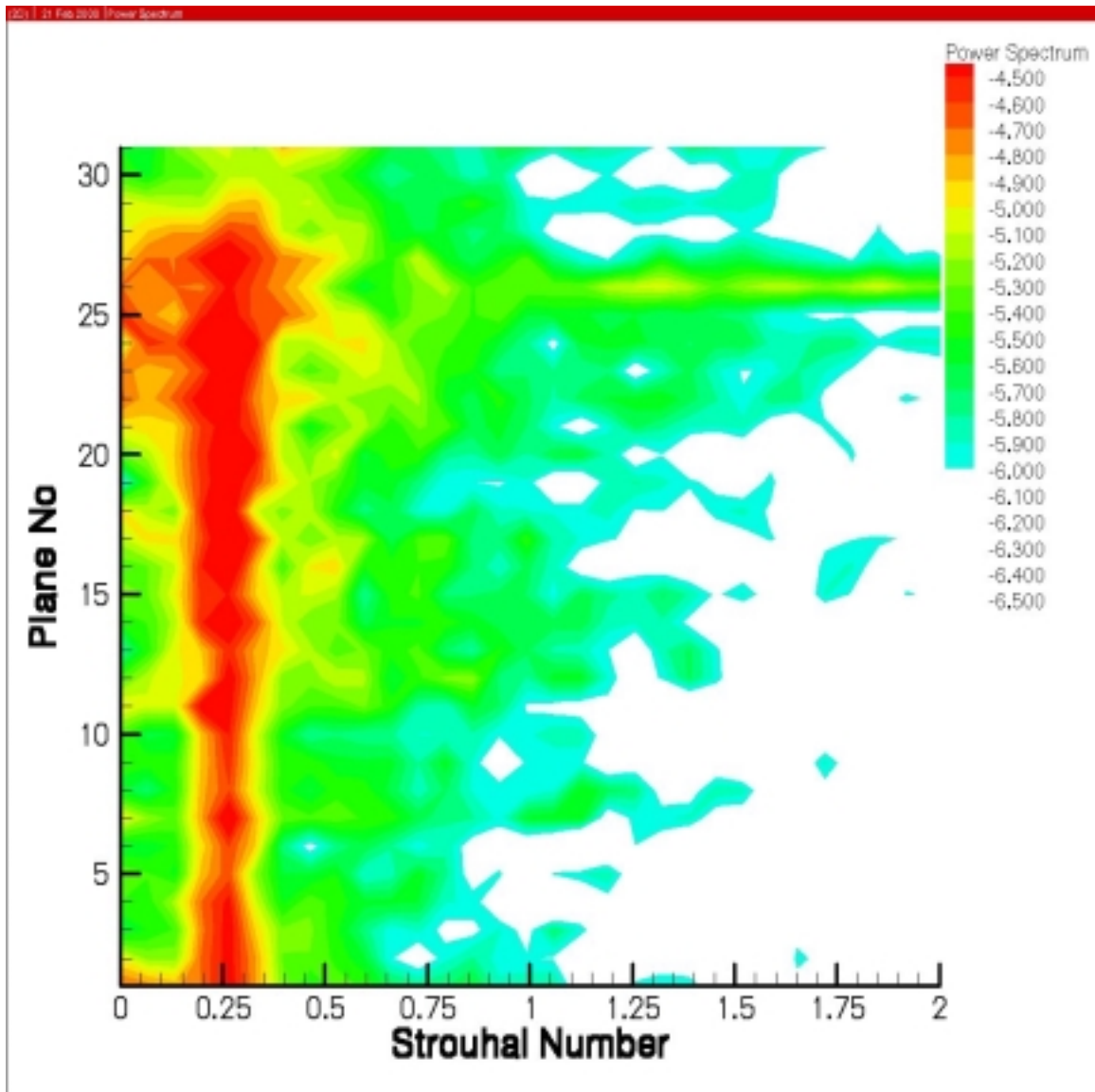


**Figure 8:** Power Spectra contours as a function of the elevation. Inclination  $\alpha = -30$  deg.,  
 $Re = 1700$ .

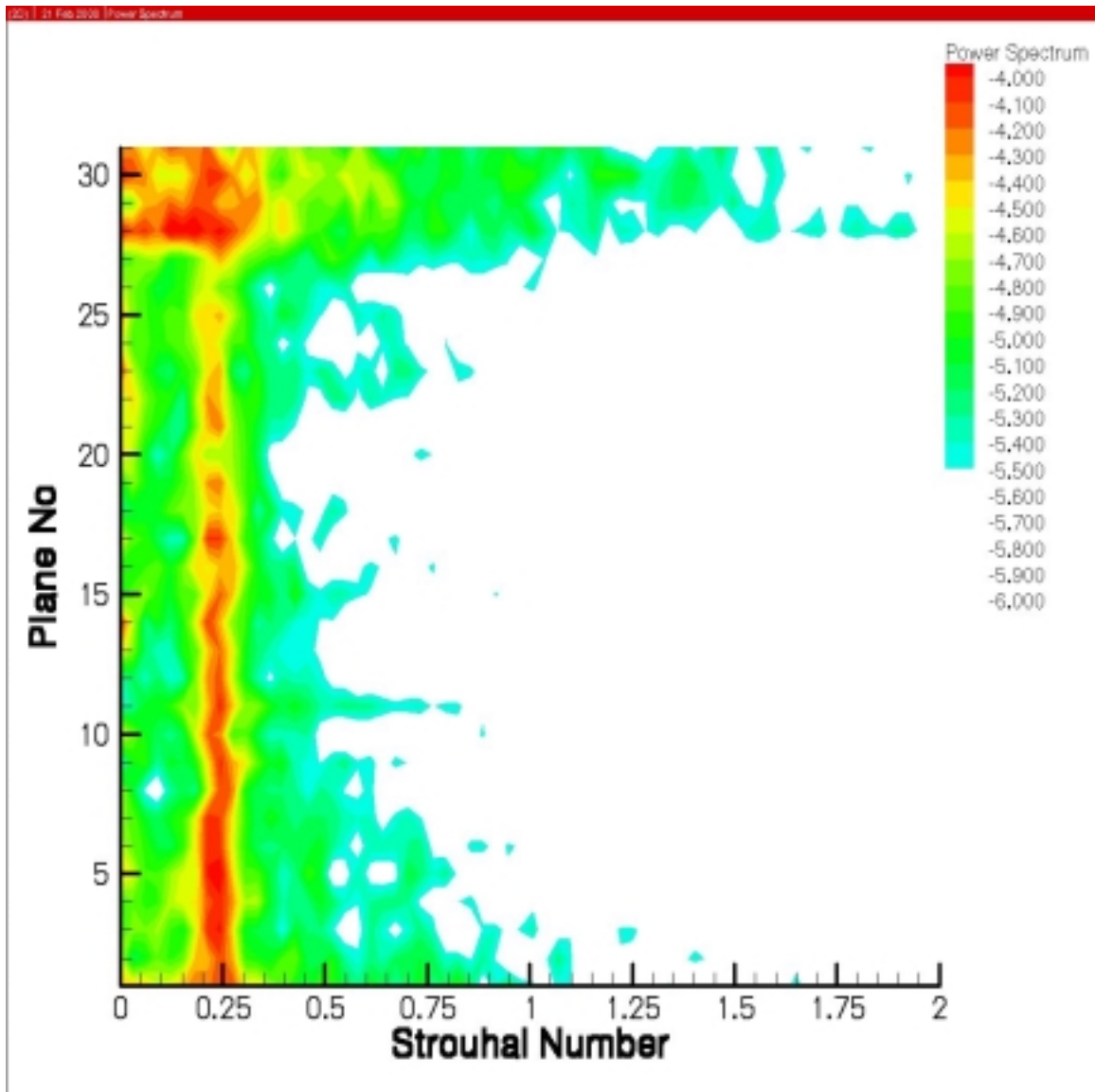


**Figure 9:** Power Spectra contours as a function of the elevation. Inclination  $\alpha = -30$  deg.,  
 $Re = 3700$ .

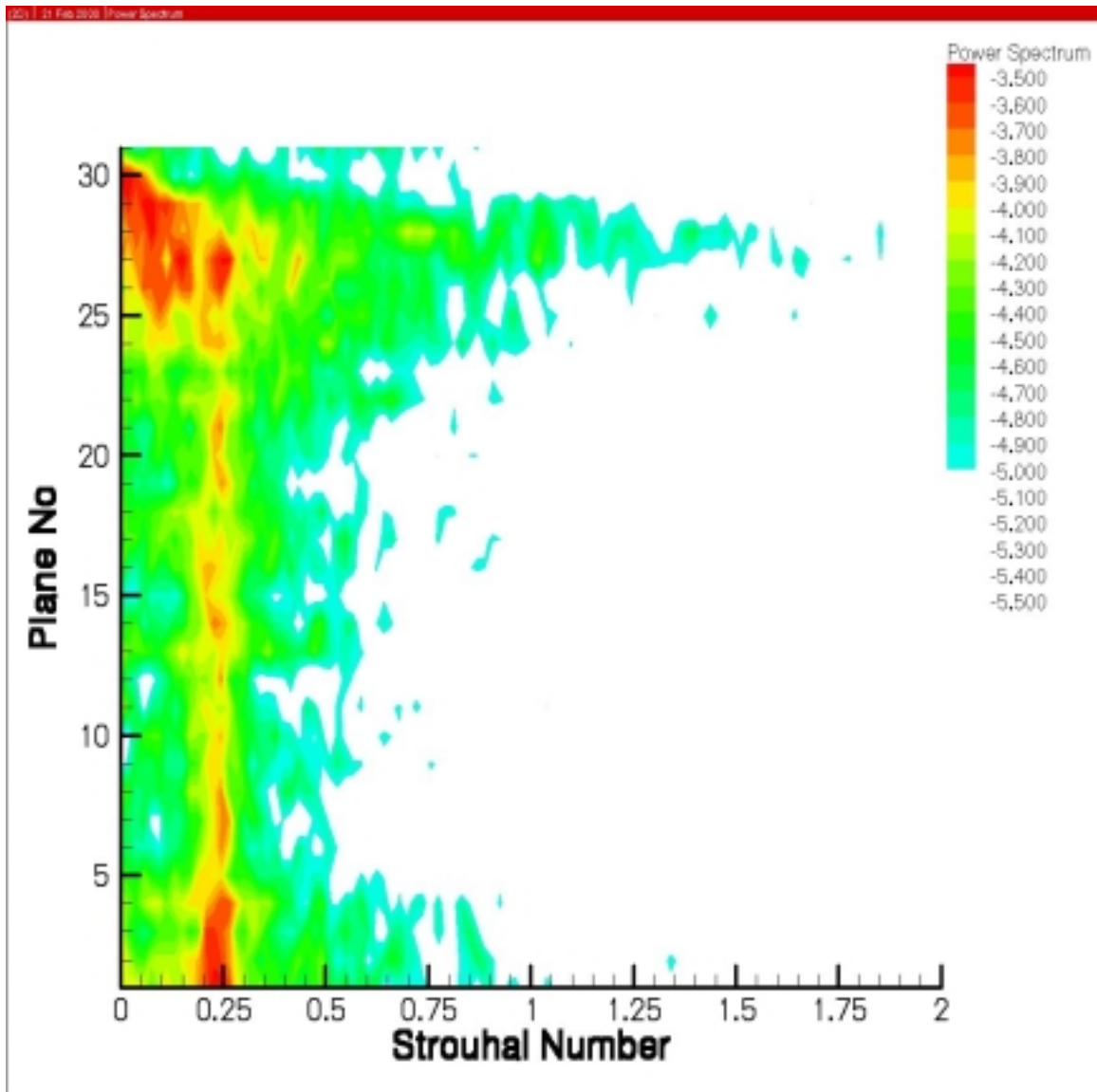


*Figure 10:* Power Spectra contours as a function of the elevation. Inclination  $\alpha = -30$  deg.,  
 $Re = 6000$

## **Chapter 5**

# **Flow characteristics of the separated region over a surface mounted prism**

### **Introduction**

Flows around surface-mounted, three-dimensional bluff-bodies represent intrinsically complicated flow fields characterized by separation, vortex formation and reattachment regions. Determining the flow parameters in these regions is important to many engineering applications ranging from the assessment of aerodynamic loads on structures, vehicle aerodynamics, dust and pollution transport as well as sediment deposition around buildings. In other applications, the character of the flow in the separation and reattachment regions is directly related to drag and heat transfer coefficients. Vortex shedding from sharp edges is also of practical interest in marine hydrodynamics when investigating flow fields around bilge corners, chines and keels. Furthermore, the three-dimensional separation from sharp corners and edges constitutes a fundamental problem of fluid mechanics. For the majority of engineering applications, time-averaged and mean flow properties provide sufficient information. However, time varying characteristics are of great importance because of the strongly unsteady behavior of such flow

fields. Understanding structural vibrations resulting from aerodynamic loads and distributions of pressure fluctuations is critical for a wide variety of engineering applications.

The case of a two-dimensional separated shear layer has been studied extensively by many researchers (e.g. Hillier and Cherry, 1981; Cherry et al., 1984; Saathoff and Melbourn, 1997). Detailed experiments by Kiya and Sasaki, 1983, 1985; Gartshore, 1984; Castro and Haque, 1988 documented the reattachment length and its dependence on Reynolds number and free-stream turbulence. Cherry et al., 1984 demonstrated the existence of low frequency variations in the flow, which were attributed to oscillations of the shear layer. Schofield and Logan (1990) performed comparisons between two-dimensional and three-dimensional separation were carried out by. In addition, for a three dimensional separation Martinuzzi and Tropea (1993) investigated the effect of the aspect ratio of the prism.

Despite the overwhelming amount of data for the case of two-dimensional separation there are noticeably fewer investigations for the case of a three-dimensional surface mounted obstacle. Of these, the majority is limited to qualitative results or point measurements. This is due to the fact that the case of three-dimensional separation presents far more complicated flow structures, which deprive us from a detailed quantitative documentation of the flow field. All earlier studies are attacking the problem of a three dimensional obstacle which forms an open separation region with no reattachment. Once reattachment occurs the separation region is no longer open to the base pressure. This fact alternates drastically the character of the flow. Furthermore, from the engineering perspective, this type of model simulates flows over low-rise structures more realistically.

The majority of the preceding investigations were employing flow visualizations (e.g. smoke, oil) to reveal the topology and the structure of the flow, however only qualitative information could be obtained this way. Quantitative measurements were carried by the means of pressure transducers hot-wire anemometry or Laser Doppler Velocimetry. Although, sufficient frequency resolution can be achieved by using these methods, the global character of the flow and velocity and vorticity distributions cannot be investigated. Additional difficulties are encountered when attempting to make measurements in reversing flow fields and in boundary

layers, which is the major reason for the lack of data on mean and turbulent flow characteristics in separated regions. For instance, hot-wire anemometry cannot be used in region where instantaneous flow reversal is possible or in regions where the level of turbulence fluctuation is large. Furthermore, the intrusive character of this method can alternate the characteristics of the flow. Trying to get detailed characteristics of the flow using Laser Doppler Velocimetry can be very time consuming and extremely difficult. All three methods provide point measurements so any attempt to investigate the spatial variations of the flow would result only into mean characteristics and any time dependence information will be removed. In the present study the velocity field is measured using an implementation of Digital Particle Image Velocimetry Cinematography (DPIVC), which provides instantaneous two-dimensional measurements of the flow. In addition, the ability to capture a sequence of instances of the flow field adds time as a third dimension. By employing high speed time-resolved DPIV we are able to achieve detailed spatial information for the in-plane character of the flow with frequency resolution approximately one order of magnitude higher than the expected frequencies in the flow field.

In the present study, we investigate the three-dimensional flow over a surface mounted prism with small aspect ratio. The objective is to reveal the underlying physical principles of the vortex formation and vortex shedding mechanism of large vortical structures generated at the leading edge of the body by experimentally documenting the mean and unsteady flow characteristics in a plane located along the axis of symmetry of the separation region. This is achieved by calculating the mean and instantaneous velocity and vorticity distributions and flow field characteristics such as, RMS of the velocity fluctuations, turbulent kinetic energy and Reynolds stresses in the separation region over a prism at three Reynolds numbers. In addition, these measurements can be used to explain flow phenomena associated with pressure fluctuations. They also provide quantitative parameters that can be used as a base for comparison with CFD calculations. Most importantly, this study demonstrates that any investigation of the mean character of such complex flow fields is in a great extent incomplete and since it ignores the effect the time variations, which can be extremely significant. For this study three different flows at different Reynolds numbers are considered

## **Experimental Setup**

The experimental study was conducted in the Engineering Science and Mechanics Water Tunnel facility at Virginia Tech. This tunnel operates in a closed loop with up to 2500 gallons of water. After the settling chamber, a three-way convergence leads to the 0.6m x 0.6m x 1.8m test section made of a clear, acrylic Plexiglas. A 4500 GPM axial flow pump drives the flow at speeds up to 1 m/s, with free stream turbulence levels less than 1%. Under the conditions of the current experiments the free stream turbulence levels were in the order of 3%. The prism (figure 1) length 50.8 mm width 38.1 mm height 25.4 mm was mounted on the flat plate extending twenty body lengths upstream from the body and covering the whole width of the test section. The prism was aligned with the short side normal to the flow, from which the flow is allowed to separate.

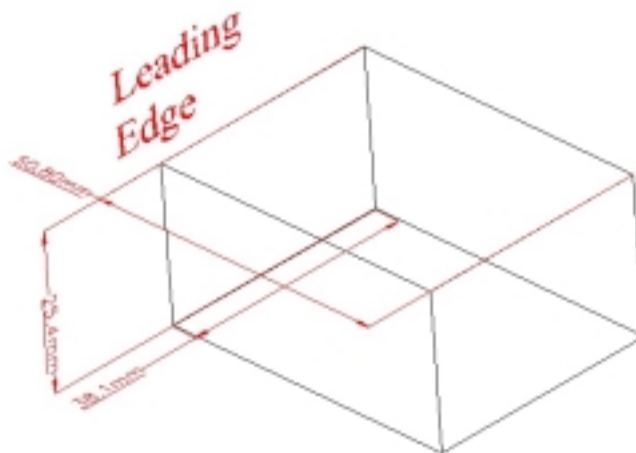


**Figure 1:** View of the prism geometry

The basic principles and advantages of DPIV method have been discussed extensively by Adrian (1991) (1996), and Willert and Gharib (1991), among others. Digital Particle Image Velocimetry falls in the general category of Laser diagnostics methods. The technique in principle can be summarized as follows. The flow is seeded with hollow glass spheres used as

flow tracers. A plane of the flow field –the interrogation area- is illuminated using monochromatic pulsing light source. In this case, a Copper Vapor pulsing laser is used. The peak power of the laser is 35 Watts at the nominal frequency of 6.5 KHz with approximately 5.5 mJoule/pulse. The pulse duration is about 30 nsecs, with duration of falling intensity of 10 nsecs. In order to illuminate the field of view the collimated laser beam needs to be delivered in the area of interest and to be converted to a thin light sheet. Using a set of sheet forming optics, a laser sheet that is 0.002m thick and 0.065m wide is delivered in the test section. The laser sheet plane is positioned in the mid-plane of the prism. The field of view is adjusted to a square region of 0.062m x 0.062m. The images are acquired with a digital camera placed normal to the plane of interest. Both the laser and the camera are controlled and synchronized by a PC computer, which serves also as an image acquisition system that has an integrated frame grabber and an image buffer for real time data storage with a transfer rate of 80 Mbytes/sec. The frame grabber buffer memory allows storing of a sequence of 2048 frames. The images are acquired using an EG&G CCD camera with a resolution of  $256^2$  and a dynamic range of 8-bit. The camera is able to acquire images with an adjustable frame rate from 30 to 1000 fps. Hollow glass spheres of 15 microns mean diameter were used as flow tracers. Figure 2 shows a schematic of the currently employed implementation of DPIV.

In order to perform high-speed imaging and still meet the requirements of high signal to noise ratio for the acquired images, we needed to take special care for the overall performance of the system. For this purpose, special optics arrangements were employed. Mirrors and lenses specially coated for the wavelength of the laser are employed in order to increase the efficiency of the laser light sheet with respect to conventional optics by 30%. In addition a wide angle 25mm scientific quality camera lens with a continuously variable F-number ( $f\#$ ) down to 0.95 is employed in order to allow more light in the sensor at the higher shutter speeds.

Even though the ground of Particle Image Velocimetry was laid in the early eighties (reviews by Hasselinc (1989) and Adrian (1991) provide a detailed discussion), it was the work of Willert and Gharib (1991), Westerweel (1993a, 1993b) and Huang and Gharib (1993) that established the digital implementation of PIV. However, their work as well as many other studies that followed, focus on a single exposure double frame digital cross correlation approach. In

addition, they focus on high-resolution (1Kx1K pixels) cameras that can sample up to 30 fps resulting in a sampling frequency of the flow field of 15Hz. These cameras are also called dual field or cross correlation cameras because of their ability to acquire two consecutive frames separated by a very small –adjustable-  $dt$  (in the order of 50 nsecs). There is very limited work addressing issues rising from the use of high-speed CCD cameras (above 500 fps). These cameras are somewhat different. The time interval between two consecutive frames is fixed as well as the transfer rate (millions of pixels per minute) and these two parameters effectively establish the feasible frame rate. Subsequently, the maximum possible frame rate affects the maximum velocities that can be measured. On the other hand, the increase of the frame rate results in significant increase of the exposure of the sensor, which limits the density of particles in the acquired images. Adrian (1996,1997) provided an analysis of different approaches to adjust the speed and the resolution of a PIV system. However, even though this study analyses both analog and digital media it does not treat such high-speed cameras as the one employed in the current research.

The use of a high repetition rate pulsing laser with pulse duration of 40 nsec and energy per pulse in the order of 5.5 mJoules delivers very low light intensity on the sensor. More importantly synchronizing the laser with the camera at 500 Hz for 4 secs is impossible since the repetition rate affects the operating temperature in the plasma tube and therefore determines the output power. Such an attempt will cause the laser to cool down rapidly and during the first 0.5 secs will be forced to shut down. In order to overcome these difficulties a multi exposure approach was adopted. Once the desired frame rate of the camera was determined, an optimization procedure of the laser was preformed using a trial and error approach in order to determine the optimum number of exposures per frame that will continuously allow the laser to run a certain frequency that will deliver high energy per frame. Multiple exposures per frame for the auto-correlation implementation of PIV have been studied extensively (Keane and Adrian, 1990 and 1991) and a procedure for optimizing the pulse separation has been proposed (Boilot and Prasad, 1996). The only paradigm of multiple exposures per frame cross-correlation approach was performed by Cenedese and Paglialuga (1990). In their approach, however they used photographic film, and instead of performing cross correlation of the particle patterns to

determine the displacement, they initially determined the centroids of the particles and then cross-correlated the projections of these centroids on each direction.

In the current approach, we perform multiple exposures per frame and we evaluate the vectors using the standard cross-correlation. In order to achieve the desired time and spatial resolution we carry out a set of optimization steps based on the findings of previous researchers. The first step requires the adjustment of the field of view in such a way that the entire domain of interest is contained and the mean particle image diameter is in the order of 1.5 pixels. In addition, the image density needs to be about five particles per  $16^2$ -pixel window. The image diameter is determined by performing a sequence of basic image processing techniques to identify each particle, find the centroid and measure the diameter and the particle concentration. The optimization of the particle image diameter and the seeding density will increase the signal to noise ratio during the cross-correlation evaluation of the velocities (Willert and Gharib (1991), and Keane and Adrian (1990, 1991)). Adjustments of the seeding density and the seeding particle size may be needed. By optimizing the particle diameter, we determine the pixel size. This allows calculating the minimum required frame rate such that the particle maximum displacement between two consecutive frames will not exceed seven pixels. Because of the limited resolution of our CCD sensor the use of a  $16^2$  window is needed in order to increase the spatial resolution of the interrogation. The laser pulse frequency is adjusted next. This is preformed by changing the number of exposures per frame in such a way that the running frequency of the laser will remain inside the operational limits of the laser but also trying to avoid the appearance of long streaks in the images. This trial and error procedure is carried out by performing free stream measurements using the PIV system and an LDV system to validate the accuracy of the evaluated velocities.

The analysis of the PIV images and the extraction of the velocity vectors, was preformed with commercial software (AEA VISIFLOW©). A total number of 3721 vectors were calculated using 75% overlapping. The vectors are placed on a uniform Cartesian grid with dimensions of 61x61. This task was carried out at a rate of one-frame/10.5 sec using a Pentium II 450 PC with 256 MB of memory. For the cross-correlation peak detection, a Gaussian fit was used. Strain vectors were removed using a local validation based on the continuity of the velocity magnitude

and angle of the neighbor vectors. A deviation of 50% of the mean value was allowed. Once the bad vectors were removed, an adaptive window weighted average was used to interpolate and finally a Gaussian kernel-smoothing filter was used to smooth the flow field. After all these tasks were carried out, the overall error of the system was estimated by comparing with the LDV free stream measurements. For the current experiment, the maximum mean error was estimated to be in the order 1% of the free stream velocity. In regions with very small displacement this error is expected to increase as high as 10%.

The current study was conducted for three free stream velocities corresponding to Reynolds numbers -based on the height of the model- of  $Re=2500$ ,  $Re=9,000$  and  $Re=16500$ . Based on the length of the flat plate that the prism was mounted on, the upstream Reynolds number for the incident boundary layer was  $Re=57500$ ,  $Re=207000$  and  $Re=379500$  respectively. The image acquisition frame rate was set at 256 fps (frames per second) for  $Re = 2500$  and at 512 fps for  $Re = 16500$ . For each case, 2,048 frames were acquired. Based on the spatial resolution of the camera and the field of view, the effective spatial resolution of the flow field is 0.961 mm corresponding to 0.95% of the height of the prism.

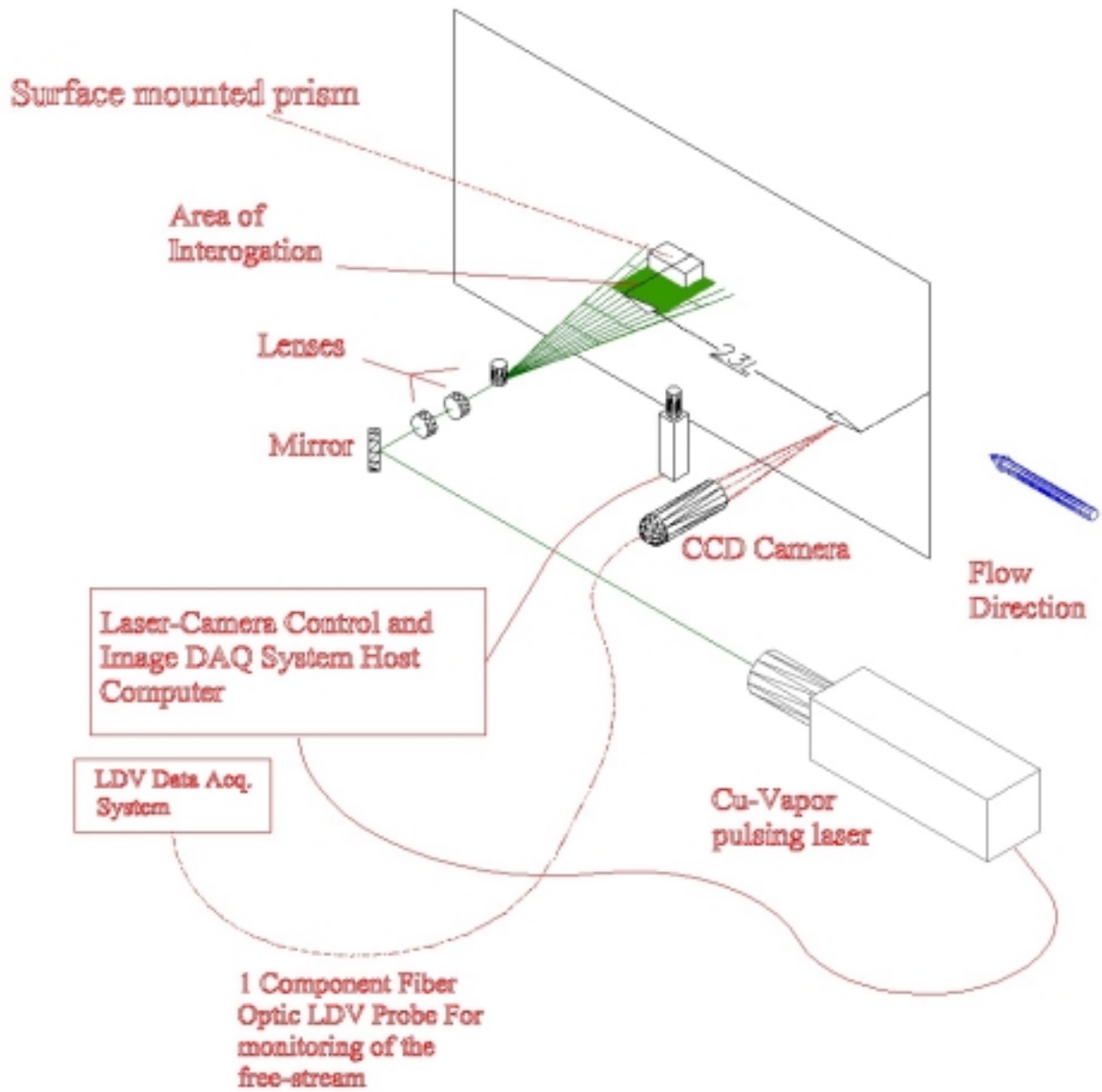


Figure 2: View of the experimental setup, showing the arrangement of the DPIV system.

## **Mean and Turbulent Characteristics**

### **Results and Discussion**

In all the plots that follow, the flow direction is from left to right.. All coordinates are non-dimensionalized with the height, ( $L$ , is the height of the prism which is used as characteristic length) of the model and measured velocities are converted to non-dimensional by dividing with the corresponding free stream velocity. The leading edge of the prism is located at  $x/L=0$  and the trailing edge at  $x/L=1$ . The variables presented resulted by processing 2048 instants of the flow field corresponding to a total time of  $T_{total}=8$  sec for the case of  $Re=2500$  and  $T_{total}=4$  sec for  $Re=9000$  and  $Re=16500$ .

Vector plots of the mean flow structure are shown in the set of plots in figure three. For all three cases, the formation of a re-circulation region with a mean reattachment position and the formation of the horseshoe vortex in the front stagnation region are evident. In addition, the acceleration of the flow over the leading edge is shown clearly. Contour plots of the magnitude of the velocity normalized with the free stream velocity are shown in figures 4-1 to 4-3. Two important features can be detected from these plots. The first feature relates to the region where  $U$  becomes larger than  $0.95U_{inf}$  and which marks the outer edge of the shear layer. Based on these criteria, the edge of the shear layer moved higher (away from the prism) into the flow as the Reynolds number increased. This is attributed to the transition point of the shear layer, which shifts towards the leading edge (Castro and Robins, 1977). The second feature to note in figures 4 is the locus of  $U=0$  which falls in a region just below contour level 2 for all plots. The highly unsteady character of the flow in this region results in frequent changes of the velocity sign. This frequency is significant enough to result in a time averaged velocity magnitude near zero.

This feature is better illustrated in figures 5 (1-3), which show contour plots of the reverse coefficient of the flow. The reverse coefficient is defined as the fraction of time during which the flow moves in opposite direction to the mean flow. For all three flow fields the region where the reverse coefficient is larger than 0.4 matches with the corresponding open region in figures 4-1,2,3 where the velocity magnitude is near zero. A comparison of figures 5 shows that

the region where reverse flow takes place increases as  $Re$  increases. This is very indicative of the higher level of unsteadiness exhibited by the flow at the higher  $Re$ . Moreover, the mean reattachment point is usually defined as the location, where the fraction of time during which the flow moves upstream is 0.5 (Kiya and Sasaki, 1983). For  $Re=2500$  and  $Re=9000$ , the reverse coefficient exhibits a peak of about 0.5 near  $x/L=0.85$  and thus would be defined as the mean reattachment point for this flow. For the higher  $Re$  flow,  $Re=16500$ , the reverse coefficient contours have a peak value of 0.65 near  $x/L=0.85$  also. By noting that the contour with reverse coefficient value of 0.5 covers a small region around this peak, we will conclude that the mean reattachment point is near  $x/L=0.85$ . Consequently, while the reverse flow region is larger for the higher Reynolds number, the mean reattachment point is almost at the same location near  $x/L=0.85$ .

Figures 6-1 through 6-3 show contour plots of the average vorticity over the prism. The plots show the horseshoe vortex that forms in front of the prism. For all three cases, the location of the forward stagnation point can be identified from the change of vorticity sign and is approximately at 65% of the height of the prism while the strength of vorticity is of the same order of magnitude.

For the vorticity field around the prism, there are several features to be noted. Initially, we note that vorticity exhibits its maximum values at the leading edge where the flow separates. Another feature is the region of negative vorticity shown in the contour plots confined below contour level 4 in figure 6-1 and 6-2 and below contour level 5 in figure 6-3. This region is related to the lower part of the reverse flow in the separation bubble. Moreover, by comparing figures 6, it is obvious that the domain of the separation bubble, in the mean, is much larger at the higher Reynolds number. For  $Re=2500$ , this region is bounded by  $0.7 < x/L < 0.9$  and  $y/L < 0.2$ . For  $Re=9000$ , this region is bounded by  $0.45 < x/L < 1$  and  $y/L < 0.2$ . The corresponding area for  $Re=16500$ , is enclosed between  $0.2 < x/L < 1.3$  and  $y/L < 0.1$ . The area confined between the shear layer and  $x/L=0.7$  for  $Re=2500$ ,  $x/L=0.45$  for  $Re=9000$  and  $x/L=0.2$  for  $Re=16500$  presents a first change of the vorticity sign which is indicative of the formation of a secondary vortex with opposite sign within this region. However, in a mean sense no well defined secondary vortical structure can be resolved, because of the instantaneous character of this phenomenon in

combination with its small scale and the limits of the spatial resolution that the experimental method employed could achieve. The second change of sign ( $x/L=0.9$  for  $Re=2500$ ,  $x/L=1.0$  for  $Re=9000$  and  $x/L=1.3$  for  $Re=16500$ ) defines the point after which the mean flow is fully reattached.

Contour plots of the normalized  $u'_{rms}$  variations for  $Re=2500$ ,  $9000$  and  $16500$  are shown in figures 7-1, 7-2 and 7-3 respectively. By comparing these plots we observe that the region corresponding to higher  $u'_{rms}$  values is significantly larger at  $Re=16500$ . For  $Re=2500$ ,  $u'_{rms}$  is negligible for  $y/L > 0.5$ . On the other hand, for  $Re=16500$ ,  $u'_{rms}$  exhibits large values throughout the measured flow field. Another point to address is the locations of maximum  $u'_{rms}$ . The locus along these locations is near the inflection point of the shear layer, which can be considered as the center of the shear layer. Based on this criterion, and by comparison of figures 7, one can deduce that the shear layer is much larger at  $Re=16500$  than at lower Reynolds numbers. We should also note that the x-coordinate of the maximum  $u'_{rms}$  in the flow over of the prism for all three Reynolds numbers is given by  $x/L=0.85$  which is near the reattachment point. Contours of the normalized  $v'_{rms}$  fluctuations for all three Reynolds numbers are shown in figures 8-1,2,3, respectively. For all cases, the maximum level of  $v'_{rms}$  is smaller than that of  $u'_{rms}$  at the same Re but of the same order of magnitude. Yet, the features observed and physical interpretations made for the  $u'_{rms}$  fluctuations apply for the  $v'_{rms}$  fluctuations. For instance, a comparison of figures 8-1,2 and 3 shows that the region where the levels of  $v'_{rms}$  fluctuations are significant is larger at the higher Re. Moreover, the locus of maximum  $v'_{rms}$  matches that of maximum  $u'_{rms}$  at all three Re. In addition, the x-coordinate of the maximum  $v'_{rms}$  is also at an  $x/L$  position near the reattachment point.

For all three cases of the Re number the large values of  $u'_{rms}$  and  $v'_{rms}$  for  $x/L > 1$  are indicative of the highly unsteady character of the flow. The violent alternation of vortex formation, wake expansion, and vortex shedding and subsequently reattachment of the flow has as result very high  $u'_{rms}$  and  $v'_{rms}$  values in that region of the flow. In combination with the fact that the separation bubble is bigger for the case of  $Re=16500$  –as it was shown in figures 5- justifies the observation that the area of significant values of rms is larger. However, the very high values of  $u'_{rms}$  and  $v'_{rms}$  for  $y/L < -1$  and  $x/L > 1$  for  $Re=16500$  have limited physical meaning

since they resulted from aliasing effects near the edges of the flow field that the cross-correlation procedure used for the extraction of the velocities inherited to the calculated data. This problem is a consequence of the particles leaving the area of interrogation with high velocity thus it is existent only in the aforementioned region and only for the higher Re number. High values of  $u'_{\text{rms}}$  and  $v'_{\text{rms}}$  for all three cases exist also in the region of the horseshoe vortex and they are of the same order of magnitude as the values in the reattachment region. These resulted from fluctuations of the intensity of the horseshoe vortex, which subsequently can be attributed to free-stream fluctuations. A comparison of the  $v'_{\text{rms}}$  figures for each Reynolds number in the region of the horseshoe vortex shows that while Re increases the point of forward stagnation is more clearly defined by smaller values of  $v'_{\text{rms}}$  while the vortex core continues to have high values. These observations provide solid quantitative evidence of the unsteadiness of the horseshoe vortex observed in the flow visualizations.

The distribution of the in-plane turbulent kinetic energy, resulting as the sum of  $u'^2$  and  $v'^2$  is presented in the set of plots in figure 9. The qualitative resemblance of these figures with the corresponding of the  $u'$  reveals the fact that the in-plane turbulent kinetic energy flow is primarily dominated by the fluctuations of the streamwise velocity component. The fluctuations of the streamwise component correspond to the oscillations of the reattachment point while the fluctuations of the  $v$  component are related to the oscillations of the shear layer. The position of the instantaneous reattachment is determined by the size and shape of the separation bubble, which will be affected by the interaction of the shear layer vorticity with the incident free stream. As observed earlier the increase of the Reynolds number results in a transition of the shear layer, which enhances the turbulent character of the flow.

**Figure 3:** Set of figures for the velocity vectors

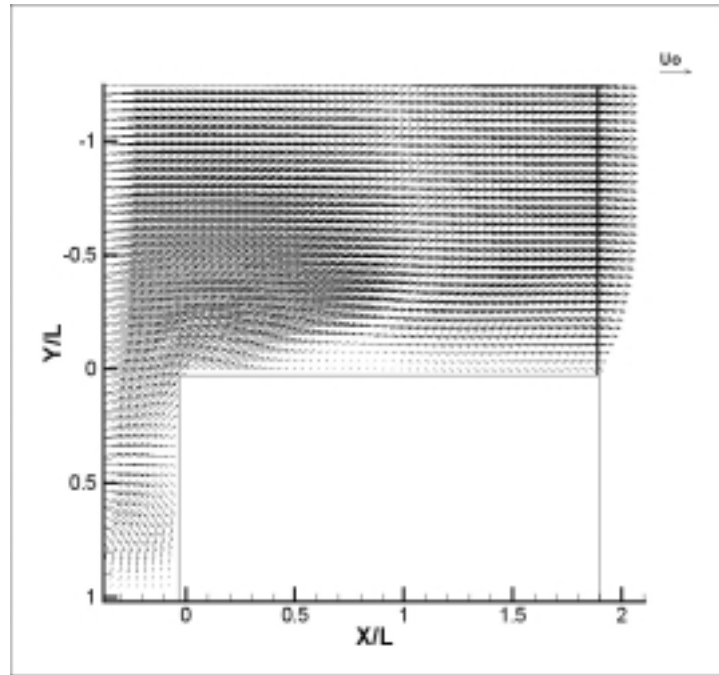


**Figure 3-1:** Velocity vectors for the first case of  $Re=2500$ .

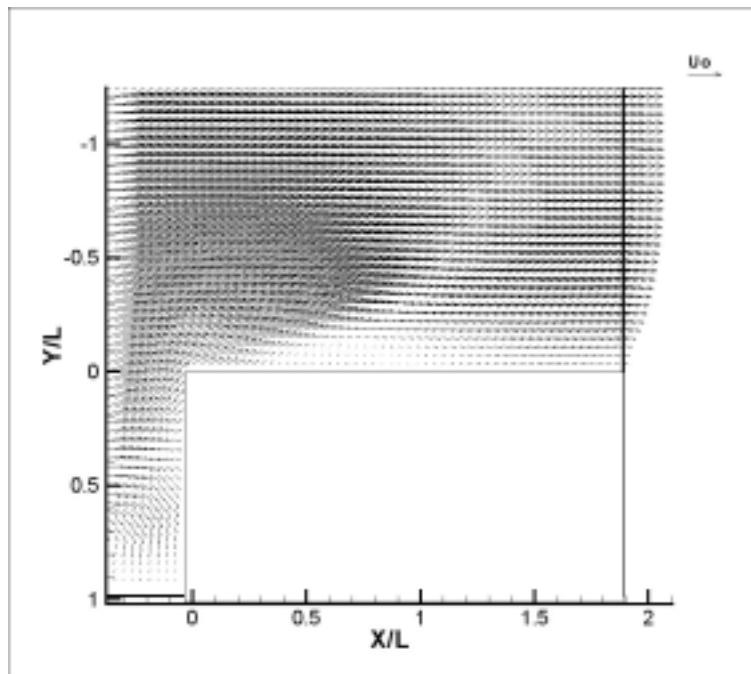


**Figure 3-2:** Velocity vectors for the second case of  $Re=9000$ .

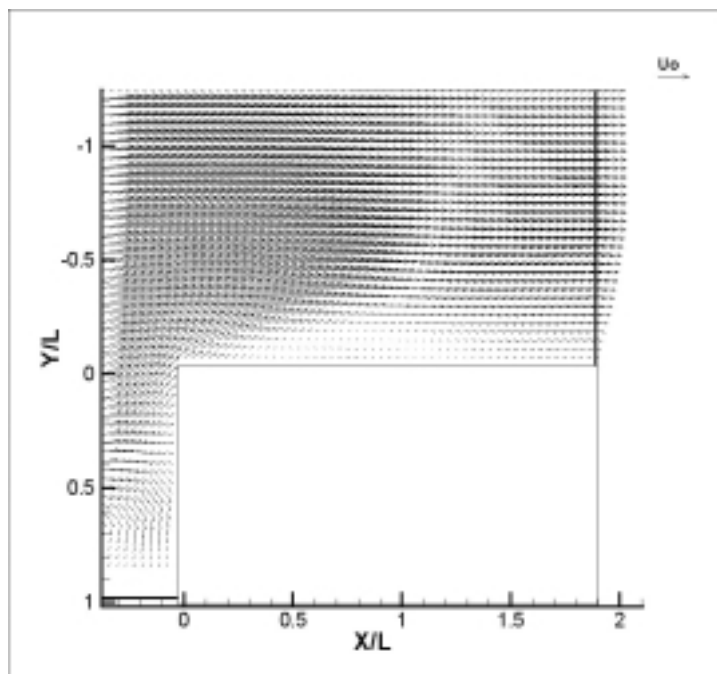


*Figure 3-3:* Velocity vectors for the third case of  $Re=16500$ .

Figure 4: Set of figures for the velocity magnitude

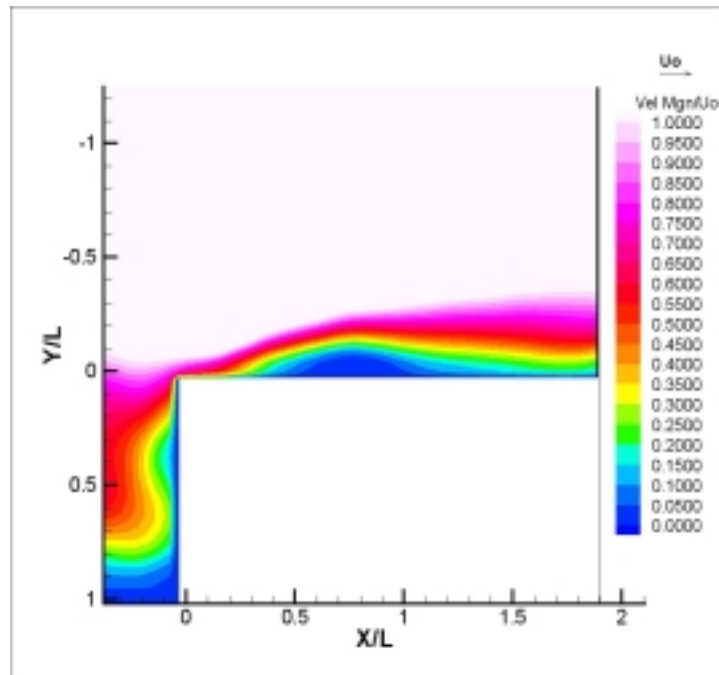


Figure 4-1: Color contours of Velocity Magnitude for the first case of  $Re=2500$ .

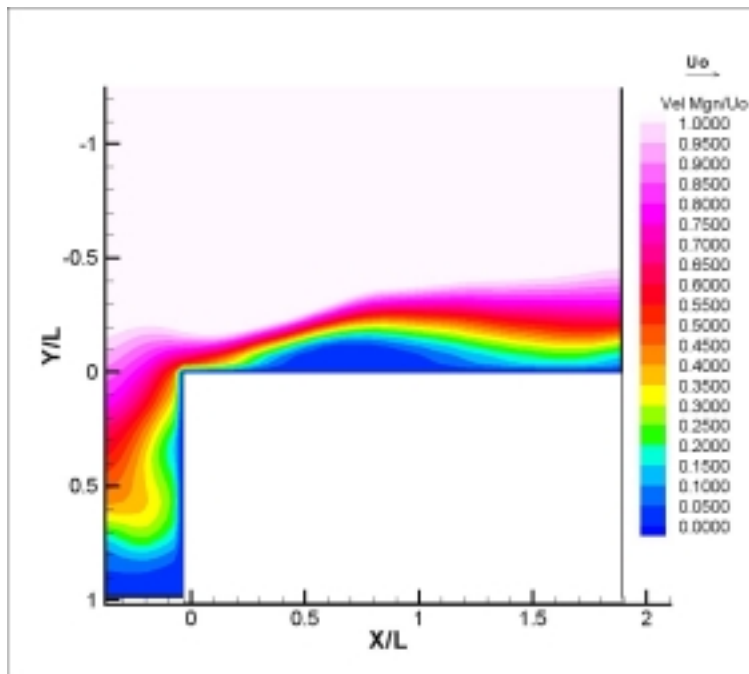
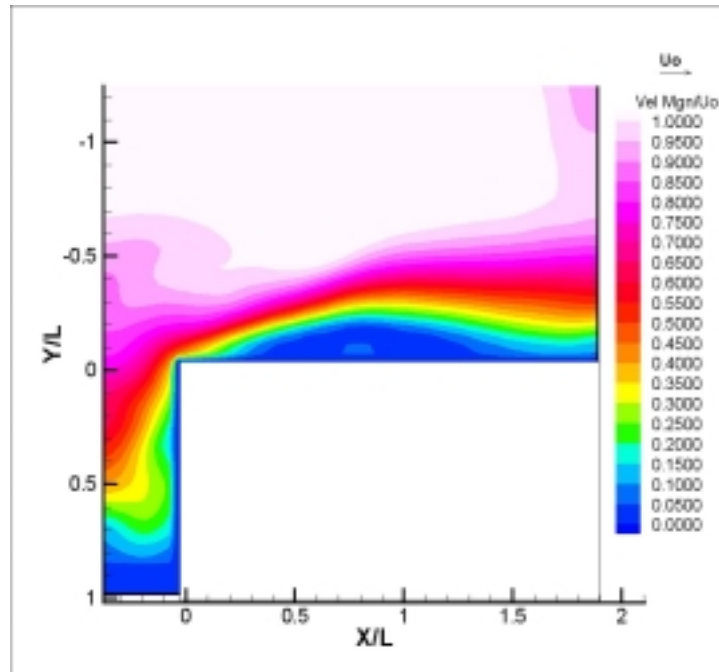


Figure 4-2: Color contours of Velocity Magnitude for the second case of  $Re=9000$ .



**Figure 4-3:** Color contours of Velocity Magnitude for the third case of  $Re=16500$ .

Figure 5: Set of figures presenting the reverse coefficient.

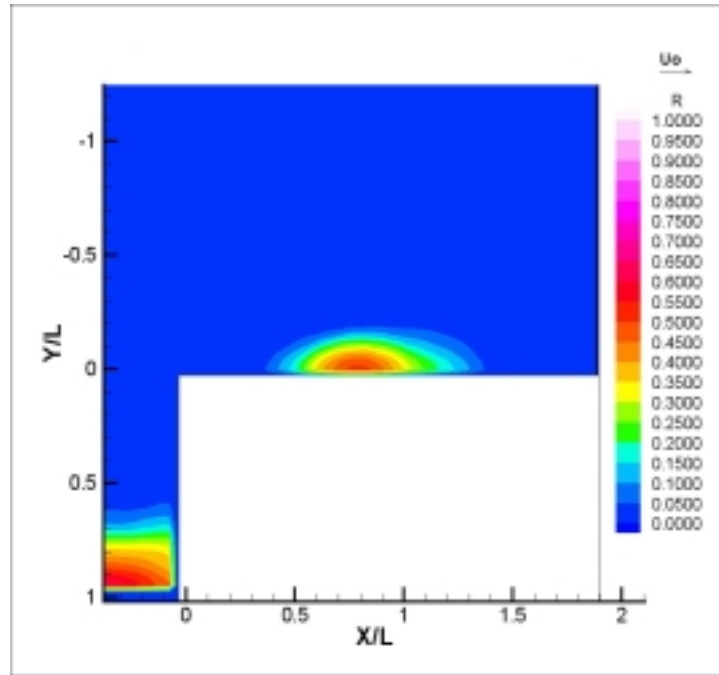


Figure 5-1: Color contours of reverse coefficient for the first case of  $Re=2500$ .

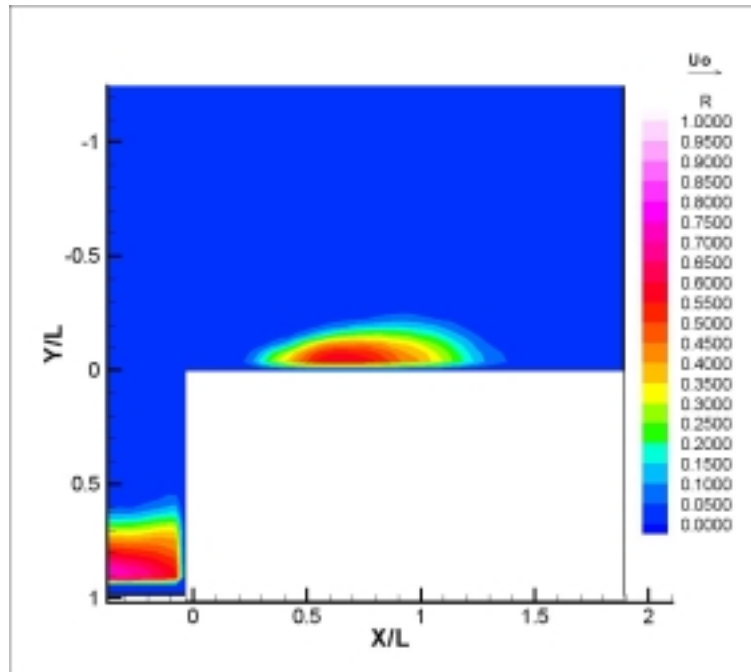
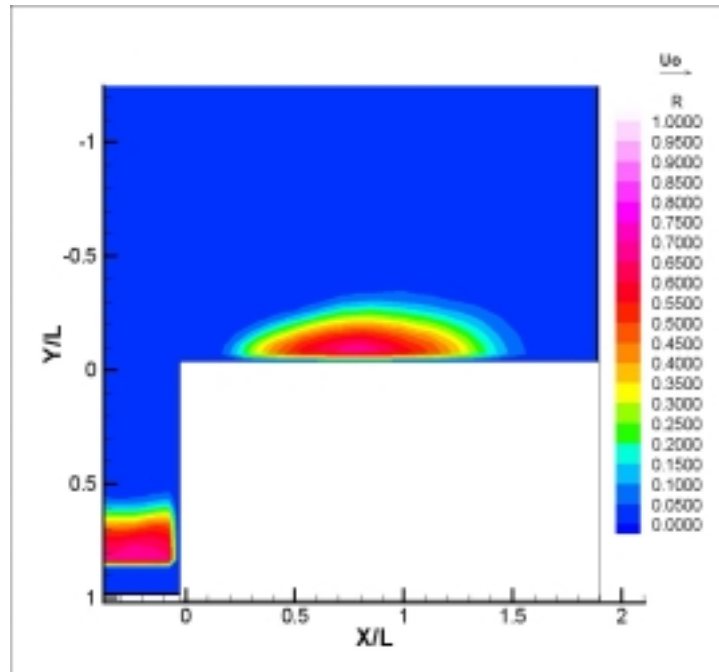


Figure 5-2: Color contours of reverse coefficient for the second case of  $Re=9000$ .



**Figure 5-3:** Color contours of reverse coefficient for the third case of  $Re=16500$ .

Figure 6: Set of figures for the vorticity distribution.

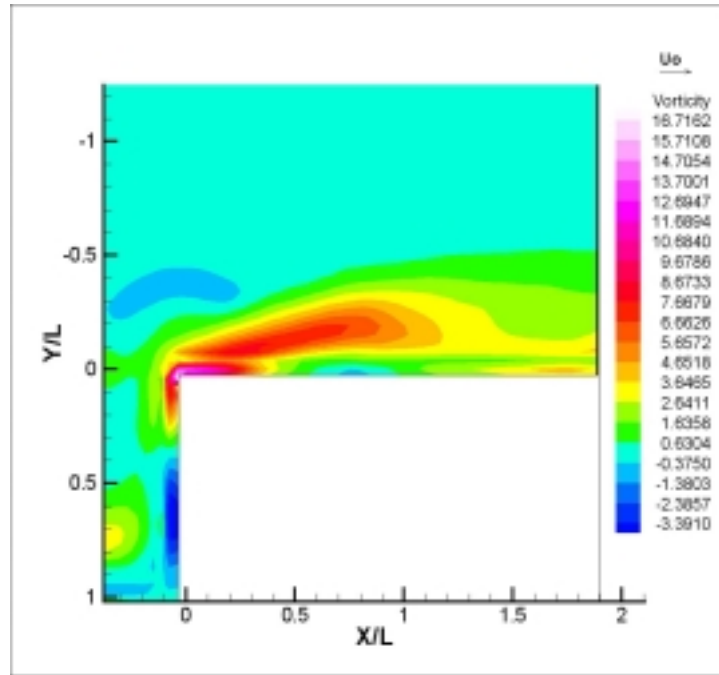


Figure 6-1: Color contours of Vorticity for the first case of  $Re=2500$ .

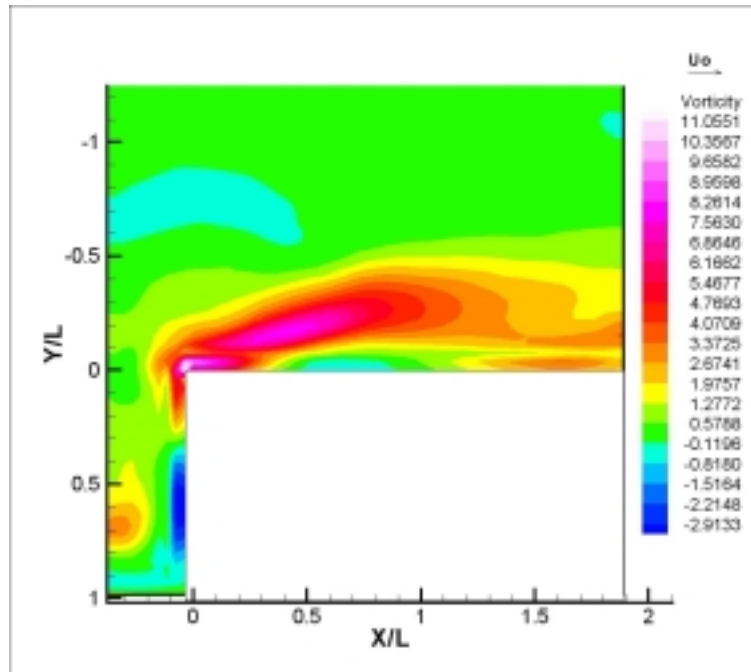
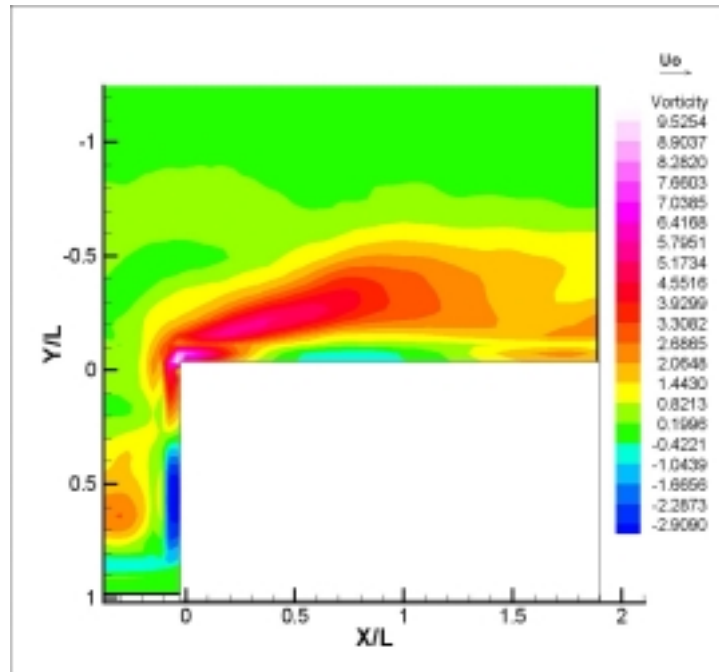


Figure 6-2: Color contours of Vorticity for the second case of  $Re=9000$ .



**Figure 6-3:** Color contours of Vorticity for the third case of  $Re=16500$ .

Figure 7: Set of figures for  $u'_{rms}$ .

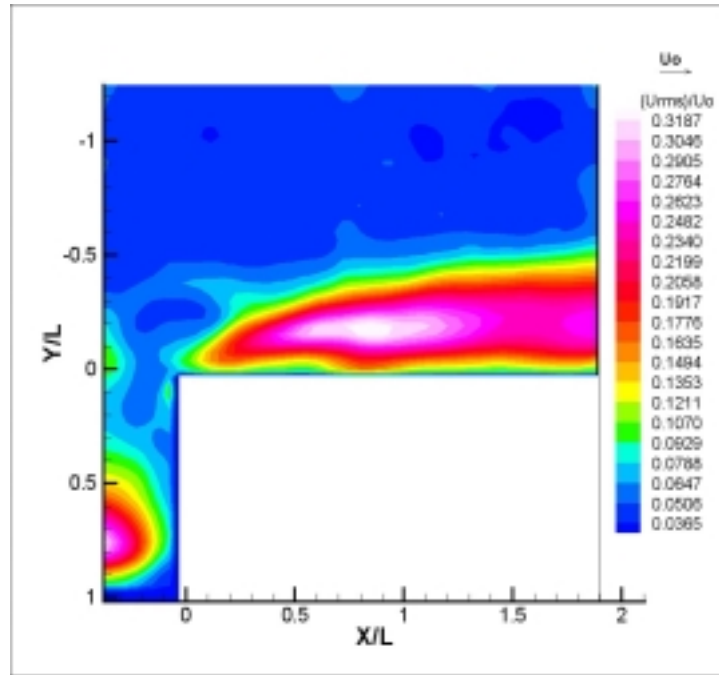


Figure 7-1: Color contours of  $u'_{rms}$  for the first case of  $Re=2500$ .

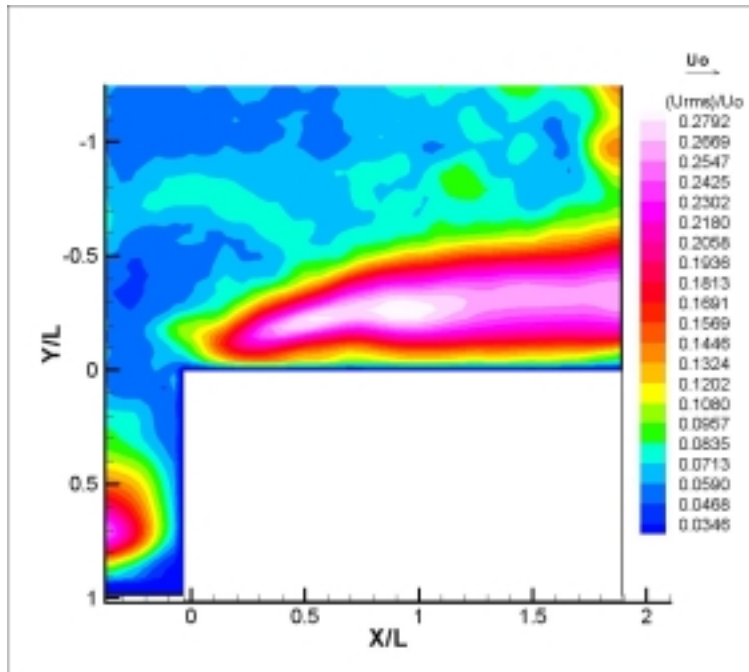
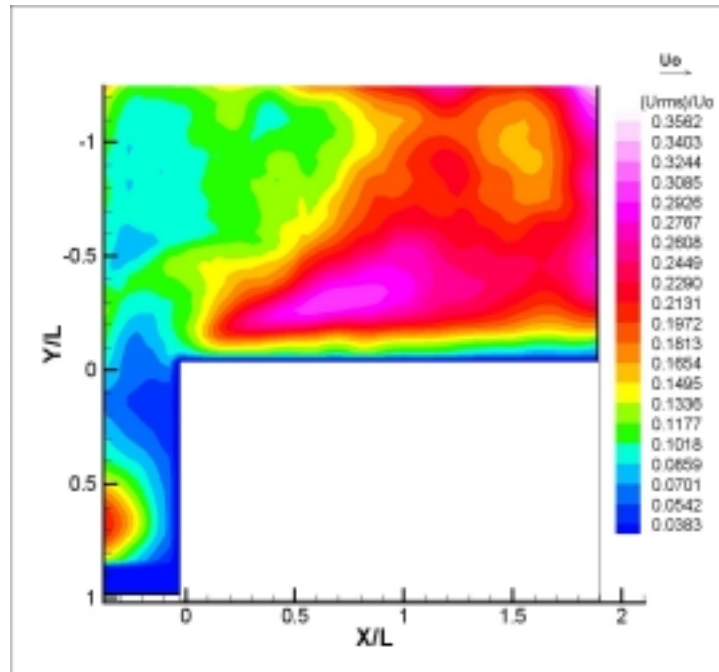


Figure 7-2: Color contours of  $u'_{rms}$  for the second case of  $Re=9000$ .



**Figure 7-3:** Color contours of  $u'_{rms}$  for the third case of  $Re=16500$ .

Figure 8: Set of figures for  $v_{rms}$

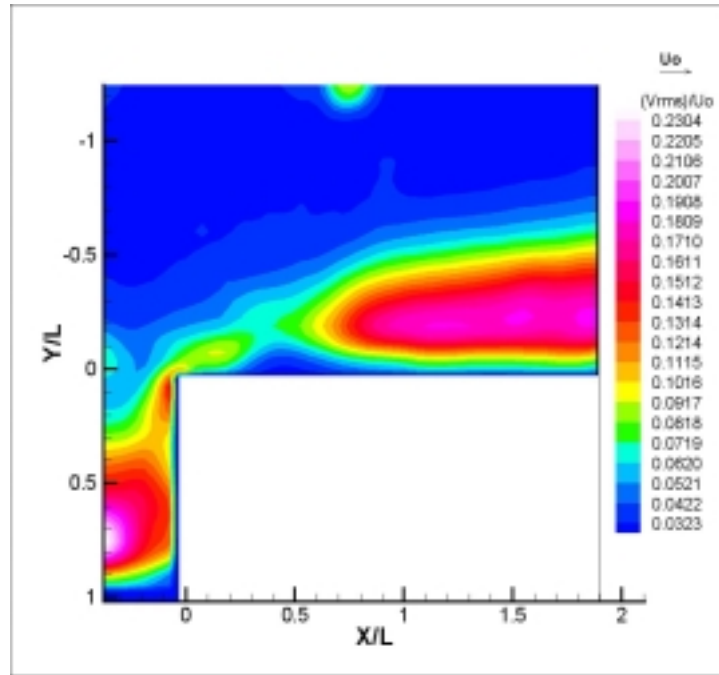


Figure 8-1: Color contours of  $v_{rms}$  for the first case of  $Re=2500$ .

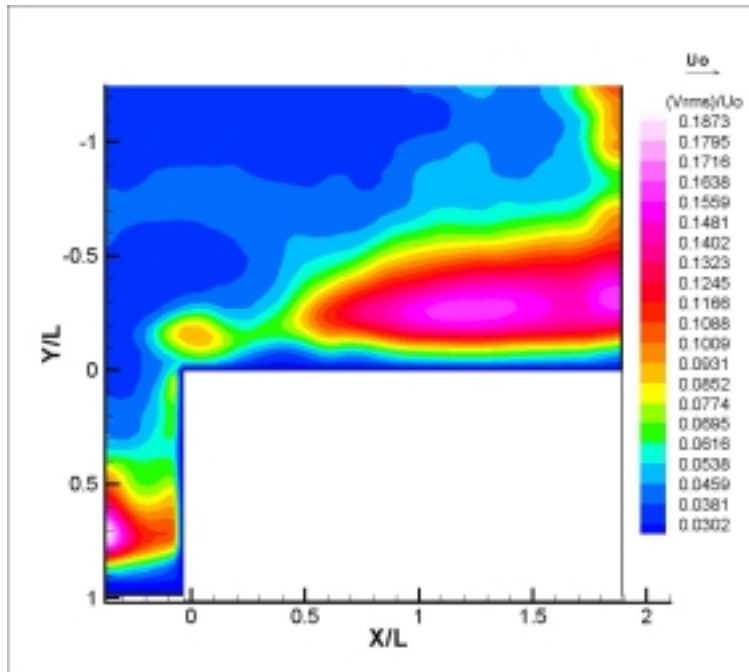
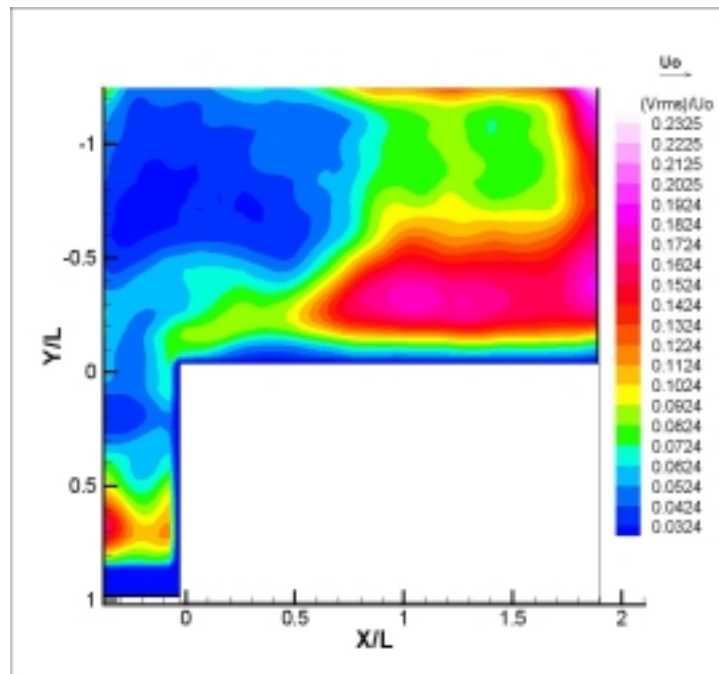


Figure 8-2: Color contours of  $v_{rms}$  for the second case of  $Re=9000$ .



**Figure 8-3:** Color contours of  $v_{rms}$  for the third case of  $Re=16500$ .

Figure 9: Set of figures for the TKE.

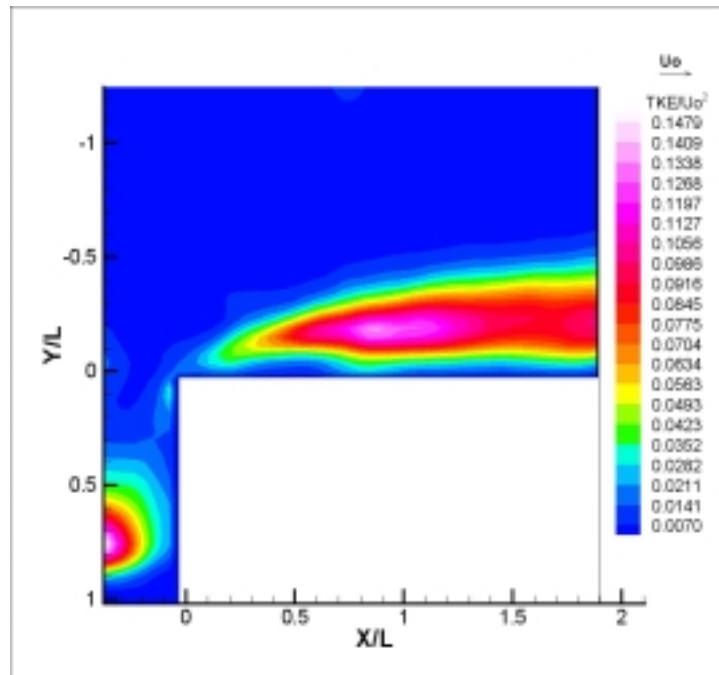


Figure 9-1: Color contours of TKE for the first case of  $Re=2500$ .

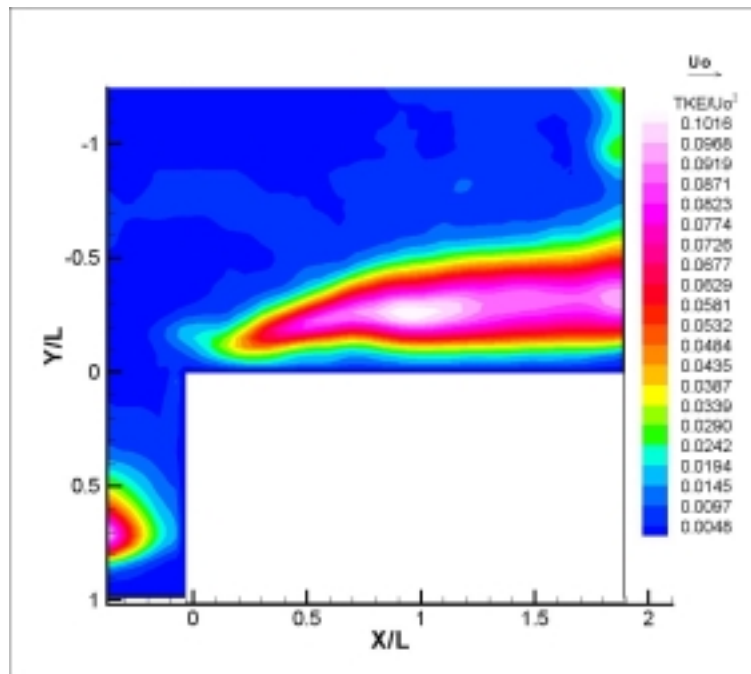
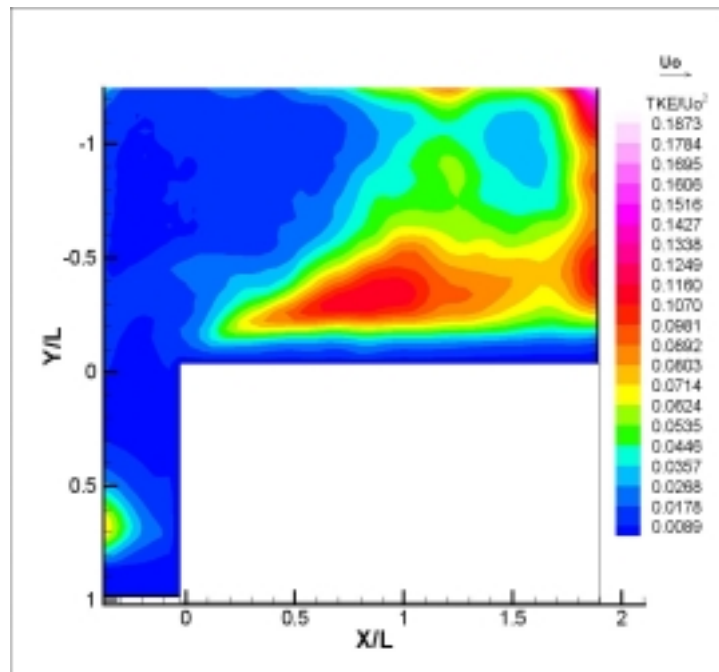


Figure 9-2: Color contours of TKE for the second case of  $Re=9000$ .



**Figure 9-3:** Color contours of TKE for the third case of  $Re=16500$ .

## **Unsteady and Instantaneous Flow Characteristics**

### **Particle Flow Visualization**

Particle flow visualizations are carried out in order to provide qualitative information for the character of the flow. The previously described image acquisition setup was used, adjusted to a low frame rate to allow the particle trajectories to appear as streaks in the image. For  $Re=2500$  and  $Re=9000$  the frame rate was set at 50 fps while for  $Re=16500$ , it was set at 100 fps. The images were acquired for 5 sec in every case. Animation of the images provided visual evidence of the natural unsteady character of the flow.

For all Reynolds numbers, the flow field can be divided into three distinct regions. First the region upstream of the front face of the prism where we have the formation of the horseshoe vortex and the front stagnation point. Subsequently, one can recognize the flow reversal and reattachment region, both bounded by the top side of body and the shear layer emanating from the leading edge. This region is characterized by the vortex formation resulting to flow reversal in the vicinity of the wall and vortex shedding in the wake of the body. The third region corresponds to the outer flow and the accelerating free stream velocity over the body.

From previous studies became evident that the flow over a three-dimensional surface mounted body is dominated by the interaction of the shear layer originating from the leading edge of the prism with the outer flow region and the horseshoe vortex. When the aspect ratio of the body is of the order of one, the effect of the horseshoe vortex is more dominant and the resulting flow structure is far more complicated than for the case of a two-dimensional body. (Martinuzzi and Tropea, 1993). The unsteadiness of the flow is better categorized in terms of the following processes:

1. Unsteadiness of the horseshoe vortex attributed to irregular mass flow flux around the two sides of the prism. (Davenport and Simpson, 1990)

2. A low frequency oscillation of the free shear layer referred to as flapping. (Cherry et. al.1984) related to a pseudo periodic shedding of large-scale vortices (Kiya and Sasaki, 1983).

The particle flow visualizations performed in this studied confirmed previously reported observations and revealed that instantaneous expansions of the separation bubble occur, forming an open wake with no reattachment. In addition, when reattachment occurs, the location is not fixed, leading to strong unsteadiness of the point of reattachment. Animations 1, 2, and 3 (presented here with still images) show the evolution of the flow through out the acquisition time for all three cases Reynolds number. The animations demonstrate the wake expansion vortex shedding and reattachment of the flow. For all cases, the free shear layer and the separation bubble are well defined. As Re number increases a more coherent vortical structure is formed. Yet, in all three cases, there is no distinct region of a steady vortex core, which can be attributed to the three-dimensional character of the flow.

Similarly with Davenport and Simpson (1990), we observe unsteadiness in the forward stagnation region where the horseshoe vortex forms. The core and the size of the horseshoe vortex show fluctuations, which are affecting the character of the shear layer that separates from the corner. Such a postulation about the character of the flow requires further quantitative evidence in order to be validated. However, the flow structures that exist and interact in such a flow field are coupled. Any fluctuations in the size of the core of the horseshoe vortex will result in oscillations of the point of forward stagnation. That is, the point from which the boundary layer that separates from the leading edge of the prism starts developing. Moderate fluctuations of the thickness of the boundary layer that develops on the front face of the prism may affect the character of the shear layer that emanates from the leading edge. In conjunction with the levels of the oncoming free stream turbulence result to the extremely unsteady character of the flow that is observed in these flow visualizations. Figure 13 shows a schematic of the above described flow structure. However, this assumption requires quantitative evidence to be validated.

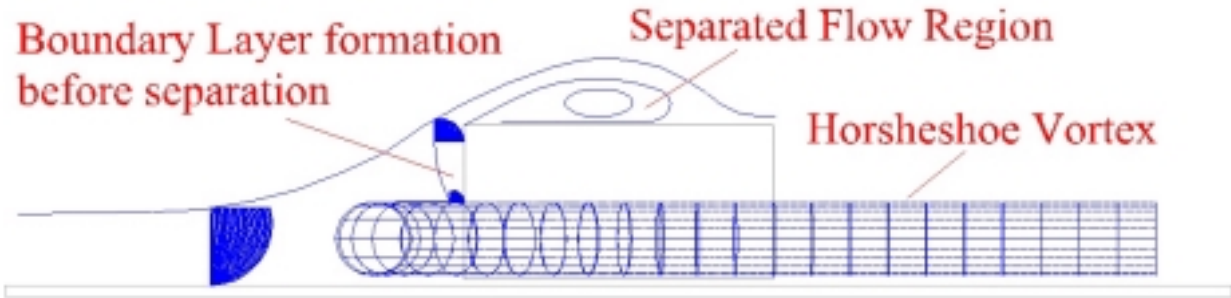
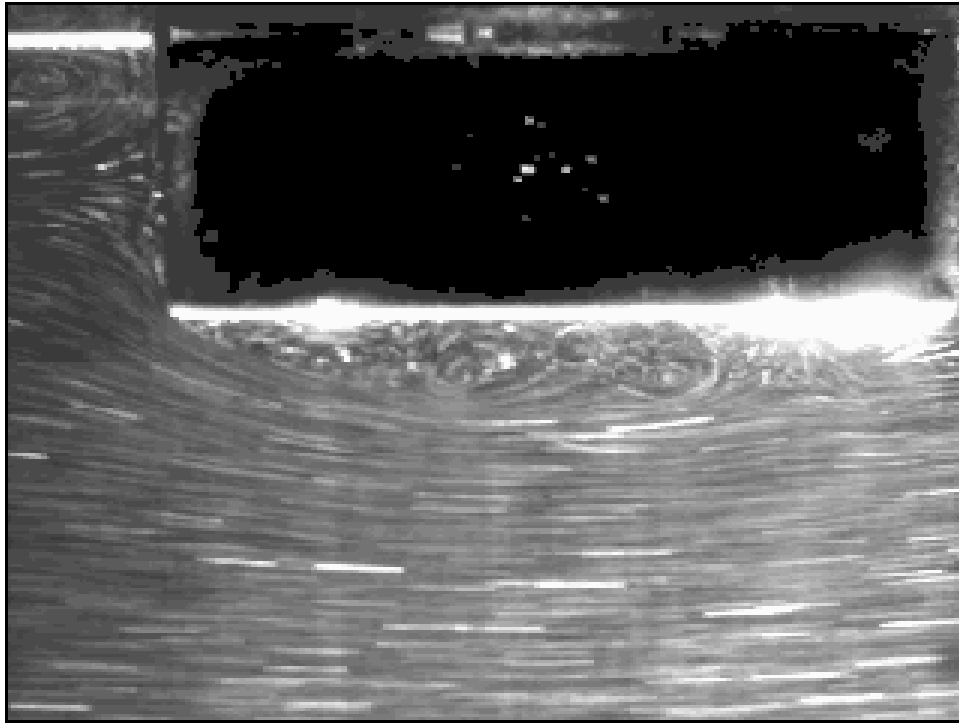
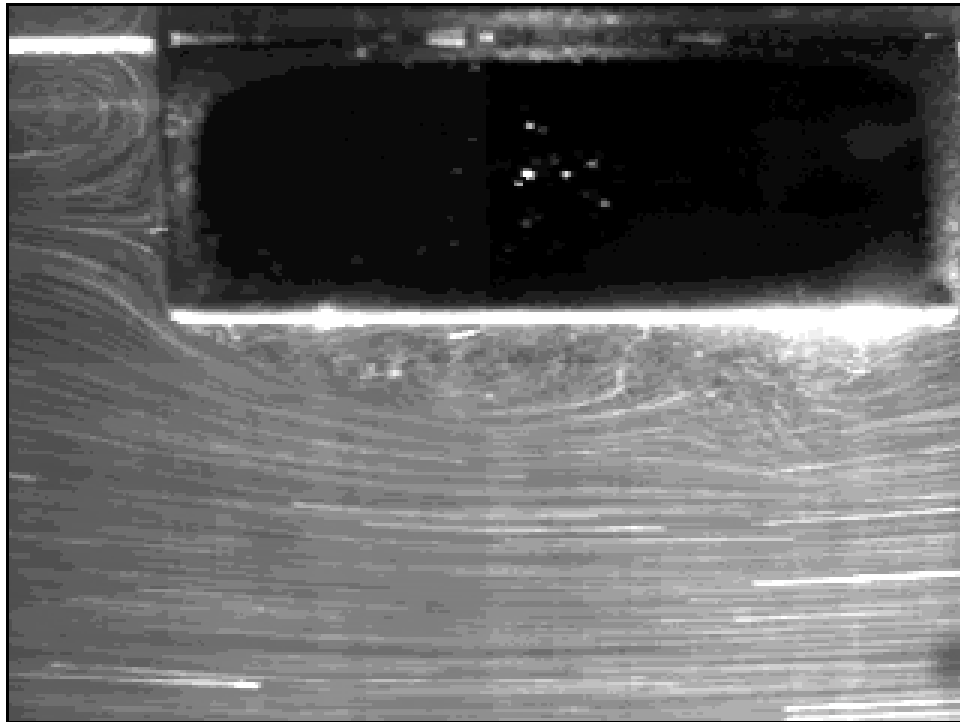


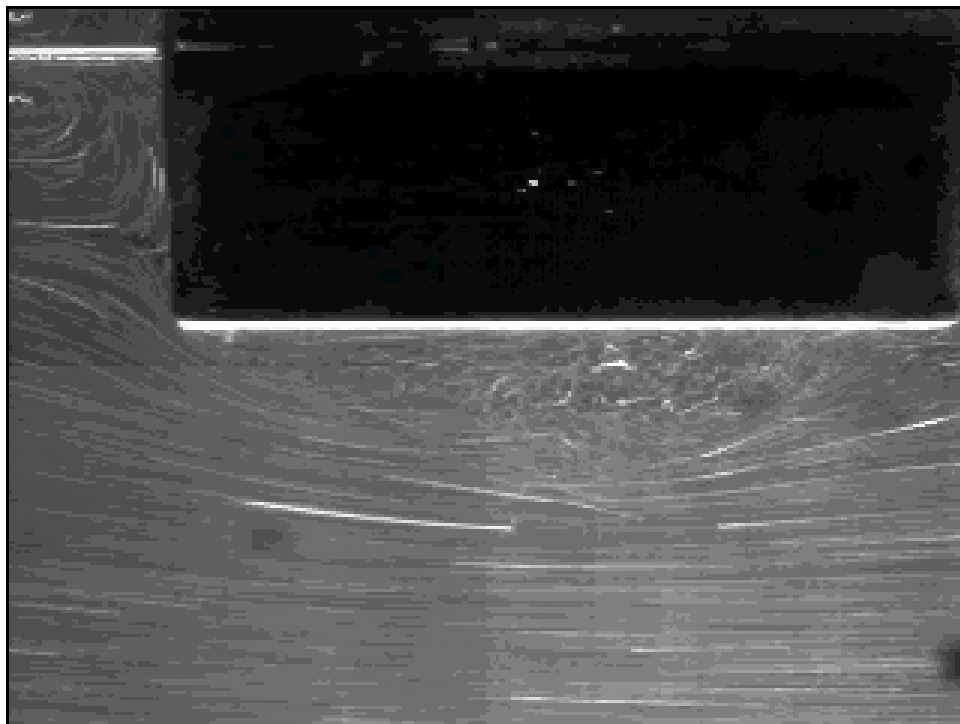
**Figure 10:** Schematic representation of the flow over the prism, the formation of the horseshoe vortex, the separation and reattachment regions.



**Animation 1:** Still image corresponding to particle flow visualization for  $Re=2500$



*Animation 2:* Still image corresponding to particle flow visualization for  $Re=9000$



*Animation 3:* Still image corresponding to particle flow visualization for  $Re=16500$

## **Instantaneous Velocity and Vorticity Measurements**

The instantaneous velocity and vorticity characteristics of the flow are treated in this section. The results are presented in terms of animated sequences of instantaneous flow fields in a multimedia AVI format and a limited number of representative individual snapshots. Animations 4,5,6 present sequences of 2048 instants of the flow field corresponding to 8 secs for the case of  $Re=2500$  and 4 secs for the cases of  $Re=9000$  and  $16500$ . These animations provide quantitative results to validate the observations resulted from the flow visualizations. The vorticity color maps are overlaid on the vector field to give a more complete view of the flow structure. The color contours that correspond to very small vorticity values have been removed in order to simplify the visual observations. The same range of vorticity values is used for the contours to provide the basis for comparison. In addition to the animations, instantaneous snapshots of the flow are presented in animation figures 4-1 through 4-12, 5-1 through 5-12 and 6-1 through 6-16.

In Animation 4, we study the flow field corresponding to a Reynolds number of 2500. The fluctuation of both the shear layer position and the core of the horseshoe vortex are immediately observed. The strength and the size of the horseshoe and the point of stagnation on the front side present a strong time variations. As a result, a well-defined region with high positive vorticity content is formed in the immediate vicinity of that point. The boundary layer developing from that point towards the leading edge is forced to separate at the corner and feeds the shear layer with vorticity. Due to the interaction of the shear layer with the incident free stream the shear layer oscillates demonstrating a flapping motion. The opposite vorticity values in the separated region (bounded from the positive vorticity distribution of the shear layer) remain very low, indicating a weak recirculation. However, even though the flow is clearly separated a careful look reveals instants were the flow on the topside of the prism remains fully attached. In addition, instants were the negative vorticity in that region obtains instantaneous peak values precede the shedding of the vortex downstream (figures 4-1 to 4-12). This vortex is convected downstream with a velocity relative to the free stream. The vortex shedding mechanism is strongly dependent on the interaction of positive and negative vorticity (Williamson, 1995, 1996; Unal and Rockwell, 1988a 188b). The separated shear layer from the

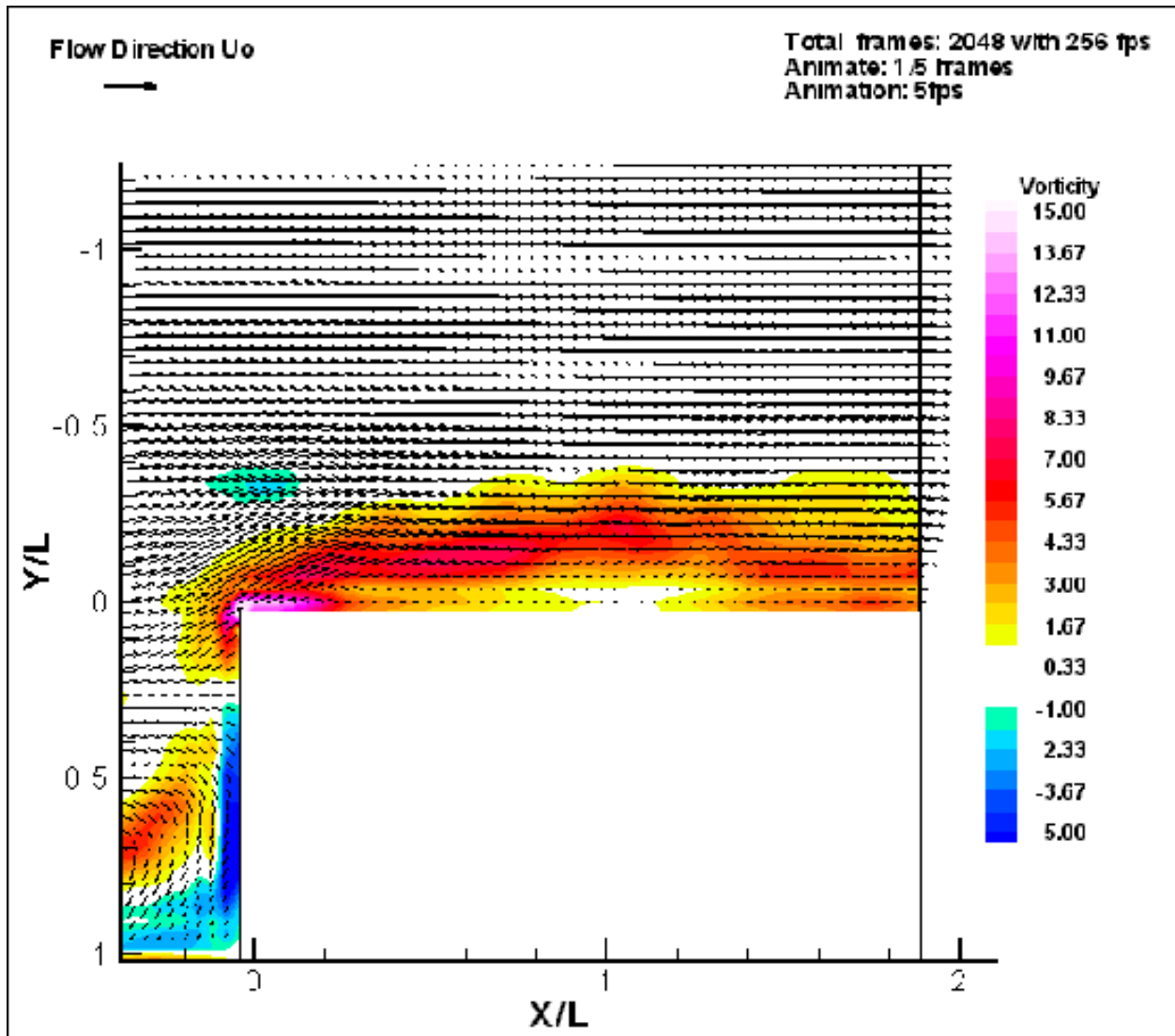
leading edge corner will develop instabilities (Bernal and Roshko, 1986) and eventually will roll to form a strong primary vortex. This vortex will increase in strength as the shear layer continues to feed vorticity into the vortex, which results in the generation of secondary vorticity in the reverse flow region. Once this secondary vorticity is strong enough to affect the formed vortex, the latter will be forced to detach and shed in the wake. Then, this process is repeated (see sequence of figures 4-10, 4-12).

In the second Animation (Animation 5) the flow field corresponding to  $Re=9000$  is presented. The observations made for the previous case are valid also here. However, the level of unsteadiness of the flow field increased with respect to  $Re=2500$ . The motion of the shear layer and the vortex shedding process occur more frequently. The first major difference observed is the fact that the position of the shear layer is now higher above the prism and demonstrates larger oscillations. The levels of negative vorticity in the reverse flow region have increased. In addition, the point of stagnation in the front of the prism is now oscillating less however, there are instants when we observe the structure of the horseshoe vortex losing its coherence and rising towards the leading edge. The underlying relation between the positive and negative sign vorticity on the topside of the prism is now more evident. More importantly, there are no instants in the flow field where the flow appears to be fully reattached. However, there are instants where the shear layer is lifting up forming an open wake with no reattachment at all.

Finally, in Animation 6 the case of  $Re=16500$  is presented. Similarly to the previous case, the fluctuations of the flow increase. The flow field is becoming more unsteady. The region on the topside of the prism where reverse flow occurs increases as well as the maximum values of negative vorticity. The interaction of both signs of vorticity with each other leading to the vortex shedding is enhanced. A careful study shows instants in the flow where negative vorticity increases in size and strength and penetrates the shear layer cutting off the supply of positive vorticity and forcing the vortex to shed. Despite the fact that the overall unsteadiness of the flow increases, the fluctuations of the point of forward stagnation are reduced significantly although the horseshoe vortex core shows variations of size and strength. Although the events of separation, vortex formation, vortex shedding and reattachment are repeated consistently, there is not a distinct periodic character in the flow. This observation is valid for all three cases. There is

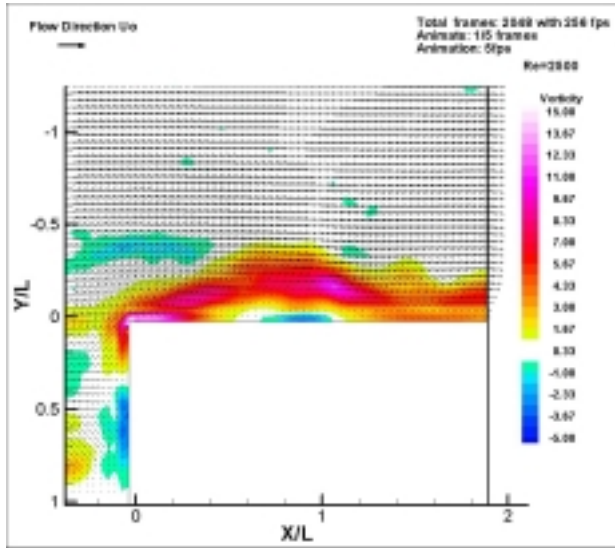
no doubt that a data acquisition period of 4 sec is not sufficient to allow us to reach safe conclusions about the periodicity of the flow. However, the intermittent behavior of the flow demonstrated in these animations proves strong time dependence and a naturally unsteady character.

From comparison of the instantaneous vorticity with the mean distribution, it is obvious that there are important differences. Even though the mean vorticity shows a well-defined shear layer and a region where the separated flow occurs, the instantaneous characteristics demonstrated a very violent and unsteady behavior. In addition, the instantaneous variations of the edge of the shear layer as well as the mean reattachment point are extremely high, even though they are well defined in an average sense.

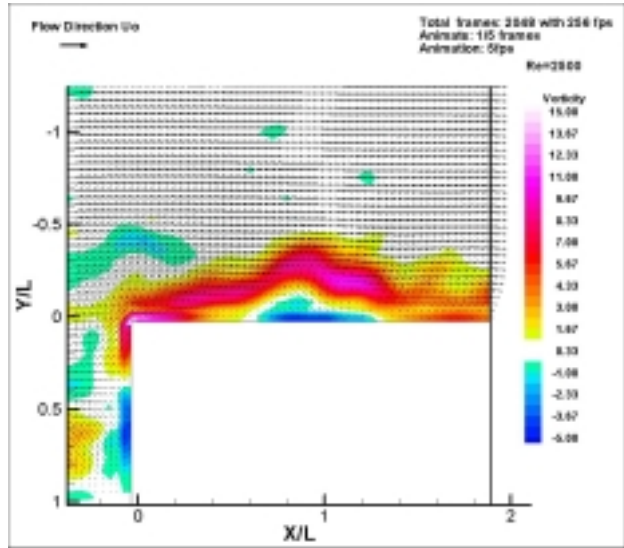


**Animation 4:** Animation of the flow over the prism for duration of 8 secs at  $Re=2500$ . Total number of frames 2048. Animated 400 frames. Speed 5 fps

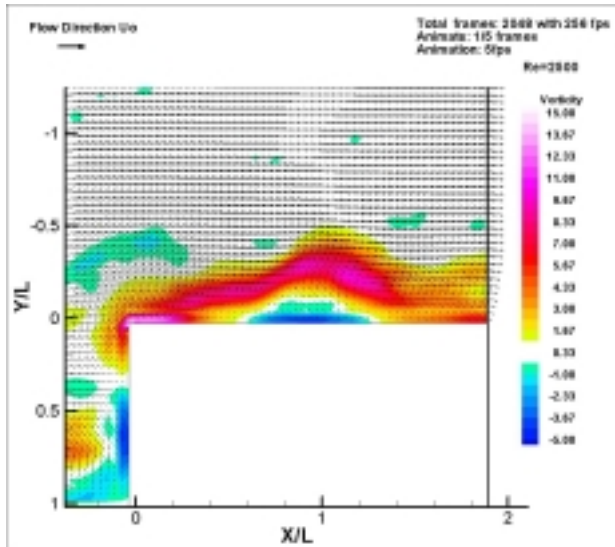
*Chapter 5. Flow Characteristics of the separated region over a surface mounted prism*



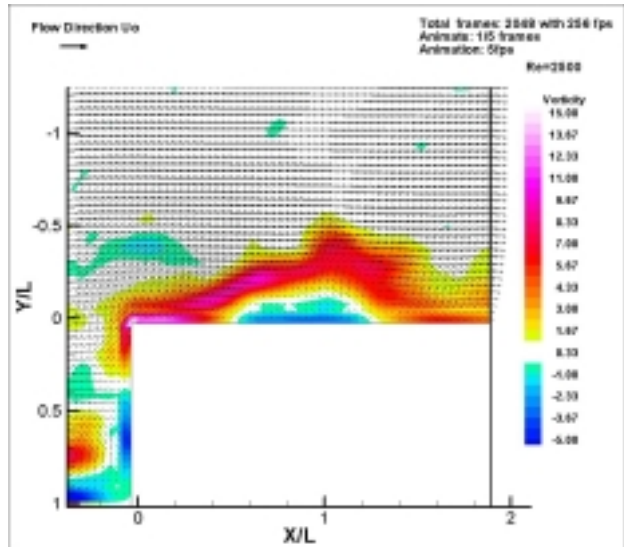
**Animation 4-1:** Instantaneous velocity field and vorticity distribution at relative  $t=0.0$  sec,  $Re=2500$ .



**Animation 4-2:** Instantaneous velocity field and vorticity distribution at relative  $t=0.04$  sec,  $Re=2500$ .

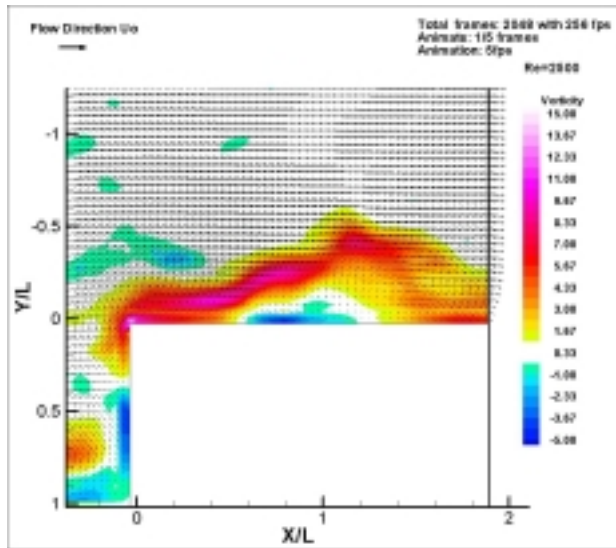


**Animation 4-3:** Instantaneous velocity field and vorticity distribution at relative  $t=0.08$  sec,  $Re=2500$ .

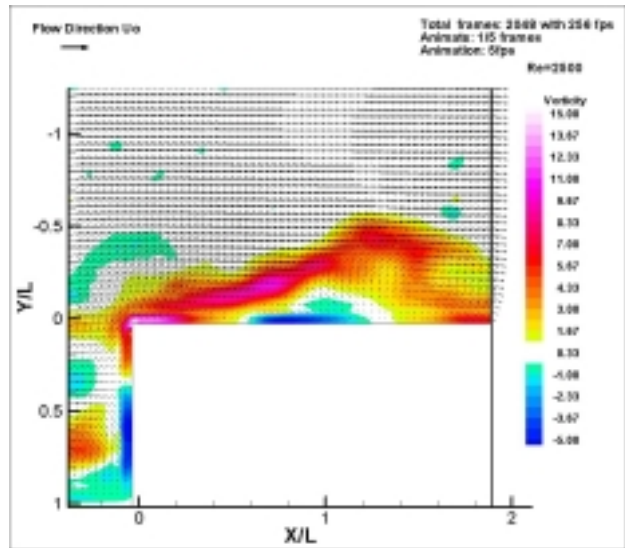


**Animation 4-4:** Instantaneous velocity field and vorticity distribution at relative  $t=0.12$  sec,  $Re=2500$ .

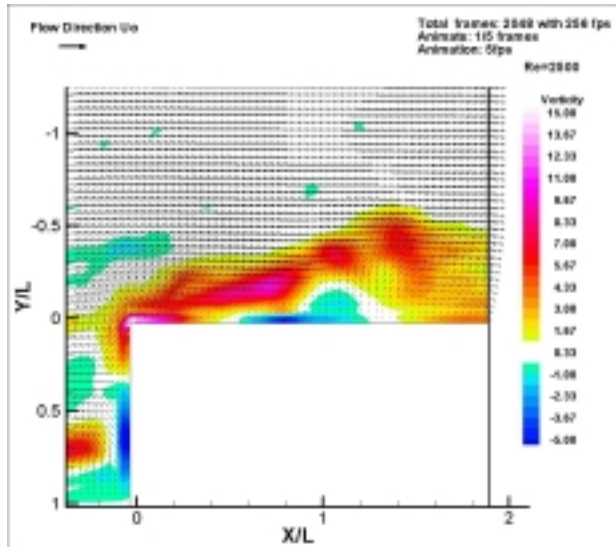
*Chapter 5. Flow Characteristics of the separated region over a surface mounted prism*



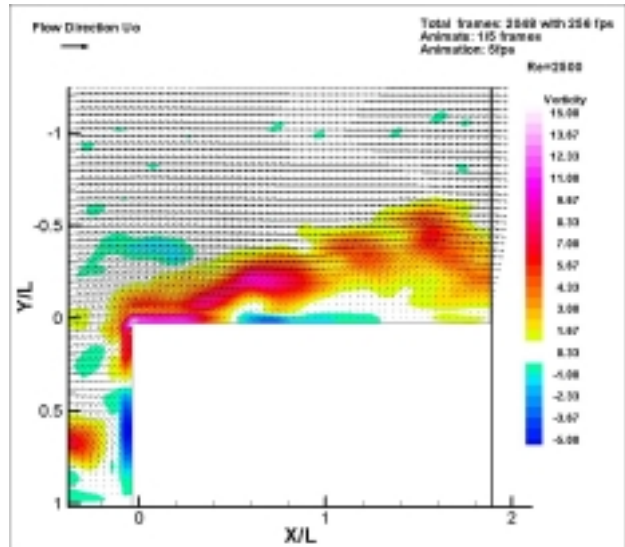
*Animation 4-5:* Instantaneous velocity field and vorticity distribution at relative  $t=0.16$  sec,  $Re=2500$ .



*Animation 4-6:* Instantaneous velocity field and vorticity distribution at relative  $t=0.2$  sec,  $Re=2500$ .

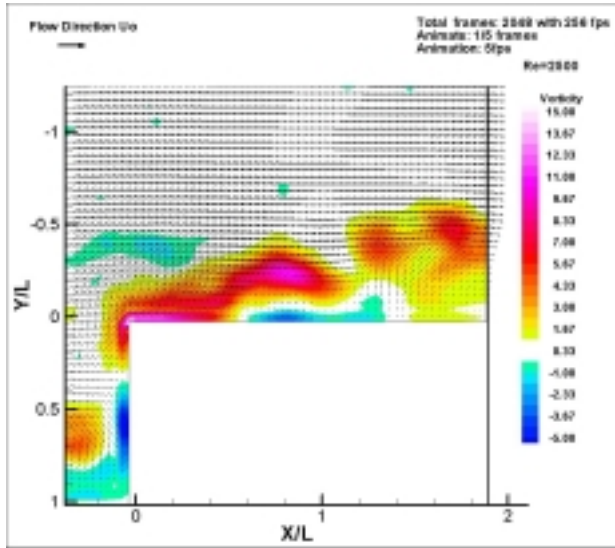


*Animation 4-7:* Instantaneous velocity field and vorticity distribution at relative  $t=0.24$  sec,  $Re=2500$ .

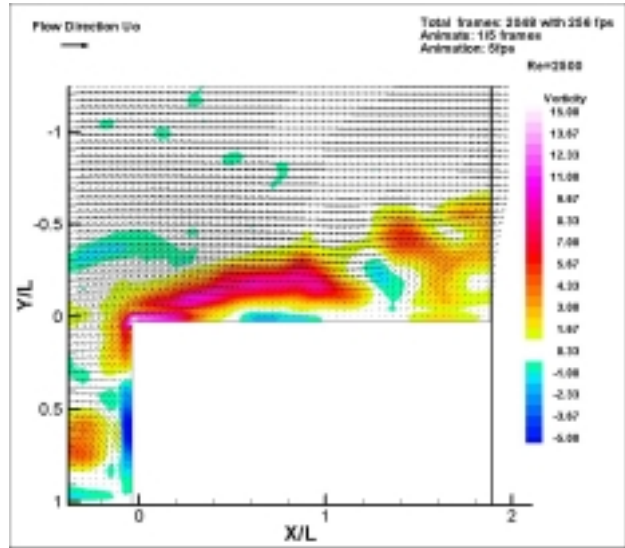


*Animation 4-8:* Instantaneous velocity field and vorticity distribution at relative  $t=0.28$  sec,  $Re=2500$ .

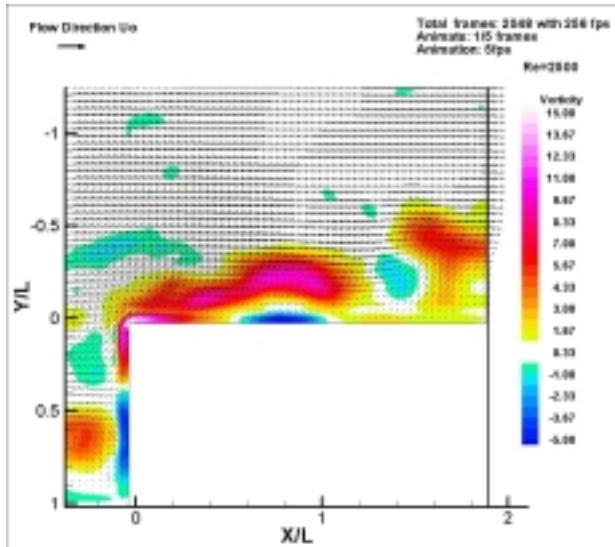
*Chapter 5. Flow Characteristics of the separated region over a surface mounted prism*



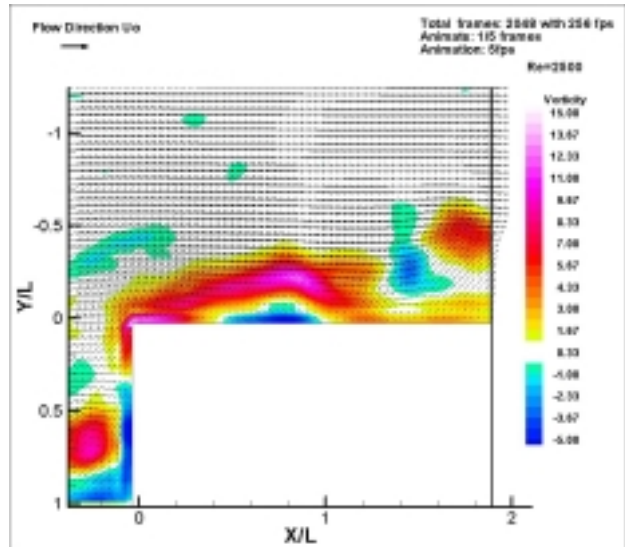
*Animation 4-9:* Instantaneous velocity field and vorticity distribution at relative  $t=0.32$  sec,  $Re=2500$ .



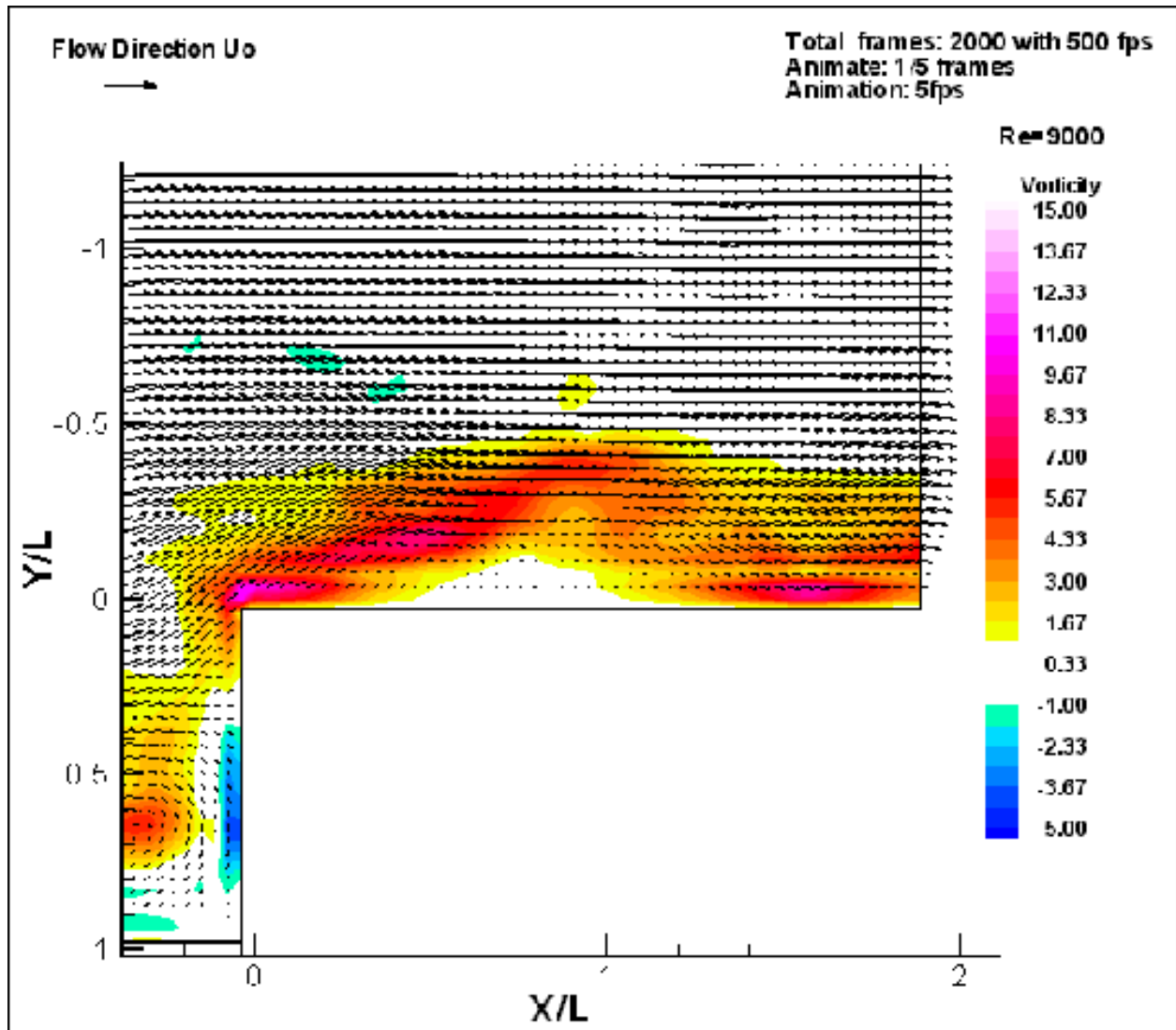
*Animation 4-10:* Instantaneous velocity field and vorticity distribution at relative  $t=0.36$  sec,  $Re=2500$ .



*Animation 4-11:* Instantaneous velocity field and vorticity distribution at relative  $t=0.4$  sec,  $Re=2500$ .

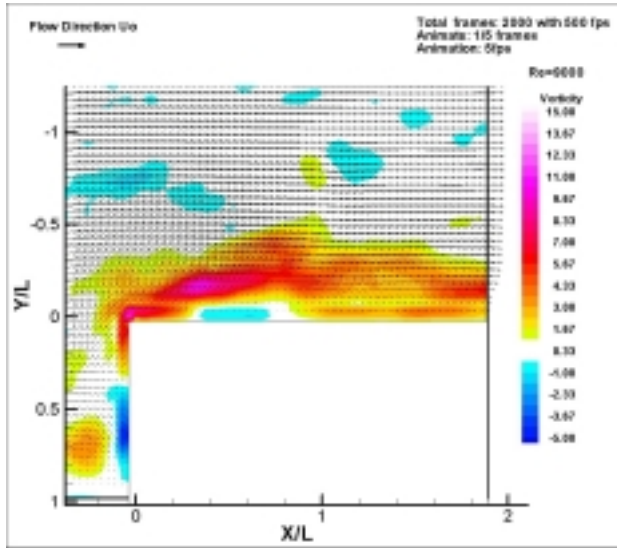


*Animation 4-12:* Instantaneous velocity field and vorticity distribution at relative  $t=0.44$  sec,  $Re=2500$ .

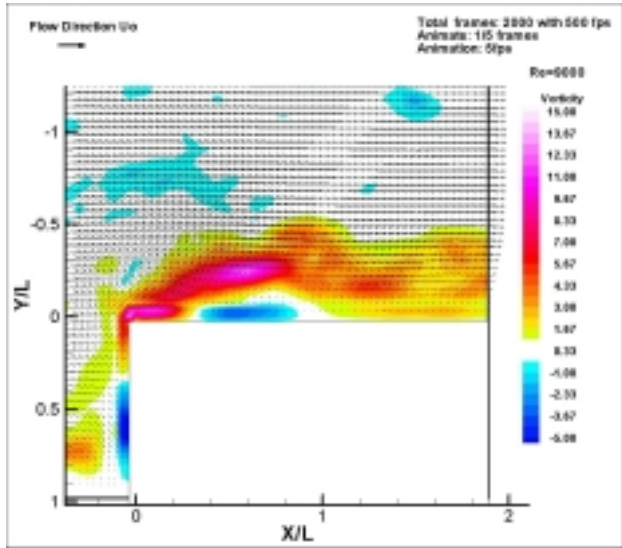


**Animation 5:** Animation of the flow over the prism for duration of 4 secs at  $Re=9000$ . Total number of frames 2048. Animated 400 frames. Speed 5 fps.

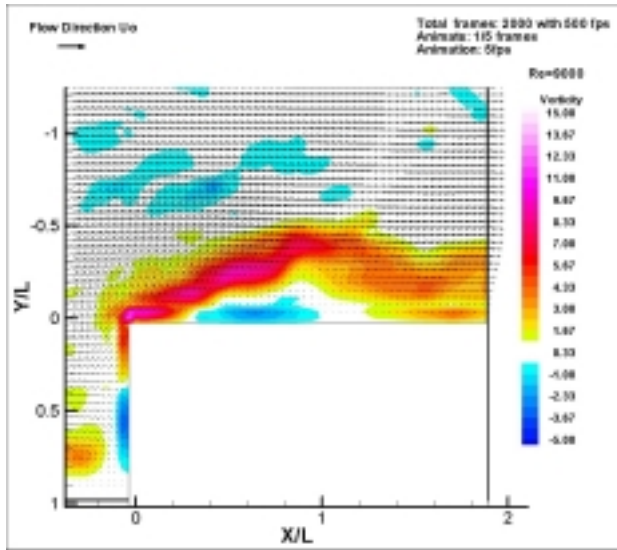
*Chapter 5. Flow Characteristics of the separated region over a surface mounted prism*



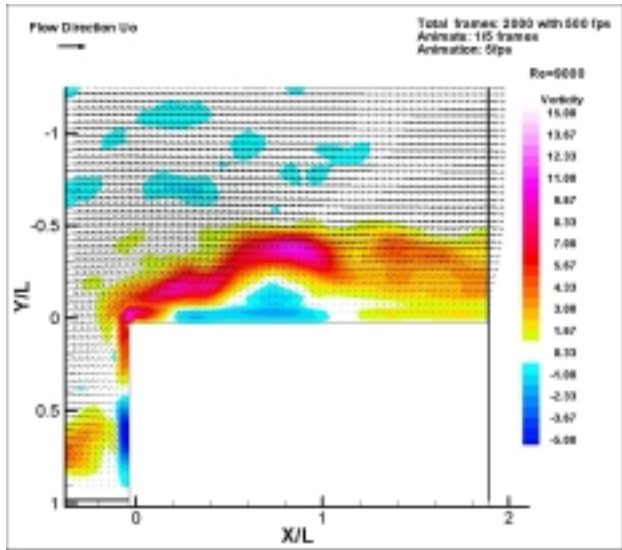
*Animation 5-1:* Instantaneous velocity field and vorticity distribution at relative  $t=0$  sec,  $Re=9000$ .



*Animation 5-2:* Instantaneous velocity field and vorticity distribution at relative  $t=0.02$  sec,  $Re=9000$ .

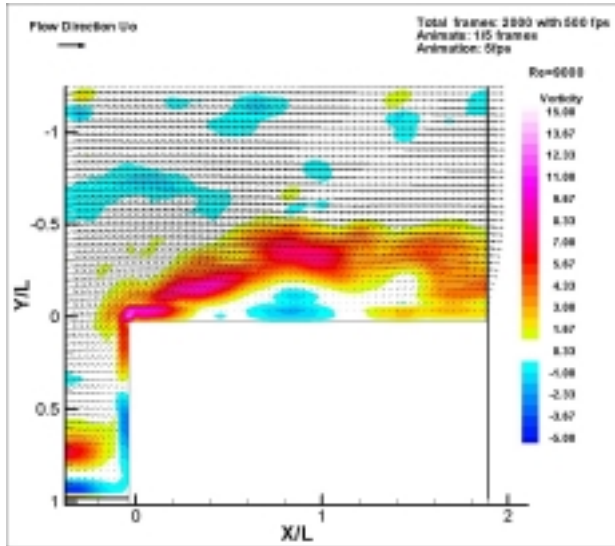


*Animation 5-3:* Instantaneous velocity field and vorticity distribution at relative  $t=0.04$  sec,  $Re=9000$ .

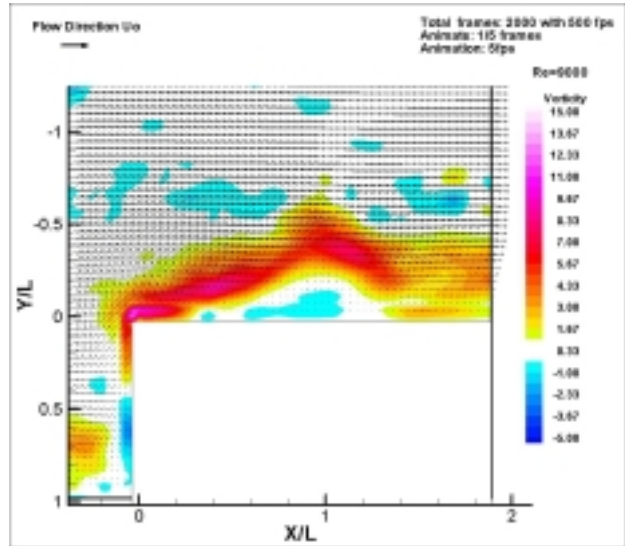


*Animation 5-4:* Instantaneous velocity field and vorticity distribution at relative  $t=0.06$  sec,  $Re=9000$ .

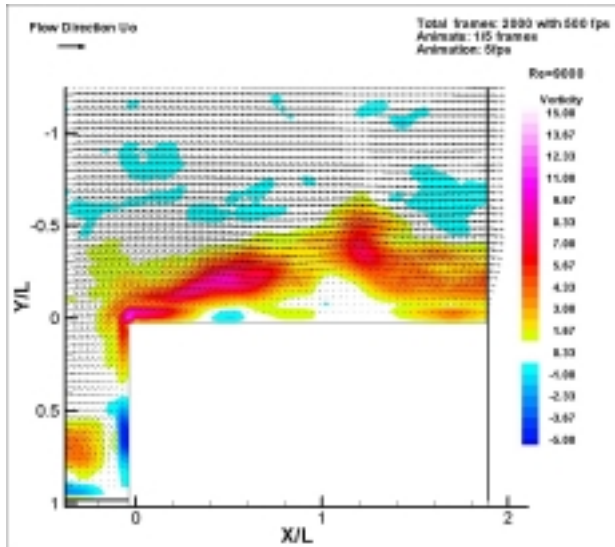
*Chapter 5. Flow Characteristics of the separated region over a surface mounted prism*



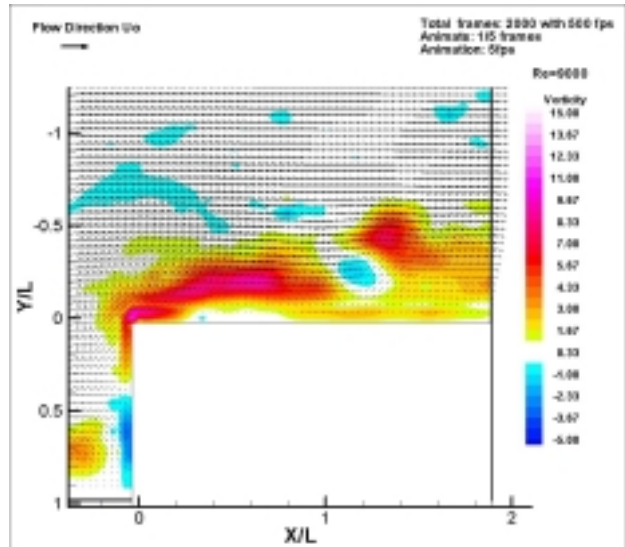
*Animation 5-5:* Instantaneous velocity field and vorticity distribution at relative  $t=0.08$  sec,  $Re=9000$ .



*Animation 5-6:* Instantaneous velocity field and vorticity distribution at relative  $t=0.1$  sec,  $Re=9000$ .

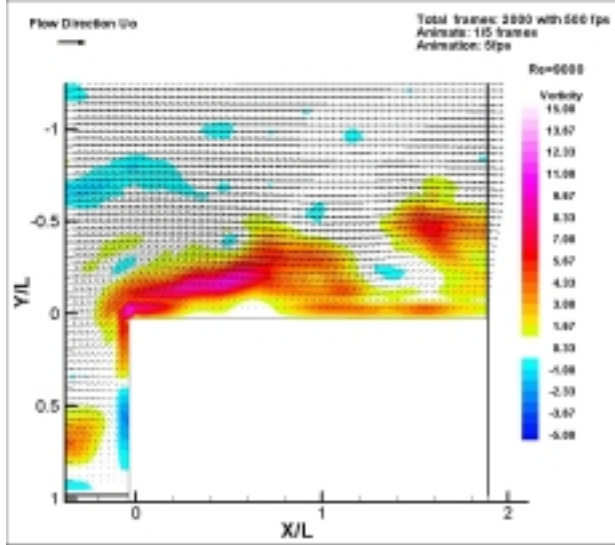


*Animation 5-7:* Instantaneous velocity field and vorticity distribution at relative  $t=0.12$  sec,  $Re=9000$ .

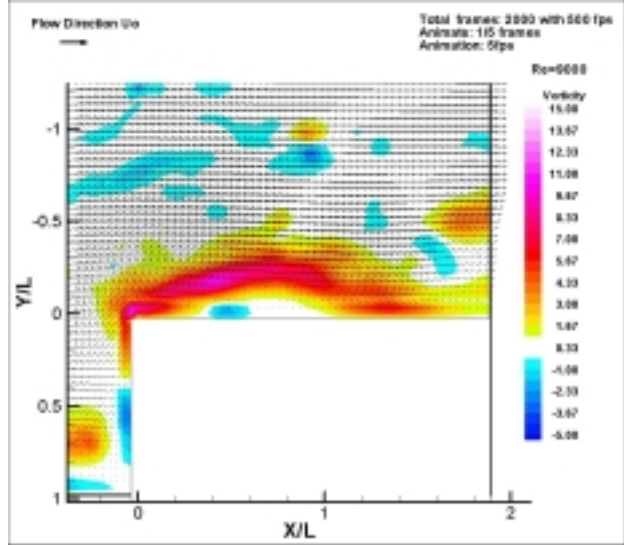


*Animation 5-8:* Instantaneous velocity field and vorticity distribution at relative  $t=0.14$  sec,  $Re=9000$ .

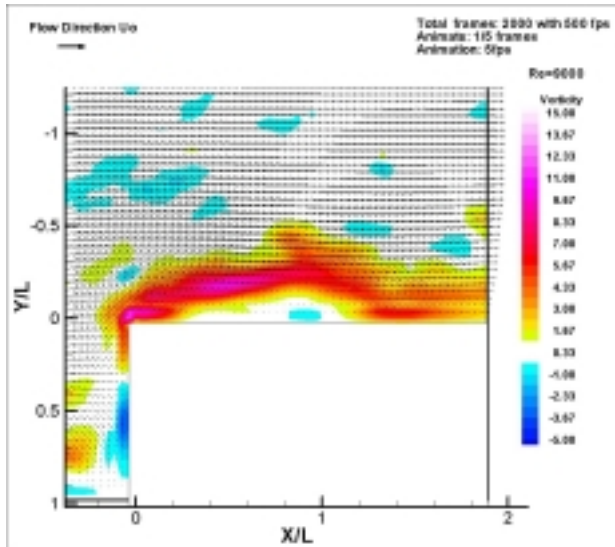
*Chapter 5. Flow Characteristics of the separated region over a surface mounted prism*



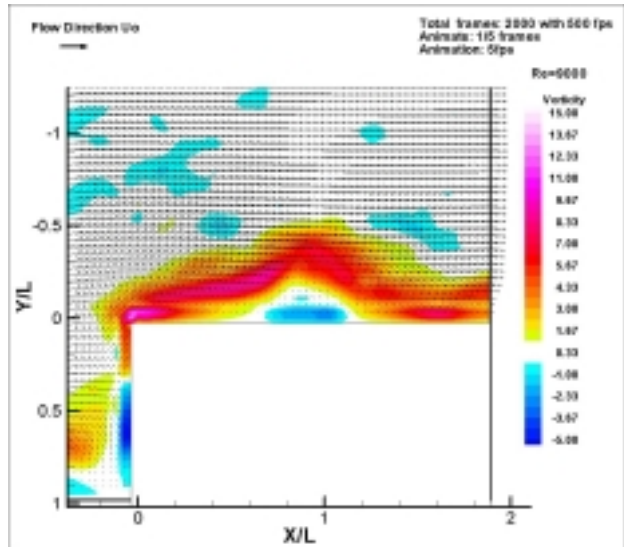
*Animation 5-9:* Instantaneous velocity field and vorticity distribution at relative  $t=0.16$  sec,  $Re=9000$ .



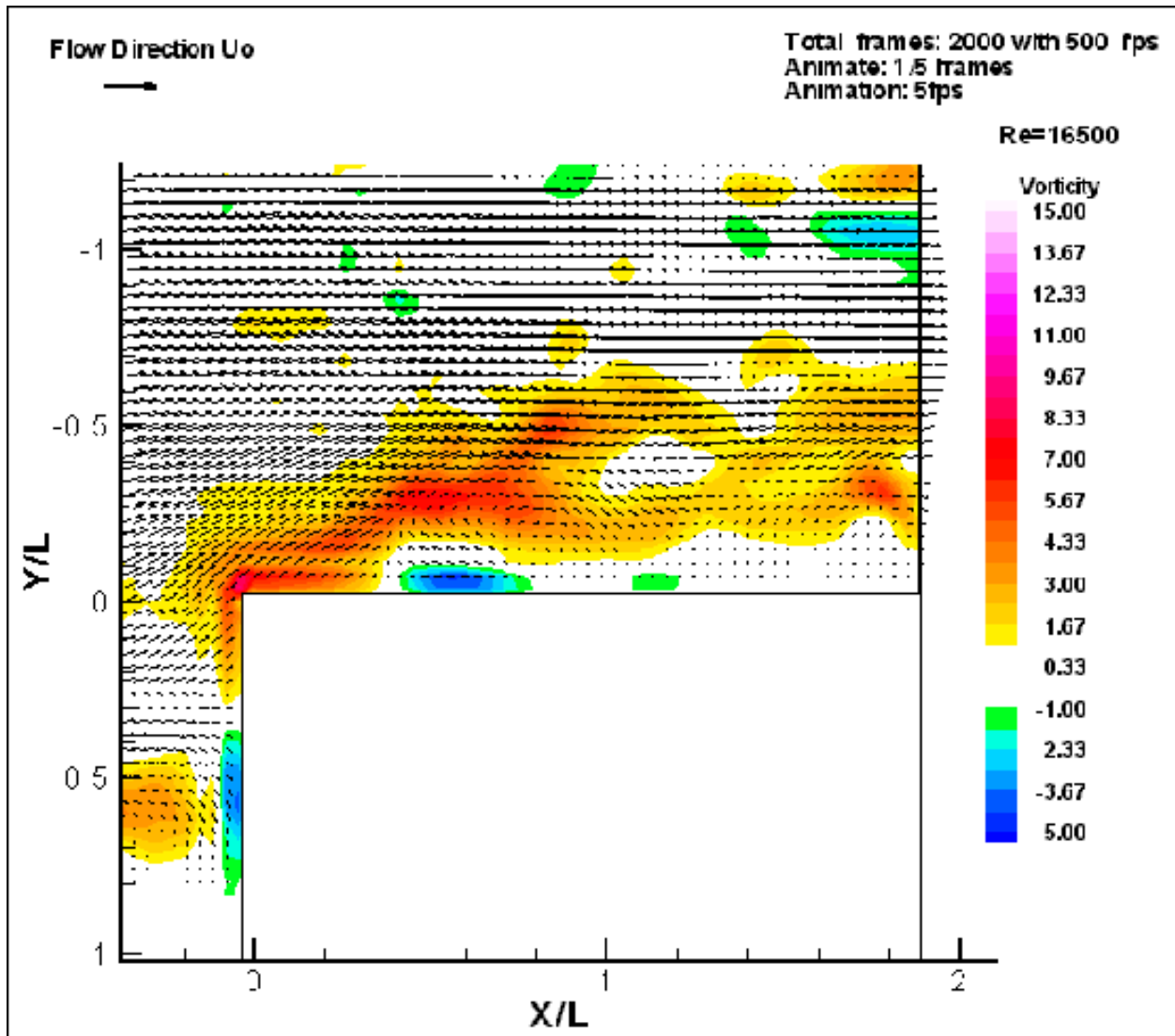
*Animation 5-10:* Instantaneous velocity field and vorticity distribution at relative  $t=0.18$  sec,  $Re=9000$ .



*Animation 5-11:* Instantaneous velocity field and vorticity distribution at relative  $t=0.2$  sec,  $Re=9000$ .

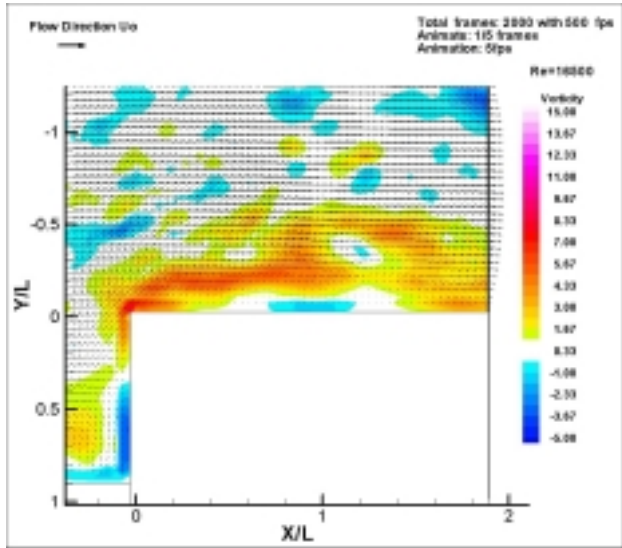
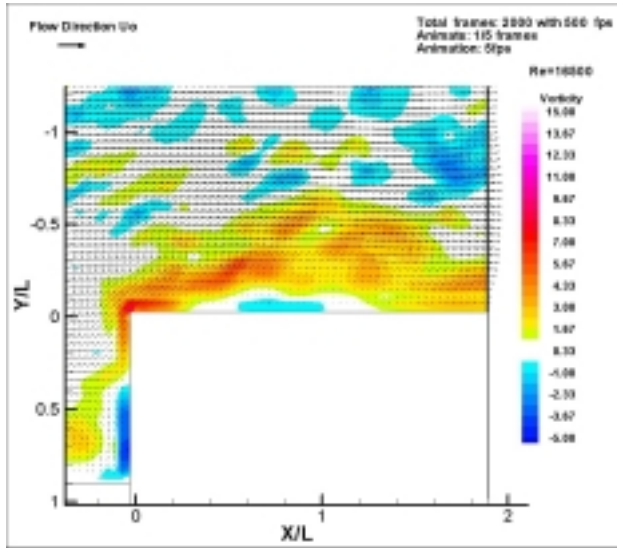


*Animation 5-12:* Instantaneous velocity field and vorticity distribution at relative  $t=0.22$  sec,  $Re=9000$ .



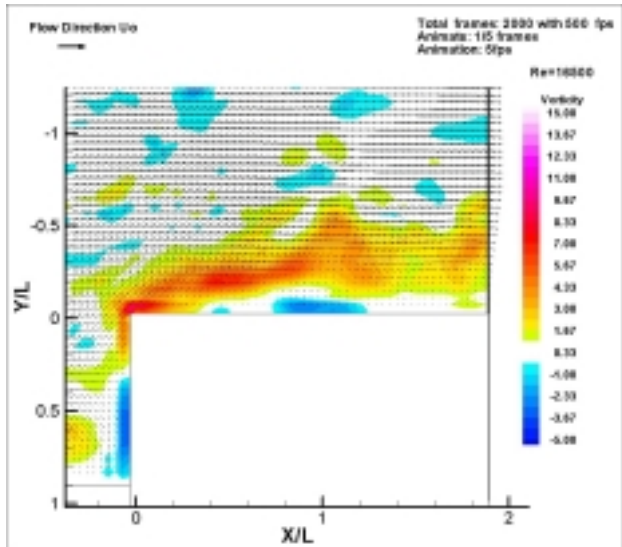
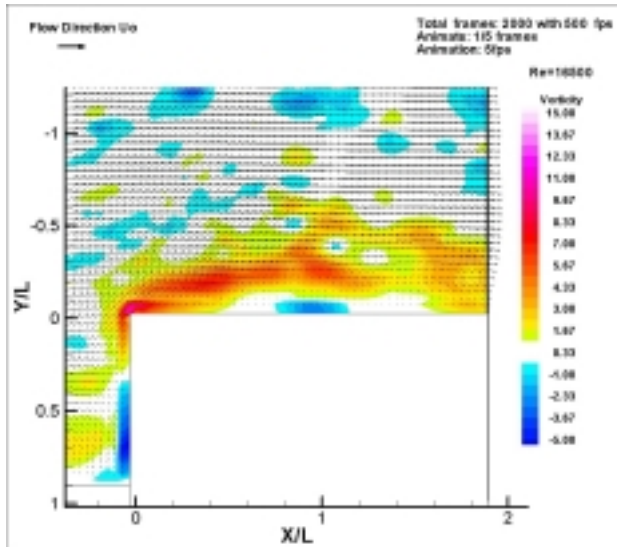
**Animation 6:** Animation of the flow over the prism for duration of 4 secs at  $Re=16500$ . Total number of frames 2048. Animated 400 frames. Speed 5 fps.

Chapter 5. Flow Characteristics of the separated region over a surface mounted prism



**Animation 6-1:** Instantaneous velocity field and vorticity distribution at relative  $t=0$  sec,  $Re=16500$ .

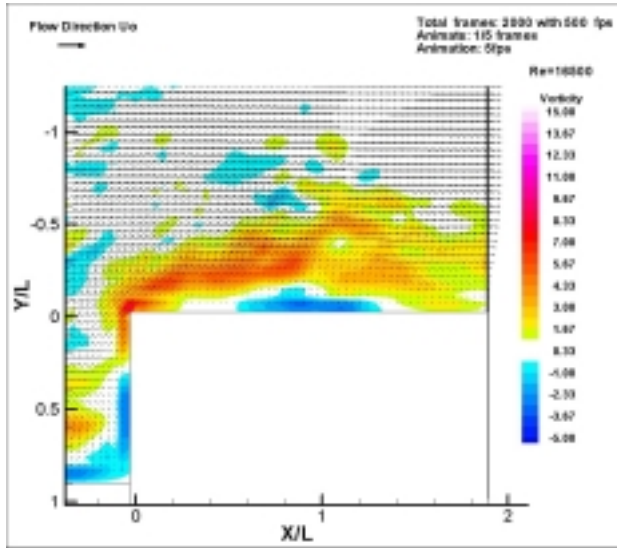
**Animation 6-2:** Instantaneous velocity field and vorticity distribution at relative  $t=0.01$  sec,  $Re=16500$ .



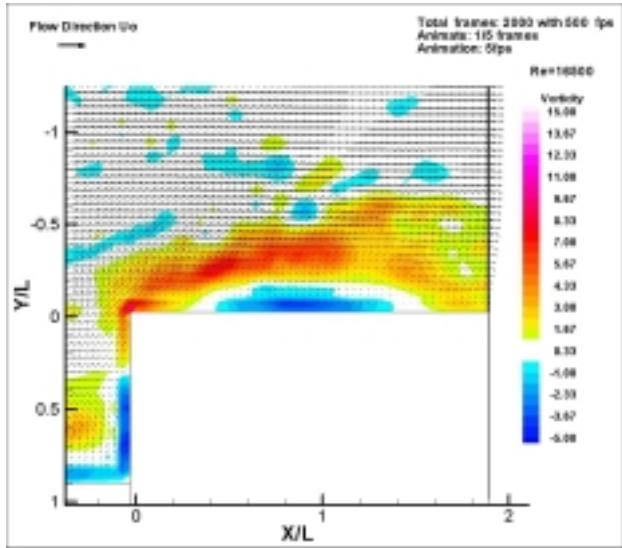
**Animation 6-3:** Instantaneous velocity field and vorticity distribution at relative  $t=0.02$  sec,  $Re=16500$ .

**Animation 6-4:** Instantaneous velocity field and vorticity distribution at relative  $t=0.03$  sec,  $Re=16500$ .

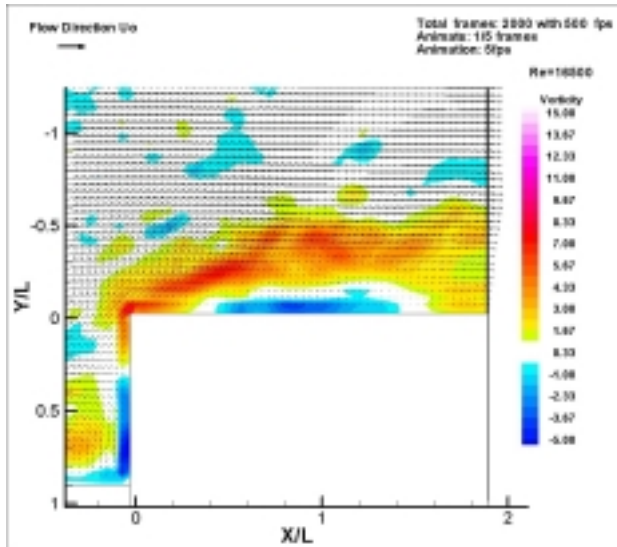
*Chapter 5. Flow Characteristics of the separated region over a surface mounted prism*



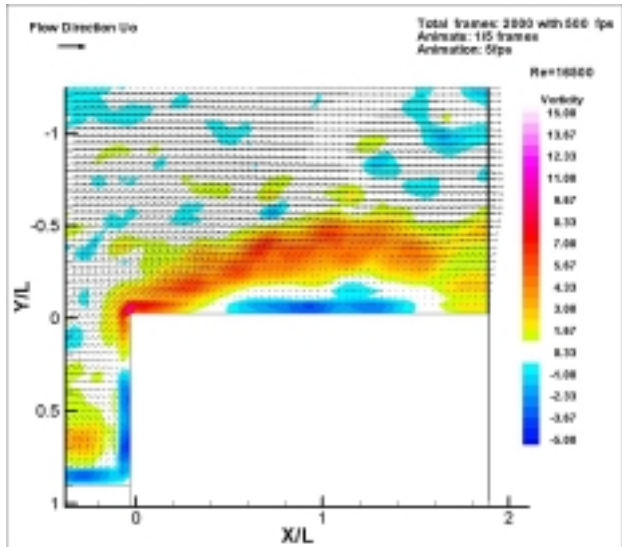
*Animation 6-5:* Instantaneous velocity field and vorticity distribution at relative  $t=0.04$  sec,  $Re=16500$ .



*Animation 6-6:* Instantaneous velocity field and vorticity distribution at relative  $t=0.05$  sec,  $Re=16500$ .

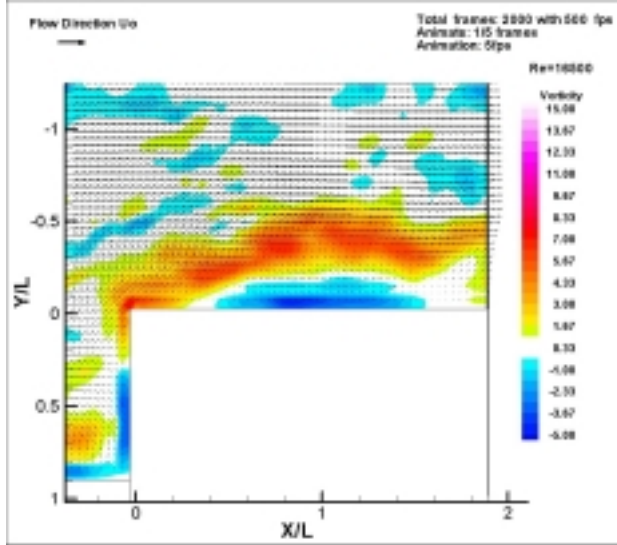


*Animation 6-7:* Instantaneous velocity field and vorticity distribution at relative  $t=0.06$  sec,  $Re=16500$ .

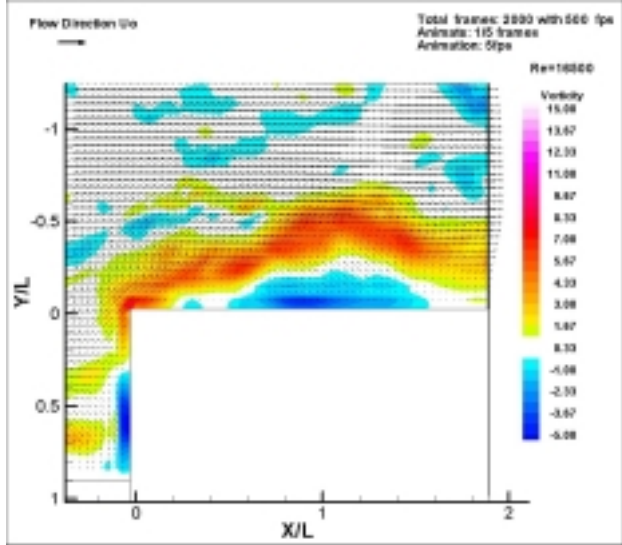


*Animation 6-8:* Instantaneous velocity field and vorticity distribution at relative  $t=0.07$  sec,  $Re=16500$ .

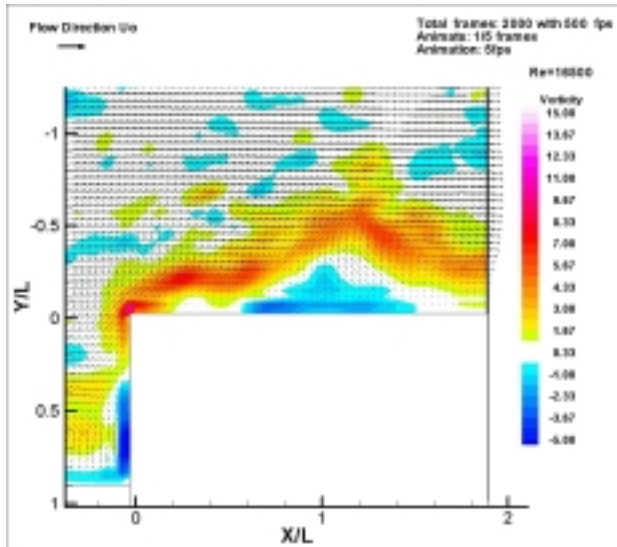
*Chapter 5. Flow Characteristics of the separated region over a surface mounted prism*



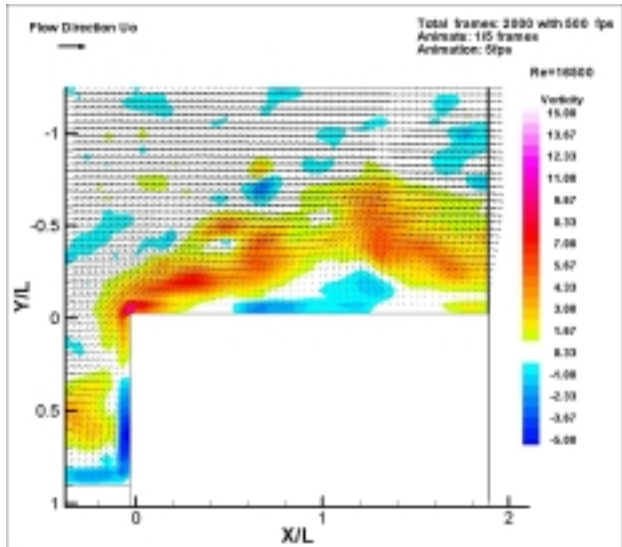
*Animation 6-9:* Instantaneous velocity field and vorticity distribution at relative  $t=0.08$  sec,  $Re=16500$ .



*Animation 6-10:* Instantaneous velocity field and vorticity distribution at relative  $t=0.09$  sec,  $Re=16500$ .

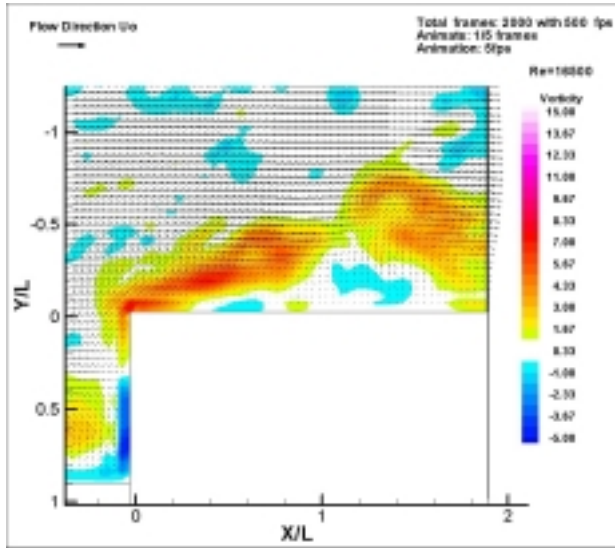


*Animation 6-11:* Instantaneous velocity field and vorticity distribution at relative  $t=0.10$  sec,  $Re=16500$ .

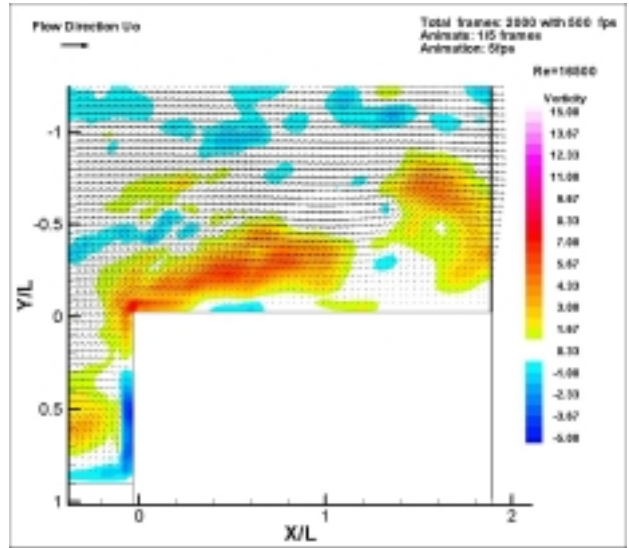


*Animation 6-12:* Instantaneous velocity field and vorticity distribution at relative  $t=0.11$  sec,  $Re=16500$ .

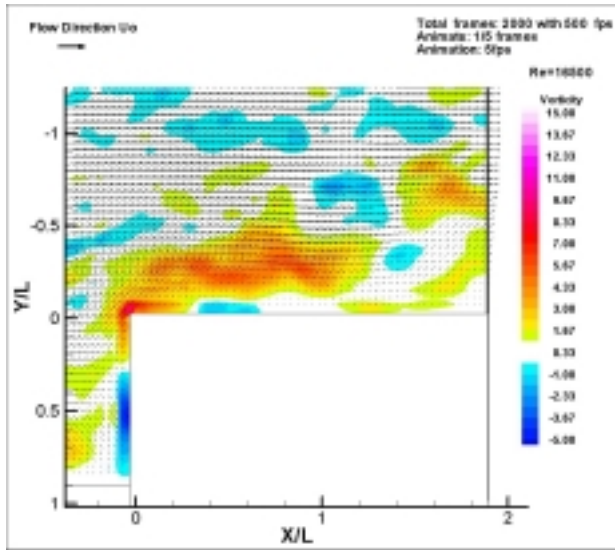
*Chapter 5. Flow Characteristics of the separated region over a surface mounted prism*



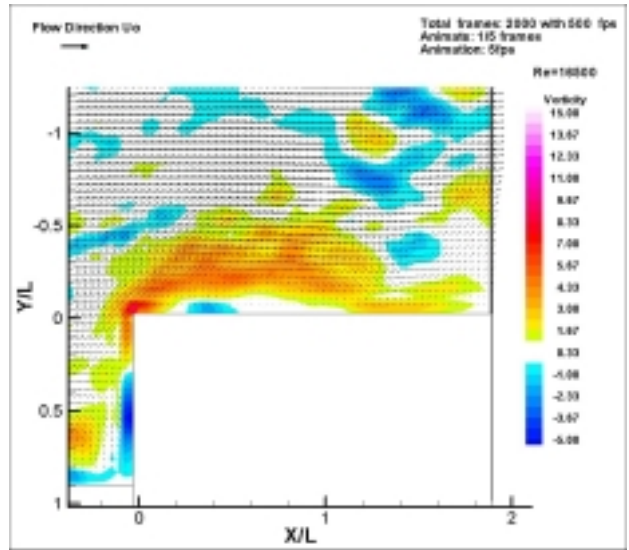
*Animation 6-13:* Instantaneous velocity field and vorticity distribution at relative  $t=0.12$  sec,  $Re=16500$ .



*Animation 6-14:* Instantaneous velocity field and vorticity distribution at relative  $t=0.13$  sec,  $Re=16500$ .



*Animation 6-15:* Instantaneous velocity field and vorticity distribution at relative  $t=0.15$  sec,  $Re=16500$ .



*Animation 6-16:* Instantaneous velocity field and vorticity distribution at relative  $t=0.16$  sec,  $Re=16500$ .

## **Conclusions**

Digital PIV Cinematography (DPIVC) is used to quantify mean and instantaneous flow parameters in the separated flow over a surface mounted prism. The measurements represent original quantitative results of the three-dimensional separated flow around a surface mounted prism and the corresponding characteristics of the separated shear layer. Plane measurements of the mean velocity, magnitude reverse coefficient, vorticity  $u$ ,  $v$  rms distributions and turbulent kinetic energy are presented. By performing such detailed two dimensional time varying velocity measurements with high sampling frequency, we provide results that can be used for validation of numerical codes and turbulence models. The instantaneous variations of the vorticity field are also presented, giving quantitative proof about the extent of the unsteady character of the flow. These results combined with the qualitative observations from the flow visualizations show that the flow undergoes significant variations between a wake expansion, vortex formation and vortex shedding and finally reattachment.

We can summarize the results into the following. The flow visualizations show that the increase of the Re number resulted in displacing the boundary that defines the shear layer, higher with respect to the topside of the prism. Subsequently the size of the recirculation area increases. In the region confined by the shear layer and the mean reattachment point, a domain of zero mean velocity magnitude is defined for all three cases as a result of high velocity fluctuations and flow reversals. For all three cases the forward stagnation point is at the same approximate location with respect to the height of the body, however this point becomes better defined as the Re number increased. The vorticity shed in the flow is generated on the leading sharp edge of the prism and its interaction with the incidence free stream turbulence. Much larger values of negative sign vorticity exist for the higher Re number indicating a stronger reverse flow, without however affecting significantly the mean reattachment point. Most importantly very high RMS values of the velocity components in the region beyond the 50% of the length of the prism, provide quantitative proof of the very unsteady character of the flow. These fluctuations are directly related to the oscillation of the shear layer combined with the wake expansion and vortex shedding mechanisms. The comparable order of magnitude of the velocity fluctuations in the region occupied by the horseshoe vortex with the velocity fluctuations on the top of the prism is

posing the question to which extent these fluctuations and the free-stream fluctuations affect the separation and reattachment process. In addition, the time accurate description of the flow field that was revealed by these measurements indicates that there is not a well defined mean flow structure and the level of periodicity of such flow fields needs to be further investigated.

Without a doubt, by performing measurements in the plane of symmetry of a small aspect ratio prism cannot lead to safe conclusions about the global character of the flow field because of the strong three-dimensionality of the flow. To obtain additional information about the interaction of the separated shear layers from the side corners of the prism with the horseshoe vortex and how these affect the character of the separation bubble on the topside of the prism will require a different experimental approach.

However, the information obtained from this study reveals that the irregular shedding of large vortices in the wake of a bluff body when reattachment occurs is greatly controlled by the generation of opposite sign vorticity in the recirculation region. Once the shear layer is forced to roll-up because of its interaction with the incident free-stream is forming a large and relatively stationary vortical structure, which continuously receives vorticity from the shear layer, thereby increasing the strength of the vortex. The interaction of the vortex with the wall will form a boundary layer on the topside of the prism and generate opposite sign vorticity. Once the circulation of the primary vortex reaches a certain level it will force the boundary layer to lift-up forming a secondary vortex (Doligalski et. al. 1984, 1994). Similarly with the case of the alternate vortex shedding from circular cylinders, (Williamson 1995, 1996) the opposite sign vortex will cut-off the supply of vorticity to the primary vortex forcing the vortex to shed in the wake. However, in the present case, the unsteady character of the interaction of the shear layer with the free stream in combination with the irregular behavior of the horseshoe vortex and the strong three-dimensionality of the flow around the prism causes this process to appear non-periodic.

Finally, a comparison of the mean and instantaneous flow characteristics shows that the concept of a mean flow that consists of a shear layer, a separation bubble and reattachment may not be of much physical significance. The strong unsteady character of the flow that has been

revealed from these results dictates that an accurate study of such complex three dimensional fields need to be performed in a time varying manner. Therefore, any kind of numerical simulation that does not take into account the time dependence of the flow field (steady,  $k-\epsilon$ , *RANS*) or an experimental approach that is carried out in an average manner ( time or ensemble) will provide useful engineering information but a limited inside of the underlying physics.

## **Chapter 6**

# **Control of separated shear layers over sharp edges**

### **Introduction**

This final chapter is somewhat different from the previous ones, thus it is included in the dissertation as an appendix. So far, we have studied the flow structures of massively separated flows with an inherited three-dimensionality imposed from the boundary conditions, or from the geometry, or from both. However, for most engineering purposes the understanding of the underlying physics does not serve any purpose if it cannot be combined with a methodology to effectively control the flow to our benefit. Most flow control studies are focusing in the measurement of loads or frequencies ignoring the flow effect of the flow control in the flow structure it self. The reason for that is obvious. A flow control study and even more a close loop feedback control system is equivalent to a multivariable optimization problem. Especially if this control needs to be applied on an unsteady separated flow, the number of possible degrees of freedom is significantly large to be considered and studied to its full extend. An approach to measure pressures, loads or frequencies allows the fast alternation and combination of many of these parameters and speeds up the process of the overall optimization of the system. A study involving LDV would be prohibitive because of the extensive amount of time necessary to map

the whole flow field with sufficient time resolution. Take into account the unsteadiness (natural or forced) of the phenomena under investigation and numerous combinations needed and it is easy to reach the conclusion that such an attempt would be pointless.

Furthermore, all the above measurement methods are point measurements, therefore measuring the whole flow field will provide only time average information and remove any time dependent characteristics. For the reason described above, one of the objectives of this chapter is to illustrate the power of a whole field measurement technique such as PIV to provide accurate and detailed information in space and time simultaneously in order to reveal the effect of flow control on complex flows. The other goal is to attempt to effectively perturb the flow in such a way that the desired result will be achieved. The flow of a double arc sharp edge airfoil in an angle of attack was chosen for the simplicity of the geometry as well as for its engineering importance.

The physical mechanisms responsible for separated and post stall flow over airfoils have been studied extensively in the past because of their importance to applications. Both numerical and experimental studies have been conducted to provide a better understanding of the physics and to indicate the most effective means of control. Most of these investigations deal with airfoils with rounded edges at small angles of attack ( $AOA < 15^\circ$  to  $16^\circ$ ). Airfoils with sharp leading and trailing edges and for angles of attack over the stall limit have not received much attention. In the case of the sharp-edge airfoil, the flow will separate even at very small angles and as we further increase the angle of attack, a fully separated flow develops and the wing behaves as a bluff body. The need for performance enhancement mechanisms becomes evident.

The control of flow separation has been discussed extensively in recent review articles (Gad-el-Hak, 1990, Gad-el-Hak and Bushnell 1991). A variety of methods has been employed with considerable success for flows about airfoils with rounded leading edges. Most recently, Seifert and Pack (1998) demonstrated that unsteady blowing (Seifert, et al. 1996) can be effective in controlling boundary layer separation over a wide range of chord Reynolds numbers. However, all this work is limited to angles of attack only a few degrees beyond stall, i.e.,  $15^\circ$  to  $16^\circ$ . For the case of deep stall, separation is unavoidable and the wakes of all wings are dominated by alternately shed vortices. The challenging task is now to control and manage this

naturally unsteady phenomenon. A few recent experimental and numerical studies proved that this is indeed possible. These studies have indicated that, for a wide range of post-stall angles of attack, for a two-dimensional airfoil or a wing with large aspect ratio and small sweep angle, the lift can be greatly enhanced by unsteady flow control (Zhou et al. 1993; Hsiao et al. 1990, 1993, 1994; Chang et al. 1992; McManus and Magill 1996; Wu et al 1997a,b).

Employing acoustic disturbance, or oscillating flap excitation, Hsiao and his associates were able to increase the lift of a NACA 63-018 airfoil by 60%. The numerical investigation of Wu et al. (1997a,b) provided further evidence on the effectiveness of this unsteady control technique. They computed lift increases for a NACA-0012 airfoil with the Reynolds number based on chord length  $Re_c = 5 \times 10^5$  at a wide range of post-stall angles of attack. They indicated that the “lift valley” beyond the stall angle of attack is almost filled up, except for a narrow region very close to stall and that the effective control range may extend to about  $\alpha = 35^\circ$  for this airfoil. They also pointed out that in a wide range of post-stall angles of attack, a disturbance near the leading edge of an airfoil may lead to lift enhancement, drag reduction and buffet suppression. The significant finding of Zhou and his associates (Zhou et al. 1993) is that a control mechanism is equally effective with sharp leading edges. They mounted a small oscillating flap on the sharp leading edge of an airfoil and showed that if the flap is oscillated in pitch with a  $5^\circ$  amplitude, at the frequency of vortex shedding, the lift could be increased by over 50%. There is also evidence that vortex shedding over highly swept wings at high angles of attack. Members of this group (Rediniotis, et al. 1993) demonstrated this with a  $70^\circ$ -sweep delta wing. Application of an oscillating leading edge flap in this case may also lead to increased lift. In this chapter, we will discuss our efforts to extend the concept of flow control to sharp-edge airfoils at high angles of attack. The success of this idea hinges on the better understanding of periodic vortex shedding over such airfoils and apparently, this aspect of the problem has not yet been investigated.

In this experimental study, we investigate the flow over a sharp-edge airfoil and methods to effectively control it. Digital Particle Image Velocimetry (DPIV) is implemented to investigate the physics related to the flow. Results for a range of angles of attack over a reference airfoil are compared to a flow control model. State of the art piezoelectric actuators are used to introduce a disturbance in the flow via a leading edge flap. For post-stall conditions

examined the alternate vortex shedding is unavoidable. Flow control at the appropriate frequency can increase the vorticity content of the stall vortices and induce its motion close to the airfoil surface.

## **Facilities and Instrumentation**

The experimental study was conducted in the Engineering Science and Mechanics Water Tunnel facility at Virginia Tech, using digital particle image velocimetry (DPIV). The advantages of DPIV method have been discussed extensively by many authors (R. J. Adrian, 1991, Willert and Charib, 1991, R. J. Adrian, 1996).

The ESM water tunnel can be run both as a closed and as a free-surface facility. The tunnel operates in a closed loop with up to 2,500 gallons of water. After the settling chamber, a three-way convergence leads to the 24" x 24" x 72" test section made of a clear, acrylic Plexiglas. A 4500 GPM axial flow pump drives the flow at speeds up to 1 m/s, with free stream turbulence levels less than 2%.

Two-dimensional velocity plane measurements were acquired providing qualitative and quantitative information for the flow. For the PIV laser sheet, the light source was a copper vapor 45 Watt pulsed laser, delivering approximately 15 mJ/pulse at its optimum operation. Using a set of sheet forming optics, a laser sheet was delivered in the test section, shown schematically in Figure 1. The laser was synchronized with a high speed CCD camera able to take 1000 images/sec with a resolution of 256x256 pixels. Hollow glass spheres of 10 microns mean diameter were used as flow tracers.

Two models were constructed for this investigation, a reference model and a flow control model. Both models were constructed with sharp leading and trailing edges. The upper and lower surfaces are circular arcs and the airfoil has a thickness to chord length ratio of 0.15. The flow control model has a leading edge flap actuated by piezoelectric actuators, see Figure 2. The leading edge flap is 6.25% of the airfoil chord length.

Thunder piezoelectric actuators were employed for this study. Based on patented technology licensed from NASA, these devices are durable, solid-state construction and can

provide significant mechanical output under load. At excitation frequencies of 2,4,and 8 Hz they oscillate the leading edge flap through an angle of  $3.3^\circ$ ,  $2.68^\circ$ , and  $2.1^\circ$  respectively.

DPIV measurements were taken over both airfoil configurations for 10, 20 and 30-degree angles of attack. These angles of attack correspond to approximate vortex-shedding frequencies of 3, 2, and 1 Hz respectively, determined from flow visualizations. All measurements were taken at a flow speed of 30 cm/s, which corresponds to a  $Re_c$  of 22114.

## **Results and Discussion**

The flow over any sharp leading edge separates at the edge. No flow control mechanism could avoid separation. Nevertheless, there is a possibility to manage the separated region in order to reduce the suction side pressure and therefore increase the lift. This can be achieved in two ways. The first is to force the free shear layer closer to the wing. This is equivalent to pushing separation downstream over an airfoil with a rounded leading edge. The second mechanism is to energize the wake by adding vorticity to it. This is equivalent to the Weiss Fogh mechanism whereby a vortex is trapped on the suction side of the airfoil. In the present case, this is not possible because the flow is going through a dynamic process of vortex shedding. However, it is possible in an average sense, as Wu et al have pointed out.

There is a natural vortex shedding activity over the airfoil, which is characterized by a distinct shedding frequency. In each case, we captured two thousand instantaneous frames, at a rate of 500 Hz, covering several periods. We then averaged these data to generate averaged velocity, streamlines and vorticity fields. In all of the plots shown the flow is from left to right and the leading edge of the airfoil is at  $x=1.0$  and the trailing edge is at  $x=0.0$ . In Figure 3 we present two average vector fields at  $20^\circ$  AOA from which we calculate vorticity, stream function, and streamlines. In Fig. 4, we present the vorticity field over the airfoil placed at an angle of attack of 10. Rather little influence of the placement of a fixed flap or an oscillating flap is observed. Apparently the vortex shedding activity is developing downstream of the airfoil and it is not easy to influence it by introducing disturbances in the free shear layer.

For the case of an airfoil at an angle of attack of 20, the results are presented in Fig. 5. Here we observe a very interesting phenomenon. The placement of a fixed flap as shown in Fig. 2 is enough to create a disturbance in the free shear layer which forces it to incline closer to the surface of the airfoil. The greatest influence on the free-shear layer inclination we obtained by disturbing the free-shear layer at a frequency of 2Hz. The frequency of the leading edge actuation, which most clearly matches the natural shedding frequency of the airfoil at this angle of attack. Moreover, the actuated cases indicated the transfer of some vorticity in the wake to a region closer to the airfoil. This is reminiscent of a trapped vortex for this time-averaged data.

The case of 30 degrees shown in Fig. 6 shows a somewhat different influence of the leading edge flap actuation. Again the contours of vorticity show a transfer of vorticity into the wake of the airfoil. This vorticity, although lower in magnitude of the 20° case, is closer to the leading edge of the airfoil. The difference between these two cases could be due to the need for larger amplitude disturbances at higher angles of attack. These results or the lack of significant influence is in disagreement with the results of Zhou et al. The discrepancy between these two cases could be because the amplitude of flap oscillation is lower for the 30° case than the amplitudes employed by Zhou et al. Moreover, it is known, that the flow control mechanism is most effective if the disturbance is introduced at the shedding frequency, which for the 30° case is lower than initial disturbance frequency of 2 Hz used in this study.

Figures 7 and 8 show streamlines plotted from a calculation of the stream function. Again these plots are time averaged over several periods of vortex shedding. Figure 7 shows the 20° angle of attack case for the reference airfoil and all frequencies of actuation. The conclusions from the streamlines coincide with those from the vorticity plots. Both a reduction in the shear layer angle, pushing it closer to the wing, and a time averaged vortex structure closer to the wing can be seen for all cases. Again, the most effective actuation frequency is 2 Hz, which is the closest frequency to the natural vortex shedding frequency. However, this time-averaged vortical structure is off the trailing edge of the airfoil, thereby reducing its contribution to the lift of the airfoil. Figure 8 again shows the reference airfoil and all frequencies of actuation at 30° angle of attack. In this case both for the reference airfoil and 0 Hz actuation control model multiple time-averaged vortical structures can be observed. Actuation of the

leading edge flap at any of the frequencies tested shows the creation of a single time-averaged vortical structure off the leading edge. It is proposed that the fixing of the shedding process into a single structure could increase lift.

## **Conclusions**

The present investigation indicated that for the three angles of attack tested the most effective flow control results were obtained for the  $20^\circ$  angle of attack case and excitation at the natural frequency. The disturbance forces the free shear layer to lean closer to the airfoil surface, thus bringing it closer to attached flow. Moreover, in all cases, we observed some increase in the vorticity level within the wake, which implies a more energized vortex. However, the results do not represent significant departures from the reference case. A more careful detection of the natural shedding frequency will be required. Moreover, it is proposed to increase the amplitude of the flap oscillation.

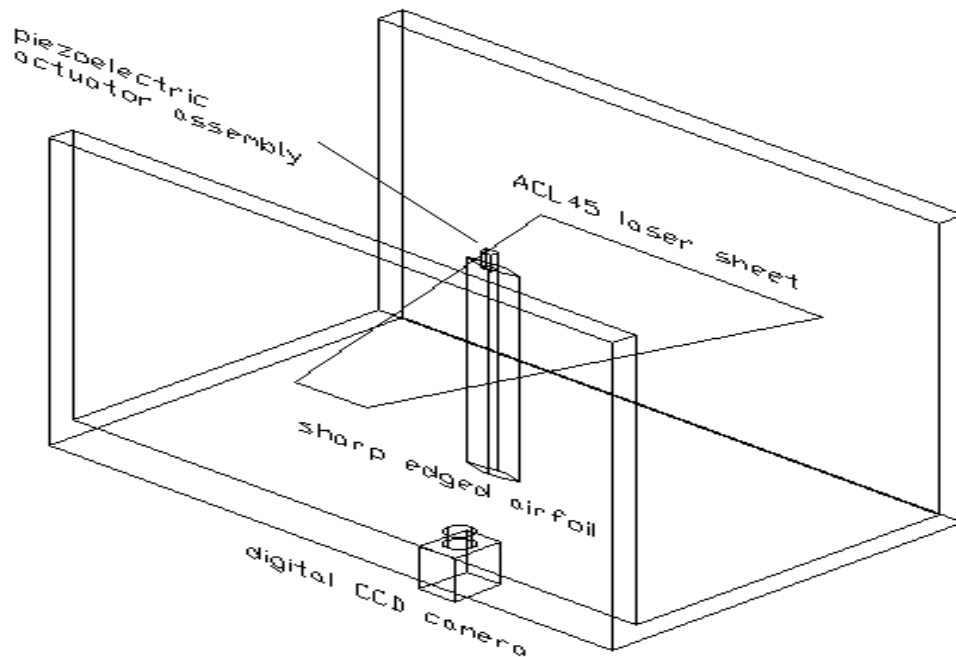


**Figure 1:** Schematic of experimental setup

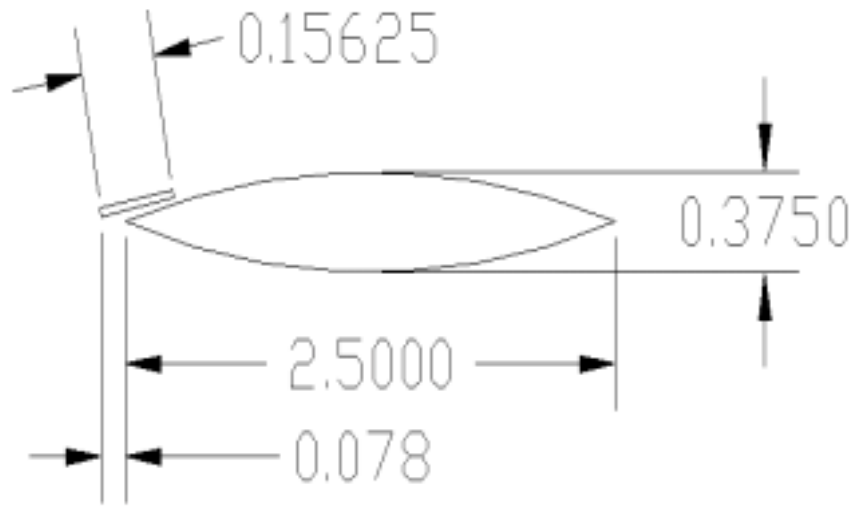


**Figure 2:** Sharp edged airfoil dimensions(all dimensions in inches)

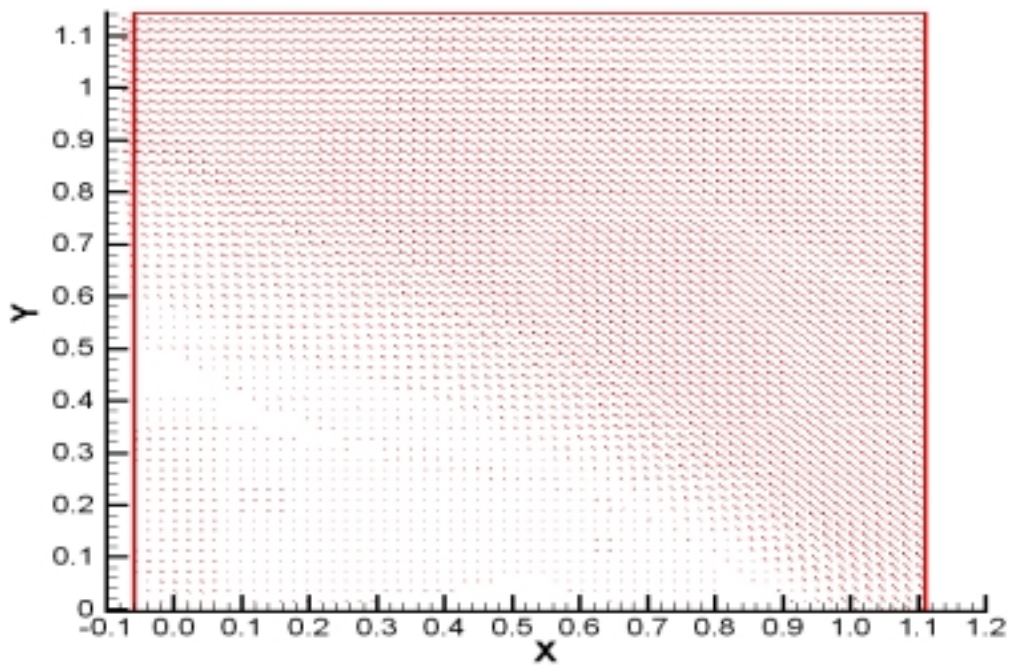


**Figure 3:** Average Vector Field, 20° AOA, Reference Airfoil

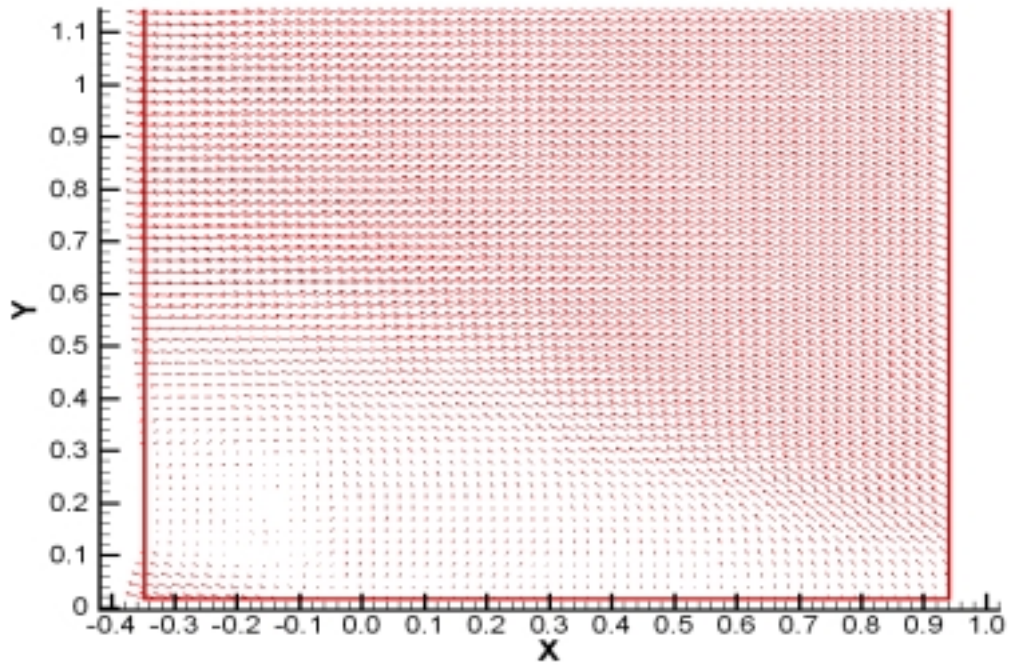


Figure 4: Average Vector Field, 20° AOA, 2 Hz Actuation

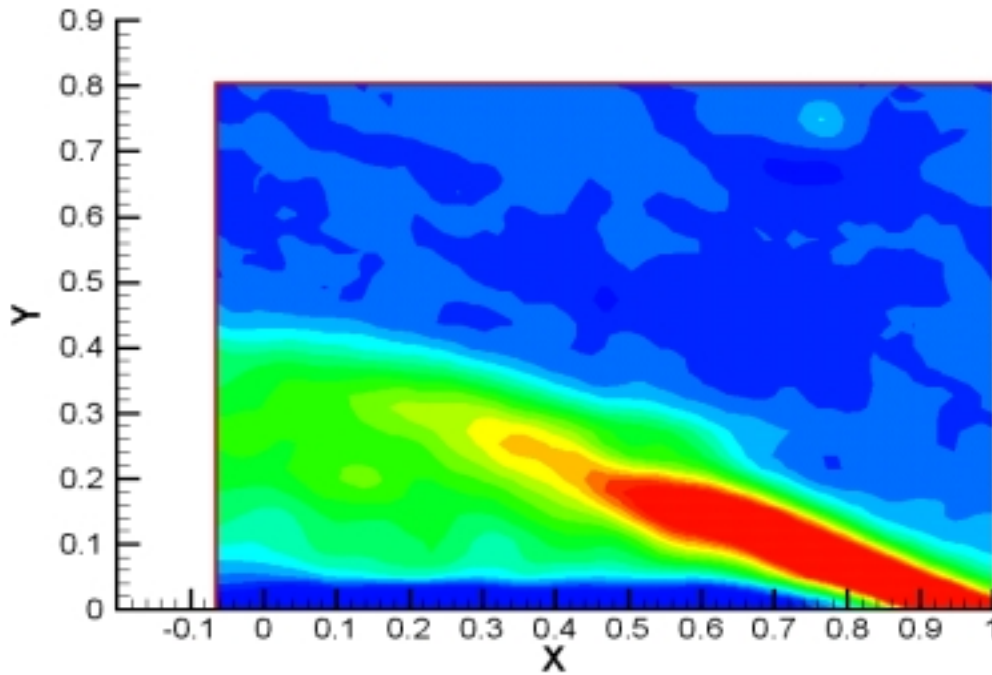
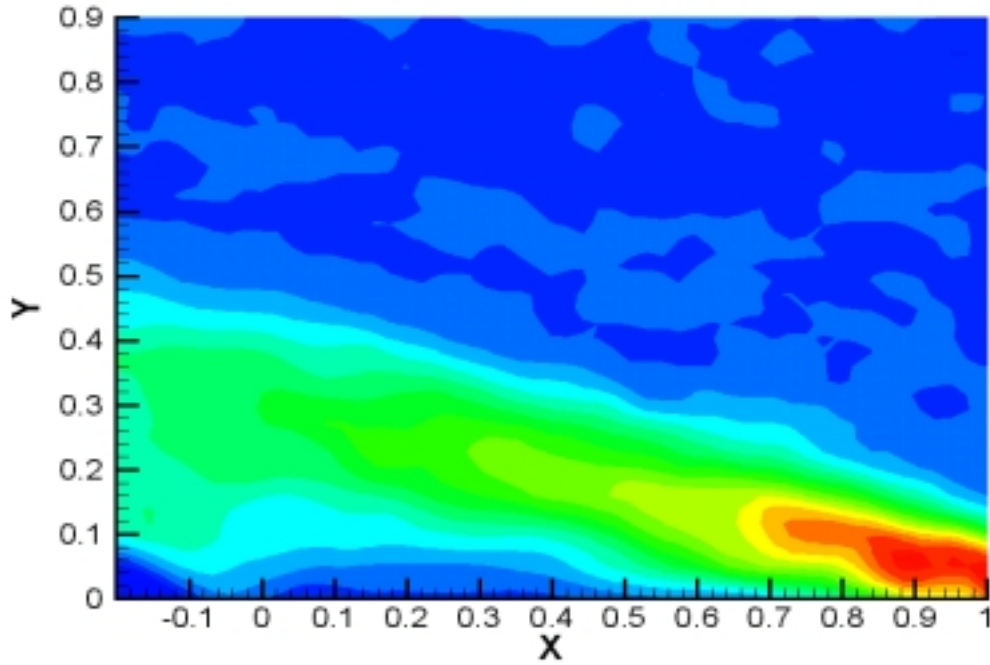
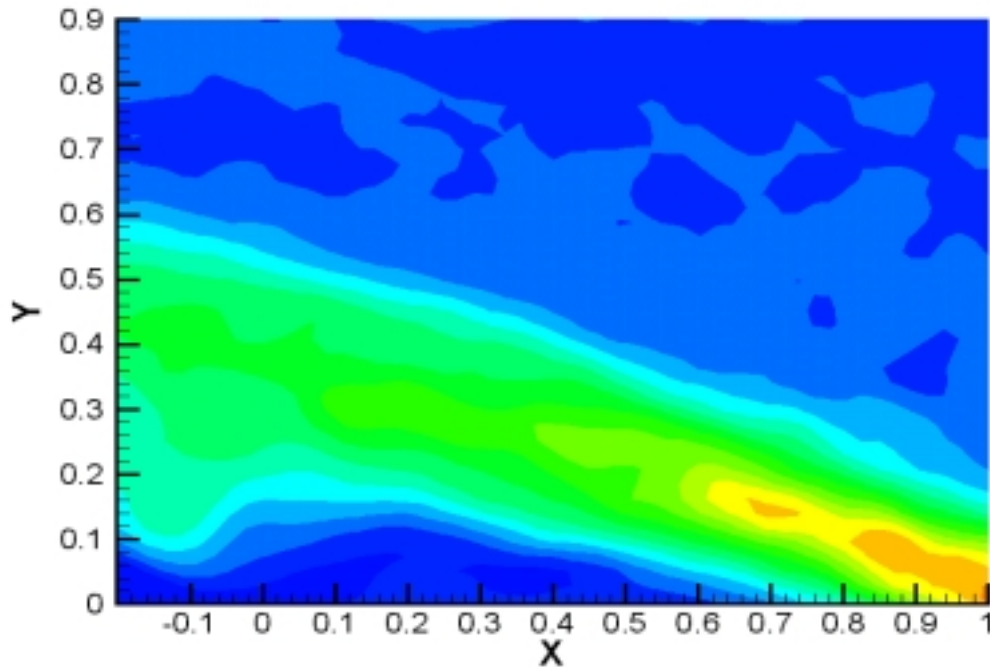


Figure 5: Vorticity 10° AOA, Reference Airfoil



**Figure 6:** Vorticity 10° AOA, 0 Hz Actuation



**Figure 7:** Vorticity 10° AOA, 2 Hz Actuation

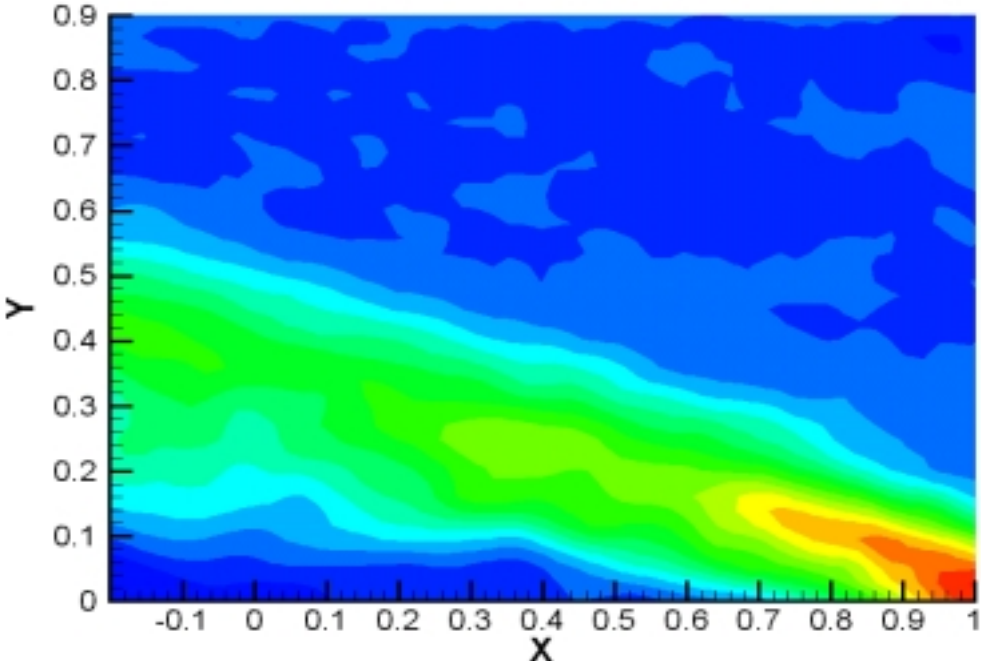


Figure 8: Vorticity 10° AOA, 4 Hz Actuation

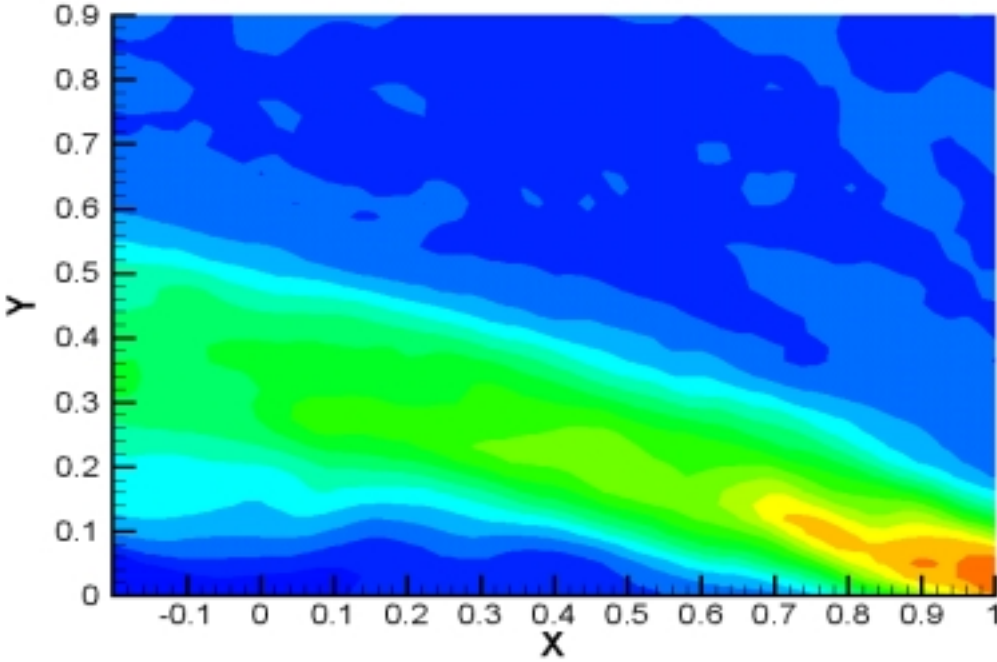


Figure 9: Vorticity 10° AOA, 8 Hz Actuation

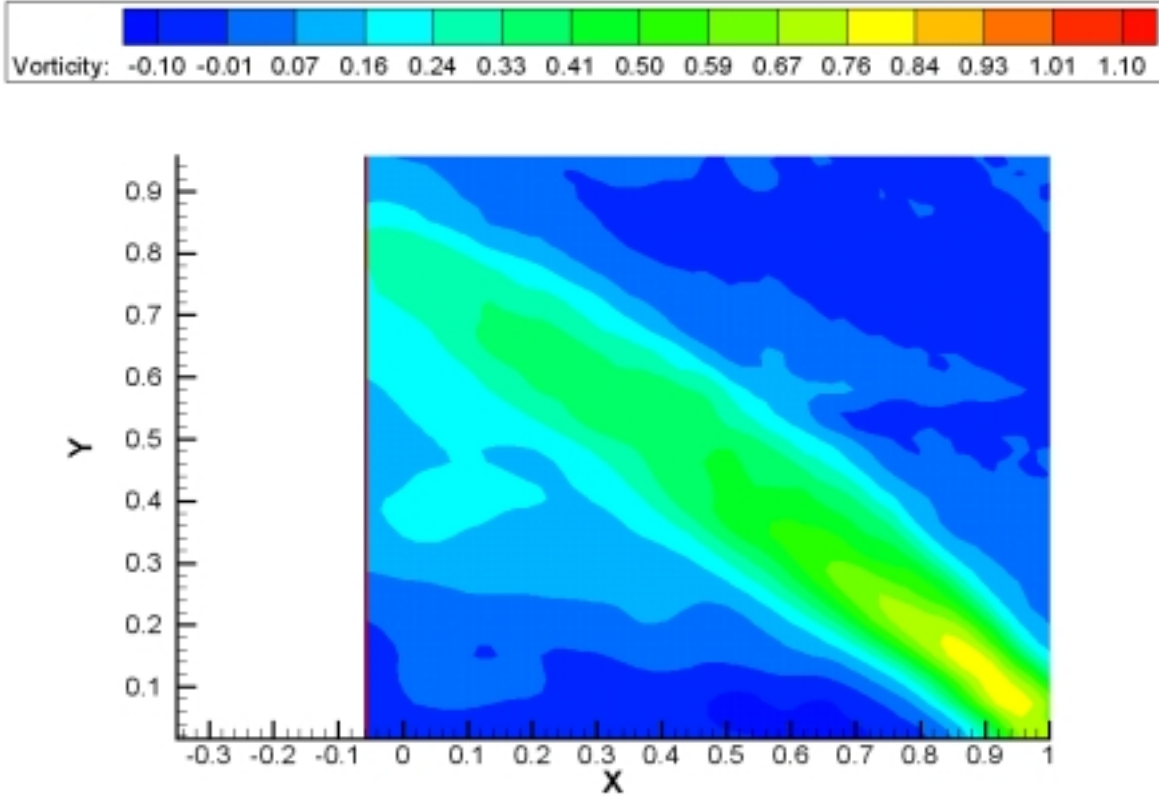


Figure 10: Vorticity 20° AOA, Reference Airfoil

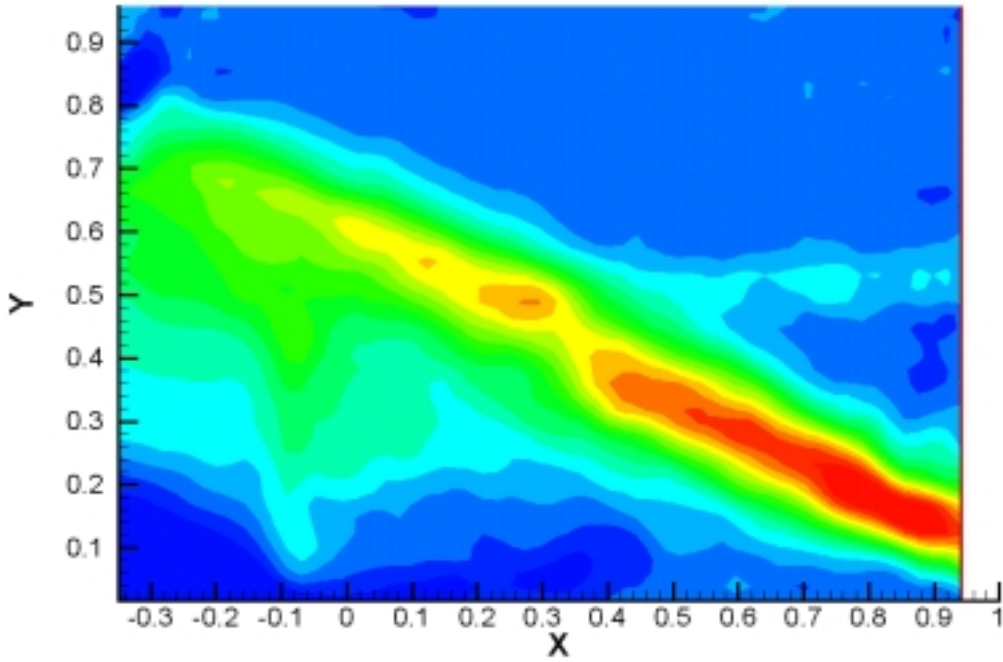


Figure 11: Vorticity 20° AOA, 0 Hz Actuation

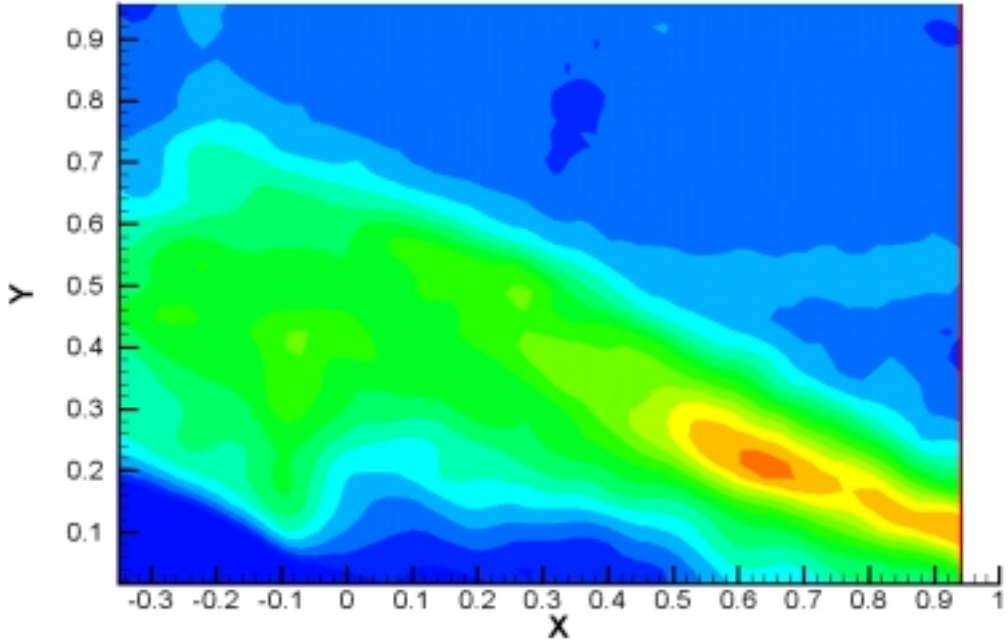


Figure 12: Vorticity 20° AOA, 2 Hz Actuation

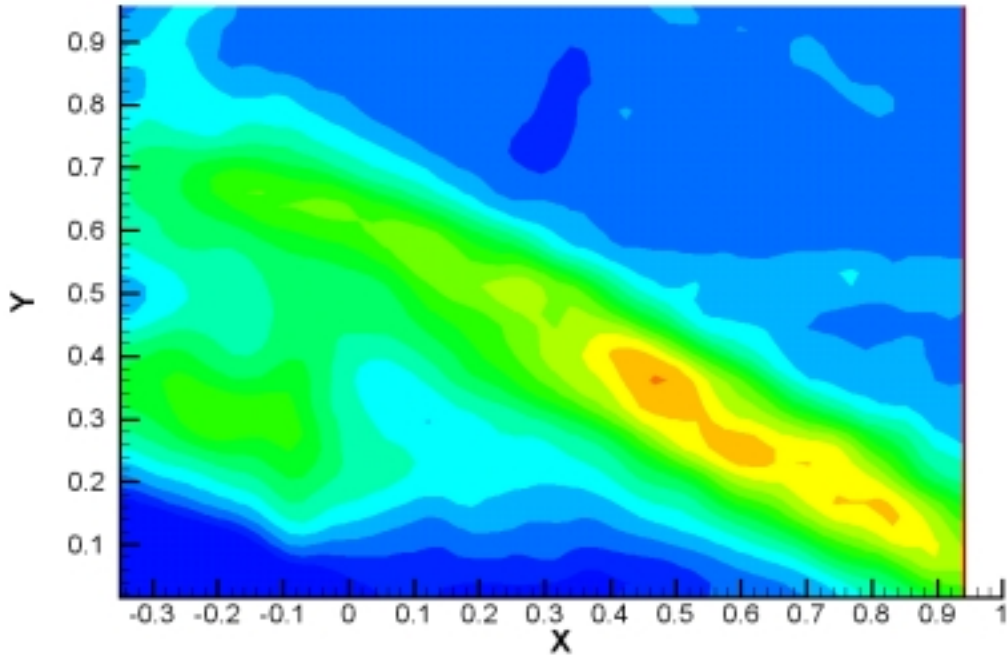


Figure 13: Vorticity 20° AOA, 4 Hz Actuation

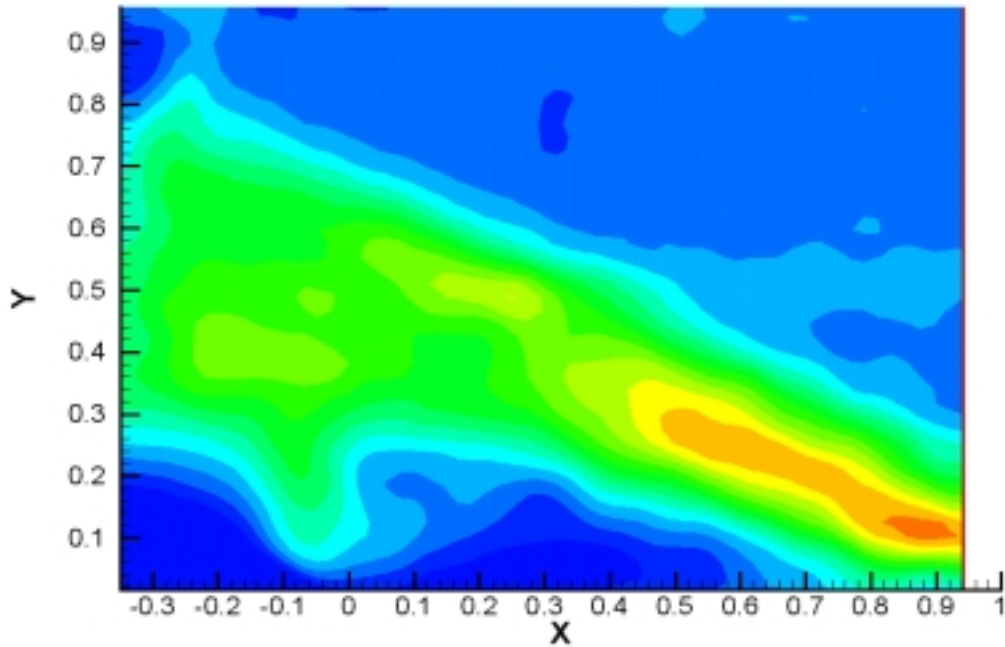


Figure 14: Vorticity 20° AOA, 8 Hz Actuation

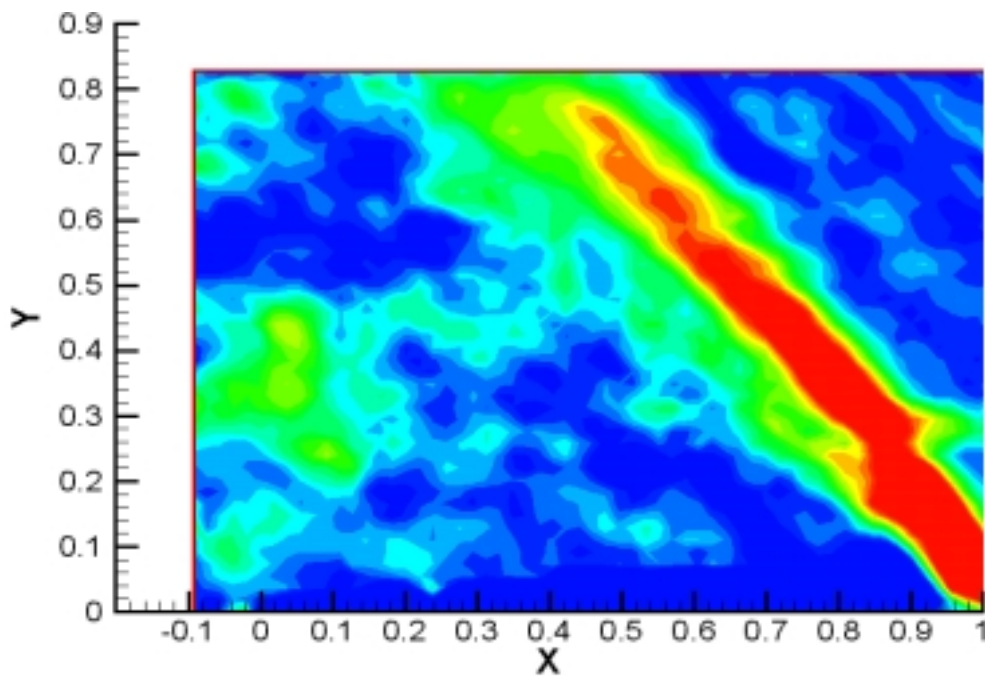
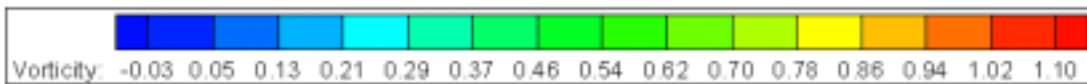
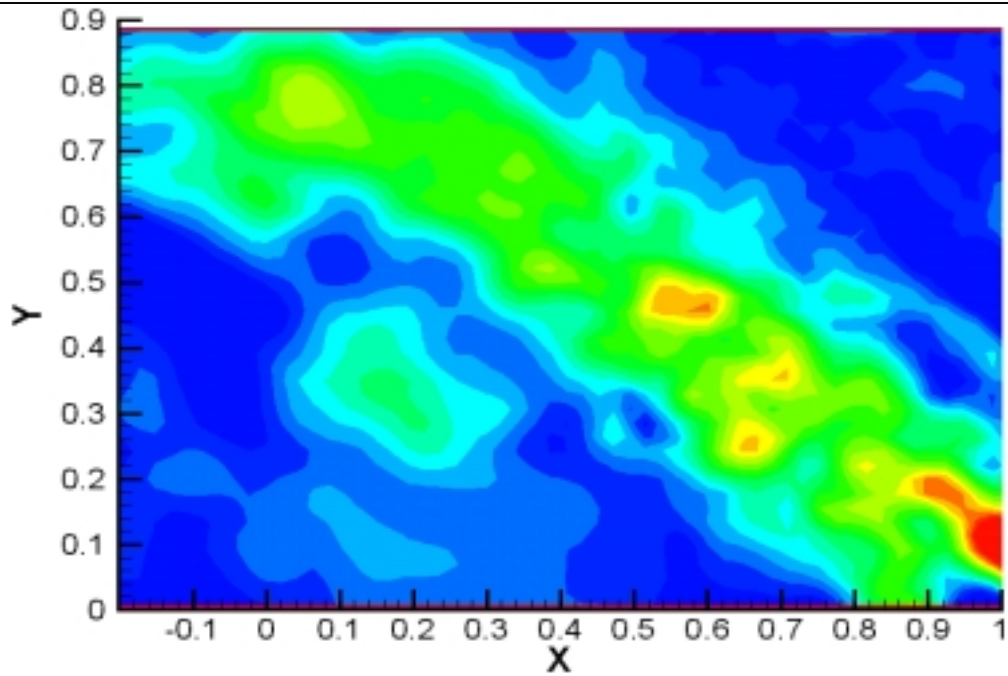
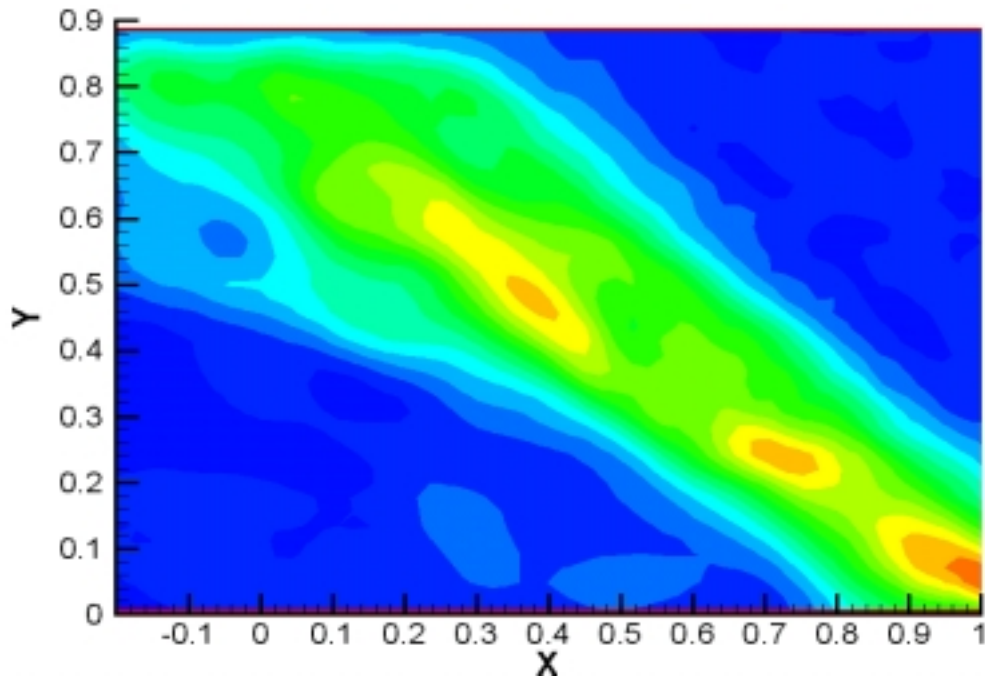


Figure 15: Vorticity 30° AOA, Reference Airfoil



*Figure 16:* Vorticity 30° AOA, 0 Hz Actuation



*Figure 17:* Vorticity 30° AOA, 2 Hz Actuation

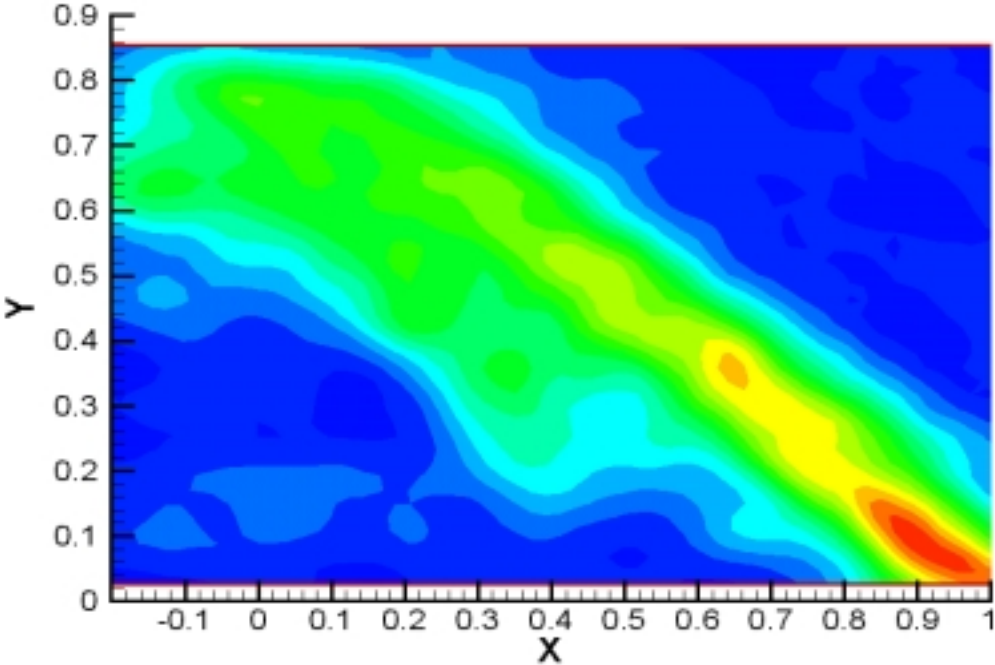


Figure 18: Vorticity 30° AOA, 4 Hz Actuation

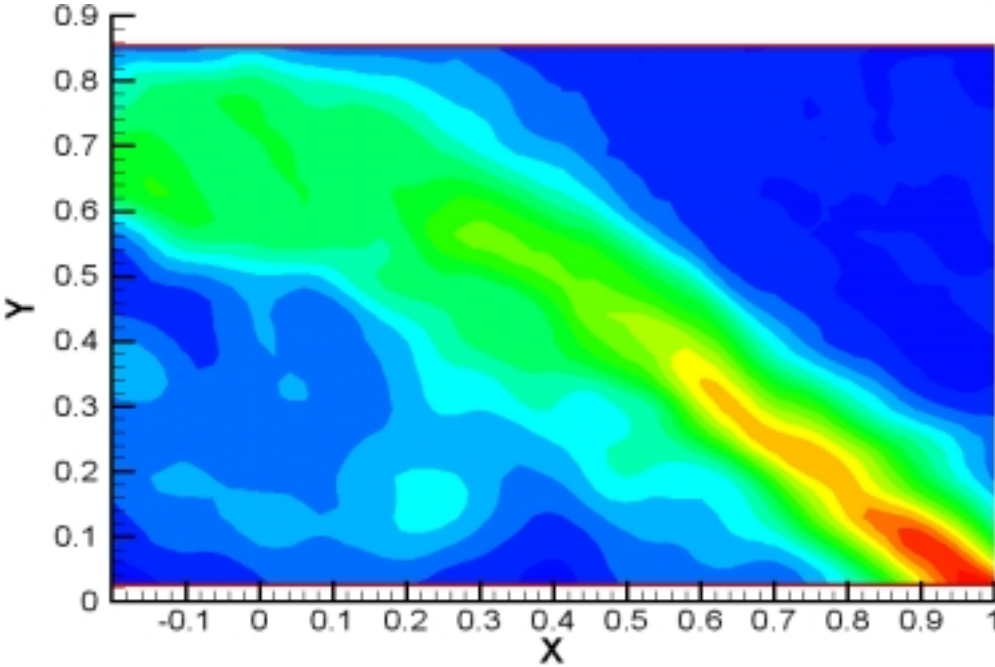


Figure 19: Vorticity 30° AOA, 8 Hz Actuation

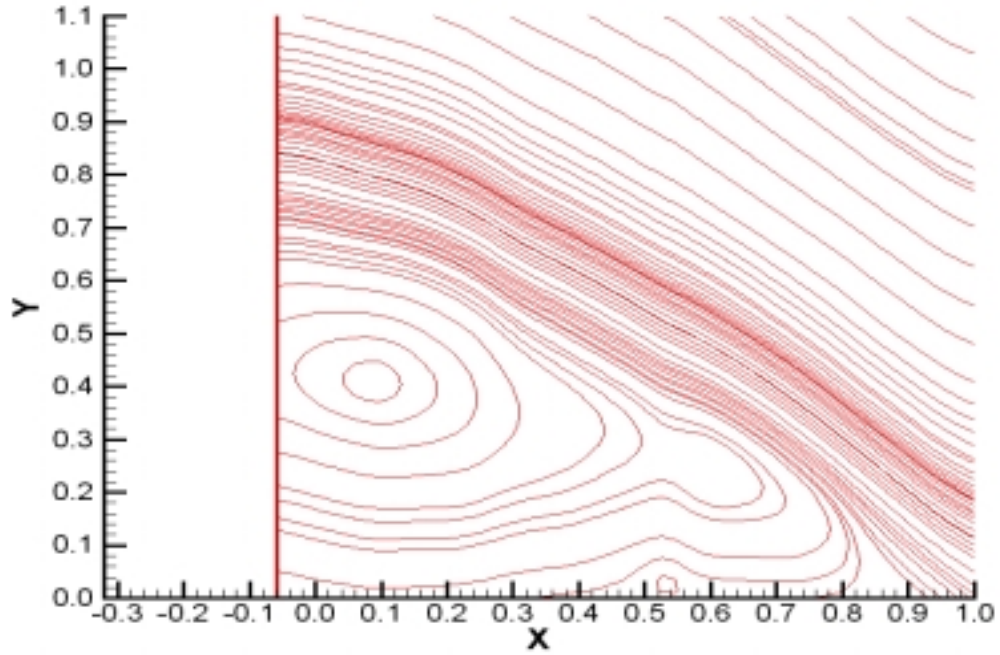


Figure 20: Streamlines, Time Averaged flow field 20° AOA, Reference Airfoil

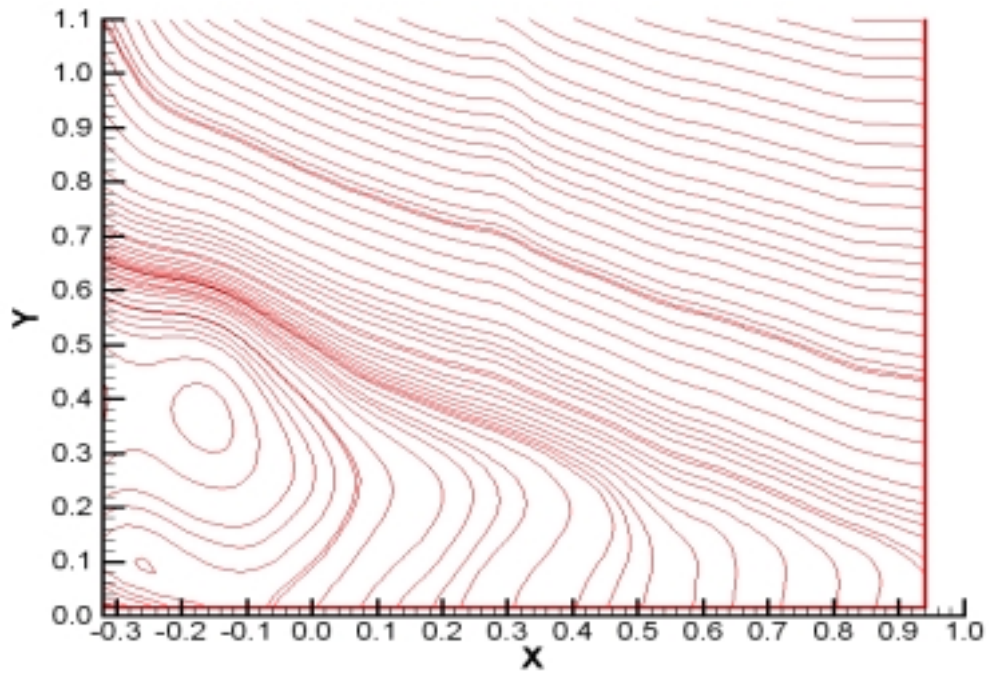
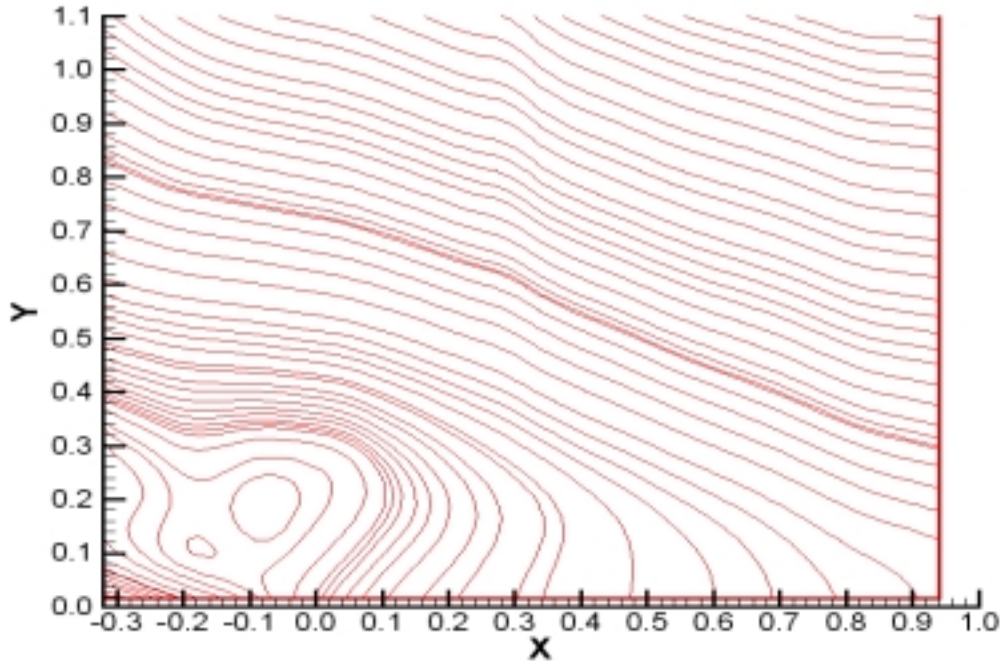
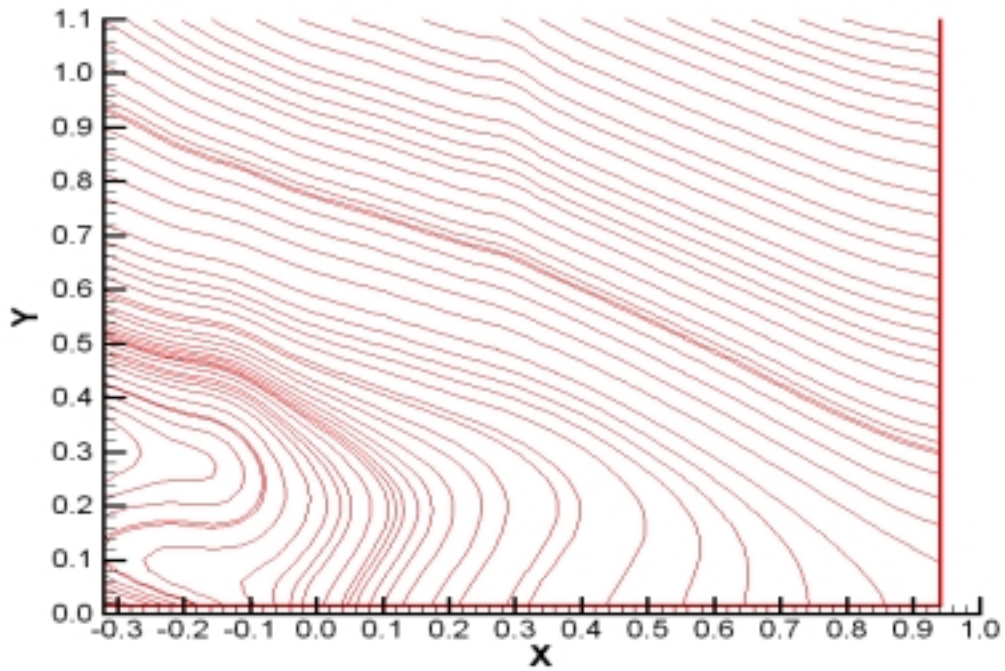


Figure 21: Streamlines, Time Averaged flow field 20° AOA, 0 Hz Actuation



**Figure 22:** Streamlines, Time Averaged flow field 20° AOA, 2 Hz Actuation



**Figure 23:** Streamlines, Time Averaged flow field 20° AOA, 4 Hz Actuation

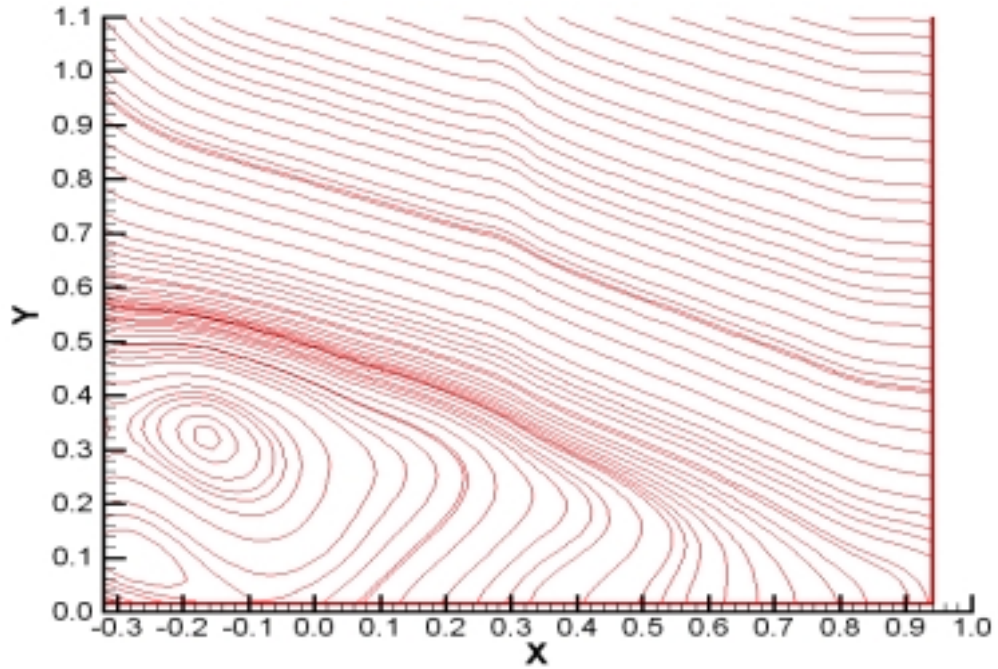


Figure 24: Streamlines, Time Averaged flow field 20° AOA, 8 Hz Actuation

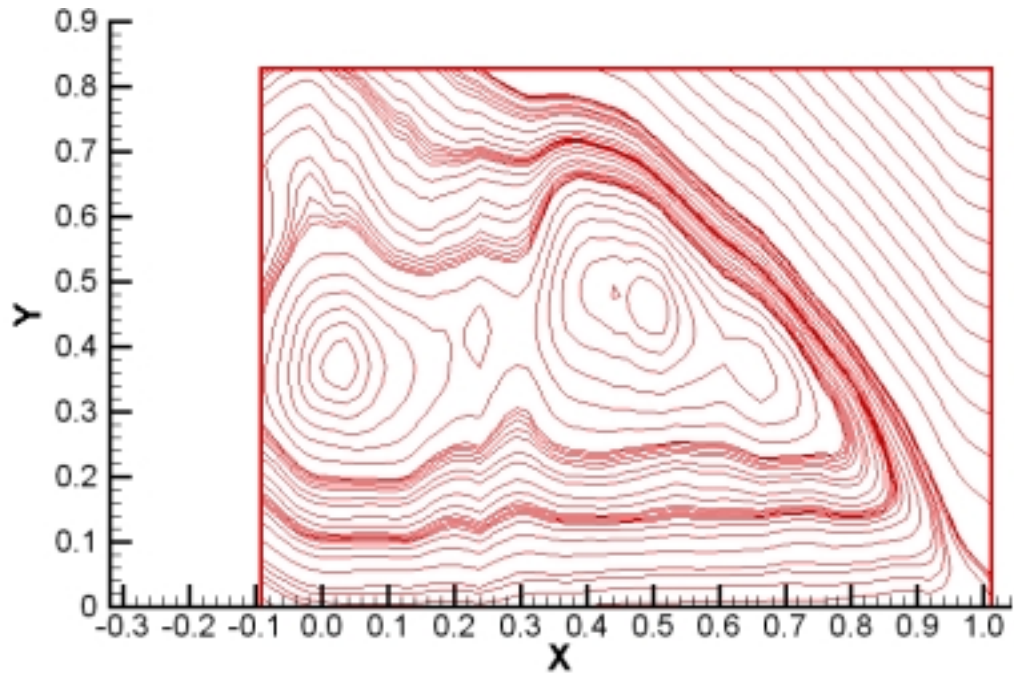


Figure 25: Streamlines, Time Averaged flow field 30° AOA, Reference Airfoil

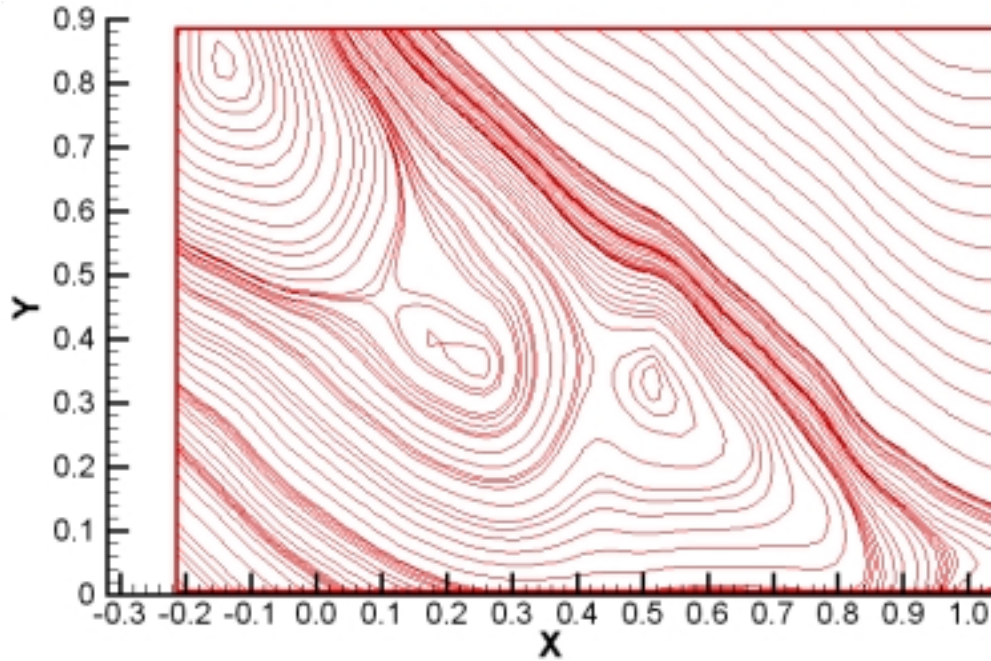


Figure 26: Streamlines, Time Averaged flow field 30° AOA, 0 Hz Actuation

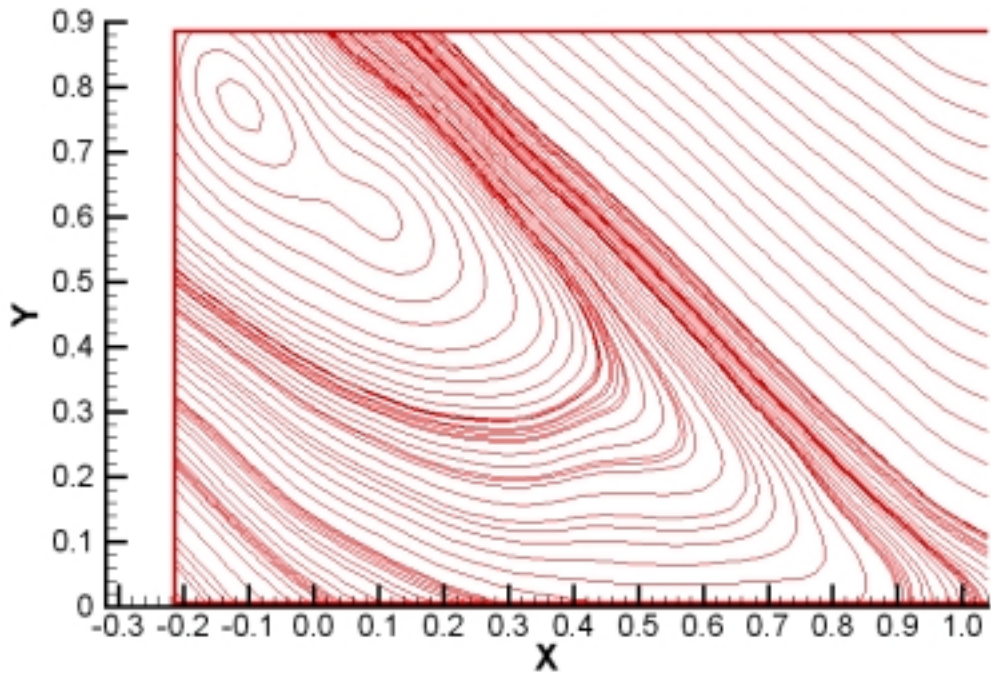
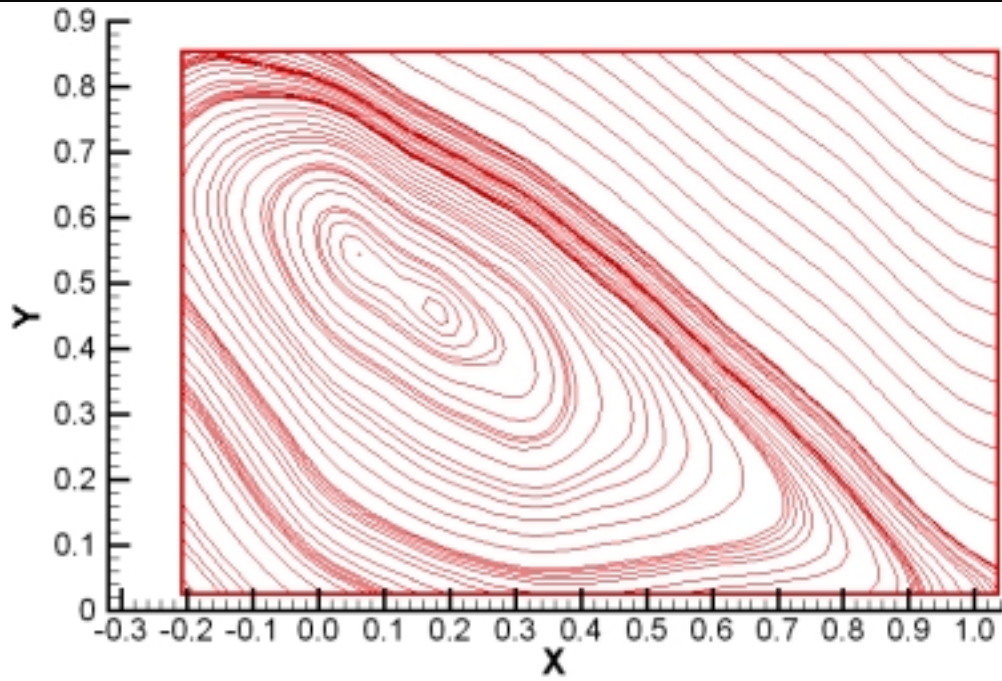
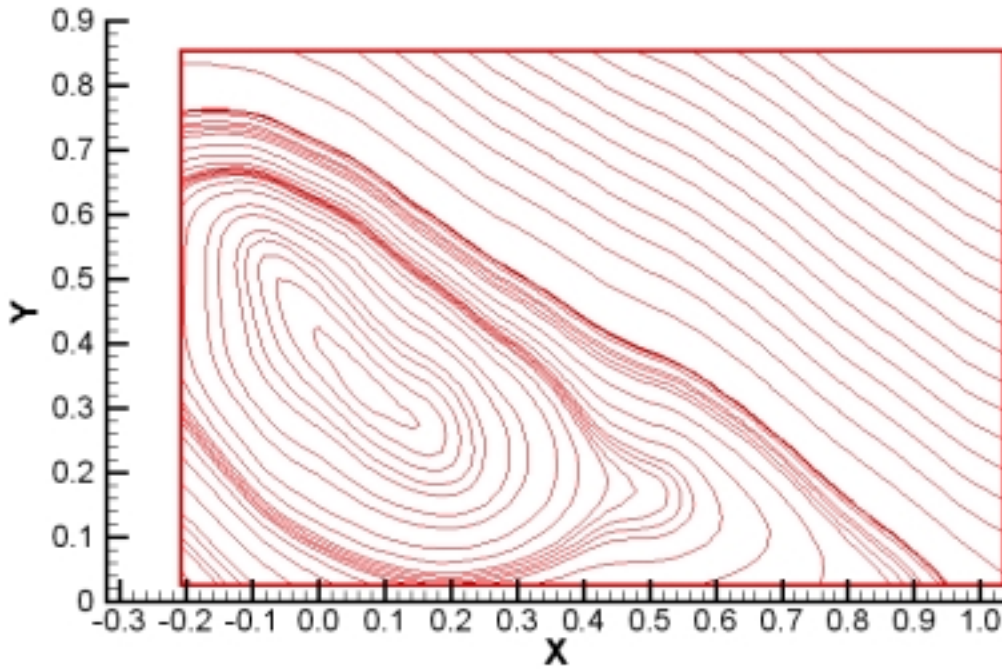


Figure 27: Streamlines, Time Averaged flow field 30° AOA, 2 Hz Actuation



**Figure 28:** Streamlines, Time Averaged flow field 30° AOA, 4 Hz Actuation



**Figure 29:** Streamlines, Time Averaged flow field 30° AOA, 8 Hz Actuation

## **Chapter 7**

### **Conclusions**

In this final section, we attempt to recapitulate the most significant results presented in the previous chapters and reach to a final conclusion. However, the versatile structure of this dissertation complicates this task. Primarily, during this dissertation a method for the investigation of spatio-temporally evolving flows was developed. The incorporation of the related theory with the necessary hardware and software lead to a system with a resolution in space and time never been matched in the past. This research tool was subsequently employed in the analysis various flow fields. The results of these studies are summarized in the following paragraphs.

Digital Particle Image Velocimetry measurements were used to investigate the characteristics of the wake of a circular cylinder near the free surface. These measurements illustrated that the vortex formation length increases as we approach the free surface extending up to 3.4 diameters downstream while the width of the wake practically doubles to approximately two diameters. The vorticity in the shear layers exhibits an increase as we move to higher elevations. Subsequently is decreasing to a minimum when we reach the last elevation, corresponding to the free surface. The turbulent fluctuations indicate that in the vicinity the free surface eddies align with the streamwise direction reducing the normal to the free surface vorticity component, and

they will turn upwards to reconnect meeting the “stress-free” boundary condition only in the immediate neighborhood of the free surface. From the instantaneous vorticity distributions at the different elevations in the wake of the circular cylinder it was observed that the shear layers emanating from the cylinder are becoming more stable and they do not roll to form vortices, but further downstream. This is the reason, for the vortex formation length to shift downstream and for the increase of the concentration of vorticity inside the shear layers. At the free surface however, the flow is becoming more turbulent and the shear layers less coherent. Finally, a volume of the flow field was reconstructed by employing a novel approach, to match in time the initiation of a periodic event. As a result, the existence of oblique vortex shedding was clearly demonstrated because of shifting of the vortex formation downstream. The onset of the effect of the free surface was determined to be in the neighborhood of 3.5 diameters below the interface. However, the free slip boundary condition at the interface by forcing the vortex to reattach normal to the free surface causes the axis of the vortex to change again. As a result, vortex lines break into cells of vorticity and generated incoherent structures at the free surface in the form of downdrafts and upwellings. As a more general conclusion we deduce that by having a free surface interface we imposed a boundary condition that is compatible to the two dimensional character of the flow, thus not allowing the three-dimensional instabilities of the shear layers to grow and eventually roll into vortices. This demonstrates the great importance of end effects on the wake of the cylinder, and illustrates the significance of the evolution of three-dimensional instabilities in the shear layers.

For the case of DPIVC measurements normal to the streamwise direction, results show braid vortices beneath the free surface with size of the same order of the cylinder diameter. Their intensity remains unaffected with respect to the downstream position. The underlying mechanism of the alternate vortex shedding is revealed even though the interrogation planes were placed normal to the free stream. This provides further evidence that there is not vortex shedding suppression at the free surface for this values of  $Re$  and  $Fr$ .

However, for higher values of  $Re$ , and  $Fr$ , analysis of hydrogen bubble flow visualization images with particle visualizations and calculated frequencies indicates that vortex shedding is been suppressed and that free surface more than two to three cylinder diameters below the free surface. Discontinuities of the vortex axis and cells of shedding induce a phase difference in the vortex shedding mechanism. Moreover, the positive inclination counteracts the effects of the free surface recovering the vortex shedding process while for the negative inclination the neighborhood of the free surface presents a very turbulent broad spectrum. The introduction of asymmetry in the boundary condition of the wake of a circular cylinder in combination with a yaw angle with respect to the free-stream generates a three-dimensional flow field with character strongly dependent on the respective values of the  $Re$  and  $Fr$  numbers as well as the position in the spanwise direction.

For the case of a surface mounted prism, DPIVC is used to quantify mean and instantaneous flow parameters in the separated flow over a surface mounted prism. These quantitative results show that the increase of the  $Re$  number resulted in displacing the line that defines the shear layer, higher with respect to the topside of the prism. Subsequently the size of the recirculation area increased resulting to a small confined region of zero mean velocity magnitude. For all cases, the forward stagnation point is at the same approximate location with respect to the height of the body. The vorticity shed in the flow is generated on the leading sharp edge of the prism. Increase of  $Re$  number increases the vorticity levels indicating a stronger reverse flow, without however affecting significantly the mean reattachment point. In addition, the cross-correlation term,  $u/v'$  of the Reynolds stresses shows two well-defined regions of positive and negative values on the topside of the prism. Most importantly very high RMS values of the velocity components in the region after the 50% of the length of the prism provide quantitative proof of the very unsteady character of the flow. These fluctuations are directly related to the oscillation of the shear layer combined with the wake expansion and vortex shedding mechanisms. The comparable order of magnitude of the velocity fluctuations in the region occupied by the horseshoe vortex with the velocity fluctuations on the top of the prism is posing the question to which extent these fluctuations and the free-stream fluctuations affect the

separation and reattachment process. Moreover, a comparison of the mean and instantaneous flow characteristics shows that the concept of a mean flow that consists of a shear layer, a separation bubble and reattachment may not be of much physical significance. The strong unsteady character of the flow that has been revealed from these results dictates that an accurate study of such complex three dimensional fields needs to be performed in a time accurate manner. Therefore, any kind of numerical simulation that does not take into account the time dependence of the flow field (steady,  $k-\epsilon$ , *RANS*) or an experimental approach that is carried out in an average manner (time or ensemble) will provide useful engineering results but a limited insight into the underlying physics. Finally, a spatio-temporal analysis of the separated flow over a surface mounted prism during a continuous acceleration of the free stream velocity showed the time variation of the reattachment point, and the time series of the circulation within pre-specified domains in the field along with instantaneous vorticity distributions. It is found that the reattachment point experiences high fluctuations, while there are instants with no reattachment forming an open wake. Vorticity in the region of the shear layer increases almost proportionally with the increase of the free stream velocity and by the same factor. Similar increase is observed for the vortex shedding domain but with higher fluctuations due to the unsteady character of the shedding process. The vortex shedding is affected by the enhancement of the negative vorticity in the reverse flow region. The regions of the horseshoe vortex and the area of reverse flow demonstrate a very turbulent unsteady character that does not relate linearly to the acceleration of the free stream resulting to an increase by a factor of ten.

Finally, the investigation of the effect of introducing a disturbance in the shear layer in terms of a forced oscillation clearly illustrated that it can affect the formation of a vortex resulting to a more coherent flow structure. The most effective flow control was obtained for the  $20^\circ$  angle of attack and excitation at the natural frequency. The disturbance forces the free shear layer to move closer to the airfoil surface, thus bringing it closer to attached flow. Moreover, in all cases, we observed some increase in the vorticity level within the wake, which implies a more energized vortex.

## *Chapter 7 Conclusions*

---

Incorporating the conclusion into the same frame, we deduce that three-dimensional massively separated flows are dominated by the characteristics of the emanating shear layers. It is the instabilities of these layers and the interaction of opposite signs of vorticity that determines the character of the flow. The strong spatial and temporal variation of such flows was illustrated dictating that an adequate study needs to be performed with sufficient space and time resolution. Steady state, mean or point measurement approaches are extremely limited and misleading for the interpretation of the underlying physics. The results presented here demonstrate the power and the need of spatio-temporal analysis for such unsteady flows. Furthermore, they provide detailed and accurate quantitative results with a resolution never reported in the past. These results can be used to carry on the analysis of the turbulent characteristics of the flow fields and for the validation of numerical codes

## **References**

## Chapter 8: References-Related Publications

---

- [1] Adrian RJ (1991): Particle-Imaging techniques for experimental fluid mechanics. *ARFM*, 23, 261-304.
- [2] Adrian RJ (1996): Bibliography of Particle Velocimetry using imaging methods. *TAM Report. Produced and distributed in cooperation with TSI Inc.*
- [3] Adrian RJ, Meinhart CD, Barnhart DH and Papen GC (1995): An HPIV System for turbulence research. EP Rood (ed.), *ASME FED*, 148,17-21.
- [4] Adrian, R. J. (1996): Strategies for Imaging Flow Fields with PIV. *AIAA 96-1988*
- [5] Adrian, R. J. (1997): Dynamic Ranges of Velocity and Spatial Resolution of Particle Image Velocimetry. *Meas. Sci. Technol.* 8 1393-1398.
- [6] Agui J. and Jimenez J. (1987): On the performance of particle tracking. *J. Of Fluid Mechanics vol 185 pp 447-468*
- [7] Asimopoulos N, Vlachos P. P. Telionis D. P (1999): A high speed, high particle density particle tracking method for turbulent flows. *ASME FEDSM'99-7139*.
- [8] Batchelor G. K. (1964): Axial Flow in trailing line vortices. *J. Of Fluid Mechanics vol 20 pp 645-658*.
- [9] Bernal L. P and Roshko A. (1986): Streamwise Vortex Structures in a plane mixing layers. *J. Fluid Mech., vol. 170 pp. 599-525*
- [10] Bloor, S. and Gerrard, J.H. (1966): Measurements on turbulent vortices in the wake of a circular cylinder. *Proc. Roy. Soc. (London) Ser. A., Vol. 294, pp. 319-342*.
- [11] Boillot A. and Prasad K. (1996): Optimization procedure for pulse separation in cross-correlation PIV. *Exp. In Fluids 21 87-93, Springer Verlag*.
- [12] Carosone F. & A. Cenedese (1996): Image Analysis for velocity evaluation and Neural Networks. *VKI Lecture Series 1996-03*
- [13] Castro .P. and Haque A. (1988): The structure of a shear layer bounding a separation region. Part 2. Effects of free-stream turbulence. *J. Of Fluid Mechanics vol. 192 pp. 577-595*

## Chapter 8: References-Related Publications

---

- [14] Castro .P. and Robins A.G. (1977): The flow around a surface mounted cube in uniform and turbulent streams. *J. Of Fluid Mechanics vol. 79, part 2, pp. 307-335*
- [15] Cenedece A. Paglialunga A. (1990): Digital direct analysis of a multi-exposed photograph in PIV. *Exp. in Fluids 8, 273-280.*
- [16] Chang, R C., Hsaio, F.-B., and Shyu, R.-N., (1992): Forcing Level Effects of Internal Acoustic Excitation on Improvement of Airfoil Performance. *J. Aircraft 29, 823-829.*
- [17] Cherry, N.J., Hillier R. and Latour, M. E. P. (1984): Unsteady measurements in a separated and reattaching. *J. Fluid Mech., vol. 144, pp.13-46.*
- [18] Dalziel SB (1993): Decay of rotating turbulence: Some particle tracking experiments. FTM Nieuwstadt (ed.). *Flow Visualization and Image Analysis, 27-54*
- [19] Davenport W. J. and Simpson R. L. (1990): Time-Dependent and Time Averaged Turbulence Structure Near the Nose of a Wing-Body Junction. *J of Fluid Mechanics vol. 210 pp 107-119.*
- [20] Derou & Herault (1994): A new paradigm for particle tracking velocimetry based on graph theory and pulsed neural networks. *7th Int. Symp. Appl. Laser Techniques to Fluid Mechanics, Lisbon, pp: 35.3.1-35.3.8*
- [21] Doligalski T. L. and Walker.J. D. A. (1984): The boundary Layer induced by a convective two –dimensional vortex. *J. Fluid Mech., vol. 139 pp. 1-28*
- [22] Doligalski T. L. Smith C. R. and Walker.J. D. A. (1994): Vortex Interaction with walls. *ARFM vol 26:573-613*
- [23] Dracos Th. and A. Gruen (1998): Videogrammetric methods in velocimetry. *Appl. Mech. Rev. vol. 51, no. 6 1998.*
- [24] Eaton E., (1987): Analysis of laminar vortex shedding behind a circular cylinder by computer aided flow visualization. *J. Fluid Mech., vol. 180 pp. 117-145*
- [25] Gad-el-Hak, M., (1990): Control of Low-Speed Airfoil Aerodynamics. *AIAA Journal, Vol. 28, pp. 1537-1552.*

## Chapter 8: References-Related Publications

---

- [26] Gad-el-Hak, M., and Bushnell, D. M., (1991): Separation Control. Review, *Journal of Fluids Engineering, Vol. 113, pp. 5-29.*
- [27] Gartshore, I.S. (1984): Some Effects of Upstream Turbulence on the Unsteady Lift Forces Imposed on Prismatic Two Dimensional Bodies. *J. Fluids Eng. Vol.106, pp. 418-424.*
- [28] Gerrard, J. H. (1978): The wakes of cylindrical bluff-bodies at Low-Reynolds number. *Philosophical Transactions of the Royal Society of London, 288,351-382*
- [29] Gharib M. Willert C. (1991): Particle Tracing: Revisited (article copy from unknown source).
- [30] Grand I (1997): Particle Image Velocimetry: A Review. *Proceedings Institute of Mechanical Engineers*
- [31] Grant and Pan (1995): An Investigation of the performance of multi layer neural networks applied to the analysis of PIV images. *Experiments in Fluids, pp 159-166.*
- [32] Grant I (1994): Selected papers on Particle Image Velocimetry. *SPIE Milestone Series MS99, SPIE Optical Engineering Press, Bellingham, Washington*
- [33] Hammache M. & Gharib M. (1991): An experimental study of the parallel and oblique vortex shedding from circular cylinders. *J. Fluid Mech., vol. 232 pp. 567-590*
- [34] Hasselinc L. (1988): Digital Image Processing in Flow Visualization. *ARFM 20:421 85*
- [35] Hetz A., Dhaubhadel M. N., D. P. Telionis (1991): Vortex Shedding Over Five In-Line Cylinders. *J. Fluid and Structures, vol. 5 pp. 243-257*
- [36] Hillier HR. and Cherry N. J. (1981): The effects of stream turbulence on separation bubbles. *J. of Wind Engineering and Industrial Applications.*
- [37] Hsiao, F. B., Liu, C.-F., and Shyu, J.-Y.,(1990): Control of Wall-Separated Flow by Internal Acoustic Excitation. *AIAA J, 28, 1440-1446.*
- [38] Hsiao, F.-B., Shyu, R.-N., and Chang, R. C., (1994): High-Angle-of-Attack Airfoil Performance Improvement by Internal Acoustic Excitation. *AIAA J, 32 j655-657.*

## Chapter 8: References-Related Publications

---

- [39] Hsiao, F.-B., Wang, T.-Z., and Zohar, Y. (1993): Flow Separation Control of a 2-D Airfoil by a Leading-Edged Oscillating Flap. *Intern. Conf. Aerospace Sci. Tech., Tainan, Taiwan, Dec. 6-9, 1993.*
- [40] Huang H. T. and Gharib M. (1997): Processing Error in Digital Particle Image Velocimetry. *FEDSM97-3068.*
- [41] Inoue M., Baba N. and Himeno Y. (1993): Experimental and numerical study of viscous flow field around a advancing vertical circular cylinder piercing a free surface. *J. Kansai Soc. Naval Archit. Of Japan, 220:57-64.*
- [42] Jahne B. (1991): Lectures in Computer Science. *Spatio-Temporal Image Processing. Springer-Verlag.*
- [43] Jahne B. (1997): Image Processing for Scientific Applications. *CRC Press*
- [44] Kawamura Takafumi (1997): Numerical Simulation of 3D Turbulent Free-Surface Flows. *International Research Center for Computational Hydrodynamics (ICCH) T*
- [45] Keane R. D. and Adrian R. J. (1990): Optimization of particle image velocimeters . Part I: Double pulsed systems. *Meas. Sci. Tech. 1 1202-1205.*
- [46] Keane R. D. and Adrian R. J. (1991): Optimization of particle image velocimeters . Part I: Multiple pulsed systems. *Meas. Sci. Tech. 2 963-974.*
- [47] Kinser, E. E. Furey, D. A. and Rediniotis O.K.(1996): Calibration Neural-Network for a Novel Omni-Directional Velocity Probe-PROBENET. *ASME International Mechanical Engineering Congress, Atlanta, Georgia, 1996.*
- [48] Kiya, M. and Sasaki, K. (1983): Structure of a turbulent separation bubble. *J. Fluid Mech., vol. 137, pp. 83-113.*
- [49] Kiya, M. and Sasaki, K.(1985): Structure of large-scale vortices and unsteady reverse flow in the reattaching zone of a turbulent separation bubble. *J. Fluid Mech., vol. 154, pp. 463-491.*

## Chapter 8: References-Related Publications

---

- [50] Lang A.W, Gharib M.(1998): On the effects of surface contamination in the wake of a surface-piercing cylinder. *FEDSM-98 Washington DC 1998*.
- [51] Lele S. K. (1992): Compact Finite Difference Schemes with Spectral like Resolution. *J. of Computational Physics, vol 103, pp 16-42, 1992*.
- [52] Lian Qi Xiang and Tsung-chow Su, (1996): The application of Hydrogen Bubble Method in the Investigation of Complex Flows. *Atlas of Flow Visualization II, CRC Press Inc*.
- [53] Lighthill, J. (1978): *Waves in Fluids, Cambridge Academic Press*.
- [54] Lin J. C., P. Vorobieff and Rockwell D. (1995): Three-dimensional patterns of streamwise vorticity in the turbulent near wake of a cylinder. *J. of Fluids and Structures vol. 9, pp 231-234, 1995*.
- [55] Lin J. C., P. Vorobieff and Rockwell D. (1996): Space-time imaging of a turbulent near-wake by high-density particle image cinematography. *Phys. of Fluids vol. 8 pp:555, 1996*
- [56] Lourenco L.M. (1996): Particle Image Velocimetry, *Von Karman Institute Lecture Series, 1996-03*.
- [57] Lu L. J. and Smith C. R.(1985): Image Processing of hydrogen bubble flow visualization for determination of turbulence statistics and bursting characteristics. *Experiments in Fluids 3, 349-356, Springer-Verlag*.
- [58] Lu L. J. and Smith C. R.(1991): Use of flow visualization data to examine spatial-temporal velocity and burst type characteristics in a turbulent boundary layer. *J. of Fluid Mechanics, vol. 232, pp. 303-340*.
- [59] Luo Fa-Long and Rolf Unbehauen R. (1997): Applied Neural Networks for Signal Processing. *Cambridge University Press*.
- [60] Martinuzzi R. and Tropea C. (1993) : The flow around Surface mounted prismatic obstacles placed in a fully developed channel flow. *J. of Fluids Engineering vol 115 pp.85*
- [61] Masters T (1995): Advanced Algorithms For Neural Networks. *Willey & Sons,1995(a)*.

## Chapter 8: References-Related Publications

---

- [62] Masters T (1995): Neural, Novel & Hybrid Algorithms for Time Series Prediction. *Willey & Sons, 1995(b)*.
- [63] Masters T(1994): Signal and Image Processing with Neural Networks. *Willey & Sons, 1994*.
- [64] McManus, K., and Magill, J., (1996): Separation Control in Incompressible and Compressible Flows Using Pulsed Jets. *AIAA Paper 96-194*
- [65] Meynard R. (1983): Measure de champs de vitesse d' ecoulements fluids par analyse de suites d'images obteneues par diffusion d'un fueillet lumineux. Ph.D Dissertation, Faculte des Science Appliquees, Universite Libre de Bruxelles.
- [66] Nikias L. C. and Petropulu A. (1993): Higher-Order Spectral Analysis- A non-linear signal processing framework. *Prentice Hall 1993*.
- [67] Noca F., Park H. G. Gharib M. (1998): Vortex Formation Length of a Circular Cylinder ( $300 < \text{Re} < 4,000$ ) Using DPIV, *FEDSM'98, Washington 1998*
- [68] Pandya S. A. Macy R. (1996): Pattern Recognition With Neural Networks in C++, CRC Press
- [69] Panton R. (1996): Incompressible Flow. *Willey Interscience 2nd edition*
- [70] Prasad A. K. Adrian R. J., Landreth C.C., Offutt P.W.:(1992): Effect of resolution and accuracy of particle image velocimetry interrogation. *Exp. In Fluids 13 105-116, Springer Verlag*.
- [71] Prasad A.K. and Adrian R J (1993): Stereoscopic particle image velocimetry applied to liquid flows. *Experiments in Fluids 15, 49-60*.
- [72] Press, Teukolsky, Vetterling, Flannery. (1992): Numerical Recipes in C: The Art of Scientific Computing, Second Edition. *Cambridge University Press*.
- [73] Raffel M., Willert C.E. and Kompenhans J. (1998): Particle Image Velocimetry: A practical guide. *Series in Experimental Fluid Mechanics. Springer Verlag*.

## Chapter 8: References-Related Publications

---

- [74] Ramberg S. E. (1983): The effects of yaw and finite length upon the vortex wakes of stationary and vibration circular cylinders. *J. Fluid Mech.*, vol.128 pp. 81-107
- [75] Rediniotis O.K. and Chrisanthakopoulos G,(1995): A Wide-range, High-Accuracy Neural/Fuzzy Calibration Technique for Flow-Diagnostics and Instrumentation. *AIAA 95-0020, 33rd Aerospace Sciences Meeting,1995, Reno, Nevada.*
- [76] Rediniotis O.K. and R. Vijayagopal,(1999): Miniature Multihole Pressure Probes and their Neural-Network-Based Calibration. *AIAA*, vol. 37, 6, 1999, pp. 674-674.
- [77] Rediniotis, O. K., Stapountzis, H., and D. P. Telionis, 1993, Periodic Vortex Shedding over Delta Wings. *AIAA Journal Vol. 31*, pp. 1555-1562.
- [78] RJ Perkins and JCR Hunt (1989): Particle Tracking in Turbulent Flows. *Advances in Turbulence 2* pp. 286-291.
- [79] Robinson O. Rockwell D. (1993): Construction of three-dimensional images of flow structure via particle tracking techniques. *Experiments in Fluids 14*, 257-270
- [80] Rogers J.(1997): Object Oriented Neural Networks in C++. *Academic Press, 1997.*
- [81] Rood E. P. (1995): Vorticity Interaction with a Free Surface. Fluid Vortices, S.I. Green. (ed.), pp. 155-234
- [82] Rood, E.P.(1994): Interpreting Vortex Interactions with a Free Surface, *Journal of Fluids Engineering, Volume 116, March (1994a)*, pp. 91-93.
- [83] Rood, E.P.(1994): Myths, math, and Physics of Free-Surface Vorticity. *Applied Mechanics Review, Volume 47, No. 6, Part 2, June (1994b)*.
- [84] Roshko A (1954): On the Drag and Shedding Frequency of Two-Dimensional Bluff-bodies. *NACA Tech. Note 3169*.
- [85] Roshko A (1976): Structure of turbulent shear flows: a new look. *AIAA J 14*, 1349-1357.
- [86] Ruderich R. and Fernholz H.H. (1986):An experimental investigation of a turbulent shear flow with separation, reverse flow and reattachment. *J. of Fluid Mechanics, vol. 163*, pp. 283-322.

## Chapter 8: References-Related Publications

---

- [87] Saathoff P.J. and Melbourne W. H. (1997): Effects of free-stream turbulence on surface pressure fluctuations in a separation bubble. *J. of Fluid Mechanics*, vol. 337, pp. 1-24.
- [88] Sarpkaya T., Magee M. and Craig Merrill (1994): Vortices, Free Surface and Turbulence. *FED-Vol. 181, Free-Surface Turbulence ASME 1994*.
- [89] Scarano F. Rieuthmuller M.L. (1999): Iterative multigrid approach in PIV image processing with discrete window offset. *Exp. In Fluids 26 513-523, Springer-Verlag*.
- [90] Schofield W. H. and Logan E. (1990): Turbulent Shear Flow over surface mounted obstacles. *Journal of Fluids Engineering, Vol. 112, pp.376-385*.
- [91] Seifert, A., and Pack, L. G., (1998): Oscillatory Control of Separation at High Reynolds Numbers. *AIAA 98-0214*.
- [92] Seifert, A., Dorabi, A. and Wygnanski, I., (1996): On the Delay of Airfoil Stall by Periodic Excitation. *AIAA J. of Aircraft, Vol. 33, pp. 691-699*.
- [93] Starck J.L., Murtagh F. and Bijaoui A. (1998): Image Processing and Data Analysis . *The Multiscale Approach, Cambridge University Press*.
- [94] Stern F. Parthasarathy R. Huang H. P. and Longo J. (1994): Effects of waves and free surface on turbulence in the boundary layer of a surface-piercing flat plate. *FED-Vol. 181, ASME 1994*.
- [95] Techet A. H., Hover F.S, and Triantafyllou M.S (1998): Vortical patterns behind a tapered cylinder oscillating transversely to a uniform flow. *J. of Fluid Mechanics, vol. 363, pp. 79-96*.
- [96] Unal M. F. & Rockwell D. (1988a): On vortex formation from a cylinder. Part1. The initial instability. *J. Fluid Mech., vol. 190 pp. 491-512*
- [97] Unal M. F. & Rockwell D. (1988b): On vortex formation from a cylinder. Part2. Control by splitter-plate interference. *J. Fluid Mech., vol. 190 pp. 513-529*
- [98] Utami T. and Ueno T. (1984): Visualization and picture processing of turbulent flow. *Experiments in Fluids 2, 25-32, Springer-Verlag*.

## Chapter 8: References-Related Publications

---

- [99] Vlachos P. P, Donnelly M. J. Telionis D. P. (1998): On the Wake of a Circular Cylinder Piercing the Free-Surface. *FEDSM'98-5177*.
- [100] Vlachos P.P. and Hajj M.R. (2000): A Cinema DPIV study of the unsteady character of the flow over a surface mounted prism. *4th International Colloquium on Bluff Body Aerodynamics*.
- [101] Vlachos P.P., and Telionis D. P., (2000): Three-Dimensional Streamwise Vortical Structures of a Turbulent Wake near the Free Surface. *FEDSM2000-11262, Boston, MA, 2000*.
- [102] Vlachos P.P., Hajj M. R. (1999): Flow Characteristics in the Separated Shear Layer. Proc. Of 10th Intern. *Wind Conf. On Wind Engineering, Denmark 1999*.
- [103] Vlachos P.P., Hajj M. R. (1999): PIV Measurements of Flow Characteristics in Separated Shear Layers. *ASCE EMD'99, Baltimore 1999*.
- [104] Vlachos P.P., Telionis D. P. Donnelly M. J (1999): The Design and Testing of a Smart Balance System. *AIAA 99-3165, Norfolk, 1999*.
- [105] Vlachos Pavlos P., Martin J. Donnelly, Tavis L. Potter, Demetri P. Telionis, Norman W. Schaeffler (1999): Post-Stall Flow Control of Sharp Edged-Wings. *AIAA99-0924, Reno, NV, 1999*.
- [106] Vlachos, P. P. and Telionis D. P., (2000) :Turbulence Characteristics in the Wake of a Circular Cylinder near the Free Surface, *FEDSM2000-11320, Boston, MA, 2000*
- [107] Vlachos, P. P., Zeiger M. D., and. Telionis D. P, (2000): The effect of free surface on the vortex shedding from inclined circular cylinders. *FEDSM2000-11266, Boston, MA, 2000*
- [108] Wei T. & Smith C. R.. (1986): Secondary vortices in the wake of circular cylinder. *J. Fluid Mech., vol. 169 pp. 513-533*
- [109] Westerweel J (1997): The effect of a discrete window offset on the accuracy of cross-correlation analysis of digital PIV recordings. *Exp. In Fluids 23 20-28, Springer Verlag*.

## Chapter 8: References-Related Publications

---

- [110] Westerweel J. (1993a): Digital Particle Image Velocimetry, Theory and Application. *Delft University Press*
- [111] Westerweel J. (1993b): Optical Diagnostics in fluid and thermal flow. *SPIE 2005 624-35*
- [112] Westerweel J. (1997): Fundamentals of Digital Particle Image Velocimetry. *Meas. Sci. Technol. 8 1379-1392.*
- [113] Willert C E and M Gharib (1991): Digital Particle Image Velocimetry. *Experiments in Fluids 10, 181-193 1991*
- [114] Williamson C.H.K (1992): The natural and forced formation of spot-like “vortex dislocations” in the transition of a wake. *J. of Fluid Mech. 243, pp 393*
- [115] Williamson C.H.K. (1988): The existence of to stages in the transition to three-dimensionality of the cylinder wake. *Physics of Fluids 31,pp 3165-3168.*
- [116] Williamson C.H.K. (1995): Vortex Dynamics in the Wake of a Cylinder, Fluid Vortices. *S.I. Green. (ed.), pp. 155-234*
- [117] Williamson C.H.K. (1996): Vortex Dynamics In the Cylinder Wake, Annual. Rev. *Fluid Mech., pp. 477-539*
- [118] Williamson C.H.K. and Brown G. L. (1998): A series in to represent the Strouhal-Reynolds number relationship of the cylinder wake. *Journal of Fluid and Structures, vol. 12, 1073-1085, 1998.*
- [119] Wu, J.M., Lu, X.Y., Denny, A.G., Fan, M., and Wu, J.Z. (1997): Post-stall lift enhancement on an airfoil by local unsteady control. Part I. Lift, drag, and pressure characteristics. *AIAA paper 97-2063.*
- [120] Wu, J.Z., Lu, X.-Y., and Wu, J.M. (1997): Post-stall lift enhancement on an airfoil by local unsteady control. Part II. Mode competition and vortex dynamics. *AIAA Paper 97-2064.*
- [121] Wu, J.Z., Lu, X.-Y., Denny A, Fan M. and Wu, J.M. (1998): Post-stall flow control on an airfoil by local unsteady forcing. *J. of Fluid. Mech. vol. 371 pp. 21-58.*

## *Chapter 8: References-Related Publications*

---

- [122] Wung T. S. and Tseng F. G. (1992): A color-coded particle tracking velocimeter with application to natural convection. *Experiments in Fluids* 13, 217-223
- [123] Wung T.S (1997): Quantitative visualization of 2D and 3D flows using a color-coded particle tracking velocimetry. *Atlas of Visualization III* edited by *The Visualization Society of Japan*.
- [124] Zdravkovich M. M., Brand V. P. Mathew G. & Weston A. (1989): Flow past short circular cylinders with two free ends. *J. Fluid Mech.*, vol. 203 pp. 557-575

## **Appendix I**

# **On The Wake Of A Circular Cylinder Near The Free Surface. Additional Data**

### **Effect of the asymmetry boundary conditions on the vorticity distribution.**

A supplementary experiment was performed in order to document the effect of the asymmetry of the boundary conditions on the streamwise and spanwise vorticity distribution of the wake. By demonstrating in the previous section the feasibility of observing the passing of the primary Von-Karman vortex through a plane of interrogation normal to the free stream we can extract information for both components of vorticity. For the second experiment the same experimental setup was employed. However, in this case three downstream stations were acquired for two elevation of the interrogation plane. The downstream stations were positioned approximately at 2,4,and 6 cylinder diameters downstream, while, the first elevation was intersecting the free surface level and the second one was the second was placed approximately

## *Appendix I: On The Wake Of A Circular Cylinder Near The Free Surface.*

### *Additional Data*

---

at one diameter above the base of the cylinder. Therefore a direct comparison of the effect of the boundary conditions can be preformed. In addition the downstream stations are placed in between the interrogation planes to increase the down stream spatial resolution at the free-surface level.

Initially we present comparisons of time-averaged results. Figures set 1 correspond to the mean velocity distribution of the flow field. Figure set 2 present to the mean vorticity distribution and figure set 3 to the mean turbulent kinetic energy. The free surface planes correspond to sub-figures 1,3,5 for each of the three station respectively, while sub-figures 2,4,6 correspond to the interrogation planes at the base of the cylinder for each station. The unsteady characteristics of the flow are presented in Animations 1 through 6 for each plane of interrogation. These results will be discussed. They are simply added as complementary visual information for the structure of the flow.

**Figure 1:** Time averaged velocity distributions

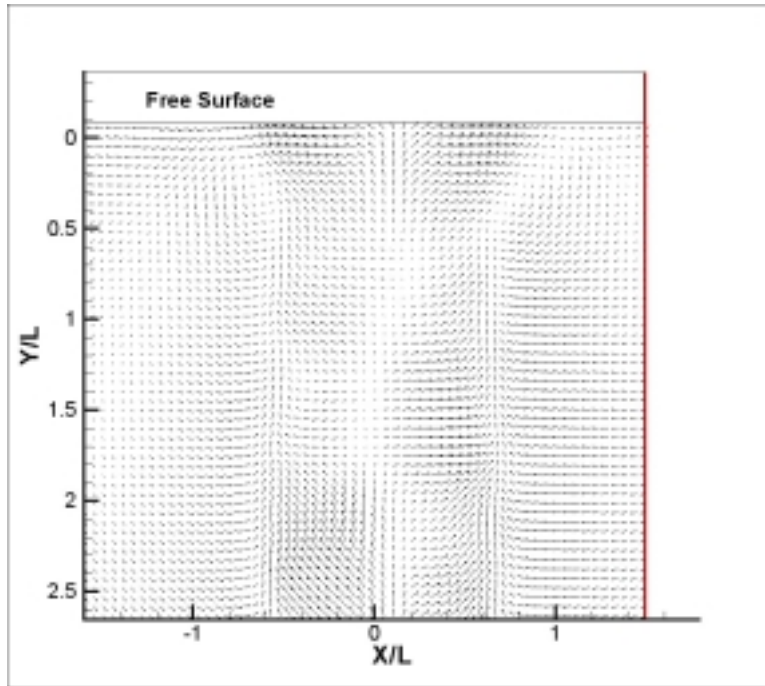


**Figure 1-1:** Time averaged velocity vectors for the first plane at the free surface.

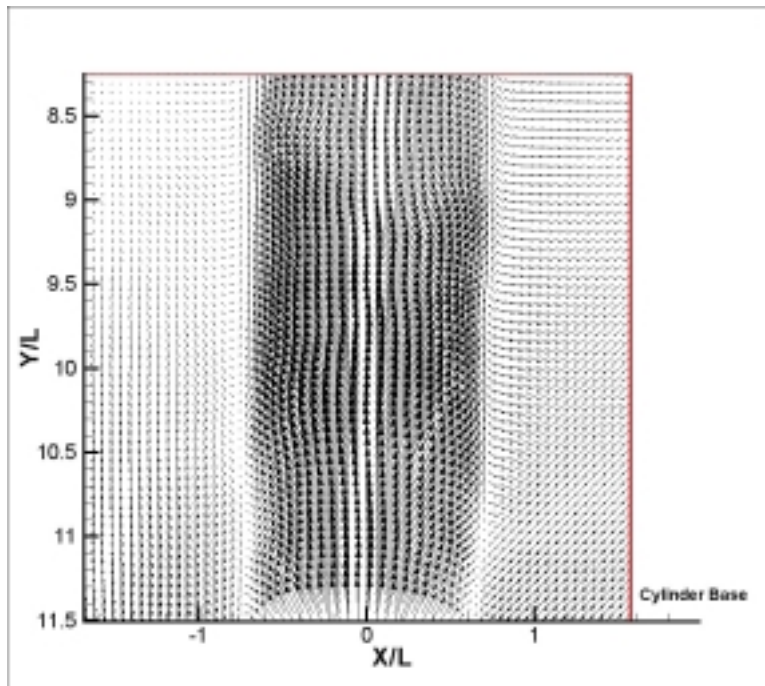


**Figure 1-2:** Time averaged velocity vectors for the first plane at the base of the cylinder

*Additional Data*

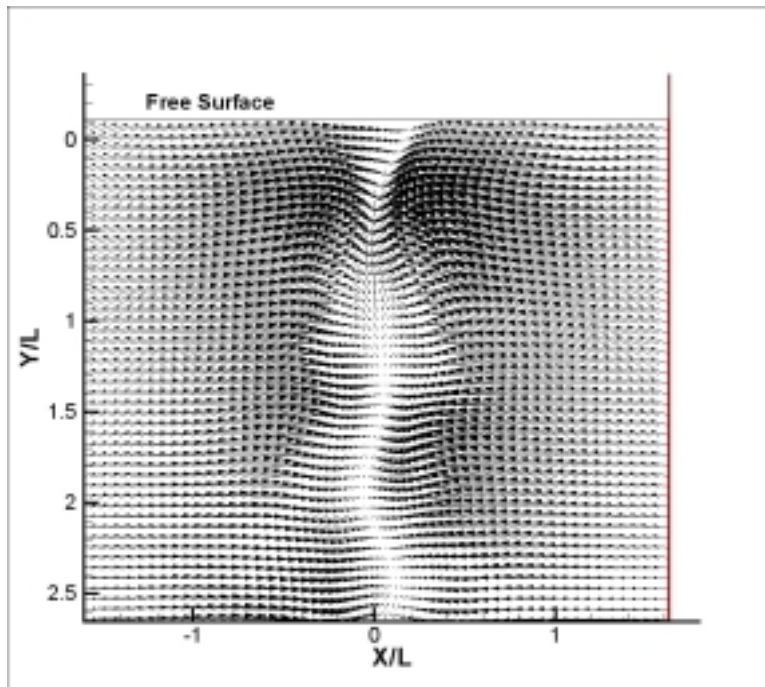


*Figure 1-3:* Time averaged velocity vectors for the second plane at the free surface.

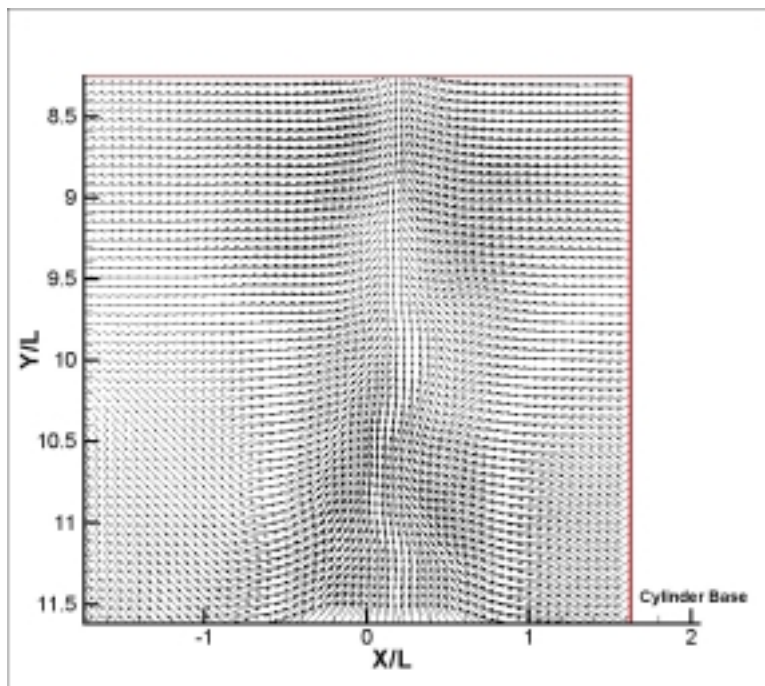


*Figure 1-4:* Time averaged velocity vectors for the second plane at the base of the cylinder

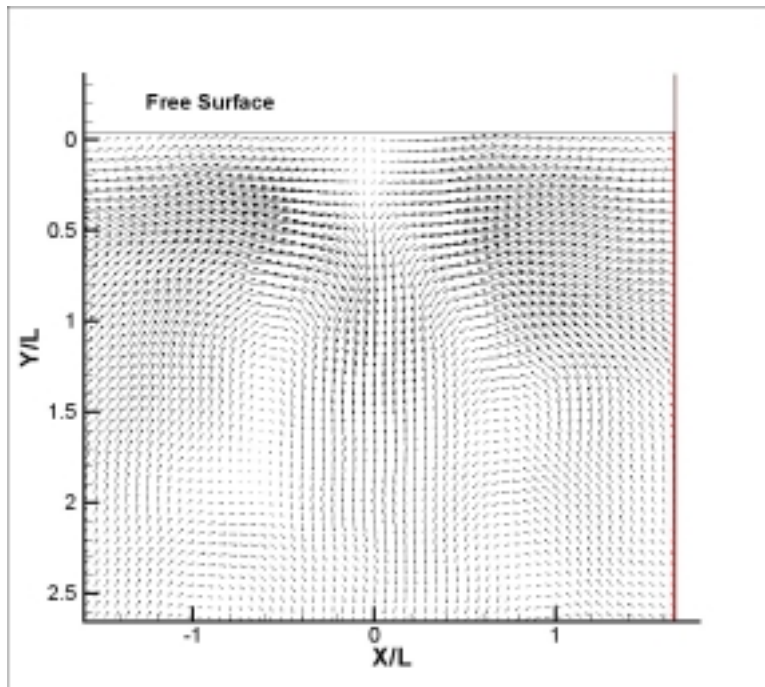


*Figure 1-5:* Time averaged velocity vectors for the second plane at the free surface.

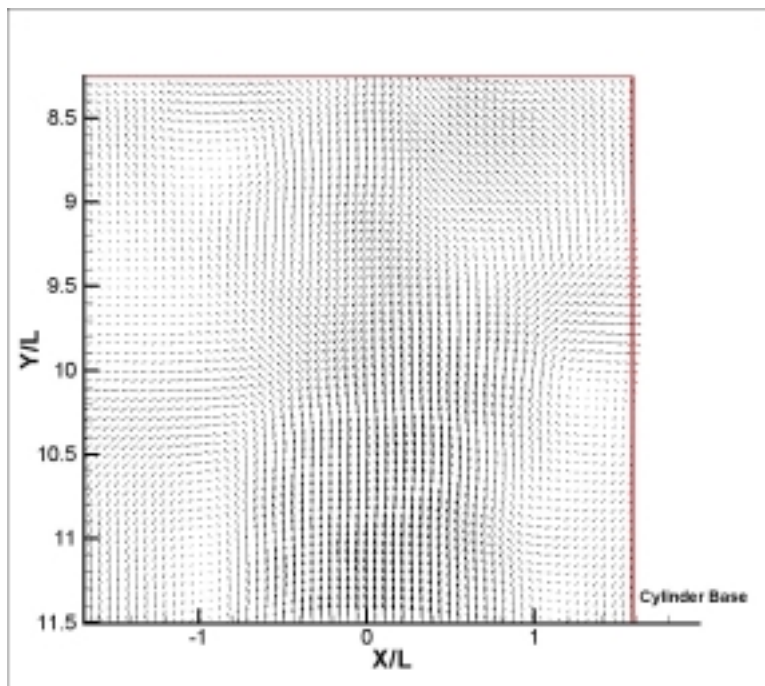


*Figure 1-6:* Time averaged velocity vectors for the second plane at the base of the cylinder

Figure 2: Time averaged vorticity distributions

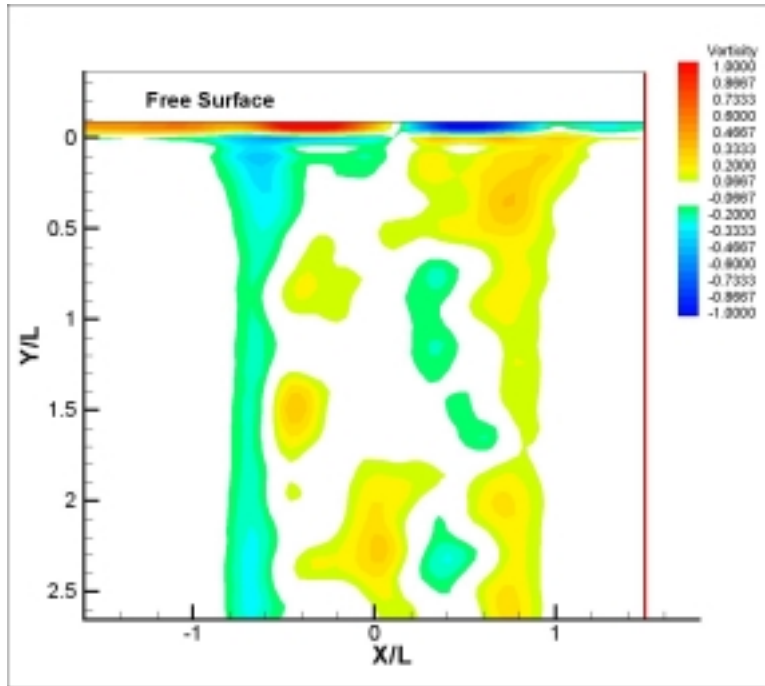


Figure 2-1: Time averaged vorticity for the first plane at the free surface.

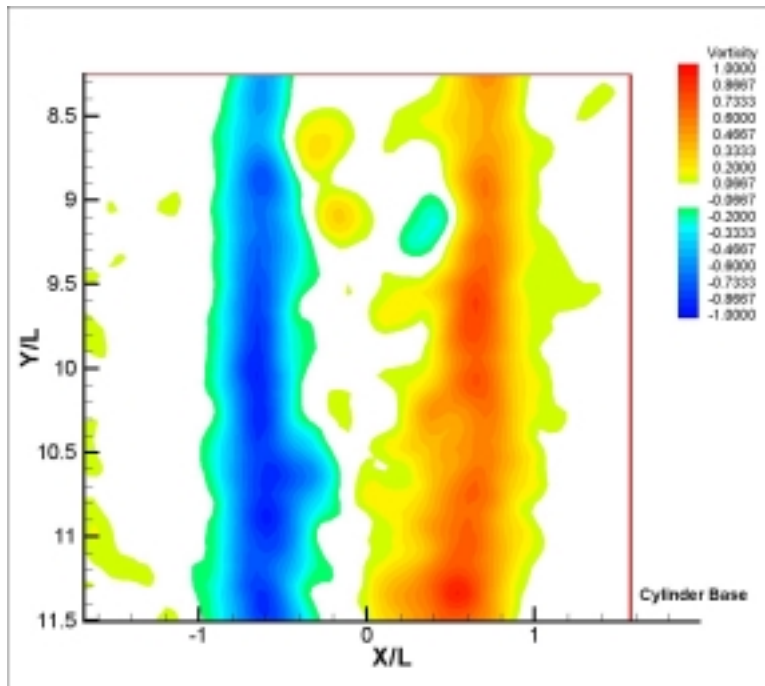
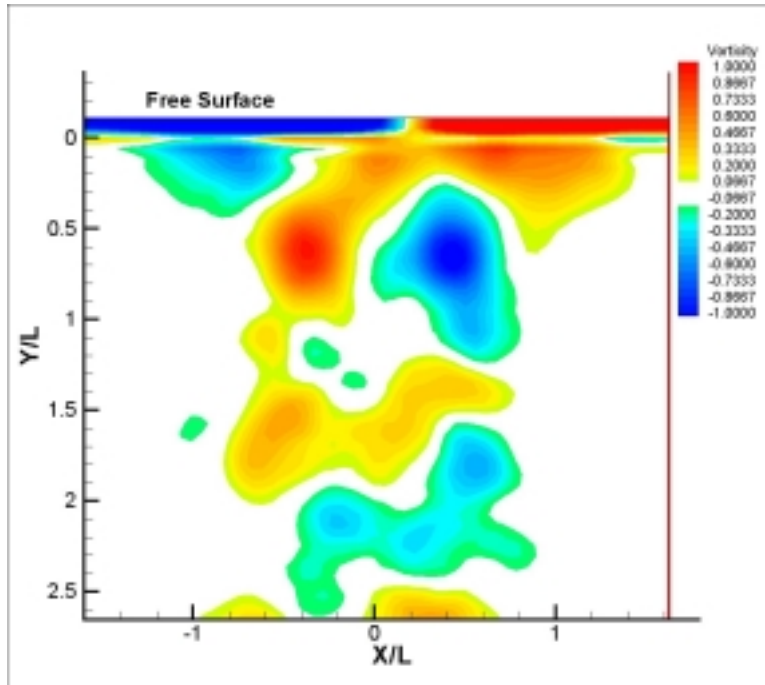


Figure 2-2: Time averaged vorticity for the first plane at the base of the cylinder

*Appendix I: On The Wake Of A Circular Cylinder Near The Free Surface.*

*Additional Data*



*Figure 2-3:* Time averaged vorticity for the second plane at the free surface.

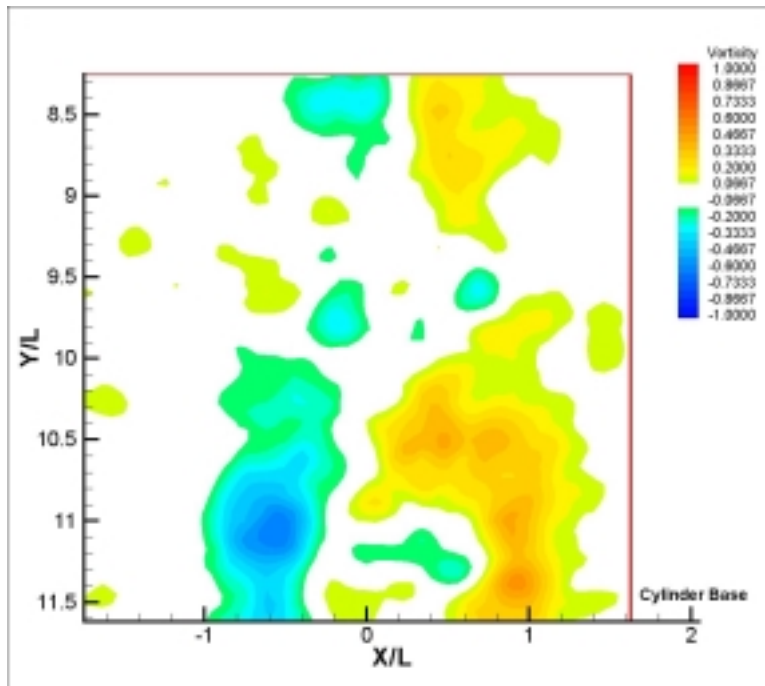


*Figure 2-4:* Time averaged vorticity for the second plane at the base of the cylinder

*Appendix I: On The Wake Of A Circular Cylinder Near The Free Surface.*

*Additional Data*

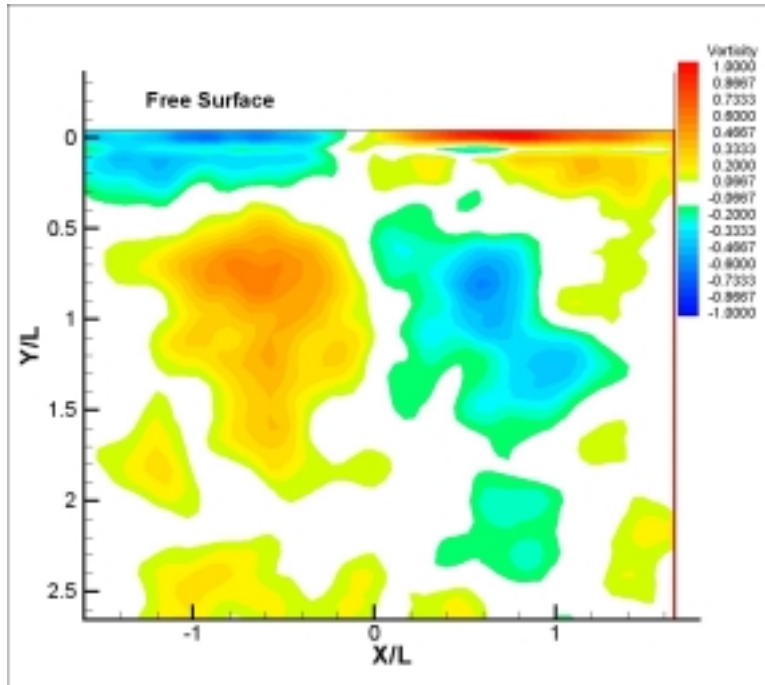


*Figure 2-5:* Time averaged vorticity for the second plane at the free surface.

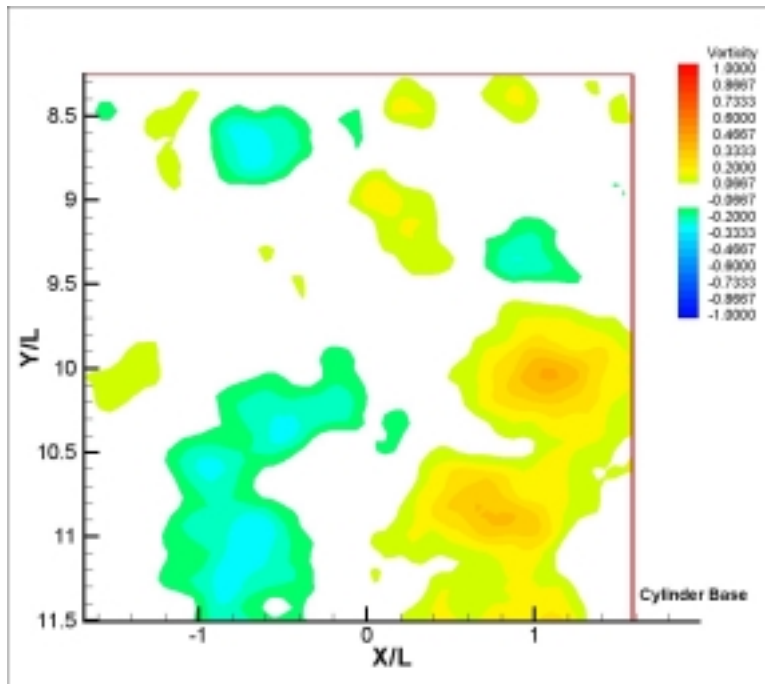


*Figure 2-6:* Time averaged vorticity for the second plane at the base of the cylinder

**Figure 3:** Time averaged in plane turbulent kinetic energy distributions

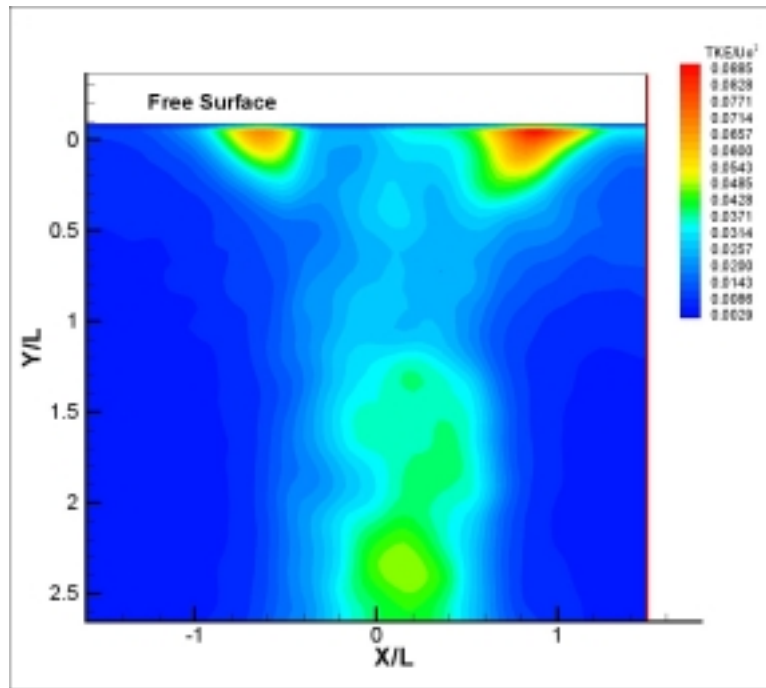


**Figure 3-1:** Time averaged in plane turbulent kinetic energy for the first plane at the free surface.

*Additional Data*

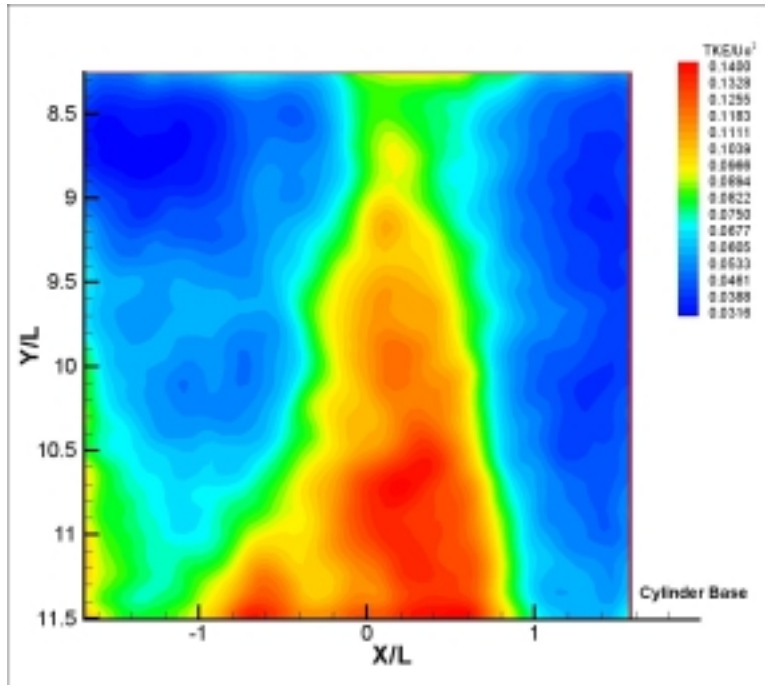


*Figure 3-2:* Time averaged turbulent kinetic energy for the first plane at the base of the cylinder

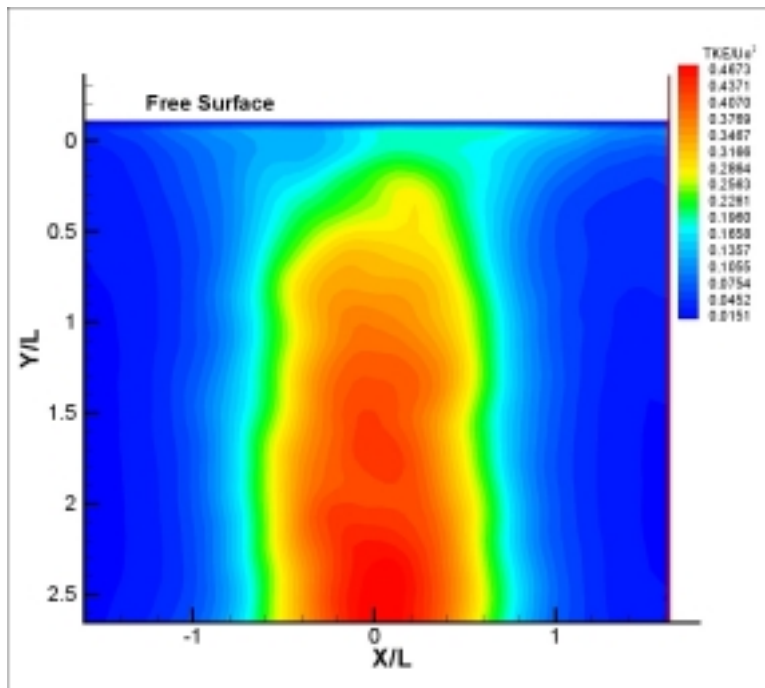


*Figure 3-3:* Time averaged turbulent kinetic energy for the second plane at the free surface.

*Additional Data*

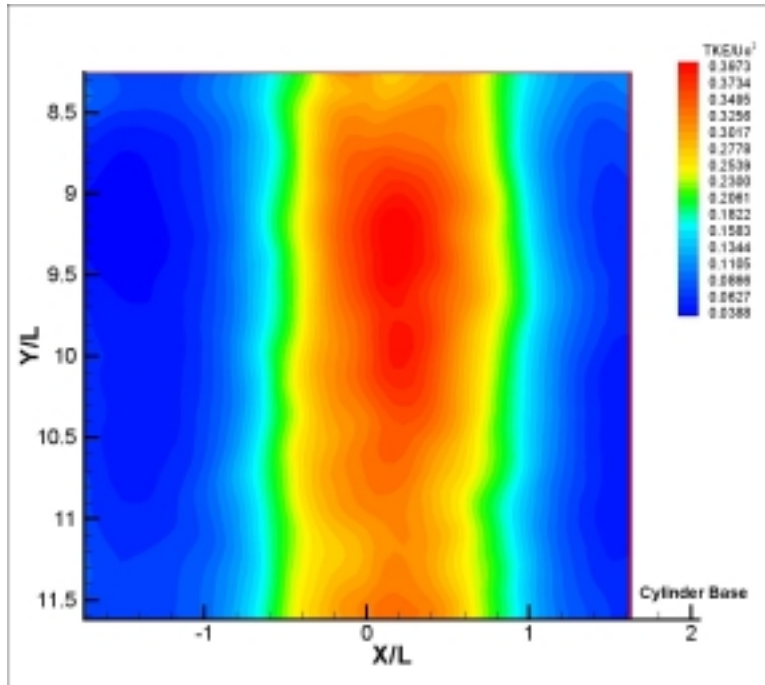


*Figure 3-4:* Time averaged turbulent kinetic energy for the second plane at the base of the cylinder

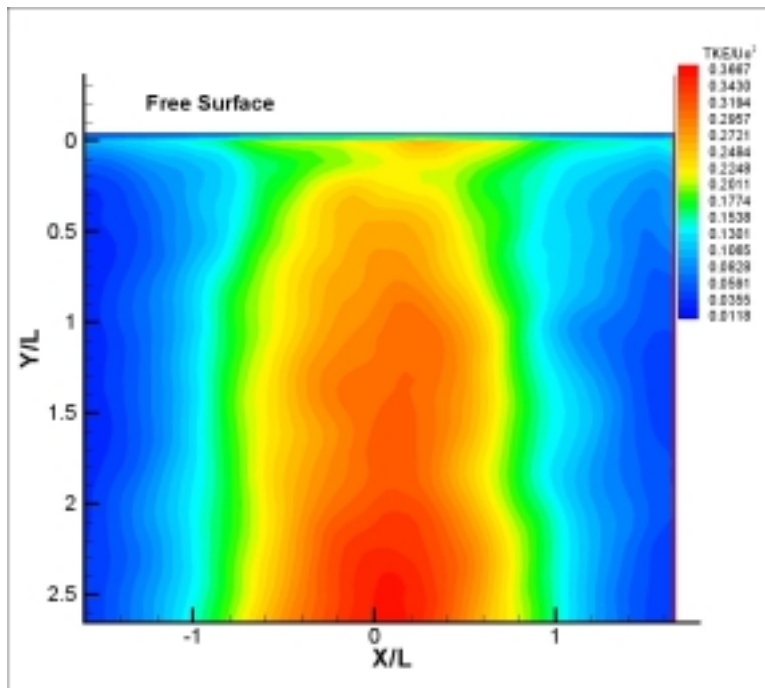


*Figure 3-5:* Time averaged turbulent kinetic energy for the second plane at the free surface.

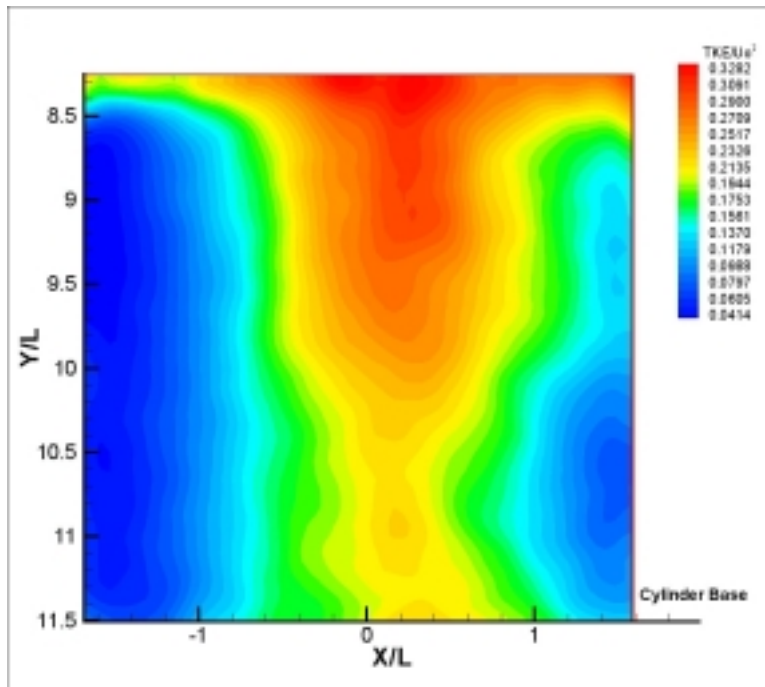
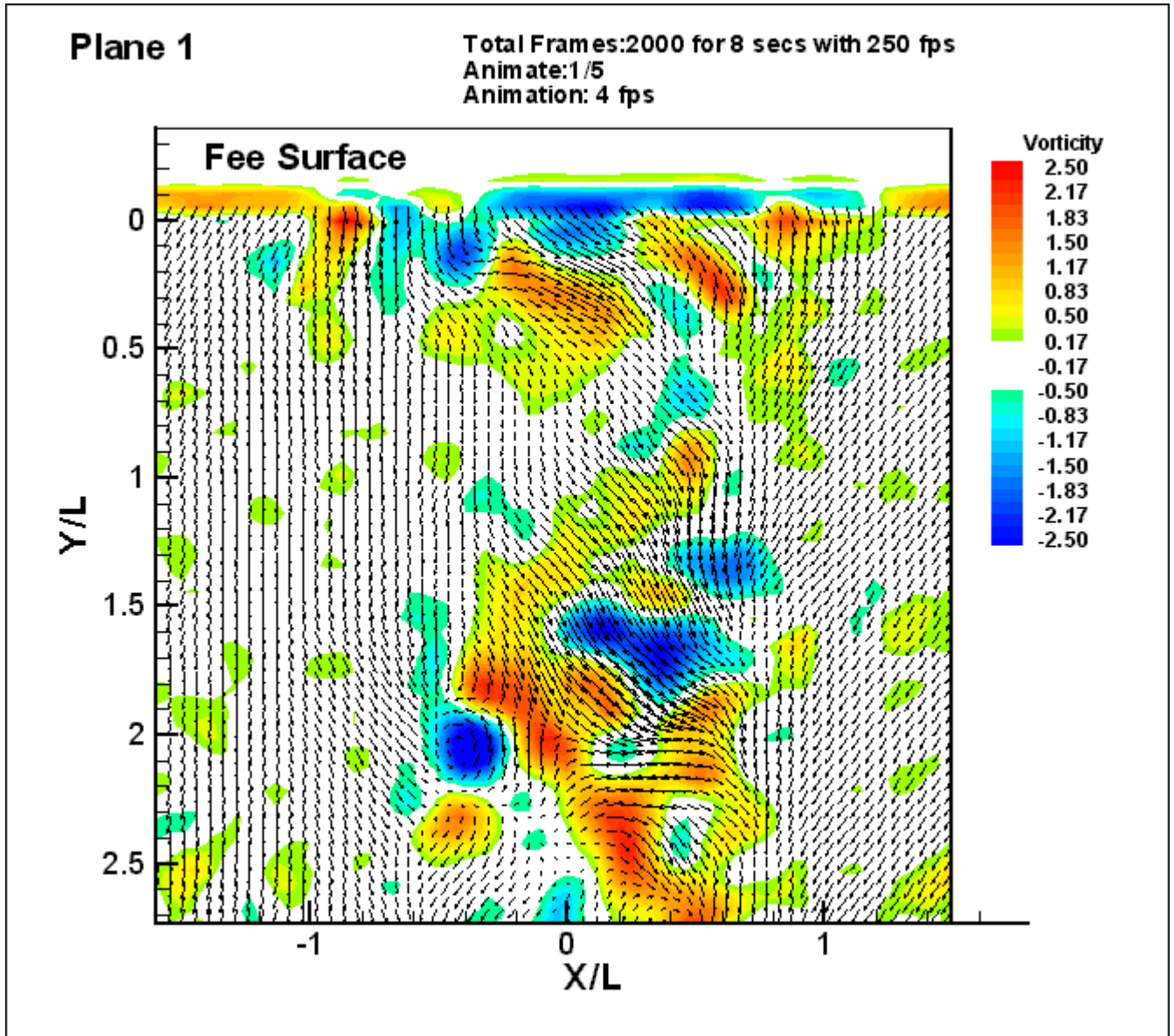


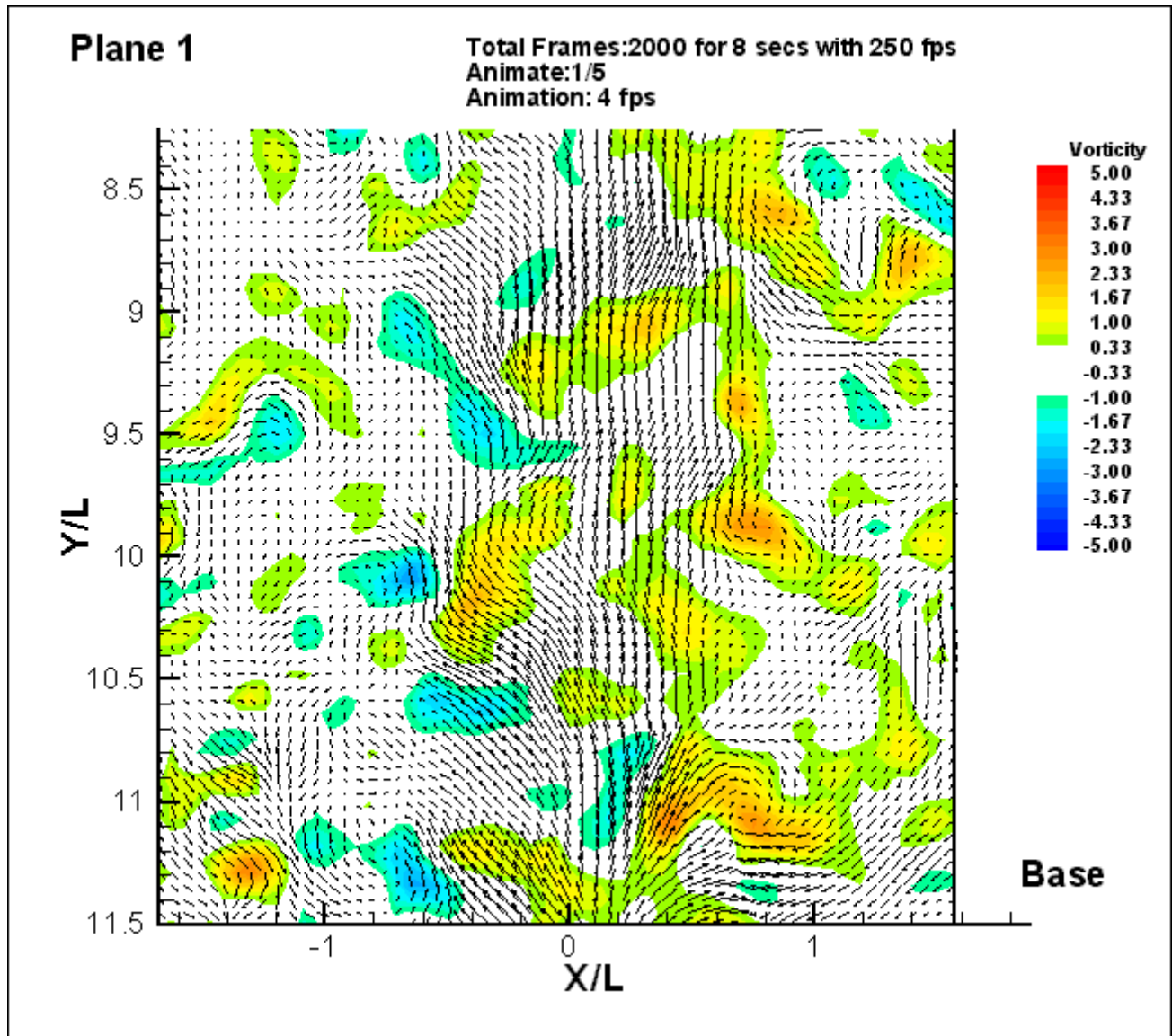
**Figure 3-6:** Time averaged turbulent kinetic energy for the second plane at the base of the cylinder

*Additional Data*

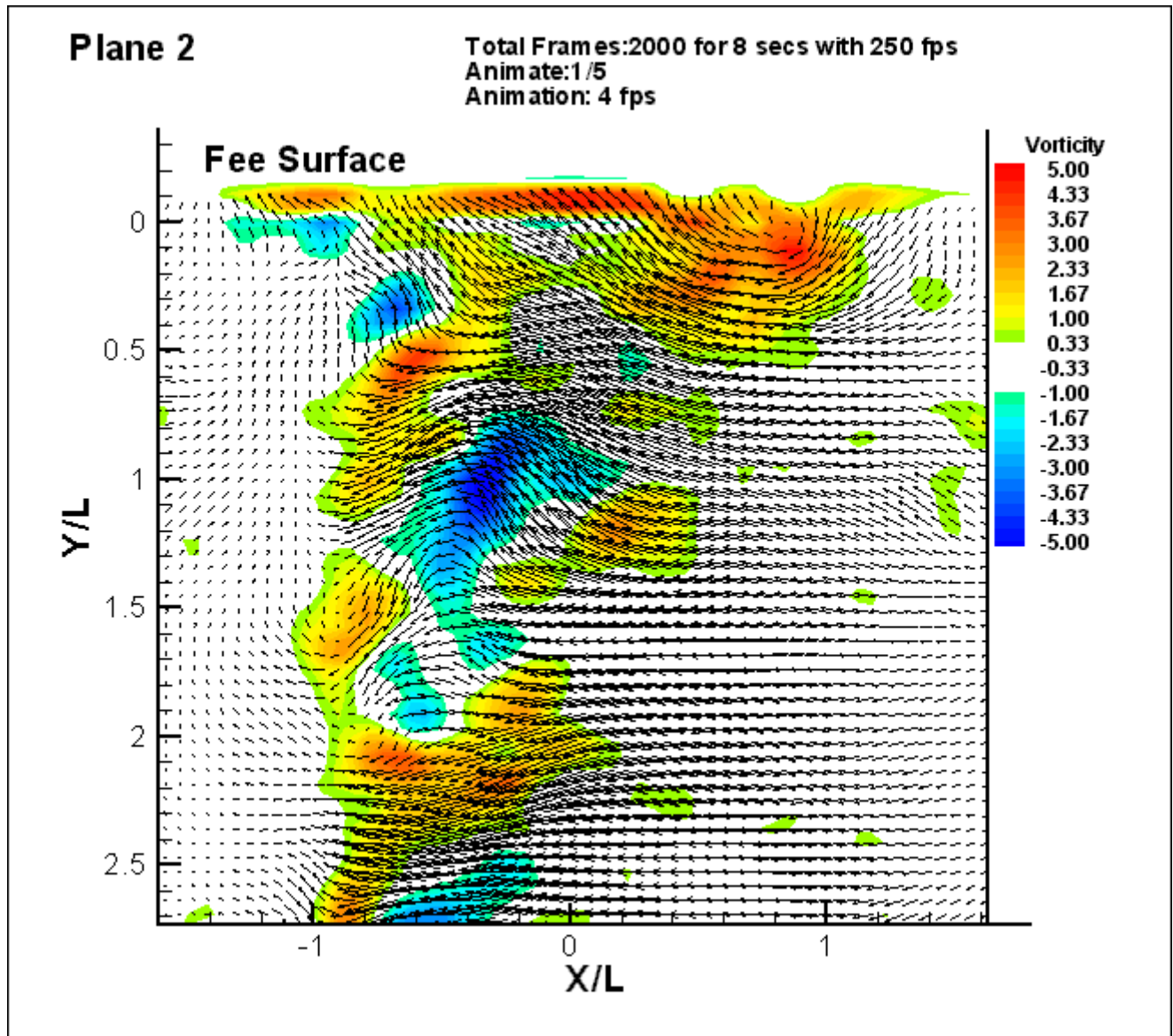


*Animation 1:* Animation of instantaneous vorticity distributions and velocity vectors at the free surface, for the first plane of interrogation

*Additional Data*

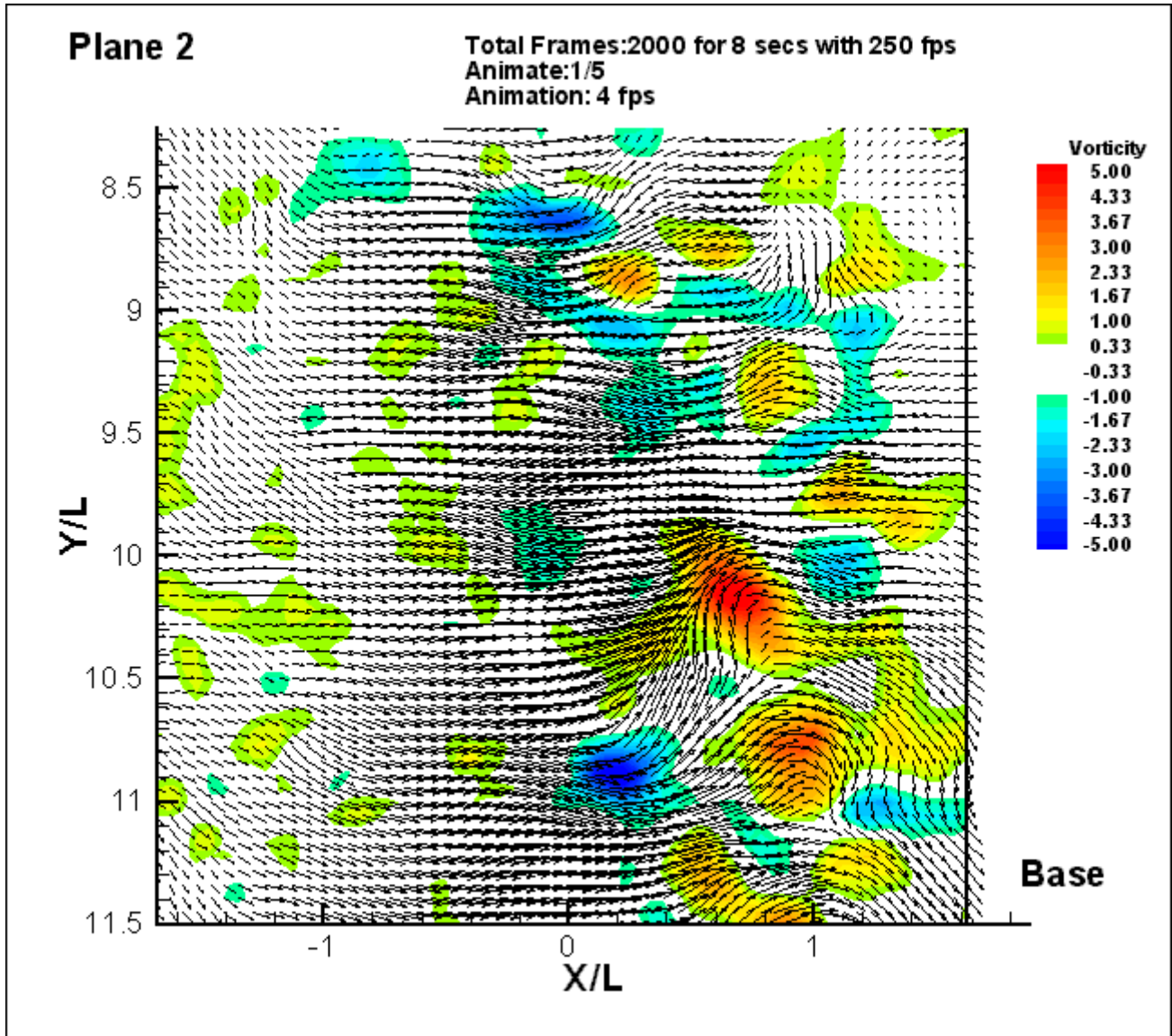


*Animation 2:* Animation of instantaneous vorticity distributions and velocity vectors at the cylinder base, for the first plane of interrogation

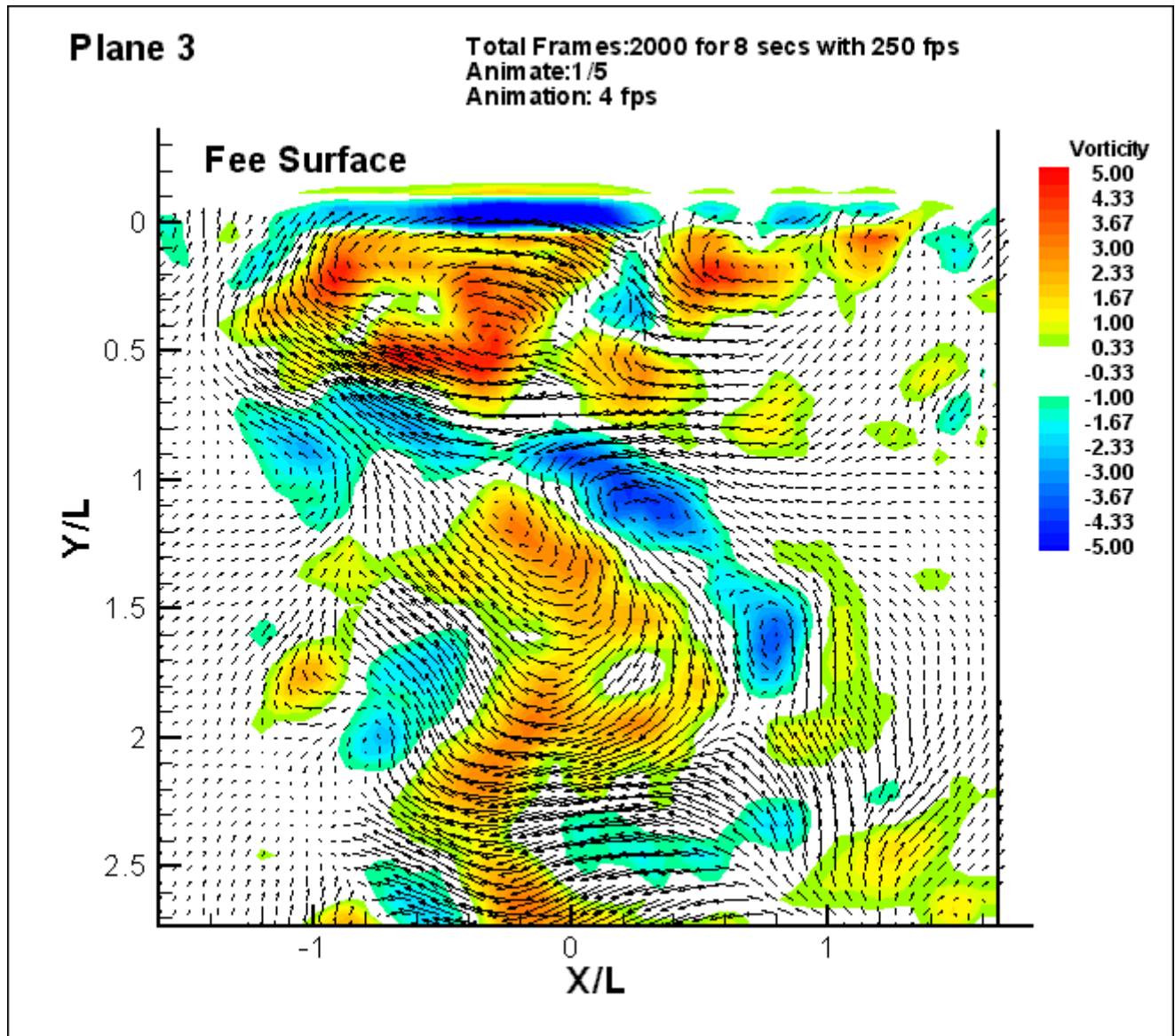


*Animation 3:* Animation of instantaneous vorticity distributions and velocity vectors at the free surface, for the second plane of interrogation

*Additional Data*

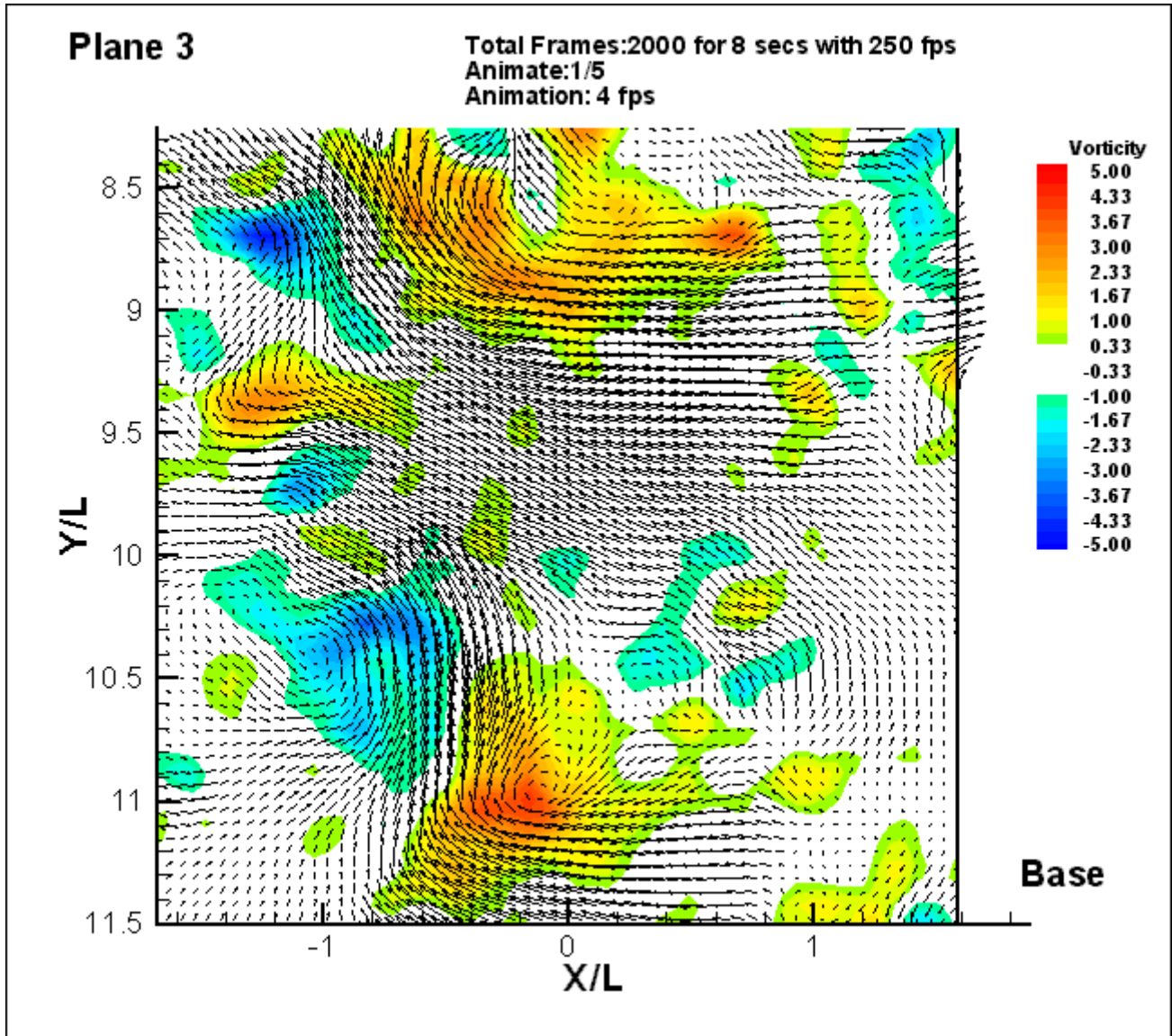


*Animation 4:* Animation of instantaneous vorticity distributions and velocity vectors at the cylinder base for the second plane of interrogation



*Animation 5:* Animation of instantaneous vorticity distributions and velocity vectors at the free surface, for the third plane of interrogation

*Additional Data*



*Animation 6:* Animation of instantaneous vorticity distributions and velocity vectors at the cylinder base, for the third plane of interrogation

## **PAVLOS P. VLACHOS**

Pavlos P. Vlachos was born on July 10 1971 in Athens, Greece. A single child with very dedicated parents and strong bonded family. During his childhood years spend most of his time between reading, listening to music and playing basketball. Loved to travel all over the Greek highlands and Europe. Soon, found great interest in studying physics and mathematics. On 1989 enter the Dept. of Mathematics of the Aristotelio University of Thessaloniki. More attracted towards engineering, on 1990 enter the Dept. Of Mechanical Engineering of National Technical University of Athens from which graduated on Sept 1995. Immediately was admitted to the Post Graduate School of NTUA where started his scientific carrier conducting research in the area of jet engines and turbomachinery. On August 26 of 1996 was admitted in the Engineering Science and Mechanics Dept. of Virginia Tech. Conducted research in the area of experimental fluid mechanics. Awarded the degree of Masters of Science in Engineering Mechanics on December 1998. Continued his graduate studies towards the degree of Doctor of Philosophy, which he completed on August 2000.